# UNIVERSITY OF SOUTHAMPTON

FACULTY OF ENGINEERING AND THE ENVIRONMENT

Engineering Sciences Unit


## Fatigue crack growth behaviour in a shot peened low pressure steam turbine blade material

by


**Binyan He**


Thesis for the degree of Doctor of Philosophy

August 2015

UNIVERSITY OF SOUTHAMPTON

# ABSTRACT

FACULTY OF ENGINEERING AND THE ENVIRONMENT

Engineering Sciences Unit

Thesis for the degree of Doctor of Philosophy

## FATIGUE CRACK GROWTH BEHAVIOUR ANALYSIS IN A SHOT PEENED LOW PRESSURE STEAM TURBINE BLADE MATERIAL

Binyan He

In this Ph.D thesis, short fatigue crack initiation and early growth behaviour under low cycle fatigue conditions has been investigated in FV448. Four different surface conditions of notched and plain bend bar samples have been considered: polished, ground, T0 (industrially applied shot peening process) and T1 (a less intense shot peening process). Fatigue crack aspect ratio (*a/c*) evolution in the early stages of fatigue in the polished and shot peened cases has been studied by interrupted heat tinted fatigue tests in both a notch root and in a plain bend bar. It was found that crack aspect ratio development in the baseline polished condition was more microstructure dependent (linked to stringer morphology) while the crack morphology in the shot peened cases was more related to the shot peening process (i.e. the distribution of the work hardened layers and compressive residual stress distributions). Shot peening has acted to change both the initiation and early crack growth processes.

A benefit to fatigue life in bending, even under LCF conditions, has been observed in these tests if a sufficiently severe shot peening condition is applied in a constrained notch configuration. The beneficial effect of shot peening (in the T0 condition) was retained even at a high strain level ($\Delta\varepsilon_{11}$ = 0.68 %), $N_{f,\ ground} < N_{f,T1} < N_{f,\ polished} < N_{f,\ T0}$. The *a/c* evolution effects were incorporated in *K*-evaluations and used in calculating better estimated *da/dN* from surface replica data. When the true crack shape evolution is incorporated into the $\Delta K$ analysis, part of the benefit of shot peening can be linked to its effects on crack shape evolution (and thus effects on $\Delta K$). Apparent residual stress (based on crack driving force $\Delta K$ difference) was then derived to further describe the benefit of shot peening in terms of reduced *da/dN* and this was seen to still extend significantly below the measured compressive residual stress profile, indicating the importance of both the strain hardened layer and possible stress redistribution effects during crack growth, as well as any crack shape morphology effects.

Serial mechanical sectioning and high resolution X-ray tomography have been used to study the three-dimensional morphology of small fatigue cracks in

these test conditions in greater detail. These studies have complemented the fractographic observations possible from the final fracture surface by studying smaller cracks produced partway through the fatigue life. In the unpeened condition, inclusions (Alumina or MnS) seem again to dominate short crack morphology. Subsurface crack coalescences were observed in T0 shot peened condition at a depth of about 150 ~ 180 μm, which can be linked to both the extent of the compressive residual stress as well as the depth of the plastic deformation arising from the intense shot peening process T0. Shot peening (in this material and particular set of test cases) appears to provide a different defect population that initiates fatigue cracks from shot peening induced cracks and then competes with the underlying metallurgical defect populations. A blend-polish-peen repair process was also conducted on shot peened notched samples which have experienced ~ 65 – 80 % of established fatigue life. Although there seems no obvious improvement in the total fatigue life (partly due to the change in macroscopic notch geometry) fatigue crack growth behaviour still benefits from the repair process (from the viewpoint of a reduced *dc/dN*), especially when there was a large pre-existing crack that was not completely removed by the re-polishing process. In summary, shot peening can be considered to derive its lifetime benefit from its slowing of the early stages of fatigue crack growth, partly via alteration of surface-breaking crack shape, which reflects the difficulty growing through the strain hardened and compressive residual stress surface layers, but also through significant deceleration of the crack growth itself through these layers. Further modeling effort to establish how stress redistribution effects and local strain hardening variations affect this crack growth in detail are necessary.

# Table of Contents

# List of tables

# List of figures

# DECLARATION OF AUTHORSHIP

I, BINYAN HE

declare that this thesis and the work presented in it are my own and has been generated by me as the result of my own original research.

'Fatigue crack growth behaviour in a shot peened low pressure steam turbine blade material'

I confirm that:

1. This work was done wholly or mainly while in candidature for a research degree at this University;
2. Where any part of this thesis has previously been submitted for a degree or any other qualification at this University or any other institution, this has been clearly stated;
3. Where I have consulted the published work of others, this is always clearly attributed;
4. Where I have quoted from the work of others, the source is always given. With the exception of such quotations, this thesis is entirely my own work;
5. I have acknowledged all main sources of help;
6. Where the thesis is based on work done by myself jointly with others, I have made clear exactly what was done by others and what I have contributed myself;
7. Parts of this work have been published as:

1) B.Y. He, K. A. Soady, B.G. Mellor, A. Morris and P. A. S. Reed. *Effect of shot peening on short crack growth rate and resulting low cycle fatigue behavior in low pressure turbine blade material*. Materials Science and Technology. 29(7), 2013, 788–796.
2) B.Y. He, K.A. Soady, B. G. Mellor and G. Harrison, P. A. S. Reed. *Fatigue crack growth behaviour in the LCF regime in a shot peened steam turbine blade material*. Accepted. International Journal of Fatigue. March 2015
3) B.Y. He, O.L. Katsamenis, B.G. Mellor and P. A. S. Reed. 3-D analysis of fatigue crack behaviour in a shot peened steam turbine blade material. Materials Science and Engineering: A, 642 (2015) 91–103

Signed:.....

Date:.....

# Acknowledgements

During these four-year Ph.D study in Southampton, I have so many people to thank. Without their generous help and support, I couldn't come to this point.

First and foremost, I wish to express my special appreciation and great thanks to my two supervisors, Professor Philippa Reed and Dr. Brian Mellor, for their unconditional support, guidance and encouragement during these four years. I am very grateful for your comfort and sympathy during one of the most difficult times of my life. I am also indebted to Dr Kath Soady (now at E.ON Technologies (Ratcliffe) Ltd.) for her great help in my research (for example, showing me how to do a replica test which I used quite often in my study), and continuous support in these years. I must also thank Professor Andy Morris and Dr. Iain Patterson for their useful discussions. I deeply appreciate the financial support from China scholarship council and University of Southampton.

Thanks to Gary Harrison at the University of Manchester for his help with XRD measurements. I recognize the support and help from Power Engineering Services (EOn) for their support of blend-polish-peen repair test. I would like to acknowledge the μ-VIS X-Ray imaging centre of the University of Southampton for provision of tomographic imaging facilities, and the invaluable support of Dr. Orestis Katsamenis and Dr. Richard Boardman in the μ-VIS centre of the University of Southampton. I would like to extend my gratitude to Chao You, who offered me great help in XRD residual stress measurement and stress concentration factor calculation; to Dr. Rong Jiang, who gave me supports from time to time; to Dr. Sam Keyes and Jennifer Crump in University of Southampton who have been an inspiration on how to play with Avizo software and 3D crack reconstruction. I am also very grateful for the help and assistance in the lab from Dave Beckett and Heather Porter. A special acknowledgement goes to my friends and office mates (too many to list here but you know who you are) of many years. Thank you all providing me support and friendship these years.

I would also like to thank my grandma, my parents, brother and sister, for their love and concern all these years. Since they can't speak English, please allow me to express my sincerely gratitude to them in Chinese. 致我最亲爱的外婆，父亲和母亲，哥哥和嫂子，姐姐和姐夫。谢谢你们这些年来，对我不论是学业还是生活上的支持和鼓励。都快三十岁的人了，既未成家，也未立业，定是让你们操碎了心。亲爱的外婆，虽然你已经离开了我们多年，我却从未忘记过你那慈祥的笑脸；时常梦里见到

你，醒来泪沾襟。 你虽不识字，许多事情却能娓娓道来，不管是旧社会的苦难艰辛，还是神话故事民间传奇，都是你给我的最好的睡前故事。是你的用心呵护，才让我度过了一个无忧无虑的童年。而在你卧病在床之时，我却没能力照顾你，保护你，没能尽一份孝心，是我一生的遗憾。父亲母亲，你们为这个家操劳了一辈子。现在就让我来接力吧，我会尽我所有，让你们安度晚年。哥哥，当年你说，要来参加我的毕业典礼，要亲眼看着我穿上博士袍。可如今，你却失守承诺，匆匆去了远方。记得儿时，你问妈妈，妹妹去哪了。妈妈逗你说，把妹妹卖给别人了。听后你就一个人躲到房里默默流泪。每次想到这个，我都泪如雨下。这辈子的兄妹情谊，我会珍藏在心。嫂子，在哥哥走了的这两年里，家里的事，也都是你来打点，辛苦你了。我能安心完成学业，有你的功劳和付出。姐姐，在我们兄弟姐妹里，就属你最细心最体贴。你一直默默地为父母分担着一切，我都看在眼里，记在心上。此外，我还要跟两个侄儿宝贝说声谢谢，你们的欢声笑语，天真稚趣，是你们爷爷奶奶最大的宽慰。姑姑盼着你们健康成长，盼着你们能一字一句地读出姑姑的这段话，读懂姑姑此时心中的珍惜和感动。这些年漂泊在外，于家，未尽到儿女的责任，于已，未能有所作为，因而惭愧。寥寥几句话，不足以表达我心中的感激和愧疚。前方路遥，你们是我前行的最大动力。

Last but not least, to my fiancé, Wei Guo, thanks for all your love, support and understanding these years. I'm really blessed to have you.

# Definitions and Abbreviations

| | |
|---|---|
| $d_0$ | The unstressed lattice inter-planar spacing |
| $\psi$ | The angle between the sample normal and the diffracting plane normal |
| $2c$ | Surface crack length |
| $2c_{project}$ | Projected surface crack length |
| 2D | Two dimensional |
| $2\alpha$ | Half of the angle of a square pyramid in the microhardness indentor with opposite edges, $2\alpha = 148°$), |
| $2\theta$ | X-ray diffraction peak position |
| 3D | three dimensional |
| $a$ | Depth of fatigue crack in sample width direction |
| $a/c$ | Crack aspect ratio |
| $a/w$ | The ratio of the crack length to specimen width ratio |
| $c/c_{project}$ | Crack tortuosity |
| $c_i$ | Half of the crack length at the $i^{th}$ fatigue cycle |
| $c_{i+1}$ | Half of the crack length at the $(i+1)^{th}$ fatigue cycle |
| $c_{i-1}$ | Half of the crack length at the $(i-1)^{th}$ fatigue cycle |
| $da/dN$ | Fatigue crack growth rate |
| $dc/dN$ | Short fatigue crack growth rate |
| $d_{indentation}$ | The diagonal of the micro indentation |
| Direction L | Longititunal direction |
| Direction S | Short transverse direction |
| Direction T | Transverse direction |
| $d_n$ | Inter-planar spacing of planes normal to the surface |
| $h_{depth}$ | The depth of the micro indentation |

| | |
|---|---|
| $H_{v,0.2}$ | Vickers hardness under 200g load |
| $J_c$ | The driving force for elastic–plastic short flaws |
| $K$ | The stress intensity factor |
| $K_{closure}$ | Stress intensity factor range at which the crack closes |
| $K_I$ | Mode I stress intensity factor |
| $K_{IC}$ | Plane strain fracture toughness |
| $K_{max}$ | The maximum stress intensity factor |
| $K_{min}$ | The minimum stress intensity factor |
| $K_t$ | Elastic stress concentration factor |
| *Lc* | Profile filter value |
| *Lr* | Required evaluation length |
| *n* | An integer |
| $N_f$ | Number of fatigue cycles to failure |
| $N_{f/2}$ | Half of the expected total life |
| $N_i$ | Number of fatigue cycles *i* |
| $N_{i+1}$ | Number of fatigue cycles *i+1* |
| $N_{i-1}$ | Number of fatigue cycles *i-1* |
| $R_a$ | Arithmetical mean of vertical deviation of the assessed roughness |
| $R_z$ | Maximum height of roughness profile |
| $S_a$ | Arithmetical mean of vertical deviation of the assessed roughness |
| $S_z$ | Maximum height of surface |
| $W_e$ | The elastic and plastic components of the remote strain energy density range |
| $W_p$ | The plastic components of the remote strain energy density range |
| Z | The atomic number |
| $Z_{Fe}$ | The atomic number of iron |

| | |
|---|---|
| $\Delta\varepsilon$ | Strain range |
| $\Delta\varepsilon_{11}$ | Strain range in the direction parallel to the tensile axis |
| $\Delta\varepsilon_{p}$ | Plastic strain range |
| $\Delta K$ | Stress intensity factor range |
| $\Delta K_{depth}$ | Stress intensity factor range at the bottom of crack |
| $\Delta K_{eff}$ | Effective stress intensity factor range |
| $\Delta K_{surface}$ | Stress intensity factor range at the surface of crack |
| $\Delta\sigma$ | The applied stress ranges. |
| $\theta$ | The diffraction angle |
| $\lambda$ | X-ray wavelength |
| $\varphi$ | The angle between a fixed direction in the plane of the sample and the projection in that plane of the normal to the diffracting plane |
| AFM | Atomic force microscopy |
| $Area_{semi-ellipse}$ | The area of semi-ellipical fatigue crack |
| B1 | Blend-polish-peen repair sample, without repeening |
| B2 | Blend-polish-peen repair sample, repeened |
| BEI | Backscattered electron imaging, |
| CTE | Coefficient of thermal expansion |
| CTOD ($\delta$) | Crack tip opening displacement |
| EBSD | Electron back scatter diffraction |
| EDS | Energy dispersive X-ray spectroscopy |
| FWHM | Full width at half maximum |
| G | Sample of ground surface condition |
| HCF | High cycle fatigue |
| LCF | Low cycle fatigue |
| LEFM | Linear elastic fracture mechanics |

| | |
|---|---|
| LP | Low pressure |
| P | Sample of polished surface condition |
| PBB | Plain bend bar |
| PSB | Persistent slip band |
| SCOD | Surface crack opening displacement |
| SEI | Secondary electron imaging |
| SRCT | Synchrotron radiation computed tomography |
| T0 | Intense shot peening process, industry applied parameter |
| T1 | Less intense shot peening process |
| XRD | X-ray diffraction |
| µ-CT | Microfocus computed tomography |

# Chapter 1: Introduction

## 1.1 Background

### 1.1.1 Power generation

A power station is an industrial facility for the generation of electric power. Depending on the energy source harnessed, a power plant can be classified as: nuclear, fossil fuel or hydroelectric. In a modern power station, mechanical power is produced by a heat engine that transforms thermal energy (which often comes from fuel combustion) into rotational energy; then a rotating machine converts this mechanical power into electrical power by creating relative motion between a magnetic field and a conductor. For electricity generation purposes, multi-cylinder turbine designs are usually utilised in power plants, and the number of cylinders is dependent on design considerations. A typical arrangement for 500-900 MW output in a fossil-fired power station (coal, oil or gas) or a gas-cooled nuclear station will have one high pressure (HP) turbine, one intermediate pressure (IP) turbine and two low pressure (LP) turbines [1].

### 1.1.2 Steam turbine material requirements

Steam turbine blades play a key role in power generation and they are critical components used to convert the thermal energy of high temperature and high pressure steam flowing down a pressure gradient into the mechanical energy of a rotating output shaft. A schematic of a steam turbine blade is given in Figure 1- 1(a). The choice of materials for steam turbine blade applications is based on their ability to provide suitable properties for the severe service conditions they must endure. The material requirements for the high pressure (HP) and low pressure (LP) steam turbines are detailed in Table 1- 1.

Both for high pressure and low pressure steam turbine blades, adequate tensile strength is required to resist the centrifugal and bending stresses due to high rotational accelerations under service conditions. Strength without ductility is not desirable; ductility is needed to accommodate stress peaks and stress concentration features, as well as required wear properties. High cycle fatigue failures take place as a result of vibrations arising from the fluctuation

of the bending stress due to the asymmetric flow of steam. It is reported that fatigue failure initiates from various locations of the blade, 26 % of failures initiate from the shroud, 20 % from the lacing hole and 40 % in the aero foil region and 14 % in the blade attachment [2, 3]. Resistance to both high cycle fatigue (HCF) and low cycle fatigue (LCF) are crucial properties for turbine blades. Low cycle fatigue loadings arise during start-stop cycles of the whole turbine. During shut down, the turbine blade experiences zero stress whilst during start-up very high stresses are experienced, when it comes in contact with steam at high temperature and pressure; the change of stress from the stress-free cold condition to the high stress value during the start-up transient and back to zero stress after shut-down forms one major stress cycle. Generally, the turbine is designed for a particular number of such cold starts during its design life of about 40-50 years [4]. The number of such cold starts is however increasing beyond these original design parameters due to the increased use of renewables in the electricity network and the concomitant need for conventional plant to cover any fluctuations in energy supply [5].

High creep resistance is particularly crucial for high pressure turbine blades, since they operate at high temperature (about 568 °C) and high pressure conditions [6]. However, creep resistance is not so important in the low pressure turbines where temperatures are relatively low (about 250 °C). Similarly, oxidation resistance is of greater importance in the HP turbine than in the LP turbine.

In addition, the low pressure turbine blade should possess an excellent resistance to corrosion and scale formation in fast flowing wet steam. Hot and ‘wet’ steam will be condensed in the low pressure turbines during the heat cycles. However, not only pure steam, but also various impurities such as oxidized scale from the superheaters or impurities from the boiler feedwater will pass through the turbine [6].This results in the deposition of impurities on the LP blades and gradually localized regions of high salt concentration.

## 1.2 Steam turbine blade materials and their manufacture

An ideal turbine blade material should have both high tensile and fatigue strength, be corrosion and erosion-resistant, exhibit high ductility, be easily formed and manufactured, be widely available from multiple sources, and of

course be obtained at reasonable cost [7]. There are two potential candidates for use in steam turbine blades: austenitic stainless steels and ferritic heat resistant steels. The creep strength of austenitic stainless steels and ferritic heat resistant steels are described in Figure 1- 2, respectively. It is apparent that austenitic stainless steels exhibit better creep resistance than ferritic heat resistant steels, which means the former will satisfy the elevated temperature and high pressure requirements best. However, as shown in Table 1- 2, the low thermal conductivity and high coefficient of thermal expansion (CTE) of austenitic steels makes them highly susceptible to thermal fatigue and this severely restricts their cyclic capabilities in a power plant [8], especially as modern power stations will endure regular shut downs and cold starts. Ferritic heat resistant steels offer an attractive alternative as they exhibit a lower CTE and higher thermal conductivity. Furthermore, they provide an ideal set of properties for turbine blading as long as the temperature does not exceed 480 °C [1].

Manufacturing is the part of the production process which is directly concerned with the change of form or dimensions of the part being produced. Nearly all steam turbine blade materials in common use are wrought materials [7]. Wrought materials usually exhibit some degree of directionality of properties such as tensile (and fatigue) strength, modulus of elasticity, and Poisson's ratio, which should be taken advantage of by aligning the long axis of the grains with the direction of the maximum alternating bending stress [7]. Mostly, the bar stock for steam turbine blades are forged into shape so no additional manufacturing process is required. Only in the blade root region, is a specified surface finish required (about $R_a = 0.8\,\mu m$) to satisfy the mechanical fit required. In addition, the stress concentration regions such as blade roots, are shot peened to improve their resistance to fatigue and stress corrosion cracking.

## 1.3 9-12Cr steel

### 1.3.1 Tempered martensite

12 Cr steels are the best choice for low pressure steam turbine blades, due to the combination of cost-effectiveness and the properties they exhibit under the expected LP steam turbine blade service conditions. They are usually 9-12

Cr-Mo-V steels. Quenching always follows austenitisation which normally occurs in the temperature range 1020-1100 °C in 9-12Cr steels, to dissolve the carbides as well as nitride particles in the austenite phase and prevent the precipitation of δ-ferrite. The δ-ferrite phase is undesirable as it alters mechanical property continuity, and the strain incompatibility near the interface makes crack initiation easier during fatigue. The martensitic transformation, which occurs on quenching from the austenite phase, is a diffusionless and rapid shear or displacive transformation (as oppose to the diffusional transformations seen at lower cooling rates); the percentage of martensitic transformation depends on the degree of undercooling achieved. During the fast cooling process to produce martensite, the supersaturation of the carbon atoms (which remain in the martensite phase as no diffusion can occur) induces a large amount of lattice strain, and also the martensite lath structure itself is highly strained and dislocated. All the above phenomena result in martensite that is inherently very strong, but low in ductility and toughness. This characteristic means that the mechanical properties must be modified by a tempering heat treatment before they are used in structural applications.

### 1.3.2 Phases present on tempering

The tempering of martensite is usually carried out in the range 150-700 °C, and sometimes different tempering stages are applied, depending on specific component requirements and their required properties, as well as the particular alloy system.

Different martensite morphologies exist in ferrous systems depending on the carbon content. Plate martensite is present in medium and high carbon steels while lath martensite appears in low carbon steel. Figure 1- 3 illustrates the microstructure of lath martensite. A three-level hierarchy is seen, namely: martensite lath, block, and packet. A martensite lath with a high density of lattice defects is a single crystal of martensite, and a block is formed by martensite laths with the same crystallographic orientation. Each packet consists of several blocks with different orientations but the same plane [9]. During tempering, the martensitic lath structure transforms to a ferritic subgrain structure and fine, dispersed precipitates (usually carbides) are also formed in the matrix. Extensive studies have been carried out on the

tempering behaviour of power plant steels, and 9-12Cr steels undergo similar microstructural changes to the most widely used steels, such as 1CrMoV and 21/4CrMo, though the transformation kinetics are much faster. Four stages have been identified during tempering [8, 10, 11].

1) Precipitation of Ɛ-carbide ($Fe_{2.4}C$) with a hexagonal crystal structure, which forms as narrow plates with a well-defined orientation relationship;

2) Retained austenite (γ') decomposes to bainite and cementite;

3) Cementite nucleates at the Ɛ-carbide – matrix interfaces or at grain boundary regions, including martensitic lath boundaries and prior austenite boundaries and replaces the Ɛ-carbide.

4) More stable precipitates form, which is often accompanied by the dissolution of the previous metastable precipitates in the later stages of the precipitation process.

Three or four different precipitates may be present after tempering 9-12Cr steels, as Figure 1- 4 developed by Soady [6] illustrates: primary MX, $M_{23}X_6$, $M_2X$ and secondary MX (where M denotes a metal and X is carbon or nitrogen atoms). In this figure, $M_{23}C_6$ and $M_2X$ or secondary MX is precipitated during tempering, depending on the temperature and time; while primary MX (such as (Nb,V)(C,N)) are thermodynamically stable phases and may form at an early stage of tempering or may even be present after austenitisation. In addition, these phases will not dissolve during the subsequent tempering process.

According to Thomson et al [12], the relatively large concentrations of carbide-forming substitutional solutes in 12CrMoV provide a larger driving force for carbide precipitation, compared to other low alloy steels. Therefore, relatively stable alloy carbides dominate the structures in high chromium alloys immediately after the stress-relief heat treatment. The phases commonly observed in power plant steels are discussed in more detailed in the following:

1) $M_3C$

$M_3C$ is not an equilibrium phase according to the results of thermodynamic calculations [13] and is only observed in short-term tempered microstructures. This phase has an approximately close packed hexagonal structure of iron atoms with localised distortions to accommodate the interstitial carbon atoms

and probably forms by a paraequilibrium transformation mechanism which involves partitioning of interstitial species [8]. Recent research in a representative high Cr ferritic heat-resistant steel (T91) reveals that the paraequilibrium coherent $M_3C$ needle-like particles are precipitated during air cooling after austenization irrespective of austenizing time and temperature. The precipitation of $M_3C$ phase thus only depends on cooling rate. When the cooling rate is fast, e.g. water quenching, the generation of $M_3C$ phase is prevented. The precipitation of $M_3C$ results in the depletion of alloy elements, giving rise to the appearance of wide martensite laths with low dislocation density [14].

2) $M_2X$ and MX

Both $M_2X$ and MX are generally found to precipitate at martensite lath boundaries after tempering. They appear as fine dispersions and therefore are considered to confer a strong precipitation hardening effect (secondary hardening) as well an significant creep strength to the alloy through precipitation strengthening. $M_2X$ with a hexagonal structure presents after the precipitation of cementite in many cases [13] but forms prior to secondary MX, since it requires little diffusion of chromium [15].

Secondary MX is an FCC crystal structure and takes a longer time to precipitate, compared to other carbides, such as $M_3C$, $M_7C_3$, and $M_{23}C_6$ [13]. In the 9-12Cr% alloy, MX shows two different morphologies. In as-quenched materials, small spheroidal MX precipitates containing titanium, vanadium and niobium are observed and therefore are thought to remain undissolved during austenitisation [16]. Plate-like MX containing chromium and vanadium nucleates on the spheroidal MX particles with a characteristic 'V-wing' morphology [17, 18].

3) $M_{23}C_6$ and $M_7C_3$

Both $M_{23}C_6$ (complex face centred cubic crystal structure) and $M_7C_3$ (trigonal crystal structure) are chromium rich carbides. The former is known to contain Mo, Fe and W, while the latter is iron and manganese soluble [19]. The sequence of carbide evolution in Cr-Mo-V low alloy steels is $M_3C \rightarrow M_{23}C_6 \rightarrow M_7C_3$; this has been confirmed by many researchers [20, 21]. In 9-12Cr steels, $M_{23}C_6$ is considered to be the equilibrium carbide at lower temperature and is particularly present at prior austenite grain boundaries and martensite lath

boundaries [13], while $M_7C_3$ precipitates either on fresh sites or in situ at the ferrite/cementite interface and its presentation depends on whether the chromium content is high enough compared to other alloying elements [22].

## 1.4 Motivation and objective of Ph.D study

Since the majority of fatigue cracks initiate at the surface, one of the most effective methods to improve a material's fatigue property is a surface treatment which improves or modifies the surface conditions so as to resist crack initiation and early crack growth to some degree. Shot peening has received special attention, as this process has provided notable increments of fatigue life in steel [6, 23-26], Ti [2, 27-29], Al [30-33] alloys and hence much effort has been put into researching the fatigue mechanism in shot peened materials. In much of the literature, the major part of this improvement has almost unanimously been attributed to the introduction of compressive residual stresses, as well as work hardening (though the effect of work hardening is still debated) in the surface region. This is considered to be responsible for both retarding fatigue crack initiation and lowering crack growth rates for small cracks. However, these investigations have not taken into account in detail exactly how short cracks initiate and propagate in the compressive residual stress field; most studies also mainly focus on the effects on high cycle fatigue life (where significant shot peening benefits are typically seen) rather than low cycle fatigue (which is more relevant to LP steam turbine blade applications).

In this project, we aim to investigate short fatigue crack initiation and early growth behaviour in the compressive residual stress field produced by the shot peening process in a typical LP steam turbine blade material. To further understand the fatigue crack growth behaviour, the S-N response of notched components and long crack growth data from previous research [8] will be combined with assessment of short fatigue crack behaviour, which will provide a more comprehensive micromechanistic understanding of the effect of the shot peening process on the fatigue life in LP turbine blade materials. These results will provide experimental validation for life assessment models being developed between the University of Southampton and E.ON [6] which will be able to take the benefit of shot peening into account, and thus reduce

conservatism and improve maintenance scheduling efficiency, which will reduce costs and the risk of enforced outages.

A further aim of this project is to explore an effective way to repair the fatigue damage found in shot peened notched components (such as LP turbine blades) which have been in service for some time where for example fatigue damage is observed during a maintenance inspection. Assessing how far to grind back and the effects of re-peening on such surfaces will require an in-depth understanding of the crack initiation and growth behaviour in the shot peened layer.

Figure 1- 5 shows the structure of this thesis.

## 1.5 Figures

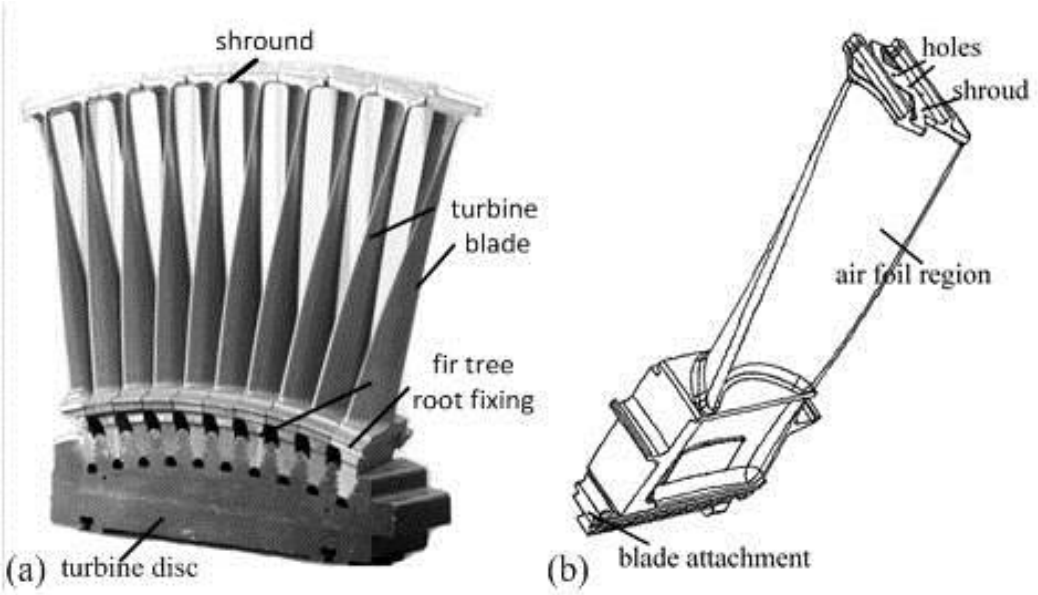


Figure 1- 1 Steam turbine blade system and (b) a schematic of the fatigue crack initiation positions in a steam turbine blade. After [34].

Table 1- 1 Material requirements for HP and LP steam turbine blades[17].

| Requirement | HP/IP Blades | LP Blades |
|---|---|---|
| Static tensile strength | Y | Y |
| Toughness | Y | Y |
| Creep rupture strength | Y | N |
| Oxidation resistance | Y | N |
| Local corrosion resistance | Y | Y |
| Stress corrosion cracking Resistance | N | Y |
| Corrosion fatigue strength | N | Y |
| Low cycle and high cycle fatigue resistance | Y | Y |
| Erosion resistance | Y | Y |
| Weldability | Y | Y |
| Type IV cracking resistance | Y | N |

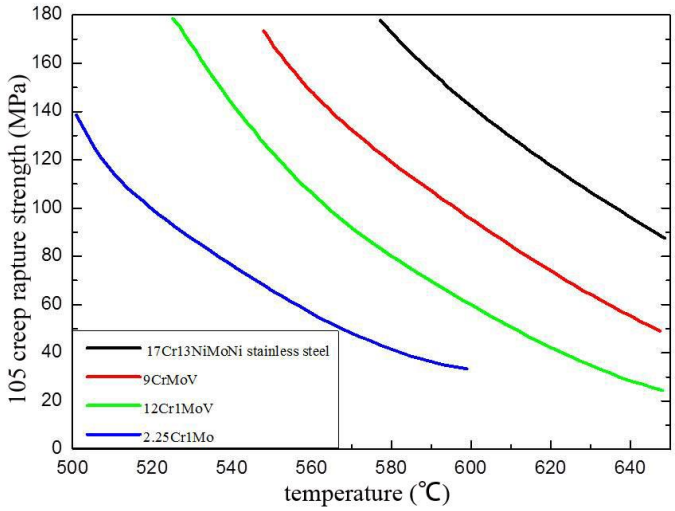


Figure 1- 2 Creep rupture strength of various steels as a function of temperature [8, 35].

Table 1- 2 Typical values for thermal conductivity and coefficient of thermal expansion for austenitic and ferritic steels [3].

| | Austenitic,e.g.304 Stainless Steel Fe-18Cr-8Ni-2Mn-1Si | Ferric, e.g. 'Goodfellow Iron 90' Fe-9Cr-1Mo |
|---|---|---|
| Thermal conductivity/$Wm^{-1}K^{-1}$ | 16.2 | 26.0 |
| Room temperature coefficient of thermal expansion /$\mu K^{-1}$ | 17.3 | 11.3 |

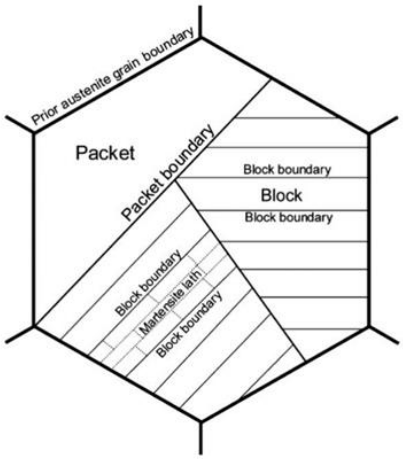


Figure 1- 3 Microstructural hierarchy of the lath martensite structure [9].

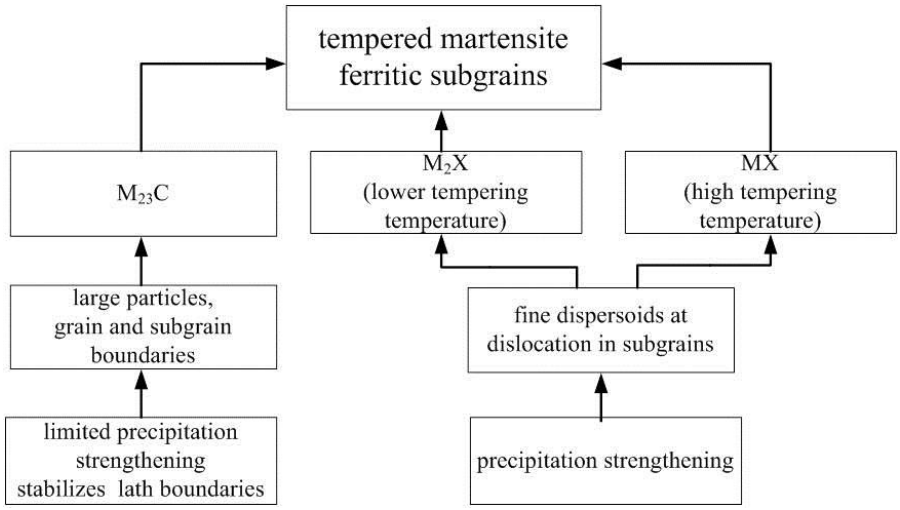


Figure 1- 4 The phases present in 9-12% Cr steels after tempering (after [6]).

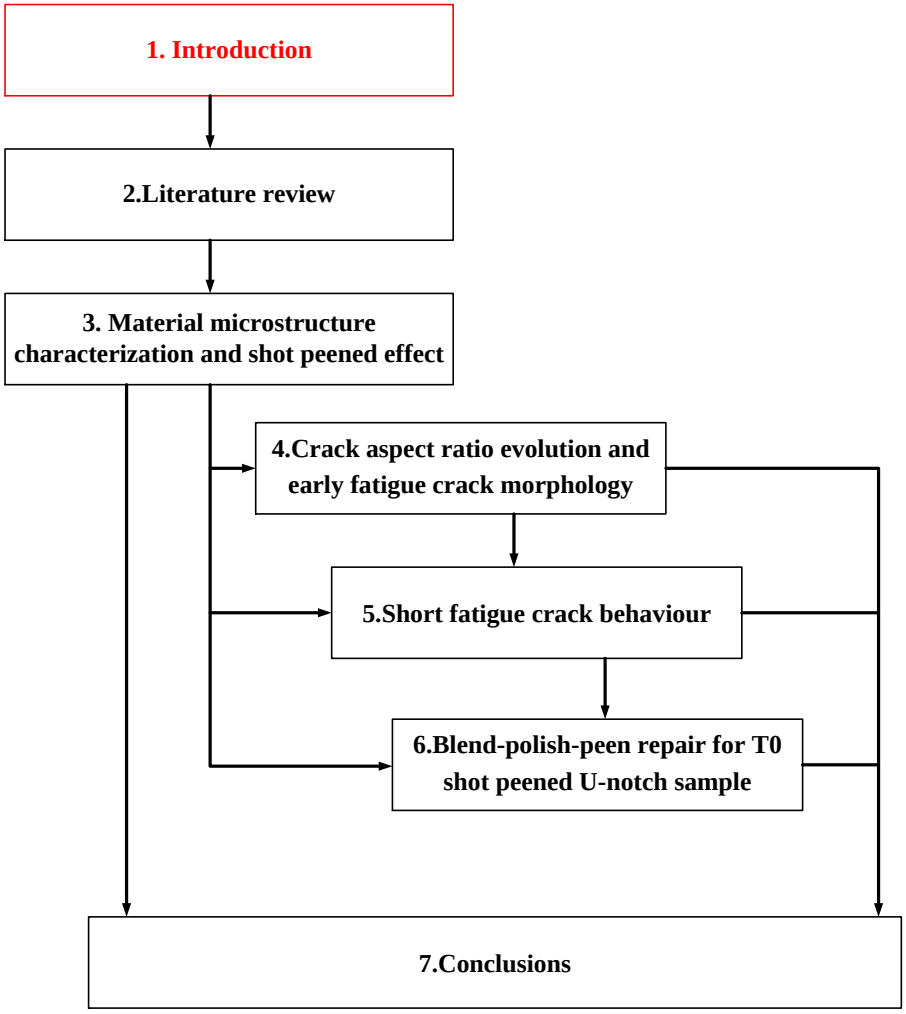


Figure 1- 5 Thesis structure.

## 1.6 References

[1] *Modern power station practice: incorporating modern power system practice*, British Electricity International, 1991.
[2] N.K. Mukhopadhyay, S.G. Chowdhury, G. Das, I. Chattoraj, S.K. Das, D.K. Bhattacharya, *An investigation of the failure of low pressure steam turbine blades*, Engineering Failure Analysis, 5 (1998) 181–193.
[3] A. Atrens, H. Meyer, G. Faber, K. Schneider, *Corrosion in power generatin equipment*, Plenum Press, 1983.
[4] G.L. Narasaiah, *Finite element analysis*, BS Publications, 2008.
[5] G. Horseman, *Parsons 500 and 660 MW steam turbines: operating experience and lessons learned*, Energy Materials, 4 (2009) 213–237.
[6] K.A. Soady, *Reducing conservatism in life assessment approaches: Industrial steam turbine blade to disc interfaces and the shot peening process*, in: Engineering Sciences Unit, Ph.D thesis, the University of Southampton, 2013.
[7] M. Singh, G.M. Lucas, *Blade design and analysis for steam turbines*, McGraw-Hill Publishing, 2011.
[8] J.D. Robson, *Modelling of carbide and laves phase precipitation in 9-12 wt% chromium steels*, in, Ph.D thesis, the University of Cambridge, 1996.
[9] H. Kitahara, R. Ueji, N. Tsuji, Y. Minamino, *Crystallographic features of lath martensite in low-carbon steel*, Acta Materialia, 54 (2006) 1279–1288.
[10] R.W. Balluffi, M. Cohen, B.L. Averbach, *The tempering of chromium steels*, Trans. ASM, 43 (1951).
[11] R. Baker, J. Nutting, *The tempering of 2¼% Cr-1% Mo Steel after quenching and normalizing*, Journal of the Iron and Steel Institute, 192 (1959) 257–268.
[12] R. Thomson, H. Bhadeshia, *Carbide precipitation in 12Cr1MoV power plant steel*, Metallurgical and Materials Transactions A, 23 (1992) 1171–1179.
[13] J. Janovec, M. Svoboda, A. Kroupa, A. Výrostková, *Thermal-induced evolution of secondary phases in Cr–Mo–V low alloy steels*, Journal of Materials Science, 41 (2006) 3425–3433.
[14] C.X. Liu, D.T. Zhang, Y.C. Liu, Q. Wang, Z.S. Yan, *Investigation on the precipitation behavior of M3C phase in T91 ferritic steels*, Nuclear Engineering and Design, 241 (2011) 2411–2415.
[15] J. Hald, S. Straub, *Microstructure stability of 9-12% CrMo(W)VNbN-Steel.*, in: 6th Liege Conference in Materials for Advanced Power Engineering, Liege, Belgium, 1998, pp. 155–169.
[16] J. Janovec, M. Svoboda, J. Blach, *Evolution of secondary phases 12% Cr steel during quenching and tempering*, Materials Science and Engineering: A, 249 (1998) 184–189.
[17] T.U. Kern, et al, *The European effort in development of new high temperature rotor materials up to 650°C-COST 522, in materials for advanced power engineering*, in: F.S. J. Lecomte-Beckers, P. Ennis (Ed.) Materials for Advanced Power Engineering, Forschungszentrum, JülichLiege, Belgium, 1998, pp. 1049–1064.
[18] H. Nickel, P.J. Ennis, O. Wachter, *The effect of heat treatment on the microstructure and creep rupture properties of 9Cr-0.5Mo-1.8W steel*, 1995.
[19] M. Hättestrand, M. Schwind, H.-O. Andrén, *Microanalysis of two creep resistant 9–12% chromium steels*, Materials Science and Engineering: A, 250 (1998) 27–36.
[20] A. Kroupa, A. Výrostková, M. Svoboda, J. Janovec, *Carbide reactions and phase equilibria in Low-alloy Cr–Mo–V Steels tempered at 773–993 K. Part II: Theoretical calculations*, Acta Materialia, 46 (1998) 39–49.

[21] A. Výrostková, A. Kroupa, J. Janovec, M. Svoboda, *Carbide reactions and phase equilibria in low alloy Cr–Mo–V steels tempered at 773–993 K. Part I: Experimental measurements*, Acta Materialia, 46 (1998) 31–38.
[22] J.H. Woodhead, A.G. Quarrell, *The role of carbides in low-alloy creep-resistance steels*, J. Iron and Steel Inst., 203 (1965) 605–620.
[23] K.A. Soady, B.G. Mellor, J. Shackleton, A. Morris, P.A.S. Reed, *The effect of shot peening on notched low cycle fatigue*, Materials Science and Engineering a–Structural Materials Properties Microstructure and Processing, 528 (2011) 8579–8588.
[24] K. Dalaei, B. Karlsson, L.E. Svensson, *Stability of shot peening induced residual stresses and their influence on fatigue lifetime*, Materials Science and Engineering: A, 528 (2011) 1008–1015.
[25] E.R. De los Rios, A. Walley, M.T. Milan, G. Hammersley, *Fatigue crack initiation and propagation on shot-peened surfaces in A316 stainless steel*, International Journal of Fatigue, 17 (1995) 493–499.
[26] M.P. Nascimento, R.C. Souza, W.L. Pigatin, H.J.C. Voorwald, *Effects of surface treatments on the fatigue strength of AISI 4340 aeronautical steel*, International Journal of Fatigue, 23 (2001) 607–618.
[27] B.X. Feng, X.N. Mao, G.J. Yang, L.L. Yu, X.D. Wu, *Residual stress field and thermal relaxation behavior of shot-peened TC4-DT titanium alloy*, Materials Science and Engineering: A, 512 (2009) 105–108.
[28] V. Fridrici, S. Fouvry, P. Kapsa, *Effect of shot peening on the fretting wear of Ti–6Al–4V*, Wear, 250 (2001) 642–649.
[29] H. Lee, S. Mall, S. Sathish, *Investigation into effects of re-shot-peening on fretting fatigue behavior of Ti–6Al–4V*, Materials Science and Engineering: A, 390 (2005) 227–232.
[30] G.S. Was, R.M. Pelloux, *The effect of shot peening on the fatigue behavior of alloy 7075-T6*, Metallurgical and Materials Transactions A, 10 (1979) 656–658.
[31] S. Curtis, E.R. de los Rios, C.A. Rodopoulos, A. Levers, *Analysis of the effects of controlled shot peening on fatigue damage of high strength aluminium alloys*, International Journal of Fatigue, 25 (2003) 59–66.
[32] Y. Mutoh, G.H. Fair, B. Noble, R.B. Waterhouse, *The effect of residual stresses induced by shot-peening on fatigue crack propagation in two high strength aluminium alloys*, Fatigue & Fracture of Engineering Materials & Structures, 10 (1987) 261–272.
[33] L. Wagner, C. Mueller, *Effect of shot peening of fatigue behaviour in Al-alloys*, Materials and Manufacturing Processes, 7 (1992) 423–440.
[34] *Severice, I.T., http://www.act-texas.com/areas-of-excellence/blade-bucket/. 2011*, in, 2011.
[35] R. Blum, J. Hald, W. Benidick, A. Rosselet, J. Vaillant, *Newly develop high temperature ferritic-martensitic steels from USA,Japan and Europe*, in: International VGB Conference–Fossi–fired Power Plant with Advanced Desiign Parameters, Kolding, Denmark, 1993.

# Chapter 2: Literature review

## 2.1 Fatigue behaviour in metallic materials

### 2.1.1 Introduction

When subjected to cyclic loading, materials will suffer progressive and localized structural damage, which is often called fatigue. Suresh [1] defined fatigue as a term which 'applies to changes in properties which can occur in a material due to the repeated application of stresses or strains', although usually this term applies especially to those changes which lead to cracking or failure. Under repeated loading and unloading conditions, fatigue failure in materials occurs under a nominal maximum stress value which is below the ultimate or even the yield stress of the material. Microcracks initiate at the component surface or at material defects, begin to grow, and eventually lead to catastrophic fracture when the fatigue cracks reach a critical size. However, there are different factors which could lead to fatigue failure, not merely periodic stresses or strains (failure under these conditions is termed mechanical fatigue). If external conditions such as temperature fluctuations, aggressive chemicals or sliding surfaces are considered in material failure processes, then the terms used are creep-fatigue, thermomechanical fatigue, corrosion fatigue or fretting fatigue respectively [2]. In these four fatigue mechanisms, not only the cycle numbers and load levels affect the crack growth rate, but also the period and waveform. They are time dependent cyclic failure processes. However, creep-fatigue, thermomechanical fatigue and fretting fatigue will not be considered further in this project, as the low pressure steam turbines (which are the focus of this study) work at a temperature around 250 °C, which is a relatively low temperature, though corrosion fatigue may occur in steam turbines. The chosen fatigue condition for this work is therefore room temperature in air. Most of the discussion in Section 2.1 is based on Suresh's Fatigue of Materials [1] and Krupp's fatigue crack propagation in metals and alloys [3].

### 2.1.2 Fatigue life approaches

In an engineering component, the different stages of fatigue damage until catastrophic fracture occurs can be basically classified into the following five stages [1]:

- Substructural and microstructural changes which cause nucleation of permanent damage;
- Microscopic cracks initiate;
- Microscopic cracks grow and coalescence, forming 'dominant cracks', which may eventually lead to catastrophic failure;
- These dominant macrocracks propagate stably;
- Structural instability or complete fracture.

The fatigue life of a component is related to its loading conditions, thus various fracture mechanics approaches have been developed based on this relationship. Yet how to define the initiation of a fatigue crack during the fatigue process is one of the biggest challenges in developing fatigue life prediction models. For instance, material scientists are likely to regard the nucleation of micrometre-size flaws along slip bands and grains as the beginning of fatigue failure, assuming that the component does not have any existing cracks; while engineers tend to link smallest observable crack or another reliable non-destructive evaluation technique to fatigue crack initiation. Generally, there are two different fatigue life approaches, the total life fatigue approach and the damage tolerant approach. In the former approach, information about the damage evolution, crack nucleation and crack growth stages of fatigue life is all characterised by just one parameter-the total number of cycles to failure; while the damage tolerant approach considers the cycles taken for the growth of an initial defect to a critical size during the fatigue process.

#### 2.1.2.1 Total fatigue life approach (stress/strain life approach)

In the total fatigue life approaches, the specimens are considered to be crack-free or have a smooth surface at the beginning of the fatigue test and controlled amplitudes of cyclic stress or strains are usually applied to estimate the number of stress or strain cycles needed to lead to the final fatigue failure. In this resulting fatigue life, the number of fatigue cycles to initiate a dominant

crack (which sometimes could be as high as 90 % of the total fatigue life), as well as the number of cycles for the dominant flaw to propagate until catastrophic fracture are combined [1]. The total fatigue life, which is usually characterized as a function of applied stress amplitude, strain range, mean stress and environment, is a crucial material parameter which indicates how many cycles of stress or strain a component can withstand at a certain load level according a set criterion of failure in engineering design.

Fatigue failures which occur under high cycle, fatigue life $N_f > 10^5$, low stress fatigue situations, where the material deforms primarily elastically, have traditionally been characterized in terms of the stress amplitude. While in low cycle fatigue, $N_f < 10^5$, stresses are usually high enough to induce appreciable plastic deformation in materials prior to failure, therefore the strain range is usually used to characterize a material's fatigue life.

#### 2.1.2.2 Damage tolerant approach

The basic premise of the damage tolerant approach is that each component inherently contains imperfections in the form of cracks, and these cracks are able to propagate only when they reach a certain critical dimension. Linear elastic fracture mechanics approaches are often used to describe the crack tip driving forces. The applicable condition for linear elastic fracture mechanics to apply is small-scale yielding, where the crack tip plastic zone is small compared to the characteristic dimensions of the cracked component (including the crack size) and where predominantly elastic loading conditions prevail. In this approach, local stresses in the region of the crack tips are related to the far-field applied stresses as well as flaw lengths. The crack tip stress field can be considered in terms of three basic loading modes: in-plane opening, in-plane shearing and antiplane shearing, each of which is associated with a local mode of deformation. The schematics of these three modes are illustrated in Figure 2- 1 [3]. Mode I represents the tensile opening mode with a load normal to the crack plane. Mode II is the in-plane sliding mode in which a shear load is in the direction of crack advance, and Mode III is the tearing or anti-plane shear mode in which the crack faces are sheared parallel to the crack front. However, it is worth noting that most loading cases in practice are a superimposition of different modes, known as mixed-mode loading. Figure

2- 2 illustrates the crack tip (when r→0) and the displacement fields in the rectangular coordinate system [4].

For simplicity, only the near-tip fields of Mode I will be discussed in the present work. For an infinite plate of isotropic, homogeneous material, if a sharp through thickness crack of length 2*a* exists in it, then the stress fields ahead of the crack tip can be expressed as follows:

$$\begin{Bmatrix}\sigma_{xx}\\ \sigma_{yy}\\ \sigma_{xy}\end{Bmatrix} = \frac{K_I}{\sqrt{2\pi r}}\cos\frac{\theta}{2}\begin{Bmatrix}1-\sin\frac{\theta}{2}\sin\frac{3\theta}{2}\\ 1+\sin\frac{\theta}{2}\sin\frac{3\theta}{2}\\ \sin\frac{\theta}{2}\cos\frac{3\theta}{2}\end{Bmatrix} \qquad \text{Equation 2- 1}$$

Here, the term $K_I$ represents the Mode I stress intensity factor which incorporates the boundary conditions of the cracked body as well as being a function of external loading state, crack length and geometry. The intensity of the stress in the stress field at the crack tip is characterised by *K*. *K* should be proportional to the applied nominal stress $\sigma_a$, since the stress state is presumed to be elastic. So in such conditions, $K_I$ can be expressed as the following:

$$K_I = \sigma_a\sqrt{\pi a} \qquad \text{Equation 2- 2}$$

However, Equation 2-2 is only applicable under the special conditions of a centre crack in an infinite plate; in engineering practice, the dimensional parameters such as *a/w* (the ratio of the crack length to specimen width ratio), always modifies the K expression:

$$K_I = f\left(\frac{a}{w}\right)\sigma \qquad \text{Equation 2- 3}$$

A fatigue crack from a pre-existing flaw or defect in a component may start to grow under cyclic loading conditions at stress intensity values that are well below the material fracture toughness. Based on the assumption that only small scale yielding exists at a crack tip, Paris [5] postulated that the growth of a crack under cyclic loading can be expressed as follows:

$$\frac{da}{dN} = C\Delta K^m \qquad \text{Equation 2- 4}$$

In the above equation, *da/dN* indicates the change of the fatigue crack length per load cycle, *a* is the crack length and N is the number of fatigue cycles; C and m are empirical constants which are mainly determined by material

properties and microstructure, and load conditions such as fatigue frequency [1].

The stress intensity factor *K* describes the local stress state at a crack tip, and can also be expressed in terms of the external loading conditions and specimen dimensions (W–width, B–breadth, *a*–crack length). Another advantage of applying the *K* concept is that of similitude, where two cracks with different sizes/geometries experiencing the same stress intensity will have plastic zones at the crack tips of similar dimension and local stress and strain distribution, which implies that the crack driving force of these two cracks is equal and the same increments in crack growth per cycle is expected for these two crack situations. Based on this, data obtained from simple laboratory test specimens can also be applied to the practical component by using *K* as the governing parameter. Therefore, *K* becomes one of the most powerful approaches in damage tolerant fatigue analysis.

However, as discussed at the beginning of this section, *K* is only valid for the characterisation of near crack-tip stress fields when small-scale yielding conditions exist, that is to say, the materials should behave quasi-elastically when applying *K* calculations. Both the *J*-integral and crack tip opening displacement CTOD ($\delta$), can be applied to analyse fatigue behaviour under elastic-plastic conditions. The former was proposed by Rice [6] to calculate the strain energy release rate in a non-linear elastic solid; it is a path independent line integral along a contour around the crack tip which represents the rate of change of potential energy with respect to crack advance.

### 2.1.3 Micromechanisms of fatigue behaviour

Crack growth behaviour can be divided into three regimes: microstructural crack initiation, microcrack propagation and long crack propagation that leads to final failure. Basically, the whole fatigue process involves the following related, but slightly different phenomena:

A. Cyclic hardening or softening induces cyclic damage in the material at the early fatigue stage;

B. Microscopic flaws occur and microcracks initiate;

C. Microcracks coalesce and grow;

D. Macroscopic flaws and macrocracks propagate;

E. Final catastrophic failure or instability

It is noteworthy that many components spend most of their life in the early fatigue stages, i.e. crack initiation and microcrack propagation, particularly for high-cycle fatigue (HCF) loading conditions. For high-strength materials up to 90 % of a technical component's fatigue life can be taken up by crack initiation and the propagation of microstructurally short crack phases [7, 8].

#### 2.1.3.1 Fatigue crack initiation

(1) Crack initiation at persistent slip bands (PSBs)

During fatigue loading, slip irreversibilities develop and accumulate due to dislocation annihilation, cross-slipping, penetrating precipitates, transmitting through grain boundaries, and piling-up. These slip irreversibilities can be considered as the earliest stages of fatigue damage. Strain localization (i.e. persistent slip bands and dislocation accumulation within a small region) is a precursor to crack initiation [9]. The formation of these PSBs is a manifestation of the instability of the dislocation (and in some cases also precipitation) structure, that leads to a mismatch of the localization of the cyclic plastic deformation between this intense slip activity and surrounding metal matrix. This cyclic plastic deformation within the PSBs leads to the formation of microscale surface extrusions and intrusions along the traces of the active slip planes, from which the fatigue microcracks can start [10].

The first measurement of slip spacing and slip height displacement by atomic force microscopy (AFM) during a fatigue process was in Ti and steel [11]. Man et al [12-15] showed how the early stages of surface relief evolution of persistent slip markings (PSMs) developed; these formed in areas where persistent slip bands (PSBs) intersected the free surface in two cyclically loaded stainless steel systems cycled with constant plastic strain amplitude. Their results showed that the mean extrusion height appeared to increase linearly with fatigue cycles in a 316 stainless steel, but non-linearly in a ferritic stainless steel. Figure 2- 3(a) reveals a real PSM topography as well as the true geometry of extrusions and intrusions.

Essmann et al [16] developed a model for surface roughening and crack nucleation based on the hypothesis that the annihilation of dislocations within

the slip bands is the origin of slip irreversibility. For two opposite signs of dislocations, annihilation may occur when the distance between them is less than a certain value (50 nm for screw dislocations and 1.6 nm for edge dislocations) [1]. In the PSBs, there are mainly edge dislocations, and annihilation will lead either to the formation of vacancies or interstitials, depending on whether the corresponding annihilating lattice half planes overlap (interstitial dipoles). Those remaining dislocations are mobile along the paths of the dashed lines, either moving to the free surface or to the bulk-PSB interface, shown in Figure 2- 3(b). Hence, rows of interface dislocations directed towards the inner PSB are formed. A protrusion of height *e* would be formed based on the assumption that all of these dislocations emanate at the free surface, which is also indicated in this figure.

In addition, crack initiation behaviour within slip bands is affected by the environment. A slip step is formed by those dislocations moving towards the surface. As Figure 2- 4 reveals, the fresh metal surface is exposed to oxygen from the environment. Local decohesion along the slip band will occur since the surface absorbs oxygen and this leads to an un-completed closed slip step, which will always act as a crack initiation site Figure 2- 4(c). Thompson's research [17] on copper fatigue cracks reveals that fatigue experiments in vacuum typically result in a substantially longer fatigue life than the corresponding experiments in air. This could be taken as indirect evidence for the mechanism discussed above.

However, as discussed previously, the definition of crack initiation strongly depends on the length scale being considered. The above discussed crack initiation mechanism such as the PSB crack initiation mechanism, is rarely considered to be the cause of fatigue crack initiation in practical engineering components. From the viewpoint of design engineers, features such as constituent particles, macroscopic stress concentrations or manufacturing defects lead to easier fatigue crack initiation.

(2) Crack initiation at a surface

As detailed above, fatigue cracks are able to initiate even in a uniform idealized material with no defects, no second phase particles, and a perfectly polished surface. This can occur by the intrinsic phenomenon of slip irreversibility. Repeated cyclic straining of the material causes different amounts of net slip

on different glide planes. The irreversible shear displacements along slip bands then lead to microscopic roughening of the surface and thus micronotches form, which act as stress concentration sites for additional slip and fatigue crack nucleation [18]. The pre-existing surface condition of a component also has a strong effect on its fatigue life; rough surfaces can induce fatigue crack initiation [18], such as machined (e.g. ground) surfaces [19, 20]. Taylor's research [21] focused on the effect of surface roughness (not considering surface microstructure or residual stress variability) on fatigue limit. Fatigue limit data were plotted as a function of roughness parameters using "Kitagawa-type" diagrams, as shown in Figure 2- 5, and compared to simple notch-based and crack-based models. It was found that, whilst both theories tended to be overly conservative, fracture mechanics approaches were useful for relatively low roughness, when the surfaces can be modelled as a series of short cracks. For higher roughness a notch-based approach was found to be appropriate. It is important to note that it is propagation dominated in LCF regime, where initiation is relatively insignificant, roughness would not be expected to be a major contributing factor to fatigue life. However, surface roughness may become an important factor to be considered due to the complex interactions of surface roughness, loading conditions and residual stress, for example, Ryu's study in a CrMoV steel indicated that low-cycle fatigue behaviour is largely influenced by the crack initiation process even for a high strain range (where lifetime is generally considered to be propagation dominated) and the observed decrease of fatigue life in specimens with a rough surface was mainly due to a reduction in the number of cycles for crack initiation [22]. Other approaches to find the relation between surface roughness and fatigue life have been based on: (i) the definition of a local $K_t$ (ii) detailed analysis of the surface tomography, or (iii) have treated fatigue crack initiation from machined surfaces by approximating the surface roughness as a micro-notch with a characteristic width, depth, and root radius, accompanied by an elastic stress concentration factor or have used (iv) a notch sensitivity factor finite element analysis approach [23-26].

Although in most cases, it has been reported that lower roughness results in longer fatigue life, for roughness values in the range 2.5-5 μm $R_a$ fatigue life has been found to be primarily dependent on workpiece residual stress and surface microstructure, rather than roughness. These findings explain why post mechanical surface treatment, such as low plasticity burnishing [27, 28],

shot peening [29-32], or laser shock peening [33-36] are frequently applied on machined surfaces of engineering components to induce compressive surface stresses, work hardening (high dislocation densities near the workpiece surface) and alteration of workpiece surface roughness/surface topography in the surface layers for the purpose of delaying fatigue crack initiation, fatigue crack growth, or both. In the absence of residual stress, and for machined surface roughness in excess of 0.1 μm, $R_a$ has a strong influence on fatigue life [37]. During research on 4340 steel, Andrews [38] noted that surface roughness becomes the key factor influencing crack initiation at the surface when the mean surface roughness $R_a$ (the arithmetical mean roughness of a surface) exceeds the diameter of intrinsic material defects or the grain size.

(3) Crack initiation at pores, inclusions or particles

Pores which form during casting and solidification processes or powder-metallurgy compaction/sintering can be generally considered as pre-existing microcracks in the fatigue process [39-43], especially when their sizes are comparable to the dimension of the most characteristic microstructural feature of the material, e.g. the grain size. Not only the pore size, but spacing, clustering and distribution will have a great influence on crack formation and even the growth of small cracks within the locally strained regions adjacent to the pores [44]. One particular analysis of the stress concentration of pores and pore-induced fatigue failure is the worst-case notch analysis [74], which treats the initiation and growth of a fatigue crack under the influence of the stress field of a notch, by assuming a pore in a cast alloy can be approximated as a micronotch [45].

Inclusions or particles are also common fatigue crack initiation sites in steels [46-49] and Al alloys [50-53]. In Tanaka's theory of crack initiation from inclusions [46], the types of fatigue crack initiation at inclusions in high strength alloys can be classified into three different types based on the inclusion strength relative to the matrix, that is: (i) a slip-band crack emanating from a debonded inclusion, (ii) inclusion cracking (or debonding) due to impinging slip bands, and (iii) a slip-band crack emanating from an uncracked inclusion. This first type typically occurs in high strength steels, where the strength of the interface between inclusions and matrix are so low it breaks at the first fatigue cycle without any accompanying plastic deformation and this crack will propagate from the interface into the matrix at a very early

stage; while for the other two types, which are reported in high strength aluminium alloys, the interface is strong enough not to break in the initial stages of fatigue (the second mechanism) or these inclusions are not debonded or cracked, but a crack initiates in the matrix from the inclusion interface (the third case).

Difference in the coefficients of thermal expansion between a ceramic or non-metallic inclusion and the surrounding metal matrix may produce residual stresses at the interface of the inclusion and matrix, especially during processing or subsequent heat-treatments involving temperature changes. These residual stresses are known as “tessellated or textural stresses”, which occur around some inclusions such as alumina, TiN, and other oxide particles in steels [54]. Figure 2- 6 presents an example of the residual stress difference inside the Alumina and regions near the matrix. During mechanical loading, the elastic properties of the inclusion material are different from those of the parent material; nonmetallic inclusions will produce mechanical stress at the interface between the inclusions and the parent material. The level of this stress induced mainly depends on the inclusion size. In addition, large nonmetallic precipitates tend to crack in a brittle manner during cold working or during service, and thus can also act as pre-existing small cracks in a similar manner to pores.

#### 2.1.3.2 Short fatigue crack behaviour

As illustrated in Figure 2- 7, there are significant differences between the growth rate of short cracks and long cracks. Under the same nominal $\Delta K$ conditions, the fatigue crack growth rates for short cracks are much greater than or at least equal to the corresponding growth rates of long cracks. Before we begin to discuss fatigue crack propagation behaviour, it is helpful to define short cracks and long cracks. Generally, short cracks can be identified as one of the following four types [3]:

A. Microstructurally small cracks. They appear when the crack size is comparable to the scale of the characteristic microstructural dimension. Its path as well as the small crack advance rate is affected by grain boundaries, inclusions and precipitates.

B. Mechanically short cracks. This kind of crack will occur where near tip plasticity is comparable to the crack size, when the strong influence of the microstructure ceases, and crack propagation is driven by the plastic zone ahead of the crack tip, i.e., crack-tip-opening displacement (CTOD).

C. Physically short cracks. The size of the plastic zone at the crack tip is negligibly small, as compared to the crack length, but the crack is typically smaller than 1 or 2 mm. Therefore the concepts of LEFM are applicable.

D. Chemically short cracks. This kind of crack shows anomalous propagation below a certain size due to environmental factors, as a result of the strong dependence of corrosion fatigue conditions at the crack tip on crack length, although they are normally amendable to linear elastic fracture mechanics.

Table 2- 1 summarizes the characteristics of different fatigue cracks. This section will mainly focus on short fatigue crack propagation behaviour.

(1) Microstructure aspects of short fatigue crack growth

Fatigue crack initiation can occur from slip bands [55], twin boundaries [56], carbides [57], inclusions [46] and precipitates [58], pores [59] or at other defects. In 9-12 Cr steel, lath boundaries are favourable sites for microcrack nucleation [60, 61]. After crack initiation, the early propagation phase of short fatigue cracks will begin. This is mainly controlled by the interactions between local microstructural features and the crack driving force at the crack tip. Miller [62] split the short fatigue crack behaviour into three regimes, as illustrated in Figure 2- 8; microstructure will influence the crack growth when the crack length $a < d_3$. Morris [63] proposed that the advancing plastic zone ahead of the crack tip will be hindered by a grain boundary, when the crack tip arrives at the grain boundary, the crack is retarded, since the irregular structure of the grain boundaries restricts the dislocation movement on slip planes. However, as proposed by Miller, there are several different microstructure barriers to crack growth in a single material [62]. For example, a crack starting from a ferrite grain boundary can propagate transgranularly and stop at the next grain boundary. However, if this crack grows longitudinally along the length of the ferrite band, before arresting at a pearlite colony, the stress required to break this barrier may in fact be less but the non-propagating crack length is longer [62]. Therefore, not only the grain size, but also material anisotropy and

texture are of crucial importance to determining the fatigue limit and the microstructurally affected short crack regime. Conventional methods of nondestructive materials testing, such as ultrasonic testing or X-ray analysis, are unable to detect these microstructural short cracks due to these techniques' limited resolutions (typically order of 0.5 mm). According to [64], the regime of microcrack propagation prevails during 65–90 % of the fatigue life, while only the last 5–10 % of the fatigue life can be considered as determined by the behaviour of long cracks and analysed by linear elastic fracture mechanics (LEFM).

(2) Short fatigue crack propagation

1) The development of the crack aspect ratio *a/c*

The short fatigue crack shape or aspect ratio, *a/c* (where *a* – the crack depth and *c* – the half surface length), correlates with crack growth behaviour [65]. When several cracks grow with a semicircular contour with a constant aspect ratio of *a/c* equal to one, these cracks will converge [66]. The main cracks which form in the later stage of the fatigue process result from the coalescence of many small, single cracks which form at the earlier stage of the fatigue progress. After coalescence, these cracks once again behave as a single crack, and continue to grow in both the surface and depth directions [67]. As discussed in section 2.1.3.1, single-slip deformation during early crack propagation is strictly limited by grain boundaries; hence the short cracks have the potential to propagate in a shallow manner, on that basis the aspect ratio *a/c* is smaller than 1; with increasing crack length, the aspect ratio approaches the stable value of the semicircular shape $a/c \approx 1$ [68], where the stress intensity factor *K* becomes homogeneous along the crack tip front [66]. One thing worth mentioning is that shallow surface cracks tend to stop at microstructural barriers; while deep cracks, since $a/c >> 1$, will propagate preferentially in the surface [3].

2) The coalescence of short cracks

In addition to the development of the aspect ratio, crack coalescence effects will also play a key role during the short to long crack propagation transition. In most cases, individual microstructurally short crack initiation determines the material's early fatigue life, especially under high or very-high cycle fatigue

conditions. Generally, coalescence of very small cracks does not tend to take place in the early stages of fatigue life, and the predominance of short crack coalescence will not occur until 50 % of total fatigue life at which point the crack density may decrease due to coalescence [3]. After coalescence, only when the two coalescing cracks have reached the new equilibrium crack depth *a* then the new-formed crack could increase surface crack length, as shown in Figure 2- 9.

3) Characterizing the growth of short fatigue cracks.

Due to the small size of the crack compared to its plastic zone size, it is not easy to characterise short crack growth rate. LEFM cannot strictly be applied to truly characterise the growth rate of short fatigue cracks as the crack tip process zone is too large with respect to the crack length and the surrounding constraining material so that the quasi-elastic assumption underlying LEFM is violated. Much research has focused on the characterization of small crack growth behaviour. Dowling [69] proposed a cyclic *J* integral "$J_c$" to characterize the driving force for elastic-plastic short flaws:

$$J_c = 3.2(\Delta w_e)a + 5(\Delta w_p)a = \frac{1.6(\Delta\sigma)^2 a}{E} + \frac{5(\Delta\sigma\Delta\varepsilon_p a)}{\frac{n+1}{n}} \qquad \text{Equation 2- 5}$$

Here $w_e$ and $w_p$ are the elastic and plastic components of the remote strain energy density range respectively, *a* is the depth of the surface flaw and n is the strain hardening exponent. $\Delta\sigma$ and $\Delta\varepsilon_p$ are the applied stress and plastic strain ranges.

Ravichandran and Larsen [66] suggested that accounting for the development of the aspect ratio of short fatigue cracks during propagation could correct the deviations of propagation rate *dc/dN* of short surface cracks from the estimated propagation rate *da/dN* of long crack growth:

$$\frac{da}{dN} = c\frac{d\left(\frac{a}{c}\right)}{dN} + \left(\frac{a}{c}\right)\frac{dc}{dN} \qquad \text{Equation 2- 6}$$

Later, the above model was improved by applying numerical calculation of local *K* values along the front of microstructural short cracks [70]. This model combines three-dimensional information which is commonly used in the theoretical analysis of short fatigue cracks. However, it should be pointed out that, whilst characterizing microstructurally short cracks using the *K* concept is

by definition not valid in terms of LEFM applicability, since the propagation behaviour of short fatigue cracks is not the same as long fatigue cracks (i.e. similitude does not apply). The reason to continue to apply this LEFM approach to characterise short fatigue cracks is to more easily compare the relationship of short and long crack behaviour on the basis of the same criterion.

#### 2.1.3.3 Long fatigue crack behaviour

As the crack length increases, the influence of the superimposed normal stresses (in mode I) becomes greater and the crack-propagation direction changes gradually from typically close to 45° (maximum shear stress, reflecting the slip-band initiated nature of much early crack growth) to 90° with respect to the remote normal stress [3]. This transition from mode I to mode II crack propagation is a characteristic of the change from short (stage I) to long (*K*-controlled stage II) fatigue-crack propagation, as schematically represented in Figure 2- 10.

(1) Fatigue crack propagation-Stage I

Stage I fatigue crack growth presents a zig-zag path, as shown in Figure 2-11(a), where the growth begins predominately by single shear in the direction of the primary slip system, when the crack and the zone of plastic deformation surrounding the crack tip are within a grain diameter. In addition, this single slip mechanism also contributes to a highly faceted appearance of the crack growth path.

(2) Fatigue crack propagation-Stage II

Stage II crack propagation begins to prevail when simultaneous dislocation movement can occur on multiple slip systems, that is, the plastic zone size ahead of the crack tip is large enough and the plastic zone encompasses many grains and the crack growth no longer depends on the local crystallographic orientation. The stage II crack growth profile is illustrated in Figure 2- 11(b). While stage I crack growth creates a faceted profile, stage II crack growth in many cases will result in the formation of fatigue striations which Laird originally termed “ripples” [71]. On a macroscopical scale, these ripples appear to be relatively smooth. The spacing between adjacent striations has been found to correlate with the average crack growth rate per cycle. The Laird-Smith model is the most popular one for striation formation in ductile

materials. During the tensile half cycle, shown in Figure 2- 12 (a)-(c), blunting of the crack tip is attributed to activation of two slip systems inclined at 60° with respect to the load axis (maximum shear stress); during unloading, because of the irreversibility of plastic deformation, the induced blunting of the crack tip cannot be cancelled completely, and hence re-sharpening of the crack produces crack advance by $\Delta a$ and one striation forms after each fatigue cycle, as shown in Figure 2- 12 (d)-(f). Since the fatigue striations reflect the load history, they provide valuable information for fatigue failure analysis in both engineering and experimental tests [3].

#### 2.1.3.4 Retardation and transients in fatigue crack growth

In the case of a crack that is perfectly sharp and behaves totally elastically, a crack should close only when unloading from tension is complete, that is, when $\sigma$ is zero. Crack growth retardation and transients, including crack closure and crack deflection can occur in materials even under constant amplitude cyclic loading. Elber was the first to identify the possibility that a fatigue crack could close even at a far field tensile load and pointed out that crack closure may influence the shape of the striation pattern on the fracture surfaces [72].

(1) Crack closure

When the crack faces touch each other under tensile far field applied loads, crack closure occurs. This closure occurs at a particular value of $K$ denoted as "$K_{closure}$" . If $K_{closure} > K_{min}$, then $\Delta K_{eff}$ equals ($K_{max} - K_{closure}$), which is less than the apparent stress intensity factor caused by the loading. Closure is generally more significant at low $\Delta K$ and low R ratios due to the lower minimum crack opening displacement. It is prevalent in long cracks (where a significant crack wake has developed), and so part of the argument for the difference observed in crack propagation rates between long and physically short cracks is the absence of closure in the latter case. There are several mechanisms that cause crack closure and these mechanisms are described in Figure 2- 13.

1) Plasticity-induced crack closure;

2) Transformation-induced crack closure. This arises from a volume increase in the vicinity of the crack tip due to deformation-induced phase transformation;

3) Oxidation-induced crack closure. Oxidation of the new surfaces generated by crack advance act to prop open the crack wake;

4) Fluid-induced crack closure. Penetration of a highly viscous fluid into the crack leading to closure;

5) Geometric incompatibilities of the crack surfaces generate roughness or geometry-induced crack closure (if there is a degree of slip irreversibility on unloading).

When fatigue crack propagation results in a wake of plastically deformed material with residual tensile strains, plasticity induced crack closure occurs [5]. Residual tensile strains are left in the material behind the advancing crack front during one cycle of crack growth, as only elastic recovery after the creation of the fracture surfaces occur. With an increase in stress intensity factor and size of the plastic zone due to crack advance, the material which has previously been deformed permanently within the plastic zone now forms an envelope of plastic zones in the wake of the crack front [1]. The premature contact of the faces in the plastic wake is the result of material extension in the loading direction. The development of a plastic wake is illustrated in Figure 2- 14. The plasticity-induced closure mechanism only has a significant effect where a plane stress state results in larger plastic zones, such as in sheet components, e.g. in an aircraft fuselage.

In plasticity-induced crack closure, the plastic wake created acts as a wedge between the two crack faces. In addition oxidation of phase transformation products may cause a volume increase around the crack tip or in the wake leading to premature contact of the crack faces after unloading [73]. Environmental factors will affect fatigue behaviour, such as new crack surfaces will oxidise in a moist atmosphere. Low load ratios, low $\Delta K$ levels, high cyclic frequencies and coarser grain sizes will also activate this process. However, this mechanism tends to predominate more for high temperature applications. For some materials exhibiting deformation-induced phase transformations, for example, metastable austenitic steel [74, 75], deformation-induced phase transformation is restricted to the crack tips; the additional volume causes premature contact of the crack faces when unloading.

During crystallographic mode II fatigue crack propagation, roughness-induced crack closure is particularly pronounced [76, 77], as illustrated in Figure 2- 15.

In this mechanism, microstructural parameters, such as grain size and the crystallographic misorientation determine the crack-closure stress-intensity factor $K_{cl}$. The value of $K_{cl}$ increases with grain size, which means the stress intensity factor $\Delta K_{eff}$ decreases with grain size, that is, the coarser the grain, the more easily roughness-induced crack closure occurs [3]. The maximum plastic zone size is normally smaller than a characteristic microstructural dimension parameter in such a grain size at relatively low $\Delta K$ levels, so crack closure is easily promoted. In addition, the roughness induced closure mechanism will be particularly pronounced under conditions of small or negative values of the stress ratio $R$, small ranges of the stress-intensity factor $\Delta K$ (HCF regime) and relatively low temperatures [73].

As an explanation for the viscous fluid induced crack closure mechanism, Endo, Okada and Hariya [78] proposed that the hydrodynamic oil pressure generated by the complete penetration of a crack by a fluid would decelerate the crack by reducing the effective stress range. In their research, several competing factors such as suppression of environmental embrittlement, minimization of oxide-induced crack closure, penetration of fluids within cracks and the hydrodynamic wedging action will determine fluid-induced crack closure. Therefore, it is complex to analyse precisely how the viscous fluid alone affects crack propagation behaviour, though theoretically a viscous fluid may work effectively in crack closure [3].

(2) Fatigue crack deflection

Even a very small deflection of a fatigue crack path could give rise to a significant reduction in crack growth rates, especially in the near-threshold fatigue regime. Under the same conditions, the effective driving force of a deflected crack is typically smaller than that of the straight crack (both of them having equal projected length). Therefore, compared to the undeflected crack, the nominal stress intensity factor range $\Delta K_I$ required to propagate a deflected crack at the same rate as a straight crack is always much greater, which implies that an apparently larger driving force is required for the propagation of a deflected crack at the same rate as that of the corresponding straight crack. If the crack length is measured along the mode I growth direction, a deflected crack propagates at an apparently slower rate than a straight crack subjected to the same effective driving force. In addition, premature contact at far-field tensile stresses may occur due to a small mismatch between the mating crack

faces during the closing of the fatigue crack, so the propensity for roughness induced crack closure also increases.

## 2.2 The effect of shot peening on fatigue crack behaviour

### 2.2.1 Introduction

As discussed in Section 2.1, fatigue is an important failure mechanism for components undergoing cyclic loading [1]; not only the microstructure and loading condition (or the environment), but also the manufacturing process, affecting for example, surface roughness [79, 80], and residual stress [81, 82], will have great influence on the fatigue limit of a component. Shot peening is a well-known surface treatment process typically applied to components, especially those containing regions of stress concentration (such as steam turbine blade disc interfaces) to improve their fatigue resistance. It is a cold work process in which the surface of a component is bombarded with small spherical media called shot, which acts as a hammer impacting on the component surface. The shot, a hard material, which usually is hardened cast steel, bombards the component surface at a relatively high velocity (40-70 m/s) [83]. The repeatability of the shot peening process is typically controlled by measuring intensity and coverage [84, 85]. The intensity of shot peening can be characterized by an Almen type gauge, which is a thin strip of SAE1070 designated as “A”, “N” and “C” type which differ in thickness but have the same width and length; while coverage is defined as the ratio of the area covered by peening indentations to the overall treated specimen surface and is expressed as a percentage. Figure 2- 16 illustrates the shot peening process. After the high velocity shot leaves the component surface, contact ceases. To avoid collision with rebounding shot, the impinging shot is fired at an oblique angle and the velocity of impact is sufficiently high to cause limited plastic flow of the surface [86]. In the near-surface layers, the elastically stressed region tends to recover to the unloaded state, whereas the plastically deformed surface region sustains some permanent deformation and develops compressive residual stresses due to the bulk elastic material surrounding it returning to its original unloaded state.

The shot peening process can therefore induce some important mechanical effects as follows:

(1) Surface roughness

Plastic flow induced when the shot with a high velocity bombards the material surface can make the surface dimpled, therefore the surface roughens. The dimples left on the surface can be reconstructed and visualized, as shown in Figure 2- 17. In addition, the surface roughness is sensitive to the shot peening process intensity, for example, in high-strength wrought magnesium alloy AZ80 where severe defects in the surface such as overlaps and microcracks were observed when the Almen intensity is higher than a critical value [87]. Normally, an increase in Almen intensity will lead to a marked increase of the surface roughness [87-89].

(2) Local surface plastic deformation

The local surface plastic deformation induces the tangling of dislocations and associated strain hardening, which leads to an increase of the material yield stress. Due to the activity of the high density of dislocations and the formation of small shear bands, mechanically-induced microstructure refinements [90-96] or even strain induced phase transformation [97-101] have been observed in steel in the surface layers. The thickness of the nanocrystalized layer is typically a few microns (depending on the material and process parameters). Figure 2- 18 from Okolo. et al. [102] gives a detailed example of how the microstructure in the near surface layer changed after being shot peened at different pressures. Figure 2- 18(a) is the microstructure of the cross section after mechanical milling and normalizing but prior to shot peening; in this stage, the microstructural gradient is confined to the top 1-2 μm of the material. Grain refinement also increases with increased shot peening intensity, as shown in Figure 2- 18 (b)-(d). Okolo et al. [102] noticed that the boundary nanocrystalline layer and the material underneath is sharp and crack-like in a normalized pearlitic steel; these steep structural gradients may have an impact on the fatigue behaviour of components, given that fatigue cracks usually originate at the surface.

(3) Compressive residual stress

As shown in Figure 2- 16, after the high velocity shot leaves the component surface, contact ceases. In the near-surface layers, the elastically stressed region tends to recover to the unloaded state, whereas the plastically deformed region sustains some permanent deformation, resulting in a residual stress distributed through the depth of the component. Based on the experimental results to date, the compressive stress formed by shot peening is generally considered to be the result of the superposition of residual stress produced by each surrounding shot [103, 104]. However, the shot peening process only affects a certain depth close to the surface and classic distribution of residual stress below the surface of a shot-peened component is described in Figure 2-19. The level of extreme surface stress is dependent on the yield point of the work-hardened surface layer: it is roughly half of the yield strength [105]. The peak compressive residual stress occurs slightly beneath the surface, then the compressive stresses decay deeper beneath the surface. The depth of this subsurface layer is directly related to the shot size that has been used. Larger shot results in deeper layers with the maximum compressive stress moving correspondingly deeper. This compressive residual stress eventually changes to become slightly tensile deeper into the sample due to self-equilibration of the stress profile. The magnitude of the balancing tensile stress depends upon the ratio of the depth of compressed layer and component thickness.

The inhomogeneous plastic deformation produced by the shot peening process in the near surface layer induces not only residual stress but also an increase in hardness, surface roughness, dislocation density, and surface defects. These outcomes depend on the shot peening parameters [106], which can be divided into two interdependent groups characterized by either the shot peening parameters or the workpiece conditions[107] , as detailed in Table 2- 2 .

### 2.2.2 The effects of shot peening on fatigue behaviour

The fatigue behaviour of a mechanical or structural component is a strong function of the loading history it experiences. The importance of surface residual compressive stresses on fatigue behaviour has long been recognized and been introduced into practical engineering components to guard against stress corrosion and fatigue failure for many years, although the surface roughening accompanying this may have a detrimental effect. The effect of a shot peening process on the component fatigue life is the result of the

complex interactions between the roughened surface, residual stress and local strain hardening.

In high cycle fatigue, the benefit of shot peening is relatively well documented in steels [57, 108-111], magnesium alloys [87] and aluminium alloys [112-114]. In the HCF regime (i.e. a relatively low applied stress amplitude), the compressive residual stress in the near surface layer may push the fatigue initiation sites back to the sub-superficial layers. However, this benefit is more complex in low cycle fatigue region due to the potential stress or strain relaxation in the early fatigue stages.

As discussed in section 2.1.3, surface roughness ($R_a$ < 0.1 μm) has a strong influence on fatigue li

fe, but the residual stress and surface microstructure condition will dominate the fatigue behaviour when the surface roughness 2.5 μm < $R_a$ < 5 μm [115]. Therefore, the rough surface induced by shot peening may not be considered to play an important role in the fatigue life while both compressive residual stress and a strain hardened layer exist in the near surface layer, both of which are believed to benefit fatigue initiation and propagation. The compressive residual stress may superpose with the applied stress range and contribute to a decrease of an effective mean stress experienced during fatigue cycling. The dislocation density in the near surface region will increase, so the subsequent dislocation movement is hindered, which may affect crack initiation. In addition, the increased yield stresses in the cold worked region result in lower plastic strain amplitudes under stress controlled cycling [116].

Kopsov's [117] research on high strength hammer peened steel revealed that peening decreased the fatigue initiation life in notched specimens compared to unpeened specimens, while the total fatigue life benefitted from the process. De los Rios et al [118] proposed that both crack initiation and crack propagation in A316 stainless steel were delayed by shot peening. In his research, shot peened specimens polished to a 1 μm finish were tested for comparison with unpolished ones to explore how the shot peening surface conditions affected fatigue behaviour. However since not only compressive

stresses, but also a severely distorted crystalline structure will be induced during the shot peening process, this will also affect early fatigue crack growth. Polishing shot peened specimens was found to be detrimental to the fatigue properties, which indicates that the immediate surface layer is just as important as compressive stress; in peened unpolished specimens, very small cracks initiated quickly and were orientated along the edges of surface dimples. These small, fast growing cracks arrested at the end of dimples for a period of time at an early fatigue stage, then short crack coalescence occurred after the end of the relaxation of the residual stresses, and they then immediately propagate. In Benedetti's study on Al-7075-T651 alloy [119], a complicated interaction between residual stresses and surface roughness greatly influenced the mechanism of fatigue crack initiation and early propagation. Combined with a tribofinishing treatment, the surface roughness is reduced and surface micro-cracks generated by peening treatment eliminated; the extent of the additional improvement due to roughness elimination depended on the type of shot peening, being more significant if the layer induced by compressive residual stresses is deeper [119].

Based on the knowledge we have to date, the number of cycles to form a crack (fatigue initiation life) during a fatigue test depends on the applied stress amplitude, while the crack propagation rate is determined by the stress amplitude as well as mean stress [120]. From this point of view, the influence of residual stress will potentially have a stronger influence on fatigue crack growth behaviour, especially when the driving force for crack growth is near threshold, and there will be relatively little effect on fatigue initiation. For example, non-propagating microcracks were observed in a shot peened low alloy steel; and the beneficial effect of shot peening was stated to relate to the ability of the residual stresses to arrest crack propagation [121]

Hack and Leverant et al. [122] performed a detailed investigation of the effects of shot peening compressive residual stresses on crack-opening and growth rate behaviour of surface and corner fatigue cracks through direct observations of the surface crack opening displacement (SCOD) in situ in a scanning electron microscope, where the SCOD is defined as the crack opening at the central portion of the crack, as opposed to the opening at the tip of the crack. Results showed that the effect of residual stress is more pronounced on fatigue crack propagation than initiation; and significantly affect crack opening

behaviour-thus growth behaviour was significantly affected even when the crack tip had grown beyond the zone of residual stress.

However, analysis of fatigue crack growth under residual stress is not as simple as just a modification of the traditional fatigue crack growth (without residual stress) methods, since crack shapes are no longer the expected semi-elliptical shapes but are distorted by the varying residual stress fields in the near surface regions. For example, when Prevéy conducted extensive research in fatigue opening distance resistance and fatigue crack arrest on low plasticity burnished IN718, he found by comparing crack shape revealed by heat tinting and the residual stress profile below the surface [123] that the initiated semicircular crack shapes had been severely distorted (as illustrated in Figure 2- 20) and the crack growth rate varied with direction and depth as a result of the high compression residual stress in the near surface layer.

Ochi et al [124] stated that whether a fatigue crack initiates surface or subsurface is dependent on the stress amplitude during service. The compressive residual stress decreases at the surface layer in the early stages of fatigue if the stress amplitude is high, thus the surface is preferable for initiation sites; while in the low stress amplitude case, little or no residual stress relaxation occurs, and fatigue cracks are reluctant to initiate in a compressive stress field, therefore, the fatigue crack tends to initiate subsurface where the compressive residual stress decays and an equilibrium tensile stress appears.

However, what should be noted here is that the shot-peening strengthening effect is not solely related to compressive residual stress. For example, the fatigue endurance limit of the shot-peened specimens is 20 % higher than the corresponding limit of un-peened samples; but the benefit in HCF life improvement from the near surface stain hardening is still obvious after stress-relief treatment in a high strength martensitic steel [125]. In addition, Altenberger's study in steel AISI 304 for both deep rolling and shot peened effects revealed that the plastic strain amplitudes and lifetime improvement is rather governed by the depth than by the intensity of strain-hardening [126].

### 2.2.3 The effects of shot peening induced surface roughness, residual stress and strain hardening on fatigue

Crack growth behaviour varies during the fatigue process, i.e., at an early stage cracks are arrested at the edge of shot peened dimples, and after a certain period, cracks begin to propagate quickly till catastrophic facture, which suggests that the compressive residual stress near the surface layer may not remain stable but diminish during service life. According to the reported literature, relaxation of residual stress (or the strain hardening layer) is widely observed. There are a variety of mechanisms for residual stress relaxation and distribution, for example, thermal relaxation [127-129], static relaxation (where the mechanical loading exceeds the yield condition of the material) [130], and cyclic stress relaxation [131].

According to Vohringer's research [130], residual stress relaxation induced by heat treatment or unidirectional or cyclic mechanical stress is due to dislocation movement, which converts the elastic strains related to residual stresses into microplastic deformation. He proposed that the onset of residual stress-relaxation is dependent on the resistance $R_i$ to the onset of plastic deformation, and an equation could be used to quantify this mechanism:

$$\sigma+\sigma_{rs}=R_i \qquad \text{Equation 2- 7}$$

Residual stress relation will not occur under the following condition:

$$\sigma+\sigma_{rs}<R_i \qquad \text{Equation 2- 8}$$

In the above equations, $\sigma$ is the applied stress, and $\sigma_{rs}$ is the residual stress. The applied stress may be zero (in conditions where the value will not change with time under thermal conditions), a steadily increasing value (under unidirectional deformation condition), or periodically varying (cyclic loads).

In cyclic relaxation, the main relaxation of residual stresses normally takes place in the first cycle, followed by further gradual relaxation during the lifetime [3]. Relaxation of residual stresses corresponds to redistribution and annihilation of dislocations and thus it is considered to be related to the dislocation density (strain hardening layer). In a study of the stability of shot peening induced residual stresses and their influence on fatigue lifetime in a pearlitic steel [132, 133], both the depth and the magnitude of the residual stresses was found to diminish with increasing total strain amplitude and

number of cycles, as shown in Figure 2- 21 (a) and (b). Straining with different amplitudes for only one cycle did not create a very big change between FWHM values, but the effects are much more pronounced after straining for $N_{f/2}$ cycles, illustrated in Figure 2- 21 (c) and (d). it is found that the surface residual stress at high strain amplitude $\Delta\varepsilon$ = 1 %) were almost totally relaxed after the first cycle; for those smaller strain amplitudes, the relaxation is successively lower and mainly takes place during the first cycle followed by incrementally reduced changes during further cyclic loading. When the strain range is low enough, the relaxation of the residual stress is very limited, as shown in Figure 2- 22.

Soady [134] has reported that the relaxation of the residual stress induced by shot peening occurred after 1 fatigue cycle in LCF regime in a U-notched ferritic heat resistant steel (the same tempered martensitic steel that has been studied in this PhD) by three point bending; both the profiles and magnitudes of the residual stress were the same after one cycle of loading and at 50 % of the expected total life $N_{f/2}$. Although related research reveals that relaxation depends on the load level applied during the fatigue process, and the relaxation level is affected by notches on components [127, 135]. Constraint effects of the notch geometries on stress relaxation was observed, where reduction in the direction of loading was relatively larger than in the orthogonal direction (approximately 80 % of the original value). This may explain why the fatigue behaviour still benefited from shot peening even in the LCF regime in her study.

Martin et al [136] also reported that the stability of strain hardening, and the profile of residual stress is strongly dependent on the applied stress amplitude during fatigue in normalized shot peened steel SAE 10451. He pointed out that two different steps would occur during the relaxation process, the degradation of the long-range macro-stress, followed by the decrease of short range residual stress by microstructural processes in the shot peened affected layer. High stress amplitudes caused the formation of dislocation cell structures in the shot peened layers, accompanied by the total disappearance of compressive stresses and the decrease of interference line half-width values from X-ray diffraction measurements down to the initial baseline state. Slightly different results were reported in austenitic stainless steel AISI 304 [126]. Although the initial compressive residual stress depth profile was diminished

by more than 50 % after LCF loading, surface strain hardening was not completely eliminated even by applying high cyclic stress amplitudes.

Under thermal exposure, stress relaxation is also found to be microstructure related. In TiAl alloys, after 50 h annealing at 650 °C, the surface hardening induced by shot peening significantly recovers, resulting in a significant reduction of the microhardness, compressive residual stress, and fatigue strength [137]. Foss et al [138] has reported that both the magnitude of the residual stress and work-hardening effects in a shot peened nickel based superalloy were considerably reduced after purely thermal exposure of 48 h, without changing the extent of the residual stresses or work-hardening effects; dwell-fatigue below the alloy yield stress caused a dramatic reduction in the shot-peening residual stresses and further work-hardening, as shown in Figure 2- 23. After dwell fatigue, the surface residual stress is ~400 MPa, the same as that produced by purely thermal exposure, but the compressive residual stress zone below the surface was almost completely relaxed or even decayed to the tensile stress state in the longitudinal direction. Recrystallization in the near surface in oxidizing environments was found to have no effect on the residual stress relaxation process.

Similar studies on the relaxation of residual stress in shot peened Udimet 720Li under high temperature isothermal fatigue was reported by Evan [139]. Under LCF conditions ($\Delta\varepsilon$ = 1.2 %), extensive relaxation occurred in the initial fatigue cycle. Over 50 % of the peak compressive residual stress reduction was observed after only 1 cycle at a range of temperatures (350 °C, 650 °C and 700 °C). This reduction was considered to be independent of temperature but due to the plastic deformation of the material which reduces the misfit between the peened surface and the unformed bulk. This study also found that the relaxation of residual stress is more pronounced under high temperature isothermal cycling than occurs under solely thermal exposure, which indicates that the relaxation of cold work is controlled by both thermal and mechanical processes.

In summary, the relaxation of the residual stress and strain hardening during a fatigue process is a complex interaction between the specific loading conditions, environmental factors, as well as specific material microstructure etc. This effect should be considered in any fatigue crack initiation and propagation analysis, especially in the LCF regime.

## 2.3 3D structure analysis in metallic materials

### 2.3.1 Introduction

Fatigue is a particular concern in many engineering components and there are two conventional approaches used in many studies to evaluate fatigue crack growth behaviour. The D.C. (direct current) potential drop (P.D.) method is often used to monitor long fatigue crack propagation from a pre-existing defect (usually a sharp notch) [140]. Crack growth can be monitored continuously using this technique, but the calibration of the P.D. evolution and the link to averaged crack growth behaviour must be based on a known crack geometry (which is usually checked post-test). In the case of short (or naturally initiating) fatigue cracks, when the site of initiation is not known before the test, surface replication methods are quite common. The replication technique reproduces the surface features via a softened acetate block or silicone compound which is applied at intervals during the fatigue process to the possible crack initiating region or a stress concentration zone on a specimen or component surface, thus providing a series of snapshots of the crack growth process on the surface. However, the growth of a small fatigue crack is a complex 3D process, especially for surface breaking or sub-surface initiating short cracks which typically have a more complex 3D crack shape than conventional through thickness long cracks. In this case the 3D interaction with other features such as local microstructure [141], residual stress [142], inclusions or second phases [51, 57], can significantly affect initiation and propagation behaviour during fatigue since the stress (or strain) intensity distribution around the crack periphery changes. In addition, simple measures of fatigue crack growth, $da/dN$, are based on underlying assumptions of a single crack with a crack driving force that can be described simply (e.g. by a single $\Delta K$ value). This is often not adequate to characterize the actual fatigue crack behaviour (for example, crack coalescence). The three dimensional fatigue crack shape also provides a better reflection of true fatigue crack behaviour and needs to be taken into account in any detailed quantitative fatigue crack behaviour analysis [143].

### 2.3.2 3D fatigue crack study in metals

In material science, the experimental techniques used to reveal 3D shapes can generally be categorized into two classes, namely destructive and non-destructive techniques. Heat tinting [65, 66] and mechanical serial sectioning [144-146] are examples of conventional quantitative metallographic 3D reconstruction approaches. The combinations of focussed ion beam (FIB), SEM or electron back scattered diffraction (EBSD) [147-150], which enables 3D reconstruction of microstructures or the interaction between microstructure and fatigue cracks with a resolution down to a few micrometres [151], have also been widely applied in recent years. However, these approaches introduce damage or even completely destroy the samples. For those cases, where the samples are too fragile to be sectioned (e.g. powders), or too valuable (for example, art treasures or archival materials), or where the serial 2D analysis is inadequate [152], non-destructive techniques, such as computed tomography using X-ray imaging, ultrasonic, magnetic fields, electric fields, becomes an important means to quantify such 3D data. In the present study, only 3D X-ray imaging will be discussed in detail [153].

#### 2.3.2.1 Conventional quantitative metallography

Serial sectioning, conventionally often combined with optical microscopy, can provide 3D data information based on a series of characterizations of 2D information, where the spatial resolution between slices is e.g. a few microns. In the early stages, serial sectioning was performed by careful manual polishing, microhardness indentations are put into the regions of interest and serve as fiducial marks for subsequent image alignment, and to calibrate the depth of material removal. The efficiency of sectioning, and the accuracy of the distance estimation between each slice is a barrier for this manual process. Significant effort has been put into the development of automated serial sectioning, leading to a greater consistency (higher repeatability) between the metallographic images produced from each section. Further details about the difference between manual and automatic serial sectioning approaches can be found in an article by Spowart [146]. Detailed open literature can be found about 3D analysis in materials science, for example, the 3D analysis of microstructures of proeutectoid cementite, ferrite, pearlite etc by Kral et al.

[154, 155], or the three-dimensional (3D) microstructure visualization of SiC particles by Chawla et al. [156], as shown in Figure 2- 24.

In recent years, the combination of FIB with an SEM allows for 3D information to be obtained from samples including: 3D imaging (e.g., phase distribution); 3D distribution of elements in a specific volume (3D elemental maps); and three dimensional texture analysis using electron backscatter diffraction (EBSD) [157]. What should be noted is, this electron tomography not only allows a complete characterization of the volume of interest, but also enables a spatial resolution down to a nanometre scale [158, 159]. In addition, SEMs with ultramicrotomy are also widely applied to study material degradation [160-162]. It should however be noted that the volumes that can be examined by such approaches are often very small (typically sub a cubic millimeter) and may not be able to capture all the phenomena relevant to the length scale of interest.

#### 2.3.2.2 X-ray computed tomography (CT) imaging

After the first clinical CT images were produced in London in the early 1970s, the application of X-ray imaging techniques has been rapidly developed in not only biomedical but also engineering applications [163]. For the latter, based on the light source difference, there are two different classifications of CT techniques typically described, i.e, lab-based microfocus computed tomography (μCT) and synchrotron radiation computed tomography (SRCT). During operation, radiographs, taken at differing orientations of the sample, are recorded. If these controlled rotational increments are small enough, then it is possible to compute the local value of the attenuation coefficient at each point of the sample from the complete set of radiographs [164]. The reconstruction is normally based on the filtered back-projection [164, 165]. The grey scale value in the reconstructed 3D volume indicates the corresponding X-ray attenuation through the sample [166].

As a non-destructive technique, X-ray computed tomography (either with a lab source or a synchrotron X-ray source) is an attractive technique, capable of achieving spatial resolutions in the sub-micron range (~ 700 nm), and in the case of nano-CT even smaller. Acquisition time ranges from several minutes to several days, depending on a multitude of factors; e.g. source intensity, the sample material, the desired resolution, etc. [152, 167, 168]. Initially, the X-

ray tomography technique was developed for medical applications [169] and it was not until early 2000 that CT started to be used for characterisation in materials science [170]. Recently CT and μ-CT have been increasingly used within materials science to visualize the microstructure in 3D [171], the interaction of microstructure and fatigue cracks [172-176] etc. It can provide important qualitative (or even quantitative) evaluation of a 3D microstructure and its interaction with crack morphologies by static or in-situ CT-imaging [174, 177]. The combination of X-ray tomography and electron back scatter diffraction (EBSD) is able to provide extra information about, for example, the relation between the crystallographic orientation of individual grains and subsequent crack path, allowing the prediction of preferred crack orientation [178]; similarly, the recently developed X-ray diffraction contrast tomography can characterize grain orientation in polycrystalline materials in 3D, and a fuller description needed to analyse local crack growth rates of short fatigue cracks in three dimensions can also be obtained by combining it with propagation-based phase contrast tomography [179].

Figure 2- 25 is an example of the 3D shape and propagation of fatigue crack in titanium alloy Ti-6Al-4V by CT imaging with ultra-bright synchrotron radiation. However, μ-CT imaging of steel can be challenging especially when sub-micrometer pixel resolution is required. The main challenge arises from the fact that, for a given photon energy, the X-ray linear attenuation coefficient, μ, of a material is dependent on the atomic number, Z, of its constituent elements as well as its geometrical characteristics. Higher Z leads to higher attenuation. In the case of steel, the determinant element is Fe ($Z_{Fe}$ = 55.8), which, for the relatively low photon energies that high-resolution μ-CT scanners use nowadays, means that, even when miniature samples are employed, only a small proportion of the generated photons will be able to get through the sample and interact with the detector. To compensate for this, long exposures have to be utilised and as a result a scanning time of tens of hours is not uncommon.

## 2.4 Summary

In this chapter, three different aspects have been focused on, namely, quantification and classification approaches to fatigue problems in general,

assessment of the shot peening process and its effect on fatigue behaviour, and 3D structure analysis in metallic materials.

When subjected to fluctuating load service conditions, fatigue is a particular concern for many engineering structures and components. Total life and damage tolerant approaches which are applied to evaluate fatigue life have been introduced in some detail. Fatigue degradation is a micro-damage accumulation process, which typically will involve fatigue crack initiation, short crack propagation and long crack growth until failure occurs. In most cases, crack initiation and short crack propagation are the dominant fatigue processes, where both the surface conditions and material microstructure will play significant roles. The micromechanisms of fatigue behaviour which have been considered to be aspects of interest in the present study are also detailed. These include fatigue crack initiation and propagation behaviour at different stages, and retardation and transients in fatigue crack growth. Specifically attention has been focused on the short fatigue crack behaviour in materials of interest.

Shot peening is a cold work process, introducing not only compressive residual stress and strain hardening in the subsurface layer which are beneficial to fatigue resistance, but also increases a component's surface roughness which is considered to be detrimental to fatigue life. The beneficial assessments of shot peening indicate that fatigue crack initiation and fatigue propagation behaviour under shot peening conditions is different to observations in the absence of shot peening. What's more, the service conditions (loading condition, thermal exposure conditions etc.) considerably affect the shot peening benefits due to the instabilities of the residual stress distribution and strain hardening. In the HCF regime, this benefit is well documented, since the stress or strain relaxation is less significant under lower stress amplitude loading. Although extensive efforts have been made to study the influence of shot peening induced factors in the near-surface layers on the fatigue life of different material systems, systematic research on fatigue crack initiation and propagation behaviour (especially those operating in the LCF regime) in this residual compressive stress region has not yet been adequately investigated. Whilst a few studies have tried to investigate the effect of the near surface layer induced by shot peening, only the total fatigue life has been focused on, not the detail of the evolution of the fatigue crack initiation or propagation

behaviour. This effect of shot peening layers on fatigue crack initiation and propagation needs to be further understood and characterised in the low cycle fatigue regime.

Conventionally, microstructure characterization usually involves 2D images. The availability of 3D microstructure reconstruction can provide more representative information and now is becoming a critical tool in many aspects of materials analysis. X-ray tomography as a non-destructive technique has been developed and widely applied in the bio-medical area as well as materials science research in recent years. Although there has been considerable improvement in spatial resolution and image reconstruction times, there are still a lot of challenges when it comes to the analysis of steel, especially when sub-micrometer pixel resolution is required. Although it damages samples, serial sectioning can provide much higher resolution due to the combination of optical microscopy or SEM resolutions. Regardless of its time consuming nature, serial sectioning is still a powerful approach to reconstruct small scale microstructure features, such as fatigue cracks or corrosion pits, etc. Research which has focused on the effect of shot peening on fatigue crack initiation and propagation behaviour or the effect of stress relaxation, were generally confined to surface observations which provide little information about the evolving three-dimensional (3D) shape of these cracks. Although the fatigue crack morphologies are indicated to vary significantly in shot peened and unpeened layers, there seems to be little detailed information available in the literature on how the 3D surface breaking fatigue crack morphologies are affected by the shot peened layers, that is, the crack propagation in the shot peened layers. Understanding this will provide important information on the evolution of the crack growth behaviour and will lead to more quantitative and micromechanically informed shot peening fatigue life assessments.

## 2.5 Figures

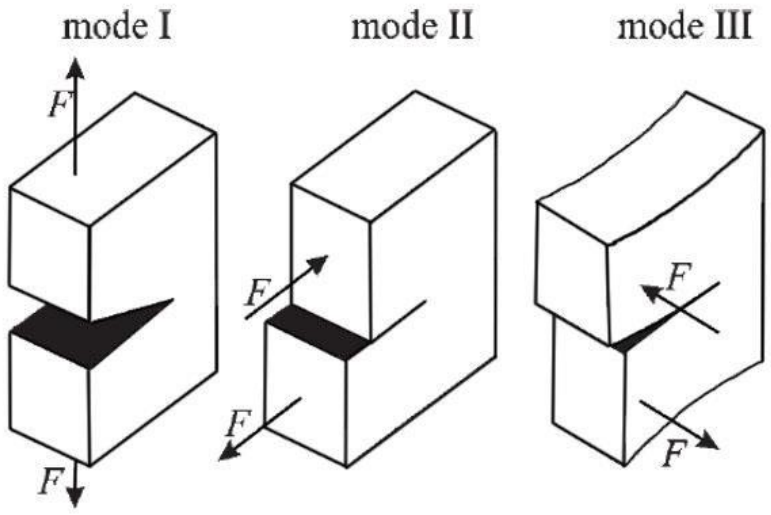


Figure 2- 1 Schematic representation of the three fundamental crack-opening modes: (a) mode I (opening), (b) Mode II (in-plane shear), (c) mode III (anti-plane shear) [3].

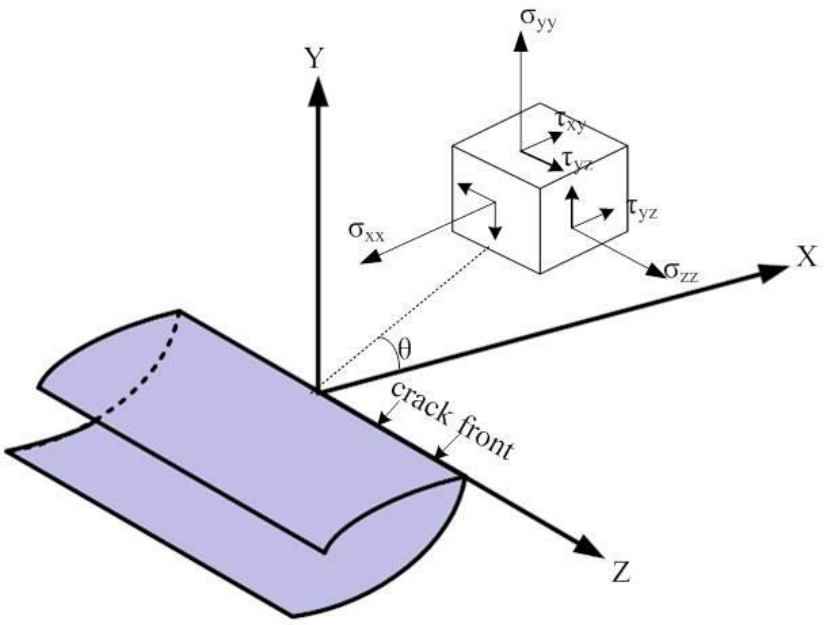


Figure 2- 2 Eight coordinate system and crack tip stress components, after [4].

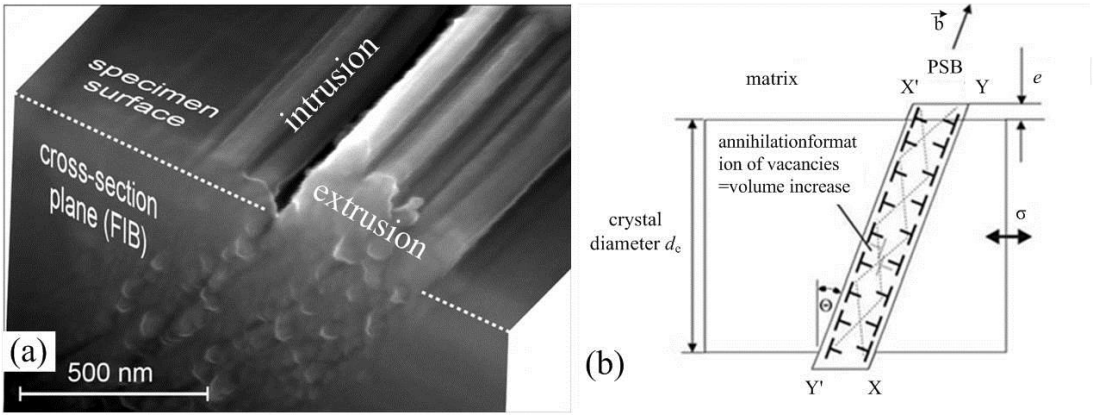


Figure 2- 3 (a) SEM-FEG micrograph of a cross-sectioned individual PSM in 316L cycled with $\varepsilon_{amplitude}$ = 0.0001. The PSM was sectioned by FIB after 500 cycles and then fatigued to 2000 cycles after[12]; (b) schematic representation of the mechanism of extrusions/protrusions at a persistent slip band according to the EGM model [3, 16].

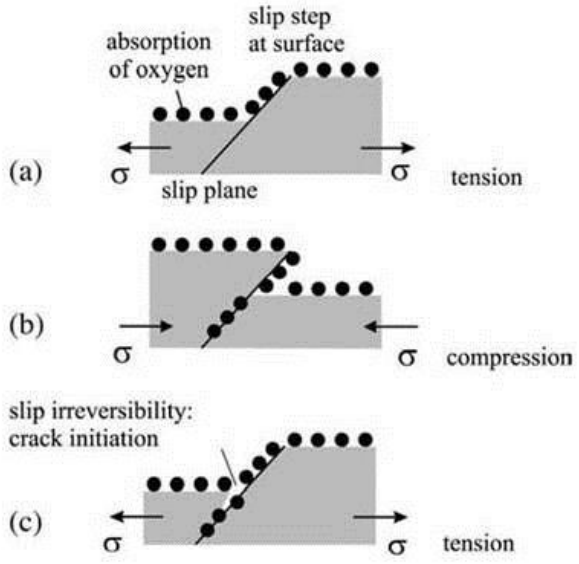


Figure 2- 4 Crack initiation due to environmentally assisted slip irreversibility: (a) exposure of fresh metal surface; (b) absorption of oxygen; (c) local decohesion [3].

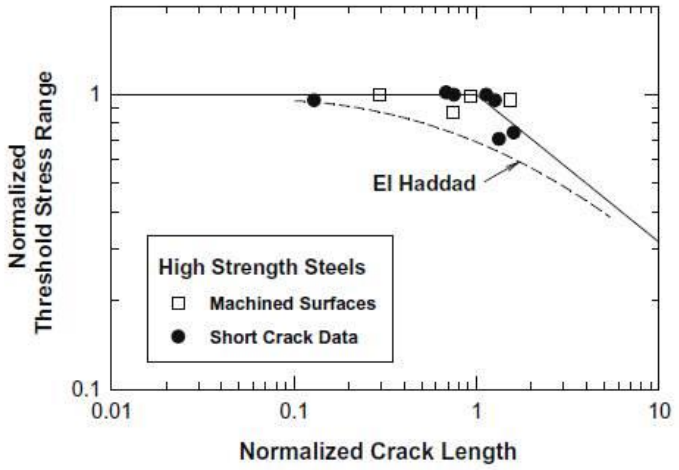


Figure 2- 5 Normalized Kitagawa diagram with fatigue data from machined surfaces with various surface roughnesses (polished, ground, or milled) compared to short crack data in high strength steels [21].

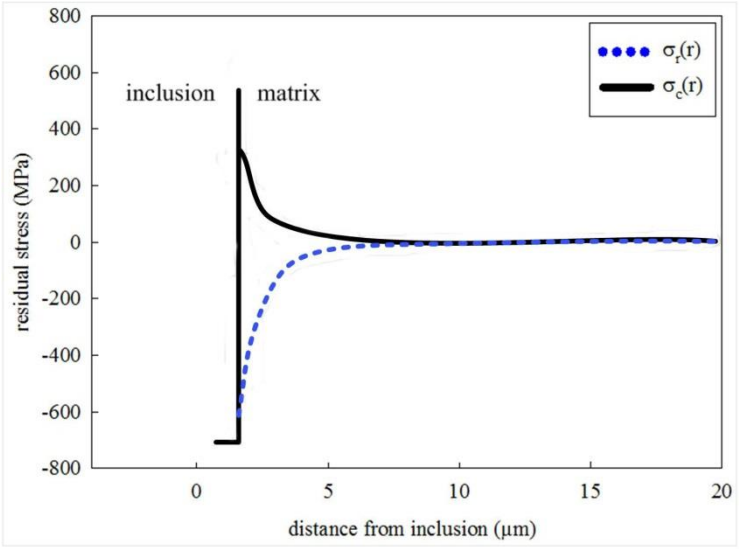


Figure 2- 6 Residual stress in steel matrix around $Al_2O_3$ inclusions, after [54, 180].

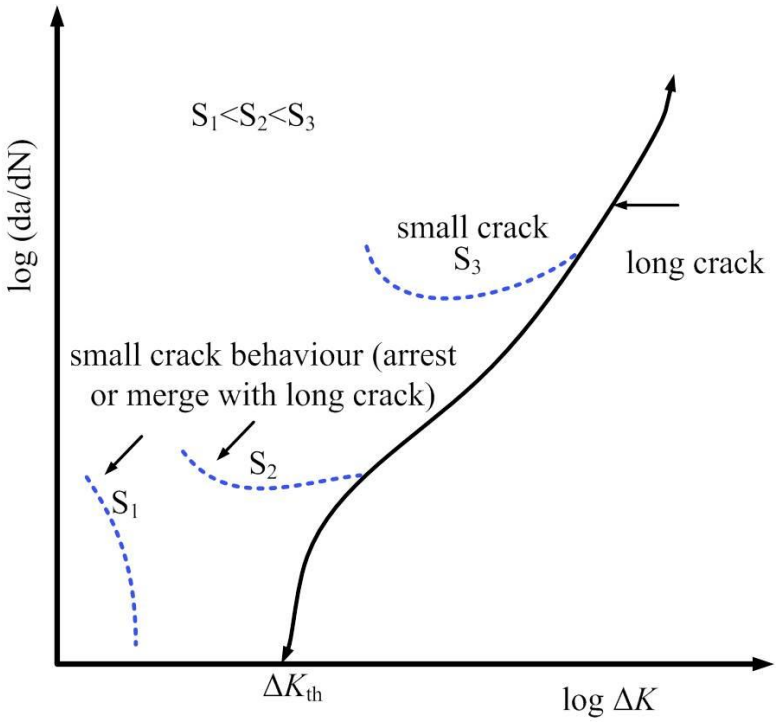


Figure 2- 7 The differences in fatigue crack growth rates between long and short cracks [181].

Table 2- 1 Definition and characteristic of fatigue cracks of different lengths [3].

| Abnormal crack-propagation behaviour | | *K*-determined crack-propagation behavior | |
|---|---|---|---|
| Microstructurally short cracks | Mechanically short cracks | Physically short cracks | Long cracks |
| • Strong influence of the microstructure<br>• Mainly mode II crack propagation (stage Ia) and transition to mode I<br>• Roughness induced crack closure | • No pronounced crack-closure effects<br>• Little influence of the microstructure<br>• Mainly Mode I crack propagation<br>• Large plastic zone ahead of the crack tip | • Little influence of the microstructure<br>• Plasticity-induced crack closure<br>• Mainly Mode I crack propagation<br>• Negligibly small plastic zone ahead of the crack tip (relative to the crack length) | • Completely developed plasticity – induced crack closure<br>• Microstructure long cracks (crack length of the order > 0.5mm) |

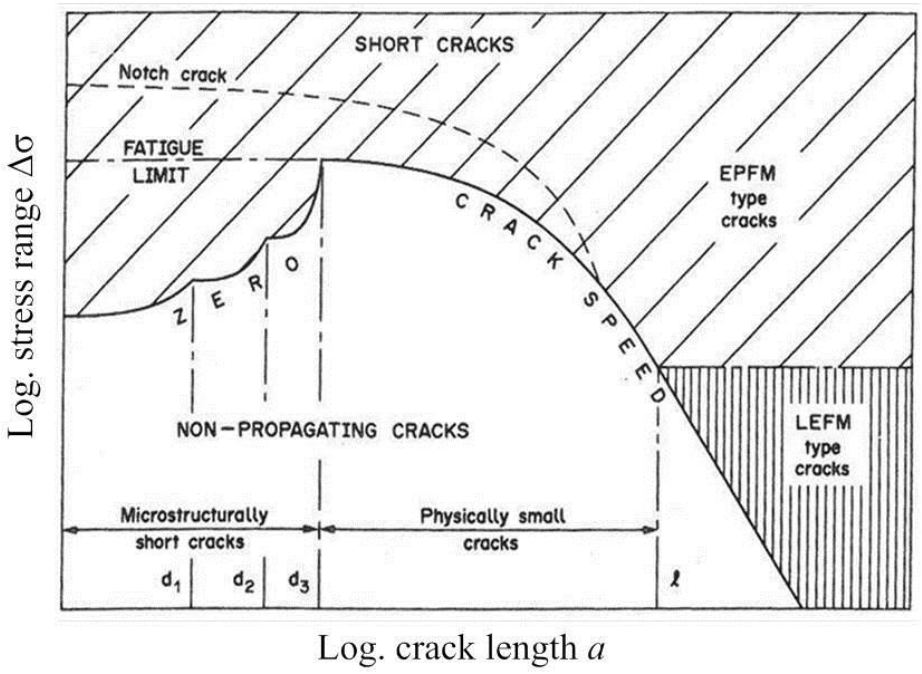


Figure 2- 8 Three regimes of short crack behaviour [62].

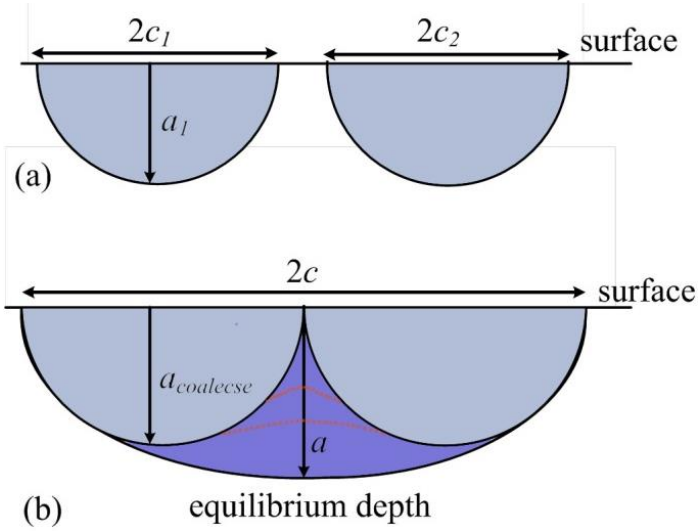


Figure 2- 9 Crack coalescence: two coalescing cracks (a) resume growing at the surface only when the new crack (b) has reached its equilibrium shape at depth *a*, after [3].

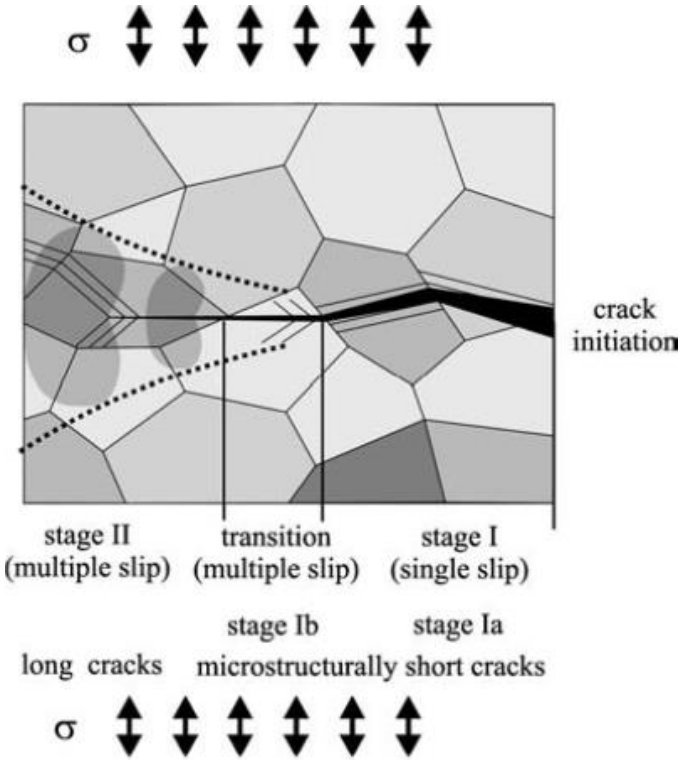


Figure 2- 10 Transition from stage I (stage Ia: shear-stress-controlled, stage Ib: normal-stress-controlled) to stage II crack propagation (normal-stress controlled) [3].

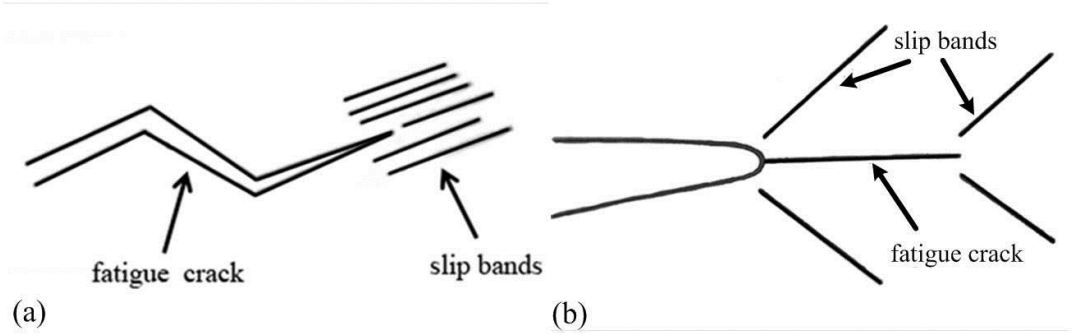


Figure 2- 11(a) A schematic of stage I fatigue crack growth (b) An idealization of stage II fatigue crack growth [1].

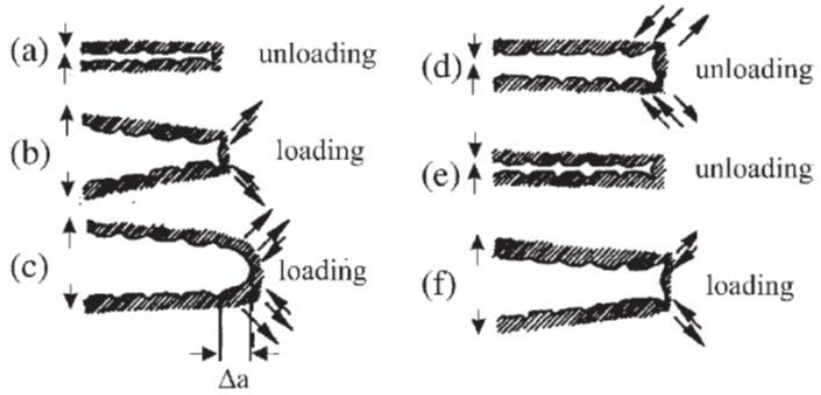


Figure 2- 12 Schematic representation of the Laird Model of striation formation [3].

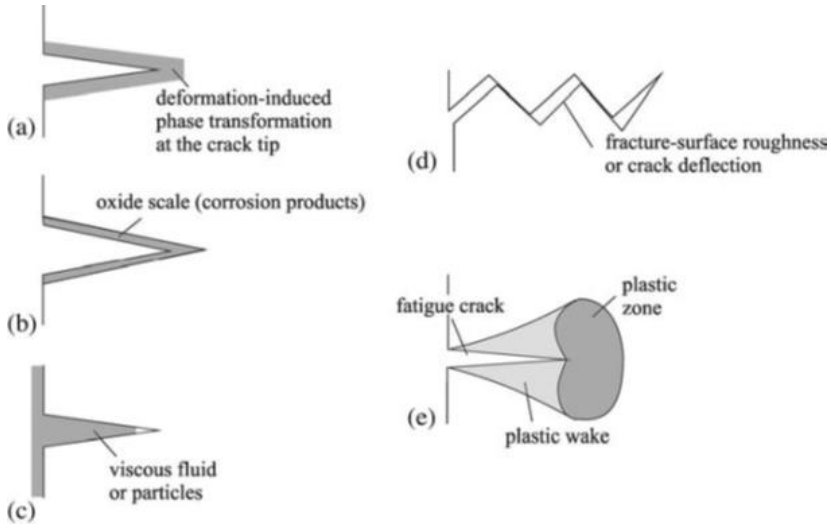


Figure 2- 13 Different crack closure mechanisms: (a) transformation induced crack closure, (b) oxidation-induced crack closure, (c) fluid-induced crack closure, (d) roughness or geometry induced crack closure and (e) plasticity-induced crack closure.

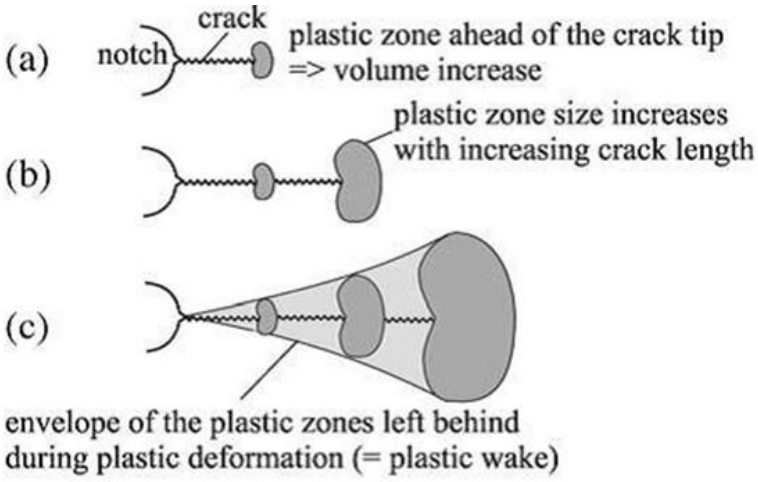


Figure 2- 14 Schematic of the development of a plastic wake [182].

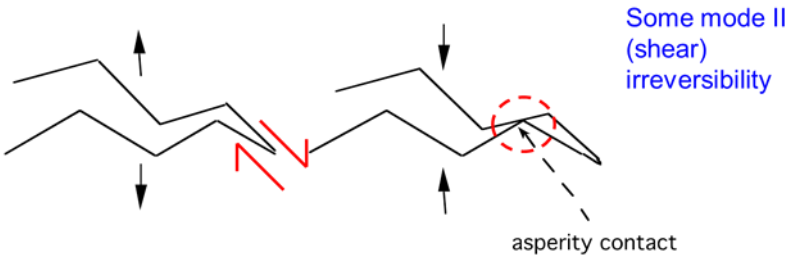


Figure 2- 15 Schematic of roughness-induced closure mechanism [183].

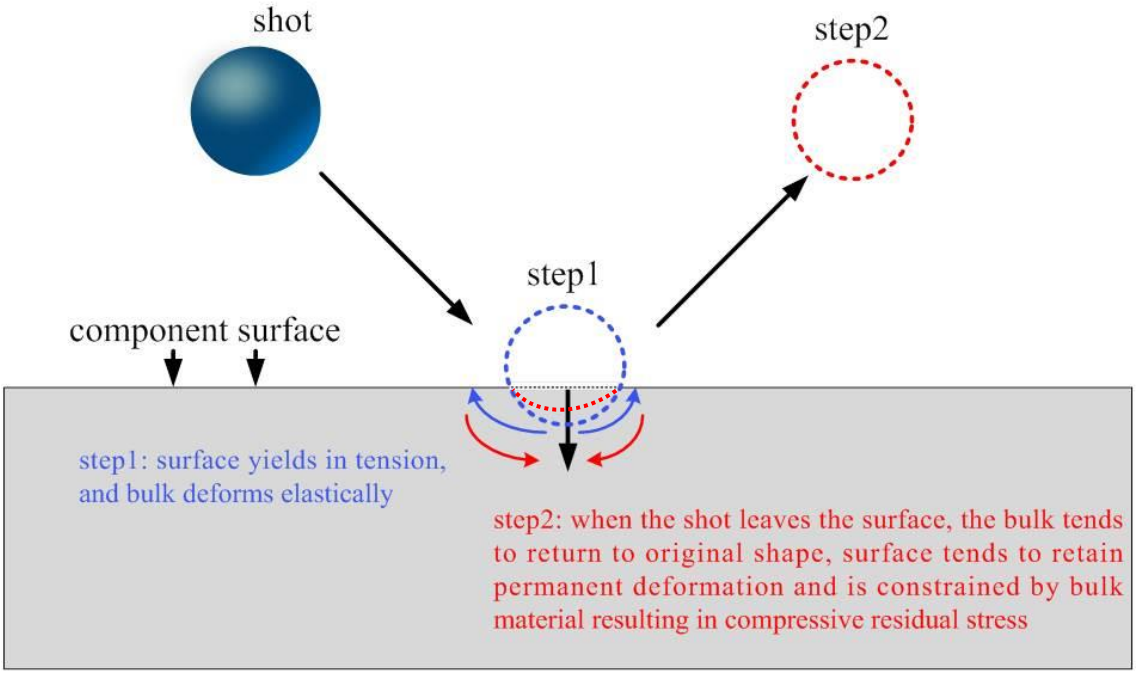


Figure 2- 16 Mechanism of formation of compressive residual stresses during shot peening, after [116].

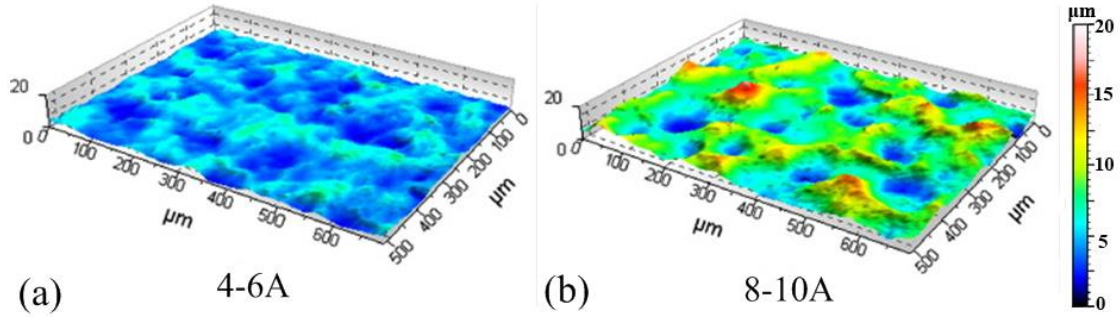


Figure 2- 17 Three-dimensional reconstructions by white-light interferometry of five different shot-peening intensities: (a) 4-6 A; (b) 8-10 A, applied to a Ni-based alloy 720Li [88].

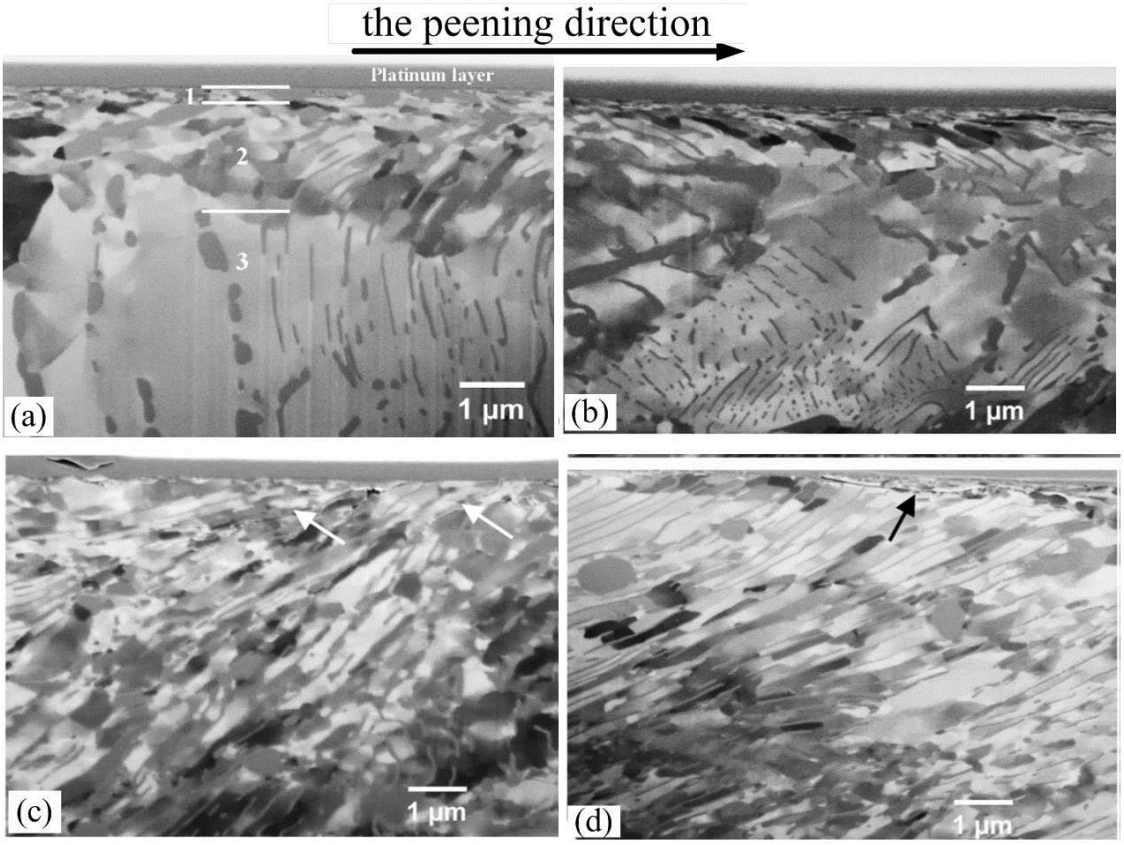


Figure 2- 18 FIB images of cross-sections of pearlitic carbon steel samples (a) subsurface microstructure obtained after mechanical milling and normalizing but prior to shot peening, where the microstructural gradient can be can be sub-divided in a very fine grained, about 300 nm thick surface layer (1) in which the grains appear to be equiaxed, followed by ~ 1-2 µm thick layer (2) in which the material appears to be sheared to one side and is still more finely structured than the bulk material (3); (b) the surface has been shot peened at a pressure of 2bar; (c) 2.5 bar, and (d) 4 bar [102].

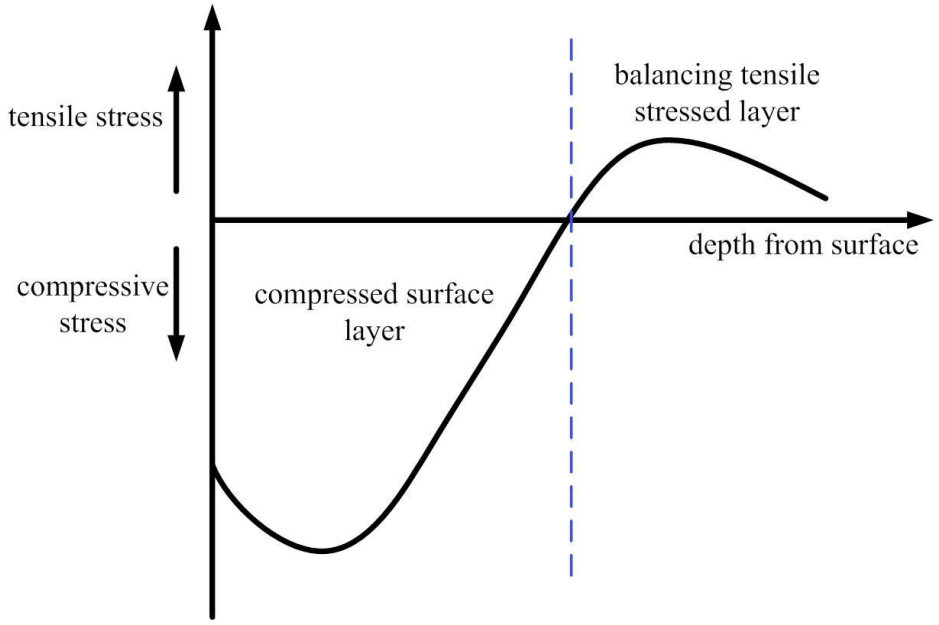


Figure 2- 19 Classic residual stress profile for shot-peened component, after [105].

Table 2- 2 The parameters affecting shot peening

| **Shot peening conditions** | **Workpiece conditions** |
|---|---|
| Type and density | Hardness or yield point |
| Shape, diameter and size distribution | Work hardening rate |
| Hardness, velocity(or pressure) | Residual stresses |
| surface topography | Phase composition |
| Exposure time or coverage | Phase stability |
| Mass flow | Defects in surface layer |
| Impact angle | |
| Nozzle diameter | |
| Distance from nozzle to workpiece | |

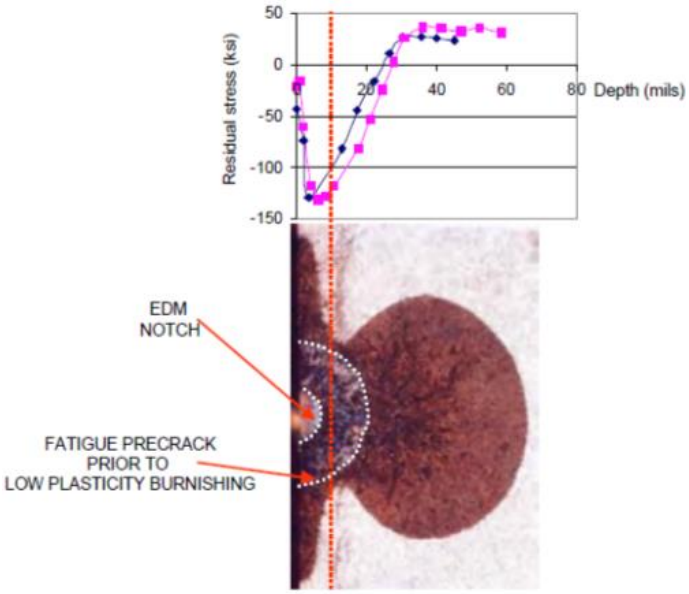


Figure 2- 20 Effect of LPB (low plasticity burnish) on crack growth in a NASA superalloys E960 specimen pre-crack not removed [123].

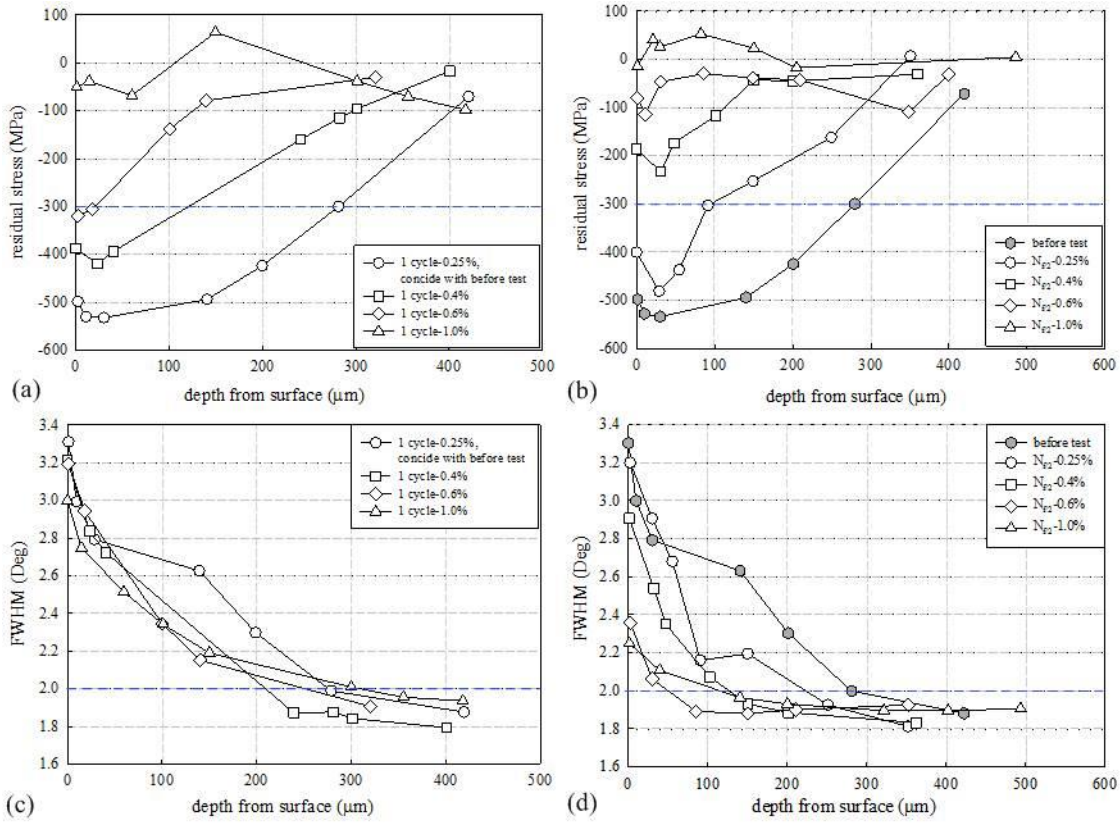


Figure 2- 21 (a) Longitudinal residual stress distribution versus the depth after the first fatigue cycle and (b) half of the established fatigue limit cycles $N_{f/2}$; (c) FWHM measured versus the depth after the first cycle and (b) after half of the established fatigue limit cycles $N_{f/2}$ at different strain amplitudes, after [133].

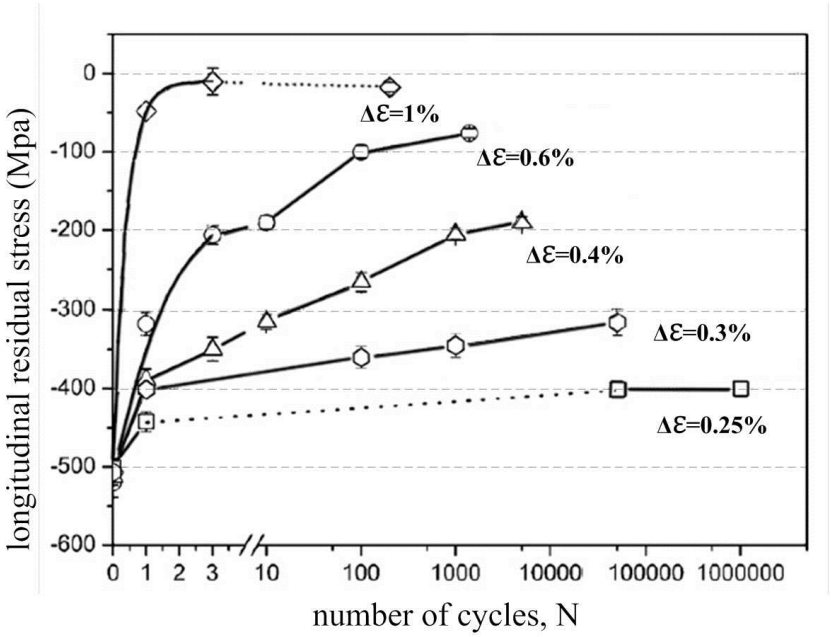


Figure 2- 22 Relaxation of the surface residual stress at differing strain amplitudes until $N_{f/2}$ cycles [133].

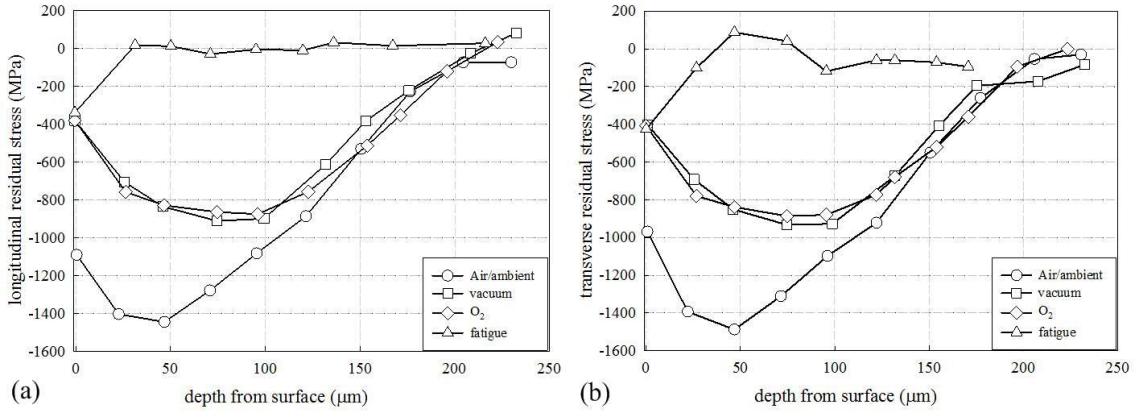


Figure 2- 23 The residual stress profile after various service conditions in nickel based alloy RR1000 following thermal exposure and dwell-fatigue in (a) longitudinal and (b) transverse direction [138].

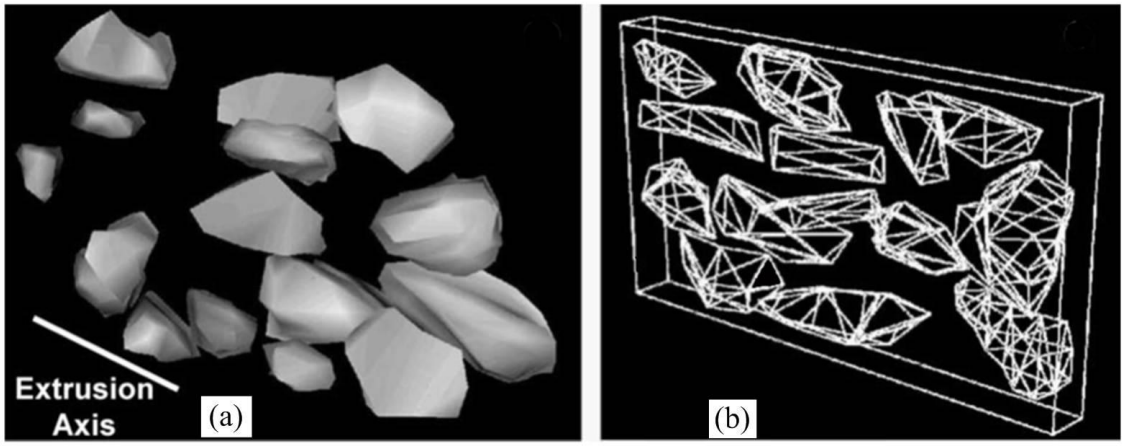


Figure 2- 24 3D reconstruction of the complex geometry of SiC particles, showing clear alignment of particles along the extraction axis [156].

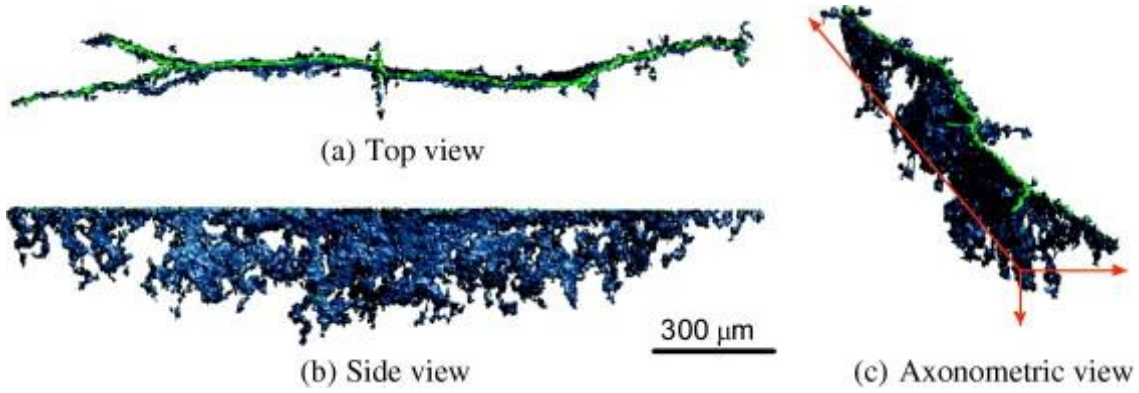


Figure 2- 25 CT image of a crack initiated in cyclic torsion in titanium alloy Ti-6Al-4V ($S_a$ = 450 MPa, N = 1.86 x$10^5$ cycles) [184].

## 2.6 References

[1] S. Suresh, *Fatigue of materials*, 2 ed., Cambridge University Press, 1998.
[2] S.A. Muhammad, *Microstructural modelling of fatigue in layered bearing architectures*, in: Material Research Group, Ph.D thesis, the University of Southampton, 2007.
[3] U. Krupp, *Fatigue crack propagation in metals and alloys*, Wiley-VCH, Germany, 2007.
[4] X.R. Wu, A.J. Carlsson, *Weight functions and stress intensity factor solutions*, 1st ed., Pergamon Press, 1991.
[5] Paris, P.C., F. Erdogan, *A critical analysis of crack propagation laws*, Journal of Basic Engineering, 85 (1963).
[6] J.R. Rice, *A path independent integral and the approximate analysis of strain concentrations by notches and cracks*, Journal of Applied Mechanics, 35 (1968) 379-386.
[7] K. Shiozawa, H. Matsushita, *Crack initiation and small fatigue crack growth behaviour of Beta Ti-15V-3Cr- 3Al-3Sn Alloy*, in: G. Lütjering, H. Nowack (Eds.) the 6th International Fatigue Congress, Berlin, 1996, pp. 301.
[8] K. Tokaji, S. Takafuji, K. Ohya, Y. Kato, K. Mori, *Fatigue behaviour of beta Ti-22V-4Al alloy subjected to surface-microstructural modification*, Journal of Materials Science, 38 (2003) 1153-1159.
[9] M.D. Sangid, *The physics of fatigue crack initiation*, International Journal of Fatigue, 57 (2013) 58-72.
[10] P. Lukáš, L. Kunz ‡, *Role of persistent slip bands in fatigue*, Philosophical Magazine, 84 (2004) 317-330.
[11] S.E. Harvey, P.G. Marsh, W.W. Gerberich, *Atomic force microscopy and modeling of fatigue crack initiation in metals*, Acta Metallurgica et Materialia, 42 (1994) 3493-3502.
[12] J. Man, K. Obrtlík, J. Polák, *Extrusions and intrusions in fatigued metals. Part 1. State of the art and history*, Philosophical Magazine, 89 (2009) 1295-1336.
[13] J. Man, P. Klapetek, O. Man, A. Weidner†, K. Obrtlík, J. Polák, *Extrusions and intrusions in fatigued metals. Part 2. AFM and EBSD study of the early growth of extrusions and intrusions in 316L steel fatigued at room temperature*, Philosophical Magazine, 89 (2009) 1337-1372.
[14] J. Man, K. Obrtlík, C. Blochwitz, J. Polák, *Atomic force microscopy of surface relief in individual grains of fatigued 316L austenitic stainless steel*, Acta Materialia, 50 (2002) 3767-3780.
[15] J. Man, K. Obrtlík, J. Polák, *Study of surface relief evolution in fatigued 316L austenitic stainless steel by AFM*, Materials Science and Engineering: A, 351 (2003) 123-132.
[16] U. Essmann, U. Gösele, H. Mughrabi, *A Model of Extrusions and Intrusions in Fatigued Metals I. Point-defect Production and the Growth of Extrusions*, Philosophical Magazine A, 44 (1981).
[17] N. Thompson, N. Wadsworth, N. Louat, *The origin of fatigue fracture in copper*, Philosophical Magazine, 1 (1956) 113-126.
[18] W.A. Wood, *Formation of fatigue cracks*, Philosophical Magazine, 3 (1958) 692-699.
[19] J.F.a.S. Flavenot, N., *Effects of grinding conditions on fatigue behaviour of 42CD4 grade steel; comparison of different fatigue criteria incorporating residual stresses*, in: L. Mordfin (Ed.) Mechanical Relaxation of Residual Stresses, Cincinnati, Ohio, 1987, pp. 91-111.

[20] N. Skalli, J. Flavenot, *Effects of grinding conditions on fatigue behaviour of 42CD4 grade steel*, in: ECF5, Lisbon 1984, 2013.
[21] D. Taylor, O.M. Clancy, *The fatigue performance of machined surfaces*, Fatigue & Fracture of Engineering Materials & Structures, 14 (1991) 329-336.
[22] J.H. Ryu, S.W. Nam, *Effect of surface roughness on low-cycle fatigue life of Cr・Mo・V steel at 550°C*, International Journal of Fatigue, 11 (1989) 433-436.
[23] M. Suraratchai, J. Limido, C. Mabru, R. Chieragatti, *Modelling the influence of machined surface roughness on the fatigue life of aluminium alloy*, International Journal of Fatigue, 30 (2008) 2119-2126.
[24] S.K. Ås, B. Skallerud, B.W. Tveiten, B. Holme, *Fatigue life prediction of machined components using finite element analysis of surface topography*, International Journal of Fatigue, 27 (2005) 1590-1596.
[25] D. Arola, C.L. Williams, *Estimating the fatigue stress concentration factor of machined surfaces*, International Journal of Fatigue, 24 (2002) 923-930.
[26] T. Yuri, Y. Ono, T. Ogata, *Effects of surface roughness and notch on fatigue properties for Ti-5Al-2.5Sn ELI alloy at cryogenic temperatures*, Science and Technology of Advanced Materials, 4 (2003) 291-299.
[27] P. Prevéy, J. Cammett, *Low cost corrosion damage mitigation and improved fatigue performance of low plasticity burnished 7075-T6*, Journal of Materials Engineering and Performance, 10 (2001) 548-555.
[28] R. Avilés, J. Albizuri, A. Rodríguez, L.N. López de Lacalle, *Influence of low-plasticity ball burnishing on the high-cycle fatigue strength of medium carbon AISI 1045 steel*, International Journal of Fatigue, 55 (2013) 230-244.
[29] L. Wagner, *Mechanical surface treatments on titanium, aluminum and magnesium alloys*, Materials Science and Engineering: A, 263 (1999) 210-216.
[30] A. Drechsler, T. Dörr, L. Wagner, *Mechanical surface treatments on Ti-10V-2Fe-3Al for improved fatigue resistance*, Materials Science and Engineering: A, 243 (1998) 217-220.
[31] A. Eftekhari, J.E. Talia, P.K. Mazumdar, *Influence of surface condition on the fatigue of an aluminum-lithium alloy (2090-T3)*, Materials Science and Engineering: A, 199 (1995) L3-L6.
[32] Y.K. Gao, X.R. Wu, *Experimental investigation and fatigue life prediction for 7475-T7351 aluminum alloy with and without shot peening-induced residual stresses*, Acta Materialia, 59 (2011) 3737-3747.
[33] R.K. Nalla, I. Altenberger, U. Noster, G.Y. Liu, B. Scholtes, R.O. Ritchie, *On the influence of mechanical surface treatments—deep rolling and laser shock peening—on the fatigue behavior of Ti-6Al-4V at ambient and elevated temperatures*, Materials Science and Engineering: A, 355 (2003) 216-230.
[34] I. Nikitin, B. Scholtes, H.J. Maier, I. Altenberger, *High temperature fatigue behavior and residual stress stability of laser-shock peened and deep rolled austenitic steel AISI 304*, Scripta Materialia, 50 (2004) 1345-1350.
[35] I. Nikitin, I. Altenberger, *Comparison of the fatigue behavior and residual stress stability of laser-shock peened and deep rolled austenitic stainless steel AISI 304 in the temperature range 25-600 °C*, Materials Science and Engineering: A, 465 (2007) 176-182.
[36] Y. Tan, G. Wu, J.M. Yang, T. Pan, *Laser shock peening on fatigue crack growth behaviour of aluminium alloy*, Fatigue & Fracture of Engineering Materials & Structures, 27 (2004) 649-656.
[37] W.P. Koster, *Effect of residual stress on fatigue of structural alloys*, in: Practical Applications of Residual Stress Technology, Conference Proceedings, Indianapolis, Indiana, 1991, pp. 1-9.

[38] S. Andrews, H. Sehitoglu, *A computer model for fatigue crack growth from rough surfaces*, International Journal of Fatigue, 22 (2000) 619–630.
[39] C.M. Sonsino, J. Ziese, *Fatigue strength and applications of cast aluminium alloys with different degrees of porosity*, International Journal of Fatigue, 15 (1993) 75–84.
[40] H. Mayer, M. Papakyriacou, B. Zettl, S.E. Stanzl-Tschegg, *Influence of porosity on the fatigue limit of die cast magnesium and aluminium alloys*, International Journal of Fatigue, 25 (2003) 245–256.
[41] M.J. Couper, A.E. Neeson, J.R. Griffiths, *Casting deffects and the fatigue behaviour of an aluminium casting alloy*, Fatigue & Fracture of Engineering Materials & Structures, 13 (1990) 213–227.
[42] J.M. Hyzak, I.M. Bernstein, *The effect of defects on the fatigue crack initiation process in two p/m superalloys: part i. fatigue origins*, Metallurgical Transactions A, 13 (1982) 33–43.
[43] S.J. Polasik, J.J. Williams, N. Chawla, *Fatigue crack initiation and propagation of binder-treated powder metallurgy steels*, Metallurgical and Materials Transactions A, 33 (2002) 73–81.
[44] J. Fan, D.L. McDowell, M.F. Horstemeyer, K. Gall, *Cyclic plasticity at pores and inclusions in cast Al–Si alloys*, Engineering Fracture Mechanics, 70 (2003) 1281–1302.
[45] S. Hudak Jr, G. Chell, T. Rennick, R. McClung, D. Davidson, *A damage tolerance approach to fod based on the 'worst case notch'concept*, in: Proceedings of the 4th national turbine engine high cycle fatigue conference, Monterey, CA, 1999.
[46] K. Tanaka, T. Mura, *A theory of fatigue crack initiation at inclusions*, Metallurgical Transactions A, 13 (1982) 117–123.
[47] Y. Murakami, H. Usuki, *Quantitative evaluation of effects of non-metallic inclusions on fatigue strength of high strength steels. II: Fatigue limit evaluation based on statistics for extreme values of inclusion size*, International Journal of Fatigue, 11 (1989) 299–307.
[48] J. Lankford, F.N. Kusenberger, *Initiation of fatigue cracks in 4340 steel*, Metallurgical Transactions, 4 (1973) 553–559.
[49] J. Lankford, *Inclusion-matrix debonding and fatigue crack initiation in low alloy steel*, International Journal of Fracture, 12 (1976) 155–157.
[50] S. Pearson, *Initiation of fatigue cracks in commercial aluminium alloys and the subsequent propagation of very short cracks*, Engineering Fracture Mechanics, 7 (1975) 235–247.
[51] Q.Y. Wang, C. Bathias, N. Kawagoishi, Q. Chen, *Effect of inclusion on subsurface crack initiation and gigacycle fatigue strength*, International Journal of Fatigue, 24 (2002) 1269–1274.
[52] C. Bowles, J. Schijve, *The role of inclusions in fatigue crack initiation in an aluminum alloy*, International Journal of Fracture, 9 (1973) 171–179.
[53] W.L. Morris, O. Buck, H.L. Marcus, *Fatigue crack initiation and early propagation in Al 2219-T851*, Metallurgical Transactions A, 7 (1976) 1161–1165.
[54] D. Brooksbank, K. Andrews, *Tessellated stresses associated with some inclusions in steel*, J Iron Steel Inst, 207 (1969) 474–483.
[55] J.R. Yates, W. Zhang, K.J. Miller, *The initiation and propagation behaviour of short fatigue cracks in waspaloy subjected to bending* Fatigue & Fracture of Engineering Materials & Structures, 16 (1993) 351–362.
[56] R.C. Boettner, A.J. McEvily, Y.C. Liu, *On the formation of fatigue cracks at twin boundaries*, Philosophical Magazine, 10 (1964) 95–106.

[57] K. Shiozawa, Y. Morii, S. Nishino, L. Lu, *Subsurface crack initiation and propagation mechanism in high-strength steel in a very high cycle fatigue regime*, International Journal of Fatigue, 28 (2006) 1521–1532.
[58] E.J. Giordani, V.A. Guimarães, T.B. Pinto, I. Ferreira, *Effect of precipitates on the corrosion–fatigue crack initiation of ISO 5832-9 stainless steel biomaterial*, International Journal of Fatigue, 26 (2004) 1129–1136.
[59] J.Y. Buffière, S. Savelli, P.H. Jouneau, E. Maire, R. Fougères, *Experimental study of porosity and its relation to fatigue mechanisms of model Al–Si7–Mg0.3 cast Al alloys*, Materials Science and Engineering: A, 316 (2001) 115–126.
[60] M.N. Batista, M.C. Marinelli, S. Hereñú, I. Alvarez-Armas, *The role of microstructure in fatigue crack initiation of 9–12%Cr reduced activation ferritic–martensitic steel*, International Journal of Fatigue, 72 (2015) 75–79.
[61] M.N. Batista, S. Hereñú, I. Alvarez-Armas, *The role of microstructure in fatigue crack initiation and propagation in 9-12Cr ferritic-martensitic steels*, Procedia Engineering, 74 (2014) 228–231.
[62] K.J. Miller, *The behaviour of short fatigue cracks and their initiation part II-A general summary*, Fatigue & Fracture of Engineering Materials & Structures, 10 (1987) 93–113.
[63] W. Morris, *Microcrack closure phenomena for Al 2219-T851*, Metallurgical and Materials Transactions A, 10 (1979) 5–11.
[64] J. Stolarz, *Multicracking in low cycle fatigue—a surface phenomenon?*, Materials Science and Engineering: A, 234–236 (1997) 861–864.
[65] K.S. Ravichandran, J.M. Larsen, X.D. Li, *Significance of crack shape or aspect ratio to the behavior of small fatigue cracks in Titanium alloys*, in: K.S. Ravichandran, R.O. Ritchie, Y. Murakami (Eds.) Small Fatigue Cracks: Mechanics, Mechanisms, and Applications 1999.
[66] K.S. Ravichandran, J.M. Larsen, *An approach to measure the shape of three-dimensional surface cracks during fatigue crack growth* Fatigue & Fracture of Engineering Materials & Structures, 16 (1993) 909–930.
[67] C.J. Bayley, R. Bell, *Parametric investigation into the coalescence of coplanar fatigue cracks*, International Journal of Fatigue, 21 (1999) 355–360.
[68] N. Wu, S. Zhao, P. Ding, *Small crack growth and fatigue life predictions for high-strength aluminum alloys: Part 1-Experimental and fracture mechanics analysis* Fatigue & Fracture of Engineering Materials & Structures, 21 (1998) 1289–1306.
[69] N.E. Dowling, *Cyclic stress-strain and plastic deformation aspects of fatigue crack growth.* , ASTM, 1977.
[70] K.S. Ravichandran, X.–D. Li, *Fracture mechanical character of small cracks in polycrystalline materials: Concept and numerical K calculations*, Acta Materialia, 48 (2000) 525–540.
[71] C. Laird, G.C. Smith, *Crack propagation in high stress fatigue*, Philosophical Magazine, 7 (1962) 847–857.
[72] E. Wolf, *Fatigue crack closure under cyclic tension*, Engineering Fracture Mechanics, 2 (1970) 37–45.
[73] P.K. Liaw, *Overview of crack closure at near-threshold fatigue crack growth levels*, Mechanics of Fatigue Crack Closure, ASTM STP 982 (1988) 62–92.
[74] H.R. Mayer, S.E. Stanzl–Tschegg, Y. Sawaki, M. Hühner, E. Hornbogen, *Influence of transformation-induced crack closure on slow fatigue crack growth under variable amplitude loading*, Fatigue & Fracture of Engineering Materials & Structures, 18 (1995) 935–948.
[75] E. Hornbogen, *Martensitic transformation at a propagating crack*, Acta Metallurgica, 26 (1978) 147–152.

[76] J. Petit, A. Zeghloul, *On the effect of environment on short crack growth behaviour and threshold*, The Behaviour of Short Fatigue Cracks, (1986) 163-177.
[77] S.-H. Wang, C. Müller, *Fracture surface roughness and roughness-induced fatigue crack closure in Ti-2.5 wt% Cu*, Materials Science and Engineering: A, 255 (1998) 7-15.
[78] E. Kichiro, O. Tsunenori, H. Toshiaki, *Fatigue crack propagation in bearing metals lining on steel plates in lubricating oil*, Bulletin of JSME, 15 (1972) 439-445.
[79] P.S. Maiya, D.E. Busch, *Effect of surface roughness on low-cycle fatigue behavior of type 304 stainless steel*, Metallurgical Transactions A, 6 (1975) 1761-1766.
[80] A. Javidi, U. Rieger, W. Eichlseder, *The effect of machining on the surface integrity and fatigue life*, International Journal of Fatigue, 30 (2008) 2050-2055.
[81] G.A. Webster, A.N. Ezeilo, *Residual stress distributions and their influence on fatigue lifetimes*, International Journal of Fatigue, 23, Supplement 1 (2001) 375-383.
[82] M.N. James, D.J. Hughes, Z. Chen, H. Lombard, D.G. Hattingh, D. Asquith, J.R. Yates, P.J. Webster, *Residual stresses and fatigue performance*, Engineering Failure Analysis, 14 (2007) 384-395.
[83] S.A. Meguid, G. Shagal, J.C. Stranart, J. Daly, *Three-dimensional dynamic finite element analysis of shot-peening induced residual stresses*, Finite Elements in Analysis and Design, 31 (1999) 179-191.
[84] P.S. Prevey, J.T. Cammett, *The effect of shot peening coverage on residual stress, cold work and fatigue in a Ni-Cr-Mo low alloy steel*, in, DTIC Document, 2000.
[85] J. Cammett, P. Prevéy, N. Jayaraman, *The effect of shot peening coverage on residual stress, cold work, and fatigue in a nickel-base superalloy*, in, DTIC Document, 2005.
[86] D. Hills, R. Waterhouse, B. Noble, *An analysis of shot peening*, The Journal of Strain Analysis for Engineering Design, 18 (1983) 95-100.
[87] P. Zhang, J. Lindemann, *Influence of shot peening on high cycle fatigue properties of the high-strength wrought magnesium alloy AZ80*, Scripta Materialia, 52 (2005) 485-490.
[88] D.J. Child, G.D. West, R.C. Thomson, *Assessment of surface hardening effects from shot peening on a Ni-based alloy using electron backscatter diffraction techniques*, Acta Materialia, 59 (2011) 4825-4834.
[89] K.A. Soady, B.G. Mellor, G.D. West, G. Harrison, A. Morris, P.A.S. Reed, *Evaluating surface deformation and near surface strain hardening resulting from shot peening a tempered martensitic steel and application to low cycle fatigue*, International Journal of Fatigue, 54 (2013) 106-117.
[90] N.R. Tao, M.L. Sui, J. Lu, K. Lua, *Surface nanocrystallization of iron induced by ultrasonic shot peening*, Nanostructured Materials, 11 (1999) 433-440.
[91] G. Liu, J. Lu, K. Lu, *Surface nanocrystallization of 316L stainless steel induced by ultrasonic shot peening*, Materials Science and Engineering: A, 286 (2000) 91-95.
[92] G. Liu, S.C. Wang, X.F. Lou, J. Lu, K. Lu, *Low carbon steel with nanostructured surface layer induced by high-energy shot peening*, Scripta Materialia, 44 (2001) 1791-1795.

[93] N.R. Tao, Z.B. Wang, W.P. Tong, M.L. Sui, J. Lu, K. Lu, *An investigation of surface nanocrystallization mechanism in Fe induced by surface mechanical attrition treatment*, Acta Materialia, 50 (2002) 4603-4616.
[94] T. Wang, J. Yu, B. Dong, *Surface nanocrystallization induced by shot peening and its effect on corrosion resistance of 1Cr18Ni9Ti stainless steel*, Surface and Coatings Technology, 200 (2006) 4777-4781.
[95] B.N. Mordyuk, G.I. Prokopenko, M.A. Vasylyev, M.O. Iefimov, *Effect of structure evolution induced by ultrasonic peening on the corrosion behavior of AISI-321 stainless steel*, Materials Science and Engineering: A, 458 (2007) 253-261.
[96] H. Mano, S. Kondo, A. Matsumuro, *Microstructured surface layer induced by shot peening and its effect on fatigue strength*, in: Micro-NanoMechatronics and Human Science, 2006 International Symposium on, 2006, pp. 1-4.
[97] Z. Ni, X. Wang, J. Wang, E. Wu, *Characterization of the phase transformation in a nanostructured surface layer of 304 stainless steel induced by high-energy shot peening*, Physica B: Condensed Matter, 334 (2003) 221-228.
[98] H. Sato, T. Nishiura, E. Miura-Fujiwara, Y. Watanabe, *Phase transformation in Fe Alloys induced by surface treatment*, in: T. Chandra, M. Ionescu, D. Mantovani (Eds.) Thermec 2011, Pts 1-4, Trans Tech Publications Ltd, Stafa-Zurich, 2012, pp. 1996-2001.
[99] M. Gao, S. Chen, R. Wei, *Crack paths, microstructure, and fatigue crack growth in annealed and cold-rolled AISI 304 stainless steels*, Metallurgical Transactions A, 23 (1992) 355-371.
[100] V. Shrinivas, S. Varma, L. Murr, *Deformation-induced martensitic characteristics in 304 and 316 stainless steels during room-temperature rolling*, Metallurgical and Materials Transactions A, 26 (1995) 661-671.
[101] H. Huang, J. Ding, P. McCormick, *Microstructural evolution of 304 stainless steel during mechanical milling*, Materials Science and Engineering: A, 216 (1996) 178-184.
[102] B. Okolo, F. Pérez-Willard, J. Hawecker, D. Gerthsen, A. Wanner, *Focused ion beam study of the effects of shot peening on the subsurface microstructure of normalized pearlitic steel*, Journal of Materials Processing Technology, 183 (2007) 160-164.
[103] M. Kobayashi, T. Matsui, Y. Murakami, *Mechanism of creation of compressive residual stress by shot peening*, International Journal of Fatigue, 20 (1998) 351-357.
[104] G.H. Majzoobi, R. Azizi, A. Alavi Nia, *A three-dimensional simulation of shot peening process using multiple shot impacts*, Journal of Materials Processing Technology, 164-165 (2005) 1226-1234.
[105] D. Kirk, *Shot peening*, Aircraft Engineering and Aerospace Technology, 71 (1999) 349-361.
[106] G.H. Farrahi, J.L. Lebrijn, D. Couratin, *Effect of shot peening on residual stress and fatigue life of a spring steel*, Fatigue & Fracture of Engineering Materials & Structures, 18 (1995) 211-220.
[107] Q. Qui, R. Wang, *Changes in the state of the material by shot peening*, in: Proceedings of the 3rd International Conference on Shot Peening (ICSP3), H. Wohlfahrt, R. Kopp and O. V öhringer), DGM Informationsgesellschaft Verlag, Oberursel, 1987, pp. 231-238.
[108] K. Shiozawa, L. Lu, *Very high-cycle fatigue behaviour of shot-peened high-carbon-chromium bearing steel*, Fatigue & Fracture of Engineering Materials & Structures, 25 (2002) 813-822.

[109] B. Nie, Z. Zhang, Z. Zhao, Q. Zhong, *Very high cycle fatigue behavior of shot-peened 3Cr13 high strength spring steel*, Materials & Design, 50 (2013) 503–508.
[110] M.A.S. Torres, H.J.C. Voorwald, *An evaluation of shot peening, residual stress and stress relaxation on the fatigue life of AISI 4340 steel*, International Journal of Fatigue, 24 (2002) 877–886.
[111] R. Fathallah, A. Laamouri, H. Sidhom, C. Braham, *High cycle fatigue behavior prediction of shot-peened parts*, International Journal of Fatigue, 26 (2004) 1053–1067.
[112] H. Luong, M.R. Hill, *The effects of laser peening and shot peening on high cycle fatigue in 7050-T7451 aluminum alloy*, Materials Science and Engineering: A, 527 (2010) 699–707.
[113] C.A. Rodopoulos, S.A. Curtis, E.R. de los Rios, J. Solis Romero, *Optimisation of the fatigue resistance of 2024-T351 aluminium alloys by controlled shot peening—methodology, results and analysis*, International Journal of Fatigue, 26 (2004) 849–856.
[114] L. Wagner, C. Mueller, *Effect of shot peening of fatigue behaviour in Al-alloys*, Materials and Manufacturing Processes, 7 (1992) 423–440.
[115] W.P. Koster, *Effect of residual stress on fatigue of structural alloys*, 1991.
[116] K.A. Soady, *Life assessment methodologies incoroporating shot peening process effects: mechanistic consideration of residual stresses and strain hardening part 1-effect of shot peening on fatigue resistance*, Materials Science and Technology, 29 (2013) 637–651.
[117] I.E. Kopsov, *The influence of hammer peening on fatigue in high-strength steel*, International Journal of Fatigue, 13 (1991) 479–482.
[118] E.R. De los Rios, A. Walley, M.T. Milan, G. Hammersley, *Fatigue crack initiation and propagation on shot-peened surfaces in A316 stainless steel*, International Journal of Fatigue, 17 (1995) 493–499.
[119] M. Benedetti, V. Fontanari, M. Bandini, E. Savio, *High- and very high-cycle plain fatigue resistance of shot peened high-strength aluminum alloys: The role of surface morphology*, International Journal of Fatigue, 70 (2015) 451–462.
[120] R.C. McClung, *A literature survey on the stability and significance of residual stresses during fatigue*, Fatigue & Fracture of Engineering Materials & Structures, 30 (2007) 173–205.
[121] M. Guagliano, L. Vergani, *An approach for prediction of fatigue strength of shot peened components*, Engineering Fracture Mechanics, 71 (2004) 501–512.
[122] J.E. Hack, G.R. Leverant, *Influence of compressive residual stress on the crack-opening behavior of part-through fatigue cracks*, in: Residual Stress Effects in Fatigue, ASTM STP 776, American Society for Testing and Materials, 1982, pp. 204–233.
[123] P. Prevéy, J. Telesman, T. Gabb, P. Kantzos, *FOD resistance and fatigue crack arrest in low plasticity burnished IN718*, in: Proceedings of the 5th Nat. Turbine Eng. HCF Conference, 2000.
[124] Y. Ochi, K. Masaki, T. Matsumura, T. Sekino, *Effect of shot-peening treatment on high cycle fatigue property of ductile cast iron*, International Journal of Fatigue, 23 (2001) 441–448.
[125] A.M. Eleiche, M.M. Megahed, N.M. Abd-Allah, *The shot-peening effect on the HCF behavior of high-strength martensitic steels*, Journal of Materials Processing Technology, 113 (2001) 502–508.
[126] I. Altenberger, B. Scholtes, U. Martin, H. Oettel, *Cyclic deformation and near surface microstructures of shot peened or deep rolled austenitic stainless steel AISI 304*, Materials Science and Engineering: A, 264 (1999) 1–16.

[127] G. Leverant, B. Langer, A. Yuen, S. Hopkins, *Surface residual stresses, surface topography and the fatigue behavior of Ti-6AI-4V*, Metallurgical and Materials Transactions A, 10 (1979) 251-257.
[128] M.C. Berger, J.K. Gregory, *Residual stress relaxation in shot peened Timetal 21s*, Materials Science and Engineering: A, 263 (1999) 200-204.
[129] J. Hoffmann, B. Scholtes, O. Vöhringer, *Thermal relaxation of shot peening residual stresses in the differently heat treated plain carbon steel Ck 45*, in: H. Wohlfahrt, R. Kopp, O. Vöhringer (Eds.) the 3rd International Conference on Shot Peening, Garmisch-Partenkirchen, Germany, 1987.
[130] O. Vöhringer, *Relaxation of residual stresses by annealing or mechanical treatment*, Pergamon Press, Advances in Surface Treatments. Technology--Applications--Effects., 4 (1987) 367-396.
[131] V. Schulze, K. Lang, O. Vöhringer, E. Macherauch, *Relaxation of shot peening induced residual stresses in quenched and tempered steel AISI 4140 due to uniaxial cyclic deformation*, in: Proc. 6th Int. Conf. on Shot Peening (ICSP6). San Francisco, 1996, pp. 403-412.
[132] K. Dalaei, B. Karlsson, L.E. Svensson, *Stability of residual stresses created by shot peening of pearlitic steel and their influence on fatigue behaviour*, Procedia Engineering, 2 (2010) 613-622.
[133] K. Dalaei, B. Karlsson, L.E. Svensson, *Stability of shot peening induced residual stresses and their influence on fatigue lifetime*, Materials Science and Engineering: A, 528 (2011) 1008-1015.
[134] K.A. Soady, B.G. Mellor, J. Shackleton, A. Morris, P.A.S. Reed, *The effect of shot peening on notched low cycle fatigue*, Materials Science and Engineering a-Structural Materials Properties Microstructure and Processing, 528 (2011) 8579-8588.
[135] J. Bergström, T. Ericsson, *Relaztion of shot peening induced compressive stress during fatigue of notched steel samples* Surface Engineering, 2 (1986) 115-120.
[136] U. Martin, I. Altenberger, B. Scholtes, K. Kremmer, H. Oettel, *Cyclic deformation and near surface microstructures of normalized shot peened steel SAE 10451*, Materials Science and Engineering: A, 246 (1998) 69-80.
[137] J. Lindemann, C. Buque, F. Appel, *Effect of shot peening on fatigue performance of a lamellar titanium aluminide alloy*, Acta Materialia, 54 (2006) 1155-1164.
[138] B.J. Foss, S. Gray, M.C. Hardy, S. Stekovic, D.S. McPhail, B.A. Shollock, *Analysis of shot-peening and residual stress relaxation in the nickel-based superalloy RR1000*, Acta Materialia, 61 (2013) 2548-2559.
[139] A. Evans, S.B. Kim, J. Shackleton, G. Bruno, M. Preuss, P.J. Withers, *Relaxation of residual stress in shot peened Udimet 720Li under high temperature isothermal fatigue*, International Journal of Fatigue, 27 (2005) 1530-1534.
[140] in: ASTM E647-08, American Society for Testing and Materials: Standard Test Method for Measurement of Fatigue Crack Growth Rates.
[141] D. Taylor, J.F. Knott, *Fatigue crack propagation behaviour of short cracks: The effect of microstructure*, Fatigue & Fracture of Engineering Materials & Structures, 4 (1981) 147-155.
[142] Y. Mutoh, G.H. Fair, B. Noble, R.B. Waterhouse, *The effect of residual stresses induced by shot peening on fatigue cracks propagation in two high strength aluminium alloys*, Fatigue & Fracture of Engineering Materials & Structures, 10 (1987) 261-272.
[143] K.J. Miller, *The short crack problem*, Fatigue & Fracture of Engineering Materials & Structures, 5 (1982) 223-232.

[144] P. Clement, J.P. Angeli, A. Pineau, *Short cack behaviour in nodular cast iron* Fatigue & Fracture of Engineering Materials & Structures, 7 (1984) 251-265.
[145] S.I. Lieberman, A.M. Gokhale, S. Tamirisakandala, *Reconstruction of three-dimensional microstructures of TiB phase in a powder metallurgy titanium alloy using montage serial sectioning*, Scripta Materialia, 55 (2006) 63-68.
[146] J.E. Spowart, *Automated serial sectioning for 3-D analysis of microstructures*, Scripta Materialia, 55 (2006) 5-10.
[147] W. Schaef, M. Marx, H. Vehoff, A. Heckl, P. Randelzhofer, *A 3-D view on the mechanisms of short fatigue cracks interacting with grain boundaries*, Acta Materialia, 59 (2011) 1849-1861.
[148] M.A. Groeber, B.K. Haley, M.D. Uchic, D.M. Dimiduk, S. Ghosh, *3D reconstruction and characterization of polycrystalline microstructures using a FIB-SEM system*, Materials Characterization, 57 (2006) 259-273.
[149] M.D. Uchic, M.A. Groeber, D.M. Dimiduk, J.P. Simmons, *3D microstructural characterization of nickel superalloys via serial-sectioning using a dual beam FIB-SEM*, Scripta Materialia, 55 (2006) 23-28.
[150] D.J. Rowenhorst, A. Gupta, C.R. Feng, G. Spanos, *3D Crystallographic and morphological analysis of coarse martensite: Combining EBSD and serial sectioning*, Scripta Materialia, 55 (2006) 11-16.
[151] C. Schoettle, P.A.S. Reed, M.J. Starink, I. Sinclair, D.J. Child, G.D. West, R.C. Thomson, *Sustained macroscopic deflected fatigue crack growth in Nickel based superalloy 720Li*, in: 12th international symposium on superalloys, John Wiley & Sons, Inc., Seven Springs, PA, USA, 2012.
[152] M. E., W.P. J., *Quantitative X-ray tomography*, International Materials Reviews, 59 (2014) 1-43.
[153] A.C. Kak, *Computerized tomography with X-ray, emission, and ultrasound sources*, Proceedings of the IEEE, 67 (1979) 1245-1272.
[154] M.V. Kral, M.A. Mangan, G. Spanos, R.O. Rosenberg, *Three-dimensional analysis of microstructures*, Materials Characterization, 45 (2000) 17-23.
[155] M.V. Kral, G. Spanos, *Three-dimensional analysis of proeutectoid cementite precipitates*, Acta Materialia, 47 (1999) 711-724.
[156] N. Chawla, V.V. Ganesh, B. Wunsch, *Three-dimensional (3D) microstructure visualization and finite element modeling of the mechanical behavior of SiC particle reinforced aluminum composites*, Scripta Materialia, 51 (2004) 161-165.
[157] R. Wirth, *Focused Ion Beam (FIB) combined with SEM and TEM: Advanced analytical tools for studies of chemical composition, microstructure and crystal structure in geomaterials on a nanometre scale*, Chemical Geology, 261 (2009) 217-229.
[158] M. Kato, T. Ito, Y. Aoyama, K. Sawa, T. Kaneko, N. Kawase, H. Jinnai, *Three-dimensional structural analysis of a block copolymer by scanning electron microscopy combined with a focused ion beam*, Journal of Polymer Science Part B: Polymer Physics, 45 (2007) 677-683.
[159] E. Principe, P. Sobol, *High-density FIB-SEM tomography via real-time imaging*, Microscopy and Microanalysis, 11 (2005) 322-323.
[160] T. Hashimoto, X. Zhou, C. Luo, K. Kawano, G.E. Thompson, A.E. Hughes, P. Skeldon, P.J. Withers, T.J. Marrow, A.H. Sherry, *Nanotomography for understanding materials degradation*, Scripta Materialia, 63 (2010) 835-838.
[161] W. Yang, S. Ji, X. Zhou, I. Stone, G. Scamans, G. Thompson, Z. Fan, *Heterogeneous nucleation of □-Al grain on primary □-AlFeMnSi intermetallic*

*investigated using 3D SEM Ultramicrotomy and HRTEM*, Metallurgical and Materials Transactions A, 45 (2014) 3971–3980.
[162] A. Trueman, S. Knight, J. Colwell, T. Hashimoto, J. Carr, P. Skeldon, G. Thompson, *3-D tomography by automated in situ block face ultramicrotome imaging using an FEG-SEM to study complex corrosion protective paint coatings*, Corrosion Science, 75 (2013) 376–385.
[163] E.L. Ritman, *Micro-computed tomography-current status and developments*, Annu. Rev. Biomed. Eng., 6 (2004) 185–208.
[164] E. Maire, J.Y. Buffière, L. Salvo, J.J. Blandin, W. Ludwig, J.M. Létang, *On the application of X-ray microtomography in the field of materials science*, Advanced Engineering Materials, 3 (2001) 539–546.
[165] L.A. Feldkamp, L.C. Davis, J.W. Kress, *Practical cone-beam algorithm*, Journal of the Optical Society of America A, 1 (1984) 612–619.
[166] S.R. Stock, *Micro-computed tomography: methodology and applications*, CRC press, 2008.
[167] S.R. Stock, *X-ray microtomography of materials*, International Materials Reviews, 44 (1999) 141–164.
[168] S.R. Stock, *Recent advances in X-ray microtomography applied to materials*, International Materials Reviews, 53 (2008) 129–181.
[169] J.C. Elliott, S.D. Dover, *X-ray microtomography*, Journal of Microscopy, 126 (1982) 211–213.
[170] L. Salvo, M. Suéry, A. Marmottant, N. Limodin, D. Bernard, *3D imaging in material science: Application of X-ray tomography*, Comptes Rendus Physique, 11 (2010) 641–649.
[171] A. Stiénon, A. Fazekas, J.Y. Buffière, A. Vincent, P. Daguier, F. Merchi, *A new methodology based on X-ray micro-tomography to estimate stress concentrations around inclusions in high strength steels*, Materials Science and Engineering: A, 513–514 (2009) 376–383.
[172] T.O. Mbuya, I. Sinclair, A. Moffat, P. Reed, *Micromechanisms of fatigue crack growth in cast aluminium piston alloys*, International Journal of Fatigue, 42 (2012) 227–237.
[173] P. Li, P.D. Lee, T.C. Lindley, D.M. Maijer, G.R. Davis, J.C. Elliott, *X-ray microtomographic characterisation of porosity and its influence on fatigue crack growth*, Advanced Engineering Materials, 8 (2006) 476–479.
[174] W. Ludwig, J.Y. Buffière, S. Savelli, P. Cloetens, *Study of the interaction of a short fatigue crack with grain boundaries in a cast Al alloy using X-ray microtomography*, Acta Materialia, 51 (2003) 585–598.
[175] E. Ferrié, J.Y. Buffière, W. Ludwig, *3D characterisation of the nucleation of a short fatigue crack at a pore in a cast Al alloy using high resolution synchrotron microtomography*, International Journal of Fatigue, 27 (2005) 1215–1220.
[176] T.J. Marrow, J.Y. Buffiere, P.J. Withers, G. Johnson, D. Engelberg, *High resolution X-ray tomography of short fatigue crack nucleation in austempered ductile cast iron*, International Journal of Fatigue, 26 (2004) 717–725.
[177] H. Toda, *3D/4D analyses of damage and fracture behaviours in structural materials via synchrotron X-ray tomography*, Microscopy (Oxford, England), 63 Suppl 1 (2014) i3–i4.
[178] S. Birosca, J.Y. Buffiere, F.A. Garcia-Pastor, M. Karadge, L. Babout, M. Preuss, *Three-dimensional Characterization of Fatigue Cracks in Ti-6246 using X-ray Tomography and Electron Backscatter Diffraction*, Acta Materialia, 57 (2009) 5834–5847.
[179] M. Herbig, A. King, P. Reischig, H. Proudhon, E.M. Lauridsen, J. Marrow, J.-Y. Buffière, W. Ludwig, *3-D growth of a short fatigue crack within a*

*polycrystalline microstructure studied using combined diffraction and phase-contrast X-ray tomography*, Acta Materialia, 59 (2011) 590–601.
[180] K.S. Chan, *Roles of microstructure in fatigue crack initiation*, International Journal of Fatigue, 32 (2010) 1428–1447.
[181] J.C. Newman Jr, E.P. Phillips, M.H. Swain, *Fatigue-life prediction methodology using small-crack theory*, International Journal of Fatigue, 21 (1999) 109–119.
[182] W. Elber, *The significance of fatigue crack closure*, Demage tolerance in aircraft structure, ASTM STP 486 (1971) 230–242.
[183] I. Sinclair, P.A.S. Reed, *Failure of materials under stress,course notes in the University of Southampton*, 2013.
[184] D. Shiozawa, Y. Nakai, T. Murakami, H. Nosho, *Observation of 3D shape and propagation mode transition of fatigue cracks in Ti–6Al–4V under cyclic torsion using CT imaging with ultra-bright synchrotron radiation*, International Journal of Fatigue, 58 (2014) 158–165.

# Chapter 3: Characterization of material microstructure and shot peening effects

## 3.1 Introduction

Microstructure characterization is essential to the further understanding of material mechanical properties, for example, fatigue crack initiation and propagation behaviour which is the major concern in the present study. As stated in Section 1.4, the current study is part of a larger project on developing a shot peened low pressure steam turbine blade lifing methodology in order to take into account the influence of shot peening. Therefore, some of the fundamental material characterization has been conducted in previous research [1]. e.g. the material composition analysis as well as monotonic material properties in 9-12 Cr steels. In this chapter, the material microstructure is further investigated following on from previous research.

Two different shot peening processes are of interest in the present study: the T0 and T1 shot peened cases, T0 is designated as MI230R 13A 200 %, where 230R refers to the shot size and hardness, 13A is the intensity and 200 % represents the coverage (this is applied industrially to steam turbine blades) and T1 (MI110R 4A 200 %) is a lighter shot peening process. For comparison, the polished surface condition and the ground surface condition are also investigated. Evaluating and characterising the effect of the shot peening process on: surface roughness, together with the near surface residual stress present and plastic strain distribution is the first step in understanding the effect of shot peening on fatigue properties. Early fatigue crack morphology and fatigue crack aspect ratio evolution will be discussed in Chapter 4 followed by short fatigue crack behaviour in Chapter 5. Then a repair approach, namely, a blend-polish-peen repair process which was applied only to T0 shot peened U-notch samples will be presented in Chapter 6.

## 3.2 Experimental methods

### 3.2.1 Material microstructure characterization

The material used in the present study is FV448, a ferritic heat resistant steel, which is a representative 9-12 % Cr steel used in low pressure steam turbine blades. The composition of FV448 is given in Table 3- 1 [2]. The barstock material has been austenitised at 1150 °C, oil quenched, and then tempered at 650 °C [3]. The mechanical properties have been studied by Soady and the 0.2 % proof stress of FV448 was found to be 806±6 MPa [1].

In order to reveal the material microstructure, metallography was conducted. Firstly, specimens were mounted in a conducting phenolic resin (bakelite) at 150 ℃ and held for 15 mins in a Prontopress-2 hot mount machine (Struers). Then they were ground using 120, 800 and 1400 grit SiC papers successively. The specimens were then polished to a 1 μm diamond finish on an automatic polisher. Between each grinding and polishing step, specimens were washed thoroughly in order to remove any grit/diamond particles or contamination from the previous grinding/polishing processes. Vilella's Reagent (Picric Acid 1 g, Hydrochloric acid 5 ml, Ethanol 100 ml) was employed as an etching reagent to highlight features of the tempered martensitic microstructure of the ferritic heat resistant steel on these polished metallographic sections. Images of the tempered martensitic microstructure were subsequently captured on both an Olympus BH2 Optical Microscope and a JSM 6500F field emission gun scanning electron microscope (FEG-SEM). On some areas of particular interest, secondary electron imaging (SEI), backscattered electron imaging, and energy dispersive X-ray spectroscopy (EDS) were used.

### 3.2.2 Shot peening effect on FV448

In the present research, two different shot peening conditions have been studied in particular to explore the influences of the shot peening process on fatigue crack initiation and propagation behaviour; these were designated T0 and T1, respectively. Detailed parameters applied in the T0 and T1 shot peening processes are illustrated in Table 3- 2. T0 is applied industrially to steam turbine blades, while T1 (MI110R 4A 200 %) is a lighter process. In order to eliminate the effect of previous processes (such as electrical discharge

machining) on the shot peening process, samples to be shot peened were all ground to an initial surface roughness Ra of < 0.8 μm before shot peening. Therefore, for comparison, the properties of the ground surface condition, with grinding marks present, as well as the polished surface condition, where the grinding marks had been removed by polishing to a 1 μm finish, were also studied. The characterization of the shot peening effect will focus on the surface roughness, residual stress and plastic strain hardening produced.

#### 3.2.2.1 Surface topographical characterization

Optical microscopy is a convenient and direct way to study surface topography. However, it is not easy for a conventional microscope to have the entire rough surface (such as the shot peened surface as well as the ground surface) in focus simultaneously, due to the limited depth of focus of light microscopy. This problem can be solved effectively by an Olympus BX5 Optical Microscope combined with OLYMPUS Stream software. This software provides an extended focus image function and uses the fine focus adjustment to combine many images at different depth levels, thus producing a single combined image where the whole area is in focus. This function has also been extensively used in replica image analysis.

Both an Alicona Infinite Focus 3D optical microscope and a Taylor Hobson Form Talysurf 120L stylus profilometer were used to characterize surface finish. To make the results obtained in these two different approaches comparable, both the correct profile filter value, *Lc* (which filters out wavelengths shorter than roughness components), as well as the required evaluation length, *Lr* were selected according to BS ISO 4288:1996 [4]. The Alicona Infinite Focus optical profilometer is an optical noncontact method which uses a technology of focus-variation for areal based 3D measurement. Therefore, compared with conventional optical micrographs, the image obtained by an Alicona Infinite Focus optical profilometer can provide the detailed 3D morphology of the specimen surface. The dimples induced by the shot peening process are probably of the order of tens of micrometres (the shot diameter is 0.28-0.56 mm). Therefore a horizontal resolution of 2 μm and vertical resolution of 300 nm is sufficient for surface roughness analysis. On the coarse shot peened surface, regions with very high angles (close to 90 degrees), or deep dimples will cause noise in the form of spikes in the images due to no (or very limited)

reflected light being received, resulting in inaccurate analysis. Thereafter, all raw optical images were processed to remove spikes/noise or fill holes with values interpolated from nearby data points before any further analysis was carried out. An objective magnification of 10x was selected and the total scanned area was 714 μmx541 μm. Five different scanned areas were chosen randomly and analysed for each condition, and an average value of $R_a$, $R_z$, as well as $S_a$ and $S_z$ calculated. While $R_a$ and $R_z$ only measure one particular linear profile in a single direction on the surface, $S_a$ and $S_z$ represent an overall measure of the texture comprising the entire surface.

A 3D map of the shot peened surface can also be generated by Alicona Mex software from three images taken in an SEM at -5°, 0°, 5° angles. Compared to the 3D morphologies observed under the optical microscope, Alicona Mex can provide a higher resolution, thus shot peened lips as well as shot peened dimples can be clearly identified.

However, the Talysurf profilometer is a contact method and no artificial spikes are introduced in the scanned profile. Tactile horizontal resolution is dependent on the stylus tip radius and the one used in the present study was 3 μm; vertical resolution was 12.8 nm. At least 6 measurements were conducted on each sample along both the longitudinal and transverse directions (for the ground surface condition only) and the averaged values calculated.

#### 3.2.2.2 XRD for measuring residual macro stresses

The internal residual stress was determined by the $\sin^2\psi$ method using laboratory X-ray equipment available in the University of Manchester. There have been numerous papers on how this $\sin^2\psi$ method can be used to calculate residual stress [5-8]. Here only a brief introduction is given.

Bragg's Law, Equation 3-1, is the fundamental basics of XRD diffraction theory:

$$n\lambda = 2\,d_n \sin\theta \qquad \text{Equation 3- 1}$$

where $n$ is an integer, $\lambda$ is the wavelength of the X-ray and, $d_n$ is the inter-planar spacing of planes normal to the surface, θ is the diffraction angle. Both elongation and contraction will occur in a crystalline if a material is strained, hence the inter-planar spacing $d$ changes, causing a shift in the diffraction pattern.

Assuming that the specimen to be measured is in a plane stress condition, that is, the stress normal to the measured surface is zero (but the strain $\varepsilon_{11}$ is not equal to zero), $\sigma_{13} = \sigma_{23} = \sigma_{33}$. Figure 3- 1 is a schematic showing the diffraction planes parallel to the surface and at an angle ψ, where φ is the angle between a fixed direction in the plane of the sample and the projection in that plane of the normal to the diffracting plane and ϕ is the angle between the sample normal and the diffracting plane normal. The strain $\varepsilon_{\phi\psi}$ can be expressed as Equation 3-2:

$$\varepsilon_{\phi\psi} = S_1[\sigma_{11} + \sigma_{22}] + \frac{1}{2}S_2[\sigma_{11}cos^2\phi + \sigma_{22}sin^2\phi + \sigma_{12}\, sin\, 2\phi]sin^2\psi + \frac{1}{2}S_2[\sigma_{13}\cos\phi + \sigma_{23}\sin\phi]\sin 2\psi \qquad \text{Equation 3- 2}$$

$\varepsilon_{\phi_\psi}$ can be obtained by measuring the peak position 2θ and calculating the interplanar spacing $d_{\psi\phi}$ in the direction defined by ϕ and ψ by Equation 3-2 if the unstressed lattice inter-planar spacing $d_0$ is known:

$$\varepsilon_{\phi\psi} = \frac{d_{\phi\psi} - d_0}{d_0} \qquad \text{Equation 3- 3}$$

Therefore, Equation 3-2can also be expressed as following:

$$\frac{d_{\phi\psi} - d_0}{d_0} = S_1[\sigma_{11} + \sigma_{22}] + \frac{1}{2}S_2[\sigma_{11}cos^2\phi + \sigma_{22}sin^2\phi]sin^2\psi \qquad \text{Equation 3- 4}$$

Where $S_1$ and $\frac{1}{2}S_2$ can be expressed as the elastic constants $\left(-\frac{v}{E}\right)$ and $\left(\frac{1+v}{E}\right)$, respectively. They are the values for the crystallographic direction normal to the lattice planes in which the strain is measured as specified by the Miller indices (*hkl*). Hence Equation 3-4 can also be written as Equation 3-5:

$$d_{\phi\psi} = \left[\frac{1+v}{E}\sigma_\phi\, d_0 sin^2\psi\right] - \left[\frac{v}{E}d_0(\sigma_{11} + \sigma_{22})\right] + d_0 \qquad \text{Equation 3- 5}$$

Equation 3-5 describes the fundamental relationship between lattice spacing and the biaxial stresses in the surface of the sample, where the lattice spacing $d_{\phi\psi}$ can be obtained by experimental data at varying ψ. It is a linear function of $\sin^2\psi$. The intercept of the slope is $sin^2\psi = 0$,

$$d_{\phi 0} = d_0 - \frac{v}{E}d_0(\sigma_{11} + \sigma_{22}) \qquad \text{Equation 3- 6}$$

And the slope of the plot is found as follows:

$$\frac{\partial d_{\phi\psi}}{\partial sin^2\psi} = \left(\frac{1+v}{E}\right)\sigma_\phi d_0 \qquad \text{Equation 3- 7}$$

Since $d_0$ is typically unknown, but since $E \gg (\sigma_1+\sigma_2)$, so the value of $d_{\phi 0}$ differs from the $d_0$ but no more than ∓1%, so the stress $\sigma_\phi$ can be approximated by not using the stress free reference in Equation 3-8:

$$\sigma_\phi = \left(\frac{E}{1+\nu}\right)\left(\frac{1}{d_{\phi 0}}\right)\left(\frac{\partial d_{\phi\psi}}{\partial sin^2\psi}\right) \qquad \text{Equation 3- 8}$$

By measuring the change of 2θ at different tilted angles (at least two), the stress in any chosen direction can be measured.

In this study, the residual stress was measured perpendicular to the shot peened (or ground or polished) surface on samples with dimension of 7.75 x 8 x 12 mm (with an exposed area of 8x12 mm). The profile of the residual stress as a function of depth perpendicular to the shot peened or ground/polished surface is obtained by serial electro-polishing in an electrolyte consisting of 8 % (by volume) of 60 % perchloric acid and 92 % (by volume) of glacial acetic acid. A stainless steel cathode was used with a starting solution temperature of approximately 15 ℃, and 60 V, which is a similar to an electro polishing process (15 ℃, 50 V) reported for tempered martensite ferritic steels [9]. The sample was maintained constantly at about 10 mm from the cathode. Lacomit was applied to mask and thus prevent the areas not of interest from being polished. The electrolyte solution was kept in an ice bath and the polishing was carried out in 1 minute increments, in order to ensure no substantial heating took place. A micrometre with a resolution of 0.001 mm was used to determine the depth of the layer removed. Initially, in the near surface layers, the layers removed had depth increments of 10 ~ 20 μm, but this value was increased to approximately 50 ~ 80 μm after the maximum residual stress had been reached.

Cr-Kα X-rays with a wavelength of 2.291Å were obtained with a tube voltage of 20 KV and 4 mA current. Diffraction on the (211) plane was measured and the peak angle 2θ was approximately 156° (determined by half-width techniques); the diffraction elastic constant $1/2S_2\left(\frac{1+\nu}{E}\right)$ was 5.92 x $10^{-6}$ $MPa^{-1}$. A collimator with a diameter of 0.5 mm to filter the X-ray beams and only allow those parallel to a selected direction to pass was selected. This was the most appropriate size to avoid X-ray beam focus problems caused by the relatively rough shot peened surface.

The machine was warmed up for 20 minutes at the beginning of every working day. A standard ferritic steel plate with a well-characterised stress field was used to verify the alignment of the diffractometer. After each material removal step, the residual stresses on or near the specimen surface redistribute. The relaxation stress has a linear distribution over the cross section of the remaining material and had the same integrated force and moment as the stress in the removed layer but of opposite sign. Therefore, it was necessary to correct the measured residual stress values by the Moore and Evan's function [10], which is embedded in the iXRD software; this function is given by:

$$\sigma(z_1) = \sigma_m(z_1) + 2\int_{z_1}^{H}\frac{\sigma_m(z)}{z}dz - 6z_1\int_{z_1}^{H}\frac{\sigma_m(z)}{z^2}dz \qquad \text{Equation 3- 9}$$

A multiple exposure technique was applied and the peak positions for 11 values of ψ (from -27° to 27°) were recorded by 2 detectors and the inter planar distance *d* was plotted as a function of $\sin^2\psi$.

### 3.2.2.3 Plastic strain measurement technique

(a) Microhardness

Microhardness tests were conducted on polished, T0 and T1 samples to characterize their microhardness distribution. The microhardness test was in accordance with BS EN ISO 6507-1:2005 with a load of 200 g and dwell time of 15 s. As illustrated in Figure 3- 2, the distance between the sample edge and the centre of the first indentation is ~ 100 μm; it is a requirement of this standard that the distance between the centre of any indentation and the edge of the test piece shall be at least 2.5 times the mean diagonal length of the indentation. The distance of the centres between two indentations along the depth direction is 10 μm as indicated. In previous research, samples which had been subjected to uniaxial compression and tension to a given value of strain were also microhardness tested and the relationship between microhardness and strain established. Therefore, from this the strain level along the depth direction based on the microhardness can be evaluated.

(b) XRD

As stated in Section 3.2.2.2, the residual stress profile variation into the sample can be captured by the laboratory based XRD $\sin^2\psi$ approach by successive electro-polishing. For homogeneous strain, the Bragg diffraction peaks may shift when compared with the strain-free positions, but the shapes

will remain unchanged. However, the position as well as the shape of the diffraction peaks will change due to inhomogeneous strain or deformation. In the present work, the line broadening depth profiles resulting from mechanical process (machining or shot peening) can be determined by measuring the Full Width Half Maximum, FWHM, of a Gaussian profile fit when $\psi = 0$.

(c) Electron backscattered diffraction (EBSD) [1, 11]

An EBSD (local misorientation technique) was applied to characterize the plastic strain layer in T0 and T1 shot peened conditions. The sample preparation, parameter settings, as well as the data analysis optimization approaches were detailed in [11]. Here only a brief introduction will be presented.

Data were collected from both shot peened samples as well as calibration samples by an EDAX Hikari EBSD camera operating at 300 fps used with a FEI Nova 600 Nanolab field emission gun scanning electron microscope with an accelerating voltage of 20 KV and a nominal current of 24 nA. An area at least 200 x 200 μm in the region near the shot peened layers was measured using a step size of 0.2 μm (for the calibration samples) and 0.4 μm (for the T0 and T1 shot peened samples). Due to the high degree of intrinsic misorientation present in this tempered martensitic steel, the change of the misorientation data measured by grain orientation spread (GOS) near the shot peened surface is too small to indicate the strain hardened region accurately, thus another local misorientation method namely kernel average misorientation (KAM) was used. The calculation process is described in Figure 3- 3(a) (after [1, 12]): the misorientation between a point at the centre of the kernel and all points at the perimeter of the kernel (based on first nearest neighbour, second nearest neighbour etc.) are measured, excluding any points where KAM ≥ 5°(which was considered to indicate grain boundaries [13]). The average of the misorientations of the surrounding points is the KAM of the centre point. Hence a smoothed line of the mean KAM at the same depth was obtained and allowed the extent of the strain hardened region to be clearly identified as shown in Figure 3- 3(b).

## 3.3 Experimental results

### 3.3.1 Material microstructure

Optical and SEM micrographs of FV448 after etching with Vilella's Reagent are shown in Figure 3- 4(a), a tempered martensite microstructure, in which the prior austenite grain boundaries are clearly visible. The corresponding SEM image is given in Figure 3- 4(b). Both the prior austenite grain boundaries and carbides on grain boundaries or in the interior of the grains can be clearly identified. The likely precipitates present here are primary $Cr_{23}C_6$, and secondary NbN and a combination of secondary $Mo_2C$, $Mo_2N$, $Cr_2C$, CrN, NbC, VC and VN, deduced from theoretical contrast based techniques based on Soady's study in FV448 [1]. To explore whether there is any directionality in grains or aluminium oxide stringers in the longitudinal, transverse and short transverse directions in the barstock after the rolling process carried out during manufacturing, the microstructures on these three orientations are presented in Figure 3- 5. Figure 3- 6 illustrates the prior austenite grain boundaries processed by Photoshop in these three different orientations; the grain size distributions are presented in Figure 3- 7. From this microstructural point of view, there are no obvious differences in these orientations in the barstock. However, stringers (alumina and MnS) running along the longitudinal direction parallel to the longitudinal axis of the original extruded bar stock were visible in the L-T and L-S faces, as clearly illustrated in Figure 3- 8.

### 3.3.2 Shot peening effect on FV448

As stated in Section 3.2.2, four surface conditions are of interest in the present study, namely the polished surface condition, ground surface condition, T0 shot peened condition (the industry applied process) and a lighter shot peened process T1 condition. The surface morphologies of these four conditions viewed by optical microscopy under the same magnifications are shown in Figure 3- 9. These images are taken from replicas of each surface condition, so the actual surface is inverted with respect to these images, e.g. bumps on the replicas are actually dimples on the shot peened surface. Compared to the ground condition, as shown in Figure 3- 10(a), the top surface developed a significant lip after both T0 and T1 shot peening (as illustrated in Figure 3- 10(b) and (c)) due to the significant plastic deformation of the top surface

resulting from the shot peening process. The more intense the shot peening process, the more severe the plastic deformation seen. The microstructure in the near surface layers resulting from these three conditions are compared in Figure 3- 11. The microstructure in the near surface layers of the ground condition is uniform; the surface edge line is also smooth, hence it is reasonable to infer that the effect of the grinding process on the microstructure is insignificant [1]. Compared with the ground condition, some grain refinement is evident in the near surface region of the shot peened samples. For the T1 shot peening process, peening with small shot at low velocity, small dimples on the surface can be discerned clearly, but the microstructure appears unchanged. However, the surface microstructure over a region as far as 70 μm beneath the surface was refined by the T0 process [1].

#### 3.3.2.1 Surface topography

The 3D surface morphologies for the ground, T0 and T1 surface conditions are described in Figure 3- 12(a)-(e). For the ground case, the grinding marks are apparent and parallel to each other; there is a clear directionality on the ground surface seen in the Figure 3- 12(a). Profile lines were drawn along and across the grinding marks, defined as the longitudinal and transverse directions, are shown in Figure 3- 12(b) and (c), respectively. In the transverse direction, each peak on the profile represents a grinding mark, and the distance between adjacent peaks is similar, roughly between 50 ~ 80 μm; however, in the longitudinal direction, the profile in the grinding direction is relatively smooth. Shot peened dimples as well as the edges between adjacent dimples in the T0 and T1 conditions can be clearly identified, as indicated in Figure 3- 12(d) and (e), respectively. Based on the colour scale bars, the depth of the dimples in the intense shot peened condition is much larger than that in the light shot peened case, where the shot peened dimples are shallow. The diameters of the shot peened dimples in T0 and T1 condition calculated from Figure 3- 12 (d) and (e) are ~ 220 μm and ~ 80 μm, respectively. The diameters of the shot peened dimples have been quantified by both an Olympus optical microscope and Alicona Profilometer in Soady's research and the results for these two different approaches were found to be consistent [1]. 3D surface reconstruction of shot peened surfaces under higher magnifications were obtained by Alicona Mex based on SEM images tilted at -5°, 0°,5°, as shown in Figure 3- 13. In both the T1 and T0 cases, shot peened lips at the bottom or

edges of shot peened dimples and some crack-like regions are clearly revealed. However, these defects induced by the severe plastic deformation in the T0 condition appeared more frequently. The effect of these defects on fatigue crack initiation and propagation behaviour will be discussed in detail in Chapter 5.

The surface roughness measured by the Alicona 3D optical microscope and the Talysulf line profilometer is compared in Figure 3- 14. As has already been seen in Figure 3- 12, there is directionality in the ground case. To check whether this directionality still exists after the shot peening process, the surface roughness $R_a$ and $R_z$ in both the longitudinal direction (parallel to the grinding marks) and the transverse direction (perpendicular to the grinding marks) was measured by the Talysurf line profilometer, as shown in Figure 3- 14. $R_a$ and $R_z$ in the longitudinal and transverse direction in both the T1 and T0 shot peened case are the same from which it can be concluded that the shot peening across the processed surface is uniform. In the ground condition, $R_a$ in the direction normal to the grinding marks (transverse direction) is $0.3111(\pm 0.0121)\ \mu m$ while $R_a$ is $0.0397(\pm 0.0057)\ \mu m$ in the longitudinal direction. In all these three cases, there is no significant difference in the line profile roughness parameters $R_a$ and $R_z$ measured by these two different approaches. However, for $S_a$ and $S_z$, the areal measurement of maximum peak to valley height, the height difference in the area studied is much greater than in the line profile measurement, which may indicate that there is a greater chance of identifying a significant surface feature by areal scanning rather than by line scanning; this implies there is a greater possibility that the most severe surface features may be missed or undetected by line scanning.

#### 3.3.2.2 Residual stresses

Quite a thin near surface compressive residual stress layer (~ 20 μm) can be observed in the polished condition, as can be seen in Figure 3- 15. The residual stress obtained in the ground condition was based on measurements on the plain bend bar samples, which were detailed in [14]. Tensile stress was found on the ground surface in the longitudinal direction while a compressive stress (restricted to a very thin layer, ~ 5 μm) was observed in the transverse direction. In both directions, tensile residual stress increased gradually up to a maximum (~ 400 MPa in the longitudinal direction and ~ 250 MPa in the

transverse direction) at ~ 20 μm beneath the surface. After that, the value of tensile residual stress decayed to a balancing compressive stress as the depth increased. The total depth of the affected layer in the ground condition is around 100 ~ 150 μm. For T1, the stress distributions in the longitudinal and transverse direction showed no significant difference: the maximum compressive stress was -620 MPa at 50 μm depth and the total residual stress affected layer extended to about 200 μm beneath the surface. For T0, the residual stress is also similar in the two directions: the maximum compressive residual stress in both the longitudinal direction and the transverse direction is ~ 600 MPa. The depths where the compressive stress reached its maximum value in both directions were around ~ 100 μm, after which the compressive stress decreased gradually to become tensile at ~ 340 μm depth.

#### 3.3.2.3 Plastic strain

In previous research [1, 4], samples subjected to known strain conditions under monotonic uniaxial tension and compression were prepared for calibration purposes. Microhardness, XRD and EBSD measurements were carried out on shot peened samples. By using the calibration samples, the plastic strain profile in the near surface shot peened layer was calculated.

(a) Microhardness

The microhardness depth profile can be used as an indicator of plastic strain, as shown in Figure 3- 16. The hardness change resulting from the T1 process is not obvious even at a depth of ~ 70 μm, and almost all of the measurements are still within the 95 % confidence range of the ground condition (which is considered to be the baseline case as the effect of the machining process is quite shallow, only ~ 25 μm, according to the XRD result in Figure 3- 15). Increasing the shot peening intensity can result in an increase in microhardness in the near surface region. The maximum hardness increase in the T0 case is ~ 15 %, compared to the average hardness of the ground sample. Judged from the microhardness traverse profile, the shot peening process still has a significant effect even at a depth of 350 μm beneath the peened surface. A power law regression equation derived from the % change of microhardness in the calibrated tension and compression samples is illustrated in Figure 3- 17(a) [11]. Figure 3- 17(b) presents the strain profiles for T1 and T0 derived from the measured microhardness data using the regression equation. Only a

few points where the strain is ~ 0.02 at a depth of 70 μm can be captured for the T1 case. This is also in line with the results of XRD. When the depth is shallower than 200 μm, the strain level in the T0 condition is ~ 0.2 in the near surface layer; after this the strain level decreases with depth up to 400 μm beneath the surface. However, due to the low $R^2$ values in the hardness results of the calibrated samples, the uncertainty and reliability of the strain levels assessed by hardness needs to be considered thereafter.

(b) XRD

The XRD FWHM data can be used for strain profile analysis. Figure 3- 18(a) shows the correlation between FWHM and plastic strain derived from the calibration samples [11]. As can be seen, both a power law and an exponential law can be made to fit the XRD FWHM data with high $R^2$ values. To simplify the calculation, and make it comparable to the strain profile derived from the microhardness results, the power law was applied in this study [11]. The strain distribution derived from the XRD FWHM data for the ground, T1 and T0 cases are presented in Figure 3- 18(b). In the ground condition, similar to residual stress, the strain hardened layer is quite thin (only ~ 25 μm) and the maximum calculated strain value is ~ 0.02. In the T1 shot peened case, the strain on the shot peened surface reaches 0.25, and the true plastic strain layer detected is ~ 80 μm deep. Compared to the light shot peened process, the surface strain in the T0 condition is much greater (~ 0.4). The strain level achieves its maximum on the surface and it decays with distance beneath the shot peened surface; no apparent variation can be recognized confidently at a depth of greater than 150 μm.

(c) EBSD [1, 11]

The plastic strain resulting from using the EBSD technique for the T1 and T0 shot peening process is shown in Figure 3- 19. In the near surface layer, the T0 process produces a higher plastic strain than the T1 case, which is consistent with the strain profile obtained by the XRD FWHM approach. The depth of the plastic strained layer in the T0 and T1 conditions is 150 and 40 μm, respectively.

## 3.4 Discussion

### 3.4.1 Material microstructure

The microstructure (Figure 3- 4, Figure 3- 5 and Figure 3- 8) revealed in the present study exhibits similarities to other 9-12 Cr steels reported in the literature, as shown in Figure 3- 20. No obvious differences exist in the microstructure or grain size or grain size distribution in the three orientations of the barstock, as shown in Figure 3- 5, Figure 3-6 and Figure 3-7. However, a slight difference in the mechanical properties in the transverse and longitudinal directions was captured in a previous study, which is considered to be related to the stringers that are formed during the manufacturing process. The yield strength $\sigma_{0.2}$ in the transverse direction is 806 MPa, while in the longitudinal direction, it increases to 858 MPa. This indicates that the alignment of the stringers along the longitudinal axis may be contributing a slight anisotropic strengthening effect, akin to a unidirectional composite system. Perkin's research on the corrosion fatigue of a 12 % Cr low pressure turbine blade steel demonstrated that crack initiation was associated with aluminium oxide inclusions in chloride free environments, where de-bonding at the inclusion/matrix interface resulted in crack initiation at passive film free material [15, 16]. Alumina and MnS are two of the most common non-metallic inclusions present in steel, and these stringers can be clearly identified in the present study. Further discussion on the significance of the stringer orientation, as well as the effect of the stringers on fatigue crack initiation and propagation will be presented in Chapter 4, and Chapter 5, respectively.

### 3.4.2 The shot peening effect

Shot peening is a cold work process and this dynamic process can be controlled by many process parameters. Among these, the type of shot, as well as shot size, intensity and coverage, are the important parameters [17]. As described in Section 3.2.2, the shot peening intensity is assessed by means of the Almen strip. They are standardized thin strips that are placed parallel to the specimens being shot peened and therefore receive the same treatment intensity. The deflected shape gives the Almen intensity which is an indication of the residual stresses present. An intense shot peened process leads to a

severe deformed surface, deeper (or wider) compressive residual stress layer as well as a plastic deformation layer [18, 19].

In the present study, T0 with an intensity of 13A (shot diameter 0.56 mm, shot velocity 57 $ms^{-1}$,200 % coverage) results in a more severe surface plastic deformation (as evidenced by the shot peening lips illustrated in Figure 3- 10) as well as a much larger dimple size, as shown in Figure 3- 12), compared to the T1 process with an intensity of 4A (shot diameter 0.28 mm, shot velocity 26 $ms^{-1}$, 200 % coverage). Both tactile and optical approaches were used to measure the surface roughness for both T0 and T1. While these two approaches give similar results for $R_a$ and $R_z$ from line measurement for T0 and T1 conditions; the areal roughness $S_a$ and $S_z$ measured by the optical approach is significantly larger than $R_a$ and $R_z$ for both shot peened conditions. This would indicate that $R_a$ and $R_z$ by line measurement is not sufficient to capture all the features of specimen geometry. The shot peened surface features are more clearly revealed by 3D surface reconstruction by tilting at ±5° in SEM. The lips formed at the bottom of the dimples resulting from shot peening, as well as the crack-like defects on the dimple ridges may play an important role in crack initiation and propagation during the fatigue process. These shallow dimples tend to act as notches where the stress concentrates and consequently fatigue cracks are apt to initiate within these regions. In addition, the lips or the crack-like folds are likely to make the initiation or propagation process easier to occur. In De los Rios's research [20], shot peened specimens polished to a 1 μm finish were tested for comparison with unpolished ones to explore how the shot peening surface conditions affected fatigue behaviour; they found that shot peened specimens which had been polished after shot peening didn't have better fatigue properties. This indicates that the immediate surface layer is just as important as the subsurface compressive stress; in peened unpolished specimens, very small cracks initiated quickly and were orientated along the edges of surface dimples. Since not only surface roughness (or the surface defects), but also the compressive residual stress as well as the strain deformation layer are being introduced during the shot peening process, the effect of shot peening on fatigue crack initiation and propagation results from the interaction of these three factors.

From the residual stress (Figure 3- 15) in both the longitudinal and the transverse directions obtained by X-ray diffraction using the $\sin^2\psi$ technique

for the polished, ground, T0 and T1 shot peened conditions, it is obvious that the residual stress on the surface or in the near surface layer is significantly affected by mechanical processes, such as grinding, polishing or shot peening.

In the ground condition, a thin layer compressive residual stress was found in the near surface layer (~ 5 – 10 μm), then the residual stress turns tensile and achieves a maximum at a depth of ~50 – 60 μm. Residual stresses induced by a grinding process can be attributed to thermo-mechanical effects such as mechanical deformation [21], thermally-induced plastic deformation [22] or phase transformations on grinding hardenable steels [23]. It is mechanical deformation and thermally-induced plastic deformation arising from restrained thermal expansion and contraction that causes tensile residual stresses when grinding tempered steels [24, 25]. Greater tensile residual stress is found in the longitudinal direction in the present study, although more tensile residual stress would be expected in the grinding direction (the transverse direction) according to previous work [26, 27]. A possible explanation is that, the state and the amount of residual stress are affected by many grinding process parameters as well as intrinsic material properties. The compressive residual stress along the longitudinal direction is greater than that in the transverse; therefore, to balance, the corresponding tensile residual stress will be greater.

From Figure 3- 15, it seems that the polishing process can eliminate the residual stress effect of grinding. A thin compressive residual stress layer (~ 10 – 15 μm) is formed in the polished surface after polishing with 1 μm Alumina, and no obvious tensile residual stress is present beneath the polished surface. According to Poggie and Wert's work [28], surface grinding or polishing has a significant effect on surface residual stress; almost all the surface grinding conditions used in their study induced surface compressive residual stresses. Abrasion using 240 grade silicon carbide paper induced higher compressive residual stresses which were independent of grinding history. However, they found further polishing with 0.05 μm alumina slurry reduced the level of residual compressive stress, and in some cases a residual surface tensile stress resulted [28].

The shot peening process (both T0 and T1) is also able to overwhelm the residual stress caused by grinding. The results indicated that the maximum compressive residual stress level in the T1 and T0 conditions is almost identical, but the depth of the compressive residual stress field in T0 is greater

(~ 300 – 350 μm) than in T1 (~ 180 – 200 μm). In addition, the compressive residual stress at the surface resulting from the intense shot peening case is slightly greater than in the less intense condition. In Gao's analysis of the residual stress fields caused by shot peening in 40Cr steel, he proposed that the compressive residual stress introduced by shot peening is dependent on both the mechanical properties of the target and the peening regime; the maximum of the compressive residual stress field for a given material is almost the same even under different shot peening conditions but the surface residual stress values are dependent on both the mechanical properties of the target materials and the peening parameters [29]. In addition, in his study, the relationship between the average diameters of the peening indents and the compressive residual stress field was described quantitatively. As the magnitude of the residual compressive stress at the surface and the depth to which the plastic deformation extends play a most significant role in the fatigue process [30], a lot of effort has been dedicated to link shot peening effects (e.g. the maximum compressive residual stress, or the depth of compressive residual stress field) to the peening process parameters such as shot sizes, or the shot dimple sizes measured on the surface [31, 32].

There are several different methods that can be applied to evaluate the plastic strain profile, such as microhardness, X-ray diffraction (XRD) line broadening and electron backscatter diffraction (EBSD) local misorientation techniques. As discussed extensively in [11], the results calculated from the microhardness technique indicated a greater plastic strain depth (resulting in a deeper variation in subsequent hardness/yield strength profile) than the other two methods. This might be a result of the influence of residual stresses on hardness measurements, as shown in Tosha's study on the effect of "on-load" and "off-load" on surface residual stress after shot peening [33]. This would lead to non-conservative estimates of component remnant life under this situation. The plastic strain profiles obtained by the XRD and EBSD approaches are quite similar; however, since there are more data points in the EBSD approach, the calculated results are more averaged, and thus there is increased confidence in the values obtained. Hereafter, further discussion regarding the residual plastic deformation in the present investigation is based on the results from the EBSD local misorientation technique. By comparison, the industry 13A process (T0) has a higher surface strain (0.2) as well as a deeper hardened layer profile (150 μm) than that of the less intense process (T1).

## 3.5 Conclusions

The microstructure and the effects of the shot peening process on the surface roughness, residual stress and plastic strain profile were discussed in this chapter. The conclusions can be summarized as follows:

(1) FV448 has a tempered martensite microstructure. The prior austenite grain boundaries were clearly identified in the longitudinal, transverse and short transverse directions of the barstock material. In addition, the grain size distributions of the prior austenite were not significantly different in these three directions. However, inclusions of aluminium oxide/silicate and manganese sulphide were identified in the longitudinal direction on both the Longitudinal-Transverse face and the Longitudinal-Short transverse face.

(2) Two different shot peening processes were studied. To gain a better understanding of the effect of shot peening, the polished surface condition, and the ground surface condition was also studied.

   1) Compared to the less intense shot peening case T1, the T0 industry standard shot peening process induced more severe surface plastic deformation (such as the shot peening lips at the edge of samples) and produced a larger shot peening dimple size on the surface. The surface roughness $R_a$ and $R_z$ obtained by both contact and optical approaches were much lower than the $S_a$ and $S_z$ captured by an optical approach, from which it can be concluded which can be considered that the most severe surface features would not necessarily be detected by linear contact measurements.

   2) Residual stress in both the longitudinal and the transverse directions was measured by X-ray diffraction using the $\sin^2\psi$ technique for the polished, ground, T0 and T1 shot peened conditions. The grinding or polishing process had a significant influence on the residual stresses present in the material. In the ground sample, there was a thin layer of compressive residual stress in both the longitudinal (perpendicular to grinding marks) and transverse (parallel to grinding marks) directions; these stresses then decreased and became tensile achieving a maximum value at ~50 μm beneath the surface after which they

decreased. Based on the present results the polishing process could eliminate the effects of grinding since the tensile residual stress observed in the grinding condition were not present after polishing. A shallow but slightly higher residual compressive stress, in both longitudinal and transverse directions, was seen in the polished case.

3) The depth at which the maximum compressive residual stress occurs in the T1 and T0 conditions is almost the same, but the depth of the compressive residual stress layer in T0 is greater (~ 300 – 350 μm) than in T1 (~180 – 200 μm). In addition, the compressive residual stress at the surface in the intense shot peening case is slightly greater than in the less intense condition.
4) The plastic strain profiles induced by shot peening in the near surface region can be described by microhardness, XRD FMHW measurement as well as EBSD local misorientation techniques. Increasing shot peening intensity seemed to increase the strain magnitude and depth of the plastic strain layer in the near surface layer.

## 3.6 Figures

Table 3- 1 The chemical composition of FV448 [1] .

| Material | C | Mn | Si | Ni | Cr | Mo | W | V | Nb | Fe | N |
|---|---|---|---|---|---|---|---|---|---|---|---|
| Barstock FV448 | 0.12 | 0.94 | 0.31 | 0.74 | 11.0 | 0.58 | <0.01 | 0.31 | 0.34 | Bal | - |

Table 3- 2 The control process parameters applied in the shot peening process after [2].

| Process | Label | Intensity | coverage | Shot diameter /mm | Shot hardness /HRC | Shot velocity /$ms^{-1}$ |
|---|---|---|---|---|---|---|
| MI110R 04A 200 % | T1 | 4A | 200 | 0.28 | 45-52 | 26 |
| MI230R 13A 200 % | T0 | 13A | 200 | 0.58 | 45-52 | 57 |

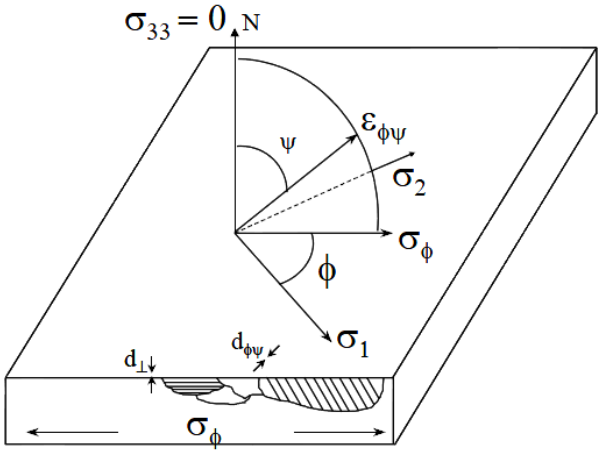


Figure 3- 1 Schematic showing diffraction planes parallel to the surface after [5].

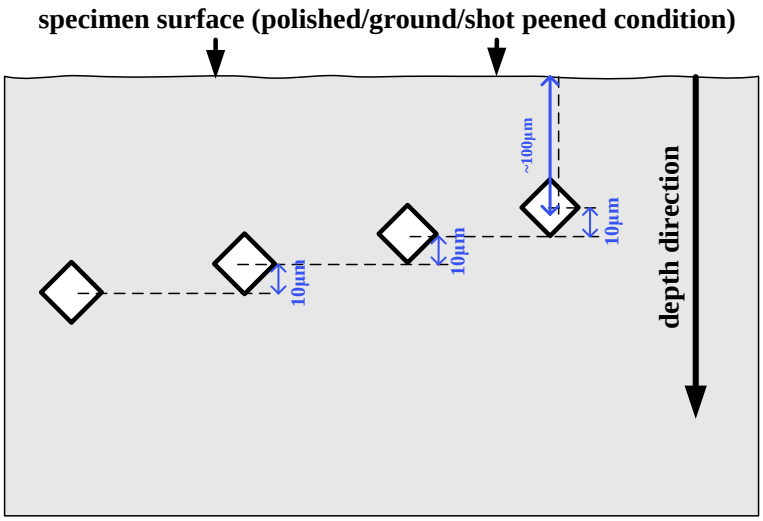


Figure 3- 2 Schematic illustrating the microhardness test in the near shot peened surface.

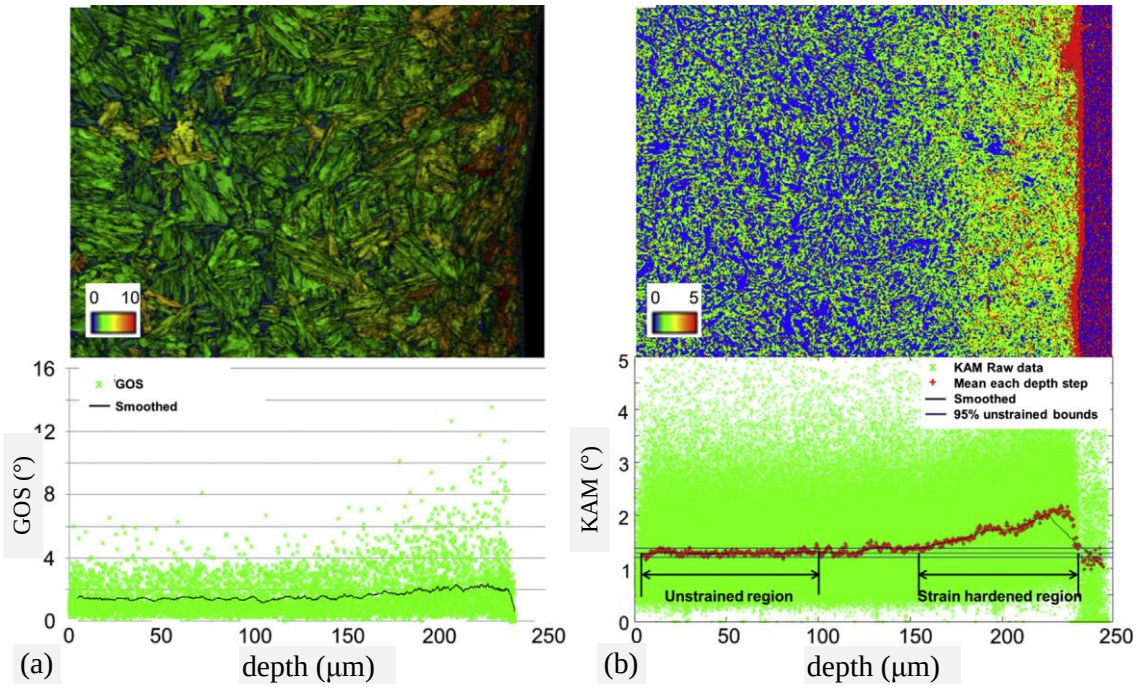


Figure 3- 3 (a) Colour coded map indicating grain orientation spread (with image quality in greyscale) and (b) kernel average misorientation for shot peening process T0 indicating the strain hardened region as identified by the local misorientation approach [11].

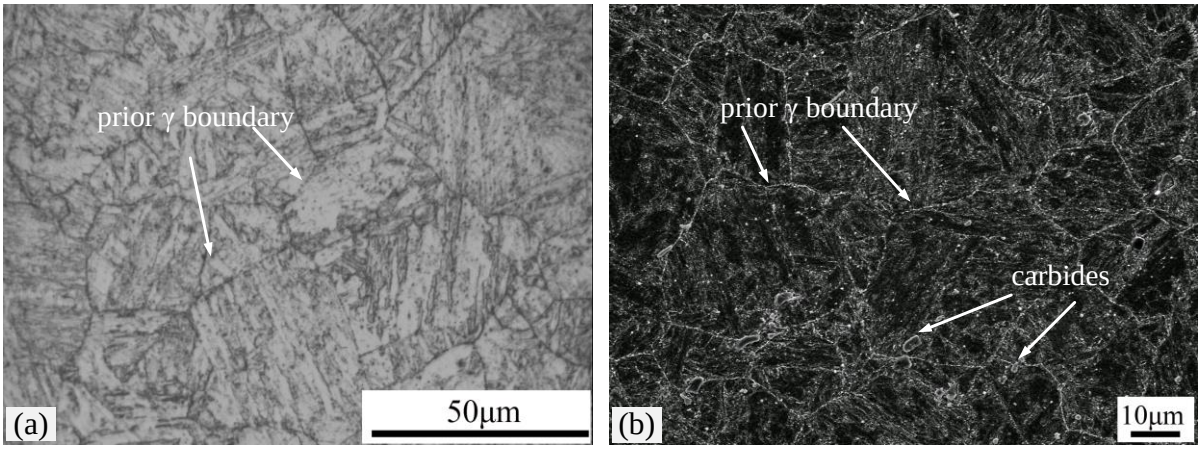


Figure 3- 4 Optical micrograph of polished and etched (by Vilella's Reagent) sample showing the microstructure of FV448; (b) FEGSEM (SEI mode) micrograph of polished and etched (by Vilella's Reagent) sample further revealing the microstructure of FV448.

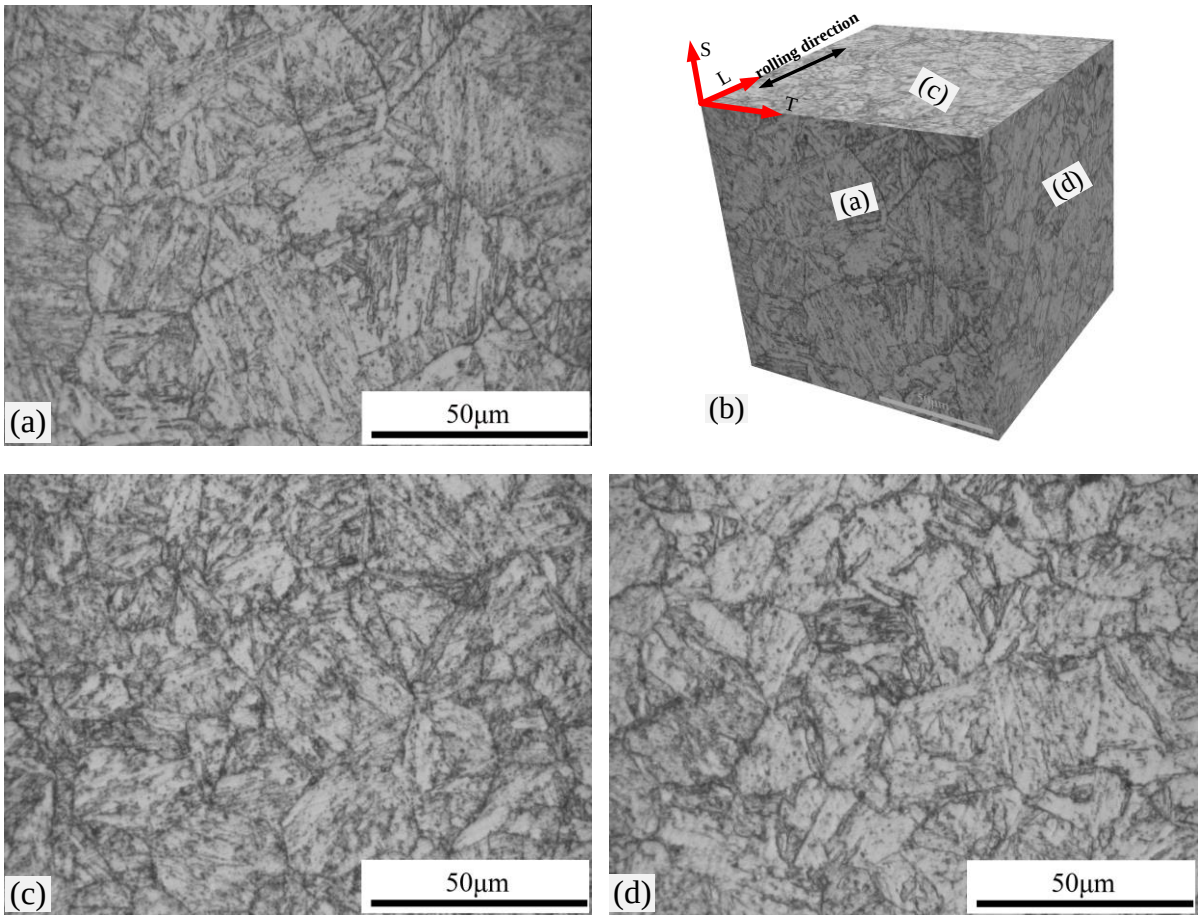


Figure 3- 5 Optical micrographs showing microstructure directionality of the bar stock.

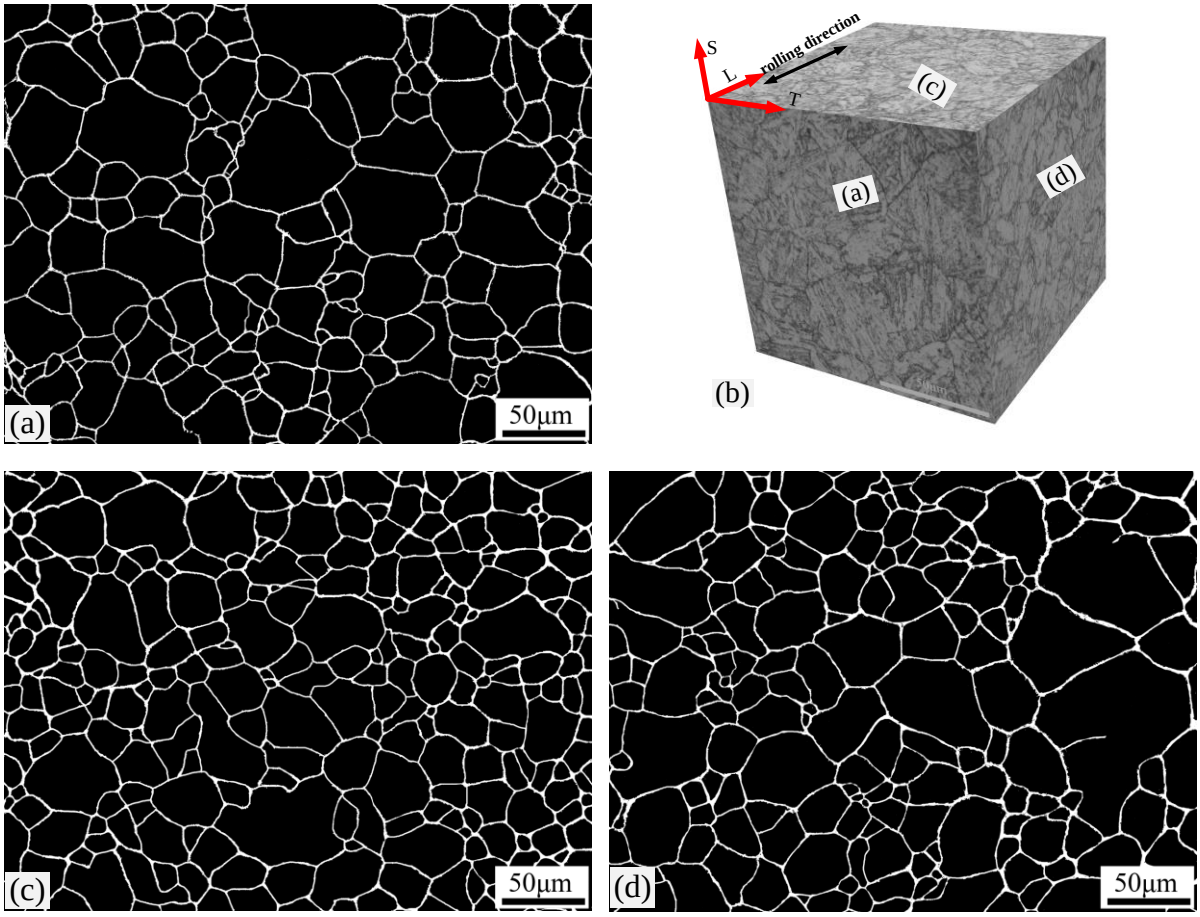


Figure 3- 6 Prior austenite grain size in the bar stock (N.B. sections have been slightly etched by Vilella's Reagent and then processed by Photoshop.

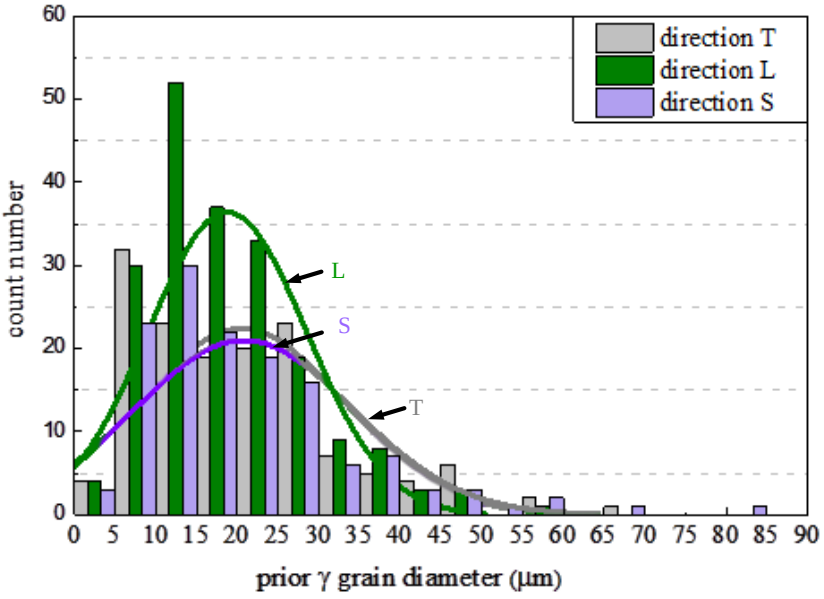


Figure 3- 7 Prior austenite grain size distribution in three different rolling directions.

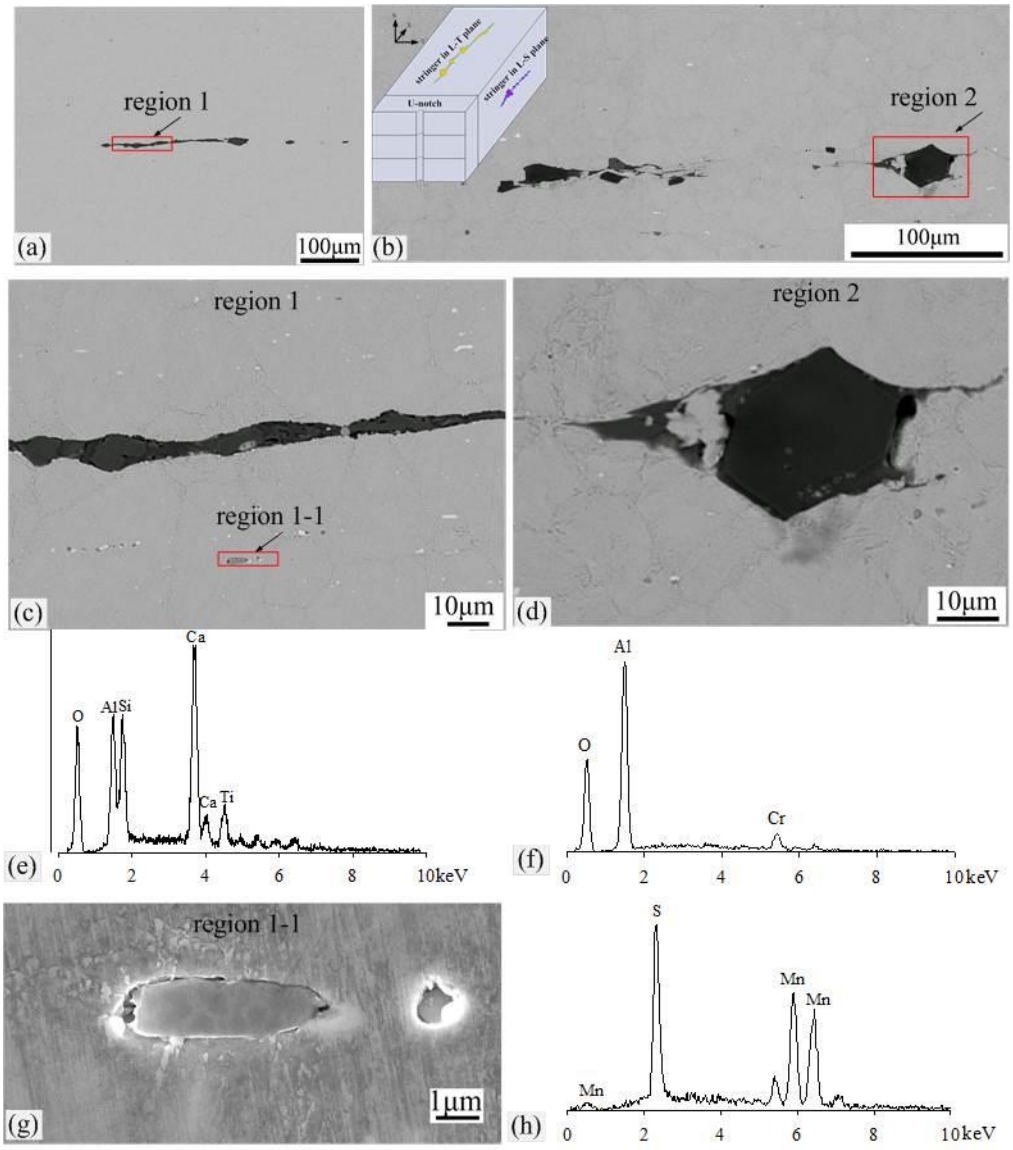


Figure 3- 8 The schematic illustration in (b) shows the positions of the stringers in the barstock; inclusions of aluminium oxide/silicate and manganese sulphide aligned in the longitudinal direction (a) on the L-T face; (b) on the L-S face within the FV448 matrix; (c) region 1 in (a); (d) region 2 in (b); (e) and (f) are the EDS results of region 1 and region 2 respectively; (g) is the inclusion in region 1-1 and (h) EDS indicates MnS.

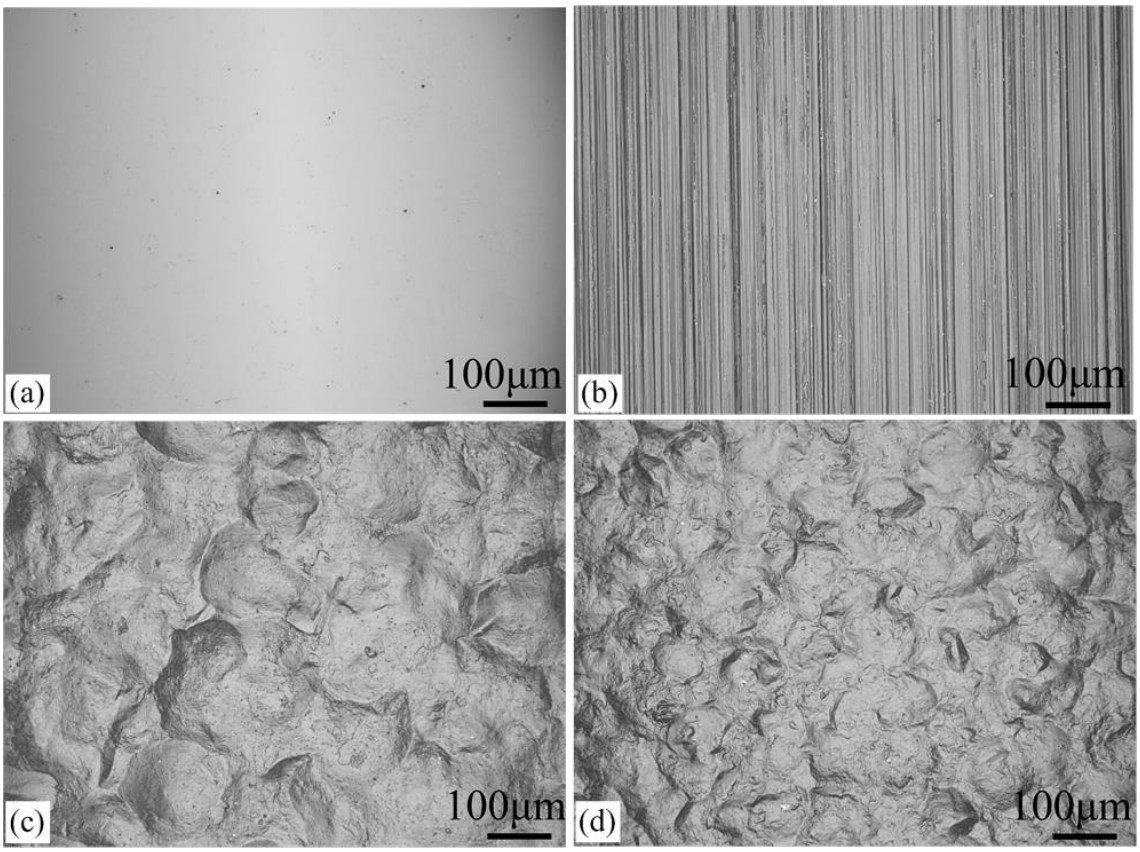


Figure 3- 9 Optical micrographs of the four different surface conditions: (a) polished, (b) ground, (c) T0 shot peened condition and (d) T1 shot peened condition.

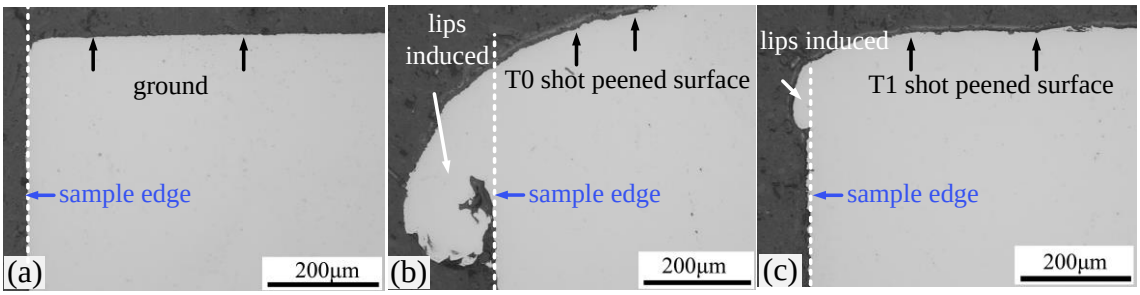


Figure 3- 10 Shot peening lips illustrating shear deformation in the edge region after shot peening: a) ground condition (no shear deformation for comparison); b) T0; c) T1.

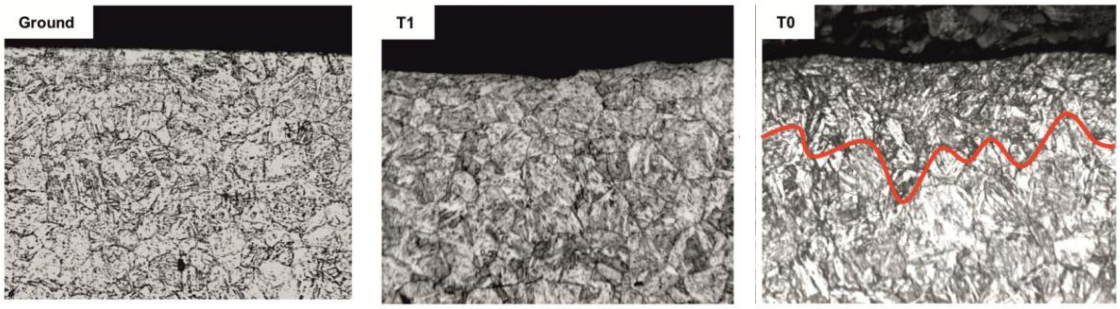


Figure 3- 11 Effect of grinding and varying shot peening processes on near surface microstructure [1].

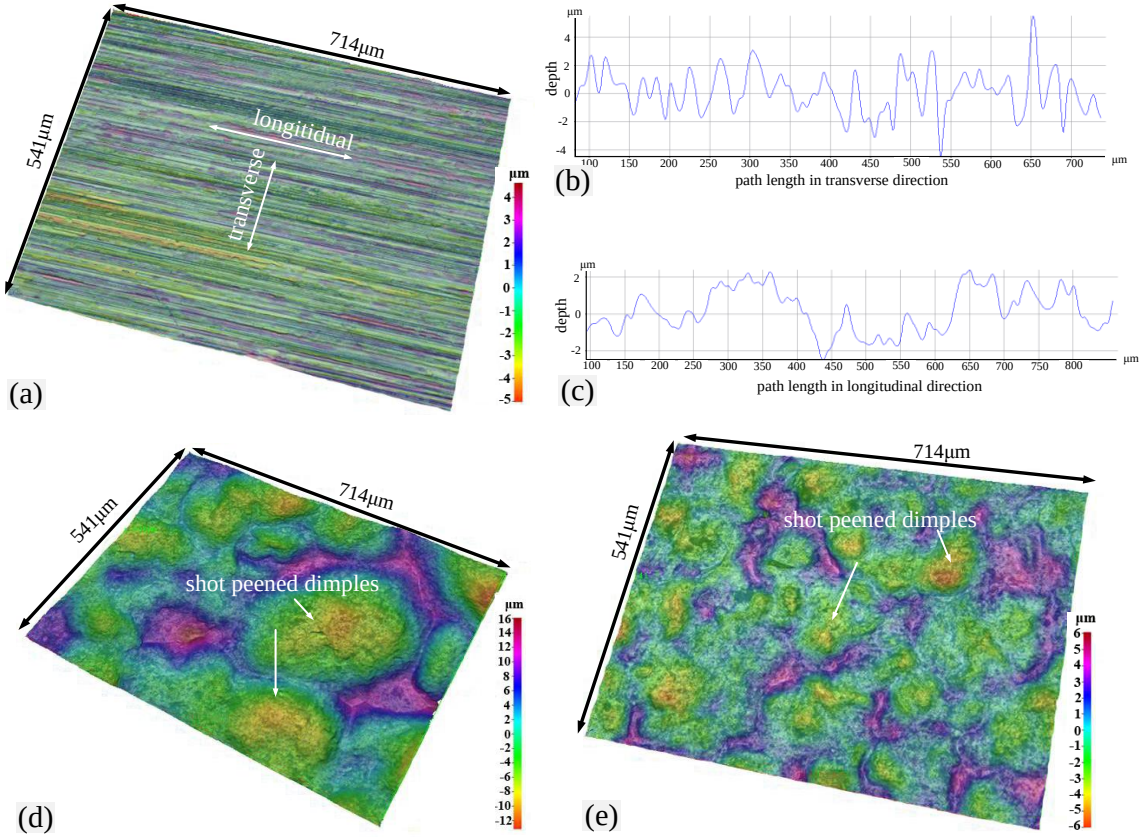


Figure 3- 12 3D surface morphology reconstruction of ground, T0 and T1 shot peened conditions revealed by Alicona Infinite Focus: (a) ground surface condition; (b) profile along the transverse direction; (c) profile along the longitudinal direction; (d) T0 shot peened and (e) T1 shot peened.

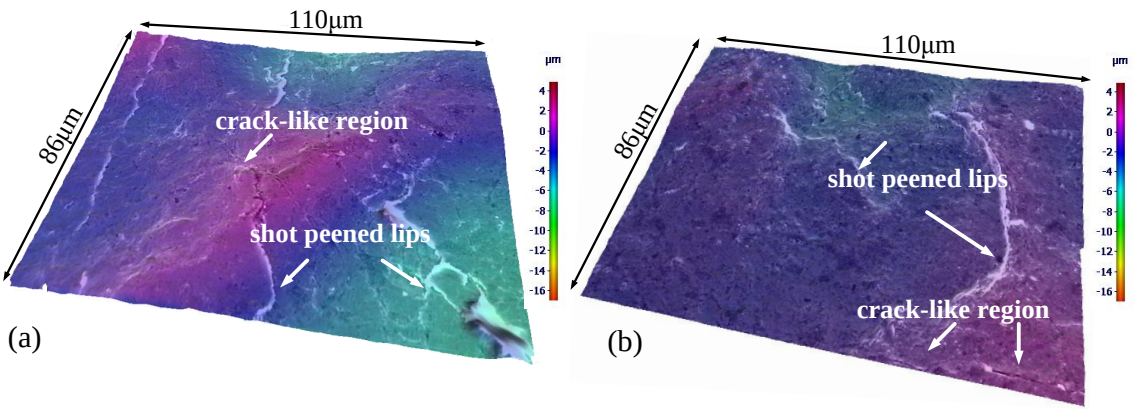


Figure 3- 13 3D surface reconstruction by Alicona Mex based on SEM images tilted at -5°, 0°,5°: (a) T0 and (b) T1.

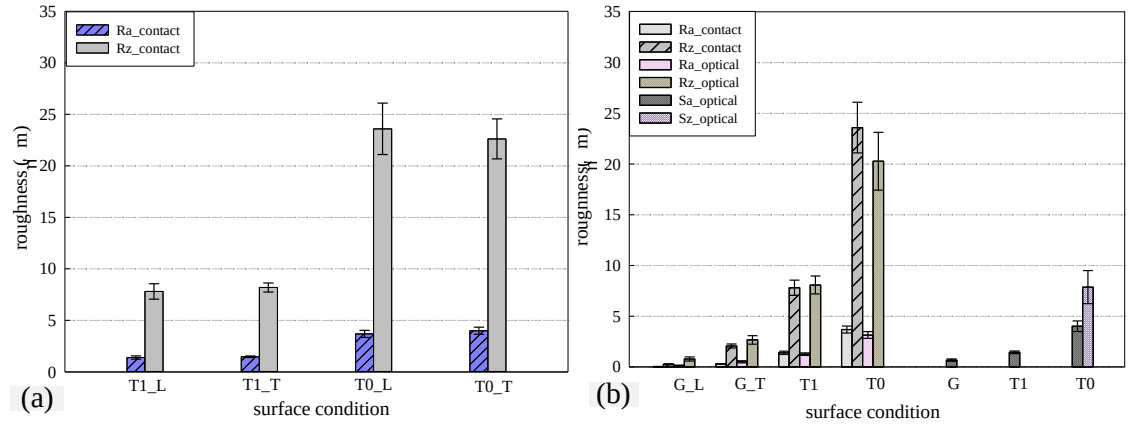


Figure 3- 14 (a) surface roughness $R_a$ and $R_z$ measured by Talysurf line profilometer in both longitudinal direction (parallel to the grinding marks) and transverse direction (perpendicular to the grinding marks) in T0 and T1 cases; (b) comparison of surface roughness measurements for each surface condition by both contact and optical approaches.

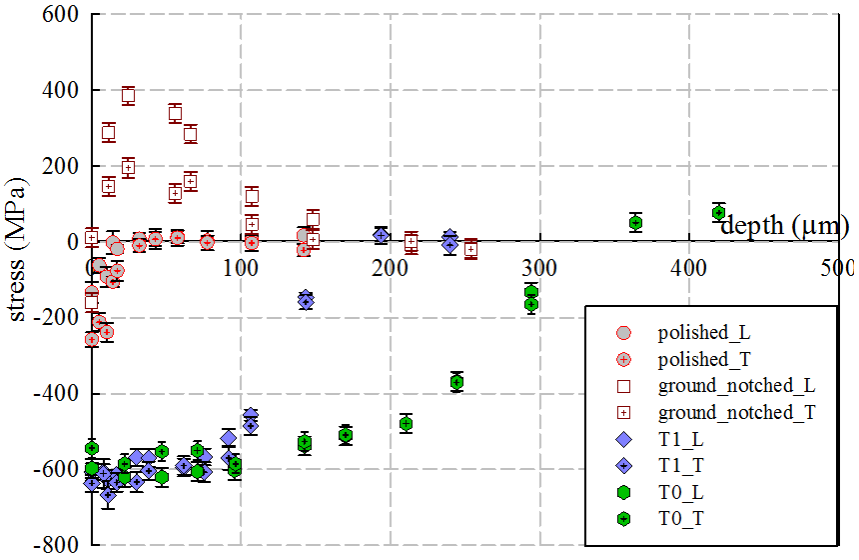


Figure 3- 15 Residual stress distribution resulting from polished, ground, T0 and T1 shot peening process (G and T0 data taken from [2]) in both longitudinal (L) and transverse (T) direction).

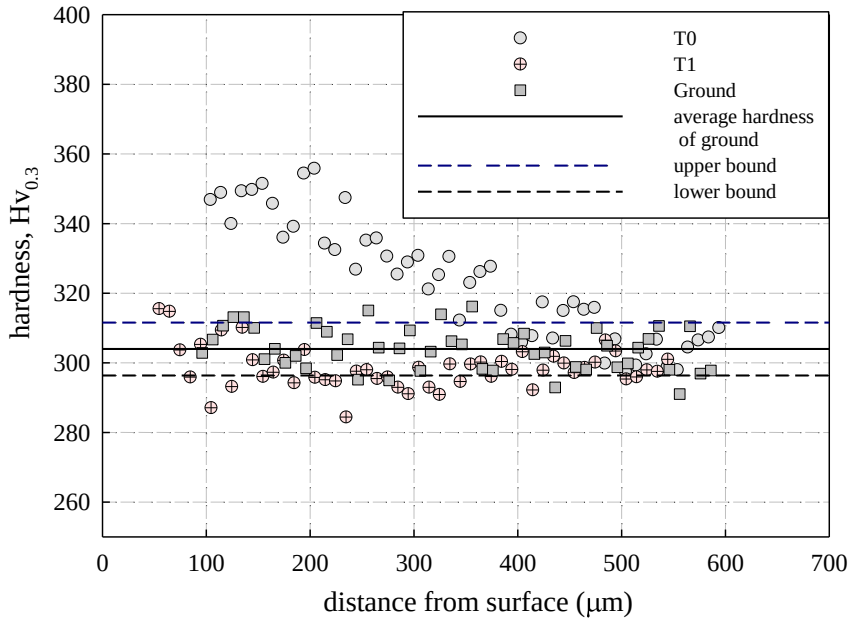


Figure 3- 16 Comparison of micro-hardness distribution in the depth direction in ground, T0 and T1 shot peened conditions.

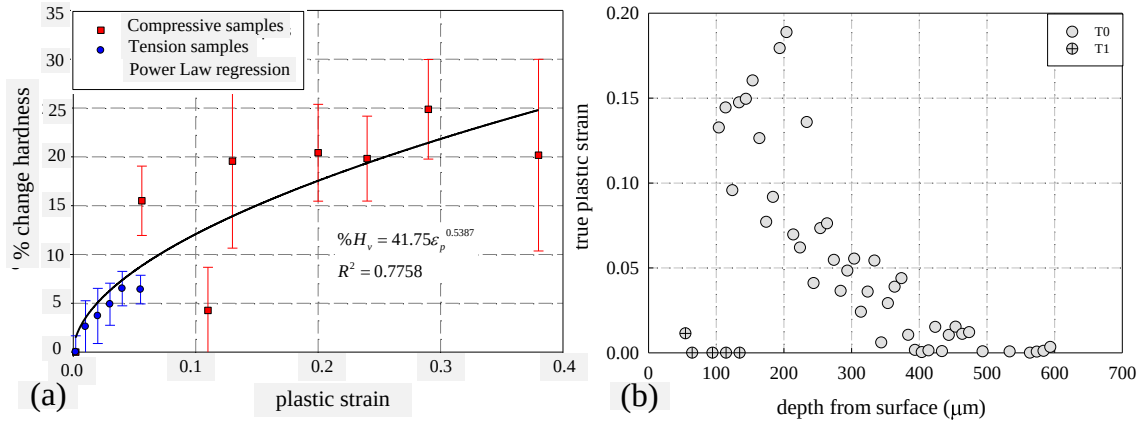


Figure 3- 17 (a) Calibration equations for monotonic uniaxial tension and compression samples relating % change in microhardness to plastic strain [11]; (b) plastic strain based on % micro-hardness change in T0 and T1 shot peened process.

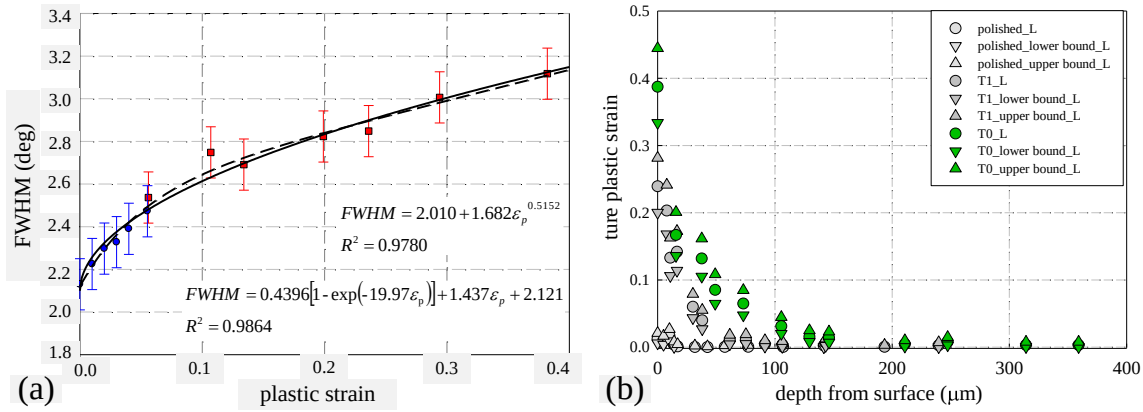


Figure 3- 18 (a) Calibration equations for monotonic uniaxial tension and compression samples relating XRD FWHM to plastic strain [11]; (b) plastic strain based on XRD FWHM in T0 and T1 shot peened process.

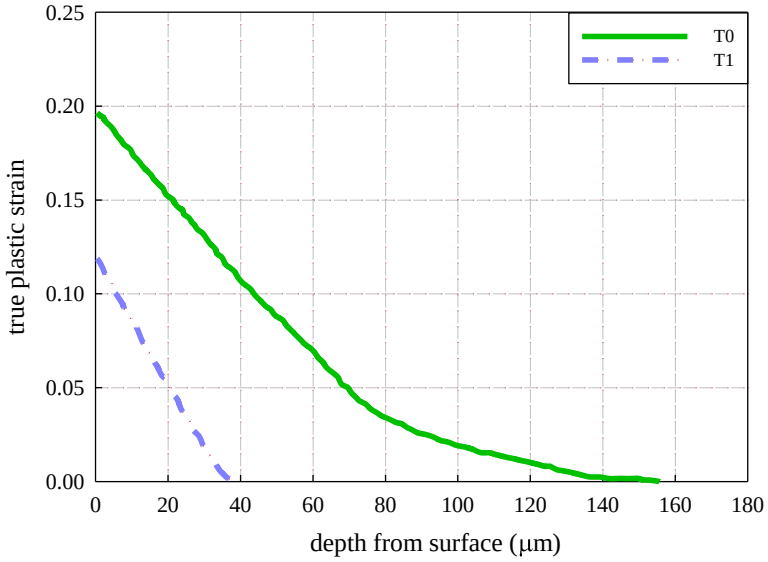


Figure 3- 19 Comparison of strain hardening layer (by EBSD) in T0 and T1 [11].

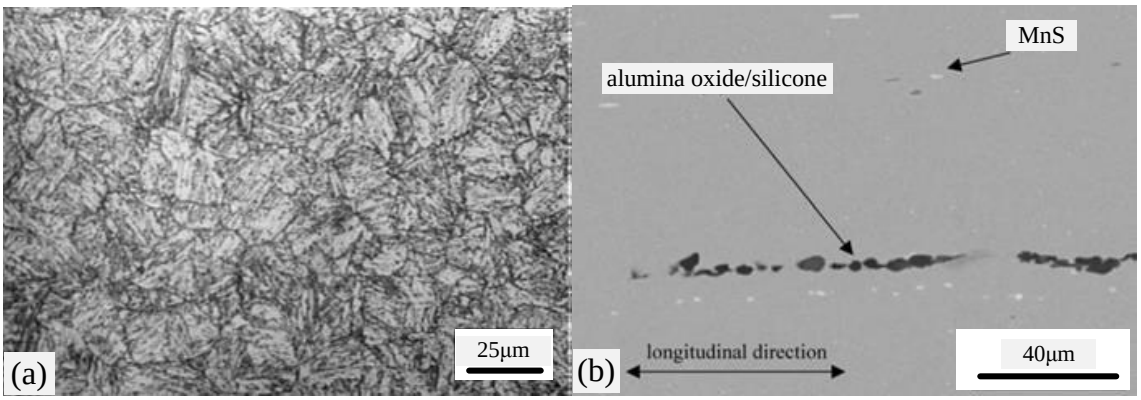


Figure 3- 20 Optical micrograph of the tempered martensite in FV566, A indicates aluminium oxide/silicate, and B is manganese sulphide, taken from [15, 16]

## 3.7 References

[1] K.A. Soady, *Reducing conservatism in life assessment approaches: Industrial steam turbine blade to disc interfaces and the shot peening process*, in: Engineering Sciences Unit, Ph.D thesis, the University of Southampton, 2013.
[2] K.A. Soady, B.G. Mellor, J. Shackleton, A. Morris, P.A.S. Reed, *The effect of shot peening on notched low cycle fatigue*, Materials Science and Engineering a-Structural Materials Properties Microstructure and Processing, 528 (2011) 8579-8588.
[3] T. Fujita, *Current progress in advanced high Cr ferritic steels for high-temperature applications*, Isij International, 32 (1992) 175-181.
[4] British-Standard, *BS ISO 4288:1996 geometric product specification (GPS)*, (1996).
[5] M. Fitzpatrick, A. Fry, P. Holdway, F. Kandil, J. Shackleton, L. Suominen, *Determination of residual stresses by X-ray diffraction*, (2005).
[6] P.S. Prevey, *X-ray diffraction residual stress techniques*, ASM International, ASM Handbook., 10 (1986) 380-392.
[7] P. Withers, H. Bhadeshia, *Residual stress. Part 1-measurement techniques*, Materials Science and Technology, 17 (2001) 355-365.
[8] P. Withers, H. Bhadeshia, *Residual stress. Part 2-Nature and origins*, Materials Science and Technology, 17 (2001) 366-375.
[9] J. Pešička, R. Kužel, A. Dronhofer, G. Eggeler, *The evolution of dislocation density during heat treatment and creep of tempered martensite ferritic steels*, Acta Materialia, 51 (2003) 4847-4862.
[10] M.G.Moore, W.P. Evans, *Correction for stress layers in X-ray diffraction residual stress analysis*, 56 (1958).
[11] K.A. Soady, B.G. Mellor, G.D. West, G. Harrison, A. Morris, P.A.S. Reed, *Evaluating surface deformation and near surface strain hardening resulting from shot peening a tempered martensitic steel and application to low cycle fatigue*, International Journal of Fatigue, 54 (2013) 106-117.
[12] EDAX-TSL, *OIM vs. 5.2 User Manual*.
[13] M. Kamaya, *Measurement of local plastic strain distribution of stainless steel by electron backscatter diffraction*, Materials Characterization, 60 (2009) 125-132.
[14] V. Schulze, *Modern mechanical surface treatment: states, stability,effects*, Wiley, New York, 2005.
[15] K.M. Perkins, M.R. Bache, *Corrosion fatigue of a 12% Cr low pressure turbine blade steel in simulated service environments*, International Journal of Fatigue, 27 (2005) 1499-1508.
[16] K.M. Perkins, M.R. Bache, *The influence of inclusions on the fatigue performance of a low pressure turbine blade steel*, International Journal of Fatigue, 27 (2005) 610-616.
[17] *Shot peening applications*, in: 9th edn, Paramus, NJ, Metal Improvement Company., 2005.
[18] K. Schiffner, C. Droste gen. Helling, *Simulation of residual stresses by shot peening*, Computers & Structures, 72 (1999) 329-340.
[19] J. Li, R. Zhang, M. Yao, *Computer simulation of residual stress field introduced by shot peening*, in: Conference Residual Stresses, 1991.
[20] E.R. De los Rios, A. Walley, M.T. Milan, G. Hammersley, *Fatigue crack initiation and propagation on shot-peened surfaces in A316 stainless steel*, International Journal of Fatigue, 17 (1995) 493-499.

[21] K. Neailey, *Surface integrity of machined components. Residual stresses and fatigue*, Metals and materials Bury St Edmunds, 4 (1988) 141-145.
[22] R. Snoeys, M. Maris, J. Peters, *Thermally induced damage in grinding*, Ann CIRP, 27 (1978) 571-581.
[23] M. Mahdi, L. Zhang, *A numerical algorithm for the full coupling of mechanical deformation, thermal deformation and phase transformation in surface grinding*, Computational Mechanics, 26 (2000) 148-156.
[24] M.J. Balart, A. Bouzina, L. Edwards, M.E. Fitzpatrick, *The onset of tensile residual stresses in grinding of hardened steels*, Materials Science and Engineering: A, 367 (2004) 132-142.
[25] X. Chen, W.B. Rowe, D.F. McCormack, *Analysis of the transitional temperature for tensile residual stress in grinding*, Journal of Materials Processing Technology, 107 (2000) 216-221.
[26] J.F.a.S. Flavenot, N., *Effects of grinding conditions on fatigue behaviour of 42CD4 grade steel; comparison of different fatigue criteria incorporating residual stresses*, in: L. Mordfin (Ed.) Mechanical Relaxation of Residual Stresses, Cincinnati, Ohio, 1987, pp. 91-111.
[27] N. Skalli, J. Flavenot, *Effects of grinding conditions on fatigue behaviour of 42CD4 grade steel*, in: ECF5, Lisbon 1984, 2013.
[28] R.A. Poggie, J.J. Wert, *The influence of surface finish and strain hardening on near-surface residual stress and the friction and wear behavior of A2, D2 and CPM-10V tool steels*, Wear, 149 (1991) 209-220.
[29] Y.-K. Gao, M. Yao, J.-K. Li, *An analysis of residual stress fields caused by shot peening*, Metallurgical and Materials Transactions A, 33 (2002) 1775-1778.
[30] S.T.S. Al-Hassani, *Mechanical aspects of residual stress development in shot peening*, in: the 1st International Conference on Shot Peening, Paris, France, 1981.
[31] D.A. Hills, R.B. Waterhouse, B. Noble, *An analysis of shot peening*, The Journal of Strain Analysis for Engineering Design, 18 (1983) 95-100.
[32] J.K. Li, Y. Mei, W. Duo, W. Renzhi, *Mechanical approach to the residual stress field induced by shot peening*, Materials Science and Engineering: A, 147 (1991) 167-173.
[33] K. Tosha, *Characteristics of shot peened surfaces and surface layers*, in: Proceedings of Asia-Pacific Forum on Precision Surface Finishing and Deburring, 2001, pp. 193-201.

# Chapter 4: Crack aspect ratio evolution and early fatigue crack morphology

## 4.1 Introduction

Much research has focussed on the effect of shot peening on the fatigue behaviour of different material systems such as steel, Al and Ti alloys [1-5]. The rough surface induced is generally considered to be detrimental to fatigue resistance [1], while both the residual stress and strain hardening profiles at, and just below, the surface are considered to improve fatigue resistance [6, 7]. The benefit of shot peening in the high cycle fatigue regime is well documented [6, 8, 9], however, in the low cycle fatigue regime, the benefit is more service condition dependent and more complex to assess, especially when residual stress relaxation or strain hardening changes during the fatigue process are taken into account.

Recent reviews [10, 11] have detailed at some length the effects of the shot peening process (surface roughness, plastic deformation as well as residual stress) on fatigue behaviour as well as how the magnitude of these effects can be determined both experimentally and numerically. Although there has been substantial investigation into the effect of shot peening on the fatigue life of different material systems, systematic research on fatigue crack initiation and propagation behaviour (especially when operating in the LCF regime) in a notch stress field has not yet been fully explored. Whilst some studies have tried to investigate the effect of the near surface layer induced by shot peening, generally they have only considered the total fatigue life and not fatigue crack initiation or early crack propagation behaviour. The present detailed study builds upon previous research [12-14], and aims to understand the micromechanisms by which the crack first initiates in and then propagates through the shot peened affected layers.

The differences in surface roughness, residual stress and plastic deformation layers resulting from different shot peening processes were characterised in Chapter 3. The effect of these differences on fatigue crack growth behaviour will be analysed in both Chapter 4 (early fatigue crack aspect ratio evolution

and crack morphologies) and Chapter 5 (fatigue crack propagation behaviour). The work presented here has also been published in:

1. B.Y. He, K.A. Soady, B. G. Mellor, G. Harrison and P. A. S. Reed. Fatigue crack growth behaviour in the LCF regime in a shot peened steam turbine blade material. In press. International Journal of Fatigue. March 2015.
2. B.Y. He, O.L. Katsamenis, B.G. Mellor and P. A. S. Reed. 3-D analysis of fatigue crack behaviour in a shot peened steam turbine blade material. Materials Science and Engineering: A, 642 (2015) 91–103.

## 4.2 Experimental methods

### 4.2.1 Interrupted fatigue test

The turbine blade material investigated in this study is FV448; its composition and microstructure is detailed in Chapter 3. The samples to be fatigued have smooth plain bend bars (PBB) (only used for the interrupted heat-tinted fatigue tests) and U-notch bend specimens, as illustrated in Figure 4- 1. The notch geometry represents the stress concentration feature in the steam turbine, and provides a stress concentration factor ~ 1.6 calculated using an elastic finite element analysis [15]. These samples were taken from barstock by electrical-discharge machining. In order to meet the industrial machined component specification of surface roughness $R_a < 0.8\ \mu m$, a grinding process was followed and a thickness of 0.25 μm was removed from the barstock material.

The fatigue crack behaviour was evaluated by three point bending (for U-notch samples) or four point bending (for PBB) at ambient temperature using a sinusoidal waveform and frequency of 20 Hz on a servo hydraulic Instron 8502 machine. Since the maximum service temperature of the low pressure turbines (250 ℃) is outside the creep regime for this material, consideration of creep-fatigue interaction is not required in the life assessment process for these components, and room temperature behaviour is considered representative for life assessment approach development. The fatigue test was under load control with a load ratio of 0.1, the true stress and strain range level experienced at the notch root or plain bend bar was simulated by an elastic plastic finite element model. A quarter model was employed by previous researchers [15] relying on specimen symmetry, and an elastic-plastic material model

employing isotropic hardening conditions based on true stress–strain data taken from (monotonic) tensile testing was implemented. Elements were full integration 20 node quadratic hexahedral C3D20 type and were 0.01 mm in depth adjacent to the surface loaded in tension. A representation of the first loading cycle was obtained through sequential static analysis of stress and strain distributions under maximum, minimum and no load. The effect of any modifications to material behavior induced by surface processing, such as surface work hardening, was neglected in this calculation. This allowed a representative comparison to be drawn between the samples tested under different surface conditions [15]. In the present study, crack initiation and propagation behavior were investigated under the same local applied strain range conditions. The applied true strain in the sample loading direction ($\Delta\varepsilon_{11}$) was 0.68 %.

Interrupted fatigue tests were carried out to evaluate the evolution of crack aspect ratio as well as the 3D crack morphologies that developed. For the former, fatigue tests were interrupted at about 65 ~ 75 % of the estimated fatigue life (based on the S/N curve determined previously); the samples were then removed from the test apparatus and oxidized in a furnace at 600 °C for 2 hours. After that, they were immersed in liquid nitrogen for up to 10 minutes to allow samples to cool down thoroughly to below their ductile to brittle transition temperature. These cooled samples were then broken open with a hammer manually and the fracture surfaces were allowed to warm up to ambient temperature in acetone. The interrupted fatigue test with subsequent heat tinting allows the evolution of crack shape in the depth direction to be assessed, since the fatigue cracked region after heat tinting is clearly different from the subsequent brittle fracture area. For 3D crack morphology analysis the fatigued samples were removed from the fatigue test rigs also at ~75 – 85 % of fatigue life followed by mechanical serial sectioning.

### 4.2.2 Early fatigue crack morphology

#### 4.2.2.1 3D crack reconstruction by serial sectioning

The crack aspect ratio assessment produced by heat-tinting can only sample those cracks that form the final fracture plane. A reconstruction of the full 3D fatigue crack field in the notch area has been attempted in order to

characterise the crack shape, interaction between cracks and hence develop further understanding of the effect of shot peening on fatigue crack initiation and propagation behaviour. Essentially, 3D crack information is derived from reconstruction of serial sections a known distance apart containing 2D crack information.

*Depth estimation:* Micro-hardness indentation testing is widely used to characterise hardness and can also be applied to assess the tensile strength and yield strength via empirical correlations [16]. The Vickers indenter itself is a pyramid with a square base and an angle of 136 degrees between opposite faces and thus it forms a square indent after penetrating the surface under a specific load, which can vary from 10 g to 1000 g. Usually the average of the two diagonals of the square indent is used to evaluate hardness. Due to the specific indenter shape, the depth of the indentation can be calculated based on the precise value of the diagonal length. Figure 4- 2 illustrates the relationship between indent depth $h_{depth}$ and indent diagonal $d$:

$$h_{depth} = \frac{d_{indention}}{2\tan(2\alpha)} = \frac{d_{indentation}}{2\,tan(74°)} = \frac{d_{indentation}}{2\times 3.487} = \frac{d_{indentation}}{6.974} \qquad \text{Equation 4- 1}$$

Since the diagonals of the indent, $d_{indentation}$, are measurable, the depth of the indent $h_{depth}$ can be obtained. In the current research, the average diagonal value is used for depth calculations.

*Depth removed correction*: Some pile-up around the indents under both 1 kg and 5 kg loading conditions was noticed, as shown in Figure 4- 3. The plastic deformation around the indents (pile up) is obvious, and this pile-up is related to the loading conditions-higher loading results in more plastic deformation, thus more pile up. A systematic study was conducted to explore whether this pile-up will affect the estimated depth of material removed from indents viewed on successive serial sections. Both 1 kg and 5 kg loads were applied on a flat sample surface for a 15 s dwell time. In the trial test, 3 indents were taken for each loading condition. Before indentation, the surface had been polished down to a 1 μm finish. The specimen had firstly undergone 5 minute polishing by 3 μm diamond paste, then 5 minute polishing on 1 μm diamond paste. After each polishing process, new indentation markings were introduced and images were taken by optical microscopy. These polishing processes were repeated 10 times. Thus the estimate of material removed per layer based on both “new” (with pile-up) and “old” (without pile-up) indentation markings can

be obtained. Figure 4- 4(a) shows the depth of material removed at specific polishing times. Due to the pile up, the depth of material removed indicated by new indents under both 1 kg and 5 kg loading is apparently larger than that obtained from pre-existing indents (without pile-up). Possibly due to the greater degree of pile up, the differences between the depth removed calculated from the new and pre-existing indents with a 5 kg load are much larger. The total depth removed indicated by these different cases are illustrated in Figure 4- 4(b). The pre-existing indents give very similar depths of material removed for the two loading conditions, while the depth removed calculated from the new indents gives significantly larger values. Correction factors can be evaluated based on the difference between the depth removed calculated from new and pre-existing indents, as illustrated in Figure 4- 5(a). The correction factors based on the individual depths removed for both 1 kg and 5 kg load cases fall in the range 0.4 ~ 0.6 at different polishing stages, possibly because of the slight change of polishing parameters, such as loading, and polishing times, as well as rotating speed. Based on the total depth removed, the trend of the correction factor for both 1 kg and 5 kg loads is similar: the correction factors decreases gradually from 0.8 ~ 0.85 as the polishing times increase and reach a 'quasi plateau'. This trend is much more clearly illustrated in Figure 4- 5(b). The correction factors decrease as the depth removed increases, which indicates the errors caused by the pile-up effects are smaller. Around 20 ~ 25 μm and onward, the correction factor seems to become constant at around 0.6 ~ 0.65. To reduce calculation errors induced by plastic deformation and pile-up around the indentation markings, the correction factor applied in this study is 0.62. This is also checked against total depth removed.

Therefore, in this study, micro-hardness indents were utilised as a fiduciary marker to assess the distance between successive layers removed by serial sectioning. In indentation testing, to maintain a regular indenter shape, and also to prevent indenter damage (for the diamond is hard but very brittle), the material surface is usually required to be as flat as possible. In the present study, the notch geometry is 4.5 (width) x 1.25 (depth) mm and the diameter of the indenter is 3 mm, thus the indenter was able to fit into the notch, as shown in Figure 4- 6(a). Compared to the size of the indents, the notch root is relatively flat. The indent made on the ground and shot peened surfaces under

various loads for a 15 s dwell time are shown in Figure 4- 6(b) and (c), respectively.

A sequence of indentation marking, serial sectioning and subsequent re-imaging (and re-indenting if necessary) was then carried out to produce a series of 2D images of the notch root at known depths. In the present research, a 1000 g load applied for 15 s was chosen for the indentation marking, and five to six indentations were made across the sample width and then images of the full width were taken by optical microscopy under x20 magnification, to allow measurement of the cracks and the diagonals of the indentations. For plain bend bar specimens, conventional grinding and polishing procedures are available. Therefore, the samples were mounted and polished in the automatic machine. However, for a notched specimen, conventional grinding and polishing procedures are not possible, so both the grinding and the polishing were conducted using a pillar drill. For the first fine grinding step a 3 mm diameter metal rod mounted in the drill to which P4000 finish SiC paper impregnated with 3 μm diamond paste was used to polish for 2 minutes. The final polishing step of 3 minutes used a dental felt impregnated with 1 μm diamond paste. During polishing, the ends of the specimen were held steady, with the dental felt kept evenly in the notch root, to ensure the material removal rate was similar around the notch root surface area. In order to reveal cracks, especially when cracks were very small with little (or no) opening, Vilella's regent was useful in highlighting these crack paths. A schematic illustrating the polishing direction in the serial sectioning process is shown in Figure 4- 7 and the experimental process is detailed in Figure 4- 8. Since new indentation markings are applied consistently during the whole process (which have pile up), the calculated depth of material removed has been corrected by the final correction factor 0.62. The overall material removed has also been checked for consistency to agree with the sum of the layers of material removed. For the plain surface, a conventional polishing process was used.

A U-notch profile has been assessed at different polishing stages, for example, the 1$^{st}$, 75$^{th}$, and the 224$^{th}$ (last) stage, were evaluated by Talysurf, as shown in Figure 4- 9. The depth changes of the notch at these three different stages are described in Table 4- 1. After the 1$^{st}$ polishing stage, the notch depth was 1253.9 μm, while the estimated original notch geometry was 1250.0 μm. After the 75$^{th}$ and 224$^{th}$ polishing stages, this value reaches 1392.8 μm and

1967.9 μm, respectively. As stated previously in this section, the material removed depth correction factor in the current study was chosen to be 0.62. To double check the validity of the indentation marking technique combined with this depth correction factor, the actual depth of material removed at different polishing stages obtained by the Talysurf measurement were compared with those calculated from indentation markings. Compared with 3.9 μm estimated from Talysurf measurement, the depth of removed after the 1st polishing calculated from indents is estimated to be 0.76 μm after correction. However, it is important to note that the surface roughness $R_a$ of the T0 shot peened surface is 3.6 μm, which may affect the estimation. In the initial polishing stages (especially when the surface is still rough), measurement errors will be easily induced because of the remaining irregular indents on the rough surface (Figure 4- 6). Thus it is understandable that 184 μm of estimated removed material after the 75th polishing step (where it is still within shot peened affected regime), rather than 142 μm as measured by the Talysurf. It can be seen that the error between the measured overall depth removed and the corrected overall depth determined from indentation markings is only 4.21 % after the 224th polishing step. Thereafter, the corrected indentation marking technique has been used in this study and the depth of material removed obtained after this correction is considered reliable.

#### 4.2.2.2 3D crack morphology by computed tomography

The cracks produced in the U-notched T1 (low intensity) and T0 (high intensity) shot peened surface conditions were chosen to be further studied by means of micro- X-ray computed tomography (μ-CT) on the 'ZEISS Xradia 510 Versa 3D X-ray microscope' at the μ-VIS X-ray imaging centre at the University of Southampton. Due to the high degree of attenuation of X-rays in steel, a 'match stick'-like sample (dimensions ~ 2 x 2 x 8 mm) was cut out from the notch root of the specimens (as shown in Figure 4- 10) so that a minimum of 10 % transmission of the incoming X-ray beam was preserved at all exposure angles.

The scan of T1 was conducted at a peak voltage of 150 kV and the beam was pre-filtered through 2.5 mm of $CaF_2$ to reduce beam-hardening artefacts. To achieve sufficient flux, the power was set at 10 W (67 μA) and the 2026x2026 detector was binned twice resulting in effective detector dimensions of

1012 x 1012. The source to detector distance was set at 93.4 mm (SrcZ: -16.7, DetZ: +76.6), which in combination with the 4x lens resulted in a pixel size of 1.2 μm; i.e. a spatial resolution of approximately 3 μm. During the tomogram, a total of 3201 radiographs were collected with an angular step of ~ 0.11° over a 360 degree rotation of the sample.

Due to small size variations between the T1 and T0 samples, T0 was scanned with slightly different parameters. A total of 2001 radiographs were collected with an angular step of ~ 0.18°, the detector was not binned and the source to detector distance was 137.8 mm (SrcZ: -36.1, DetZ: +101.7) resulting in a pixel size of 0.88 μm. All other parameters remained unchanged.

In order to capture the damaged area located at the root of the notch, and given that at the aforementioned pixel conditions the imaging volume ranges from ~ 1 - 1.5 $mm^3$, local tomography scans had to be performed (note: local tomography is defined as an acquisition mode during which only a selected volume of interest, VOI, and not the whole sample is imaged). The specimens were positioned such that the surface of their notch-root remained within the field of view during the full 360° rotation.

Prior to each scan, a fast (60 min) warm-up scan was performed in order to ensure that thermal equilibrium had been reached within the X-ray source and the scanner enclosure. Following the acquisition, the raw data were reconstructed using Zeiss' reconstruction software, which uses a filtered back projection algorithm.

### 4.2.3 Fractography

Fractured specimens were examined using a Wild Macroscope, an Olympus optical microscope, as well as a JSM 6500F field emission gun scanning electron microscope (FEG-SEM). To gain an overview of the fracture surfaces, optical microscopy under low magnification was used: oblique illumination was employed to make the ratchet marks more visible, and to distinguish between the fatigue and brittle fracture areas in the interrupted heat-tinting test. Compared with optical microscopy, SEM has a larger depth of field, which allows a large variation in height of the sample to be in focus and at the same time has a much better resolution. The fracture surface was thus analysed on a

JSM 6500F field emission gun scanning electron microscope (FEG-SEM) under 15KV Voltage, ~ 10mm working distance conditions.

## 4.3 Experimental results

### 4.3.1 Heat tinting test after interrupted fatigue process on U-notch samples

Generally speaking, the shapes of small cracks are often approximated to a semi-circular crack ($a/c$ = 1), although significant deviations from this shape have been reported. The interrupted heat-tinting fatigue tests on the polished and 13 A shot peening condition were conducted to explore the variation in crack aspect ratio in the early stages of crack growth. A baseline test was conducted on the polished condition, where the crack behaviour would not be affected by factors, such as shot peening dimples, surface hardened layers or residual stress distributions but only by the microstructure or inherent constraint conditions. The validity of comparing these two surface conditions was based on the similar applied notch root local strain range (~ 0.68 %) applied during the fatigue testing. Replicas at different numbers of cycles during the fatigue life also provided additional surface fatigue crack growth information and allowed crack initiation sites to be easily found by tracing back to the early stages of crack growth. The cracks on the polished sample and shot peened samples subjected to the interrupted heat-tinting fatigue test are designated P1 and SP1, respectively. The cracks detected are labelled $P_i$-1, $P_i$-2,...$SP0_i$-1, $SP0_i$-2,...and $SP1_i$-1, $SP1_i$-2...., here the subscribe "i" represents that interrupted fatigue test, "P" indicated polished surface; "SP0" and "SP1" are T0 and T1 shot peened conditions, respectively.

#### 4.3.1.1 Interrupted heat-tinting fatigue test on polished samples

As discussed in Section 3.3.2, the notch surface was polished down to 1 μm before being subjected to fatigue loading. Replicas were taken every 1000 cycles and then at a reduced interval of every 200 cycles when cracks were observed, in order to capture crack growth behaviour at the very early stage. The fatigue test was interrupted at 18292 cycles, about 65 ~ 75 % of established fatigue life based on the previously established S/N curve. Figure 4- 11(a) and (b) show the top surface of the notch and the fracture surface of

an interrupted polished fatigue sample, respectively. Fatigue regions were brown in colour under the optical microscope after heat tinting. The heat tinting occurred because an open crack allowed oxidization of the crack flanks at the high temperature (650 ℃). Judging from these small tinted areas, the fatigue cracks were still at an early stage when the test was stopped. For example, crack $P_i$-3,which is the longest crack which appeared on the polished notch area, is about 700 μm in length, while crack $P_i$-1 and crack $P_i$-2 are around 200 μm, as illustrated in Figure 4- 12(a) corresponding to 2200 cycles. In addition, dozens of tiny cracks were also found in the notch area. These multiple short crack initiation sites on the polished notch surface may be linked to the underlying microstructure. To explore the relationship between very early crack behaviour and microstructure in this material system, the notch area was also etched by Vilella's reagent, as shown in Figure 4- 12(b).

The inter-relationship of fatigue crack path and microstructure can also be characterized in those cracks with lengths between 10~30 μm. Figure 4- 13(a) has no additional labelling but shows an indication of a small crack. In Figure 4- 13(b), the four adjacent prior austenite grains are labelled as A, B, C, D. A crack has propagated along the grain boundaries between grain A and B, as well as B and C, both of these boundaries are parallel to the maximum tensile stress direction. Stage II crack growth usually occurs perpendicular to the maximum tensile stress direction, here the crack path can be seen to be more microstructurally determined. Crack deflection occurred at grain A and the crack then propagated along the grain boundary between C and D. Some very tiny cracks initiated within a grain and propagated along martensitic lath boundaries, shown as Figure 4- 14(b). It seems that crack initiation and propagation behaviour are quite microstructure dependent when the crack length is comparable to the grain size.

By tracing back replica records taken during the fatigue process, the crack morphology at early stages as well as the crack propagation process can be captured in detail. Figure 4- 15 shows the crack morphology at various fatigue stages for crack $P_i$-2. (The general position of all cracks mentioned is clearly indicated in Figure 4- 12 (a) and (b)). Crack $P_i$-2 was clearly identified at ~ 45 - 50 % of expected fatigue life. The crack length at 11635 cycles is about 60~70 μm, then it propagated slowly perpendicular to the maximum tensile stress direction and the crack length reached 100 μm at 18292 cycles, when

the fatigue test was interrupted for heat tinting. Although the crack length at 15160 cycles (~ 50 – 60 % of expected fatigue life) was only 70 μm, another crack, which has been called crack $P_i$-2(a), initiated at the crack tip ahead of the major crack $P_i$-2 and coalescence was observed at 18292 cycles. Crack $P_i$-2 is shown in more detail under SEM observation in Figure 4- 16(a). Crack $P_i$ -2 was more apparent under SEM observation, compared to optical microscopy. An inclusion around which the crack has bifurcated is seen in Figure 4- 16 (b) and the EDS result in Figure 4- 16(c) indicates that this is MnS, one of the most common non-me

tallic inclusions present in steel. Due to the resolution issue of surface replication, no direct evidence has been found that this crack initiated from the inclusion.

Crack $P_i$ -3, (also indicated in Figure 4- 12(a) and (b)) is the longest crack that appeared on the polished notch surface during the fatigue process. The crack morphology development is illustrated in Figure 4- 17. The initial crack was firstly identified confidently at around 8060 cycles (possibly ~30 – 40 % of fatigue life). At this point, this crack is not perhaps a real crack but really a line of possible extrusions. As the fatigue test continued, the extrusions became larger and the crack path seemed to be increasingly obvious; meanwhile, the crack tips moved forward gradually. At 11635 cycles (~40 – 50 % of fatigue life), the crack has already opened slightly since some replica material was left on the crack path. It is noteworthy that the crack tip movement during the propagation process was not smoothly continuous due to local crack coalescence events. For example, there is an obvious crack-like protrusion ahead of the crack tip at 15360 cycles, as labelled by arrows in Figure 4- 17. The crack tips of crack $P_i$-3 moved forward gradually during fatigue, as did the crack-like protrusions. At some point between 17450 and 18292 cycles, these two cracks coalesced together, as indicated by arrows at 18292 cycles. Figure 4- 18 (a) and (b) are the SEM micrographs of crack $P_i$-3 before and after the microstructure was revealed by etching, respectively. After etching, the interaction between a crack and microstructure (such as grain boundary or martensitic lath) is more visible. Region B is detailed in Figure 4- 18 (c) and (d), while Region C is clearer in Figure 4- 18 (e)-(h). Region B is the initiation site of crack $P_i$-3. It seems to have initiated from an inclusion particle. The black square is due to carbon-deposition during the period of focus at high

magnification under the SEM. Though the fatigue behaviour of the small cracks was found to be more microstructure dependent, in this relatively long crack (compared with the grain size of matrix), it is less easy to see whether the crack propagation direction is also related to grain boundaries or the martensitic laths. The general crack propagation direction was perpendicular to the maximum tensile stress axis direction, but in some local regions, crack tips preferred to propagate along grain or martensitic lath boundaries or directions parallel to these, as revealed in Regions C in Figure 4- 18 (a) and (b), with and without etching. The whole fracture surface under SEM observation is presented in Figure 4- 19. The darker coloured areas are actually heat tinted fatigue cracks. For clarity, these individual fatigue cracks are labelled as crack $P_i$-1, $P_i$-2, $P_i$-3, $P_i$-4, $P_i$-5, and $P_i$-6, respectively. The fatigue area revealed by heat-tinting is relatively small, and surface observations showed dozens of tiny cracks distributed randomly at the notch root. Thus during brittle failure on breaking open the sample, the specimen fracture plane will tend to have selected the larger (and most aligned) cracks but this has still resulted in a relatively rough fracture surface. It should be noted that only a sub-set of the cracks formed in the notch root can have their aspect ratio evaluated via this route as not all cracks will be on the final fracture surface.

Crack $P_i$-1 is shown in Figure 4- 20. The distinction between the fatigue and brittle failure region is obvious under SEM observation, since the brittle fracture area is more faceted or rough, while the fatigue damage area is relatively smooth. The overall crack shape cannot be seen clearly since part of crack $P_i$-1 is behind the main fracture surface, but the shape of crack $P_i$-1 appears quite deep. In addition, a vertical series of inclusions are found within the fatigue crack region, the EDS result shows that there are several elements, O, Mn, Al, Si, K, Ca, C, detected in the inclusion area. The content of Si is only 0.31 % (w.t.%) in this material (see Table 3-1). It should be noted that the replica is a silicone compound, and some trace may have been left on the fracture surface when the crack was partially open. This inclusion is therefore likely to be an aluminium oxide stringer, although no clear evidence of such stringers in the longitudinal direction was observed in previous metallography [15]. The orientation of this stringer on the fracture surface provides a likely initiation site for crack $P_i$-1 and offers an explanation for its high aspect ratio.

Figure 4- 21 (a) describes crack $P_i$-2, the relative position of which is also indicated in Figure 4- 19. As mentioned in section 3.3.4, crack aspect ratio information was to be obtained from these crack shapes on the fracture surface. The identification of the boundary of the fatigue crack is somewhat subjective. In each case the crack shapes used in calculations in the present research are labelled directly and compared with an unlabelled image for comparison, such as the labelled crack 2 in Figure 4- 21(b). The crack is close to a semi-circle and again a possible aluminium oxide stringer is also found in the fatigue initiation region, shown in Figure 4- 21(c) and (d), which is the possible crack initiation site. Judging from the notch surface observations, the longest crack induced by fatigue on this notch polished condition is 700 μm in length (that is crack $P_i$-3, as shown in Figure 4- 12(a) and (b)). Beneath the notch surface, the crack morphology of this longest crack is shown in Figure 4- 22(a), the artificial labelled crack shape is shown in Figure 4- 22(b). Crack $P_i$-3 is very semi-circular, and a possible stringer inclusion also exists in the middle of the crack region. Crack $P_i$-4 and $P_i$-5 are illustrated in Figure 4- 23 and Figure 4- 24, respectively. MnS inclusions were both found in Crack $P_i$-4 and Crack $P_i$-5, as indicated in Figure 4- 23(d) and Figure 4- 24(d).

#### 4.3.1.2 Interrupted heat-tinting fatigue test on shot peened sample

Fracture surfaces of samples which had undergone a shot peening process are quite different from those obtained from the polished condition. Fatigue crack initiation and propagation behaviour is likely to be affected by this very complex surface condition (in addition to the surface roughness there are associated local residual stress and work-hardening variations just below the surface). Therefore, the interrupted heat-tinting fatigue test analysis approach was also used for a shot peened sample tested under a nominally similar applied local notch root strain range condition ($\Delta\varepsilon_{11}$ = 0.68 %).

Similar to the polished sample, replicas were also taken at different fatigue stages in this shot peened sample to capture crack initiation and propagation data during fatigue. Figure 4- 25 (a) and (b) shows the top surface and the fracture surface of an interrupted shot peened fatigue sample under an optical microscope. Compared with the previous polished notch specimen, the heat tinted regions on the shot peened fracture surface are more extensive, as the fatigue cracks are a little longer since the fatigue test was interrupted at

around 70 ~ 75 % of the established life. Tiny cracks on the shot peened surface are very hard to identify due to the extensive surface roughness. Therefore, to analyse the short crack behaviour in the shot peened condition, the fracture surface in Figure 4- 26(a), as well as the optical micrograph of the fracture surface in Figure 4- 26(b) are used to identify their location.

Due to the greater proportion of fatigue life achieved and the generally longer crack lengths, some crack coalescence was observed in the shot peened samples even within what might initially be considered a 'single' crack region. By tracing back through the replication records, the evolution of the fatigue crack morphology was revealed, and can be taken into account in calculating the crack aspect ratios. Due to the short crack length and rough shot peened surface, the crack morphologies during different fatigue stages in interrupted fatigue tests are difficult to see in the replica records. However, detailed observation by zooming in on the images allows then to be identified. Figure 4- 27(a) and (b) show the crack morphologies at various stages for crack $SP0_i$-1 $SP0_i$-2 and $SP0_i$-3, respectively. In Figure 4- 27(a), $SP0_i$-1 and $SP0_i$-2 can be identified at ~5000 fatigue cycles and both of these two cracks are found at the shot peened dimples on the shot peened surface, as indicated. The crack shape of $SP0_i$-1 and $SP0_i$-2 under optical and SEM observation is shown in Figure 4- 28 (a) and (c) and Figure 4- 29(a) and (c), respectively. To illustrate the crack morphologies clearly, the fatigue area has been outlined as shown in Figure 4- 28(b) and (d) and Figure 4- 29(b) and (d) respectively. As can be seen, the fatigue region was oxidized during the heat-tinting process due to the crack opening; the oxidization products under optical microscopy present a brown colour. Comparing the brown coloured region to the fatigue regions deduced from the fracture morphologies observed under SEM allowed the calculated values of the fatigue crack aspect ratio evolution to be established with more confidence.

In Figure 4- 27(b), crack $SP0_i$-3 was also identified at the bottom of a dimple even at 5000 cycles, therefore it is likely that this crack pre-existed from the shot peening process. This pre-existing crack propagated very slowly, and it did not change significantly between 5000 cycles and 22000 cycles, as indicated. The crack morphology on the fracture surface under optical microscopy as well as SEM observation is shown in Figure 4- 30. The crack morphology of crack $SP0_i$-4, $SP0_i$-5 and $SP0_i$-6 at different fatigue stages are

illustrated in Figure 4- 31(a) and (b). Similarly to crack $SP0_i$-3, both crack $SP0_i$-4 and $SP0_i$-5 also appeared on the fracture surface at around 5000 cycles, and then they propagated slowly perpendicular to the maximum tensile stress direction. Based on the fracture surface observation by optical microscopy, heat-tinting of an elliptical fatigue area indicated that crack $SP0_i$-4 is a single fatigue crack, but in the SEM micrograph, a ratchet mark is observed clearly in this area (in Figure 4- 26 (a) and (b)), indicating there could be more than one crack within the fatigue area. The replica record of the top surface showed that there are two independent cracks within this fatigue region. The other crack, which is labelled as crack $SP0_i$-4-a in Figure 4- 31(a) appeared at around 10000 cycles. It seems that this crack had not coalesced with crack $SP0_i$-4 when the fatigue test was interrupted, or at least they have not at the surface level, but there is still no convincing evidence to show whether these two cracks were already one crack beneath the surface. Based on the fracture surface under the optical microscope in Figure 4- 32, the heat-tinted fatigue area of crack $SP0_i$-4 and $SP0_i$-5 overlap each other. This morphology is in accordance with the replica observation. At 20000 cycles, there was still a significant distance between the tips of crack $SP0_i$-4 and crack $SP0_i$-5, and then the tip of crack $SP0_i$-5 moved forward gradually and joined with crack $SP0_i$-4 at 22000 cycles, as shown in Figure 4- 31. A possible subsurface crack initiation site is observed on the fracture surface of crack $SP0_i$-4, as shown in Figure 4- 33(a) and (b), the arrows indicate the crack propagation direction. However, this smooth region could also be an artefact remaining from breaking open this crack. The possibility of subsurface initiation phenomenon requires further research.

Based on the fracture surface examined by both optical microscopy and SEM shown in Figure 4- 34, there should be several initiation sites in the crack $SP0_i$-6 fatigue region. This is confirmed from the replica analysis where, cracks $SP0_i$-6-A, $SP0_i$-6-B, and $SP0_i$-6-C, indicated in Figure 4- 31(b) are found. These three cracks initiated separately and at around 20000 cycles, they coalesced and then formed crack SP1-6. Since this crack results from the coalescence of three small cracks, its crack shape is relatively shallow, as shown in Figure 4- 34.

Due to small size (only 60 μm in surface length), it is difficult to pick out crack $SP0_i$-7 in the optical microscope or on the overall fracture surface SEM

micrograph. Hence, crack $SP0_i$-7 was only analysed at high magnification under SEM, shown in Figure 4- 35. Based on the crack morphology on the fracture surface, crack $SP0_i$-7 appears to be a coalescence crack (from crack $SP0_i$-7 (a) and $SP0_i$-7(b), as indicated in the figure). A clear distinction between fatigue damage and brittle fracture has been captured; on the micro-scale the brittle fracture area is faceted, while the fatigue damage area is much smoother.

#### 4.3.1.3 Interrupted heat-tinting fatigue test on T1 shot peened sample

The fatigue regions on the T1 shot peened samples were not revealed as clearly by optical microscopy following heat tinting as they were for the T0 case, see Figure 4- 36, where the expected "brown" fatigue regions are not clearly recognizable. However, the fatigue regions, such as those designated region 1, region 2, region 3, and region 4 were clearly captured by SEM in Figure 4- 37. The less intense shot peening process (T1) exhibits the features of early fatigue crack initiation and propagation behaviour seen in both the polished (baseline) and T0 case. Cracks initiating from inclusions (typical for the polished case) or shallow cracks (for T0) are easily identified on the fracture surface. For example, inclusions are present in the central fatigue regions of crack $SP1_i$-1 and $SP1_i$-2 in Figure 4- 38 and crack $SP1_i$-3 and $SP1_i$-4 in Figure 4- 39. For crack $SP1_i$-5 and crack $SP1_i$-6 (in Figure 4- 40), no inclusions are seen but ratchet marks are visible. Apparently, crack $SP1_i$-7 is formed by two different cracks, designated crack $SP1_i$-7a and crack $SP1_i$-7b, as illustrated in Figure 4- 41. Crack $SP1_i$-8 also tends to coalesce with crack $SP1_i$-7. Crack $SP1_i$-9 and crack $SP1_i$-10 in Figure 4- 42 are two examples of small shallow cracks.

#### 4.3.1.4 Early fatigue crack evolution in U-notched sample

As described in section 4.2.1 and 4.2.2, a surface fatigue crack which was open to the atmosphere allowed oxidation of the crack faces to occur during the heat tinting process. The distinction between the fatigue and brittle failure region was apparent under SEM observation, since the brittle fracture area is more faceted, while the fatigue area is relatively smooth.

It should be noted that the crack shape revealed on the fracture surface by the heat-tinting test is not always the actual crack shape, especially when crack

coalescence has taken place. As illustrated in Figure 4- 43, there are three different possible prior crack positions that could be attributed to the same apparent crack morphology revealed by heat-tinting on the fracture surface. The first position is where the crack tips of crack 1 and 2 are closely aligned and coalescence occurred without much deviation and here only a faint (or no) ratchet mark within the fatigue region will be present. Thus the crack shape indicates a single crack. In Figure 4- 43(b), crack 1 and 2 coalesce but are out of plane with each other, so a more 3D coalescence event occurs where the coalescence region is not at the crack tips, but perhaps between the tip of crack 2 and some point on crack 1. In Figure 4- 43(c), crack 1 and crack 2 have not actually coalesced. Their crack paths remained parallel to each other during fatigue and apparent coalescence between crack 1 and crack 2 occurred when the specimen was broken open artificially after heat tinting. Therefore, the crack shape presented on the fracture surface in this situation was also analogous to the other two situations (type a and b). Typically, type (a) is an idealised coalescence event, which is rarely observed. However type b and c happen more frequently and almost all the coalesced cracks observed in the current research belong to these two types. All the coalesced cracks of type (b) or type (c) were simplified to the idealised type (a) situation when calculating the crack aspect ratio in the current research.

The cracks identified on the fracture surface of the polished samples after the fatigue test was interrupted at 18292 cycles (about 65 ~ 75 % of the fatigue life based on the previously established S/N curve), were still quite small and individual, no apparent crack coalescence was observed. The longest crack found in this specimen is ~ 700 μm (measurement based on the fracture surface). Crack shapes were semi-elliptical or near semi-circular; within the central fatigue region, aluminium oxide stringers or MnS were revealed clearly, and are likely to be the crack initiation sites.

However, early crack behaviour in the T0 shot peening condition was quite different. This was probably due to the complex surface condition associated with local plastic deformation as well as the residual stress distribution. The fatigue process was interrupted at 36163 cycles (60 ~ 70 % of the established fatigue life). The fatigue cracks were very shallow; ratchet marks appeared in the fatigue region indicating that crack coalescence between short cracks had already occurred at this fatigue stage, and also there were several crack

initiation sites, but these were not from inclusions. However, in the less intense shot peening process (T1), early fatigue crack initiation and propagation behaviour exhibits the features of both the polished (baseline) and T0 case.

Murakami proposed [17, 18] that the effect of crack shapes and sizes on fatigue strength may be correlated with stress intensity factors, especially with the maximum stress intensity factor along the three-dimensional crack front. Therefore, a geometrical parameter equivalent crack area was proposed and the estimation of the equivalent crack √area for irregularly shaped cracks was detailed in [17-19]. Figure 4- 44(a) illustrates the difference between the real surface crack length $2c$ and the projected surface crack length $2c_{project}$. In the present study, the crack length, $2c_{project}$, can be measured from the fracture surface after the interrupted fatigue test. The crack morphology during the fatigue process was not only dependent on microstructure, but also varied with load/stress condition. To obtain the crack aspect ratio *a/c*, one possible way is to measure the surface crack projected length $2c_{project}$(based on the observation of the crack shape on the fracture surface), as well as the crack depth *a* (from the top surface to the greatest depth of the crack shape) measured manually. However, from the micrographs on the fracture surface taken by optical microscopy or SEM observation, it can be seen that the crack shape is generally not regular and these fluctuations will sometimes lead to significant variability in the crack aspect ratio results if the crack depth *a* is measured manually as above. So this definition of *a/c* was not considered sufficiently representative. If all the cracks in the present investigation are considered to be semi-elliptical, then crack aspect ratio *a/c* can be derived more systematically and consistently by calculating "*a*" from the measured surface crack length $2c_{project}$ and the total measured fatigue crack area, *A*, by assuming that the crack has an approximately semi-elliptical shape. Hence:

$$½ \pi a c_{project} = Area_{semi-ellipse} \qquad \text{Equation 4- 2}$$

The relationship between this equivalent crack depth (obtained from the surface crack length and fatigue area) and the actual maximum depth of the crack is shown in Figure 4- 45. It seems that the equivalent crack depth is normally smaller than the maximum measured value in all conditions. The irregular crack morphologies observed may probably explain this. Hence, from this point of view, the error or the uncertainty of estimated crack aspect ratio

*a/c* based on the equivalent fatigue area approached can be deduced (within 5%). The variation of aspect ratio (*a/c*) with surface crack length $2c_{project}$ and the crack depth *a* for both the polished, T0 and T1 shot peened samples illustrated in Figure 4- 46(a) and (b), respectively.

Generally speaking, the crack aspect ratio in the baseline test was around ~1, which was higher than that observed in the T0 shot peened case, at longer crack lengths the *a/c* ratio for the baseline condition tended to a value of 1.0. In terms of the baseline condition, for shorter cracks, *a/c* tends to be slightly higher, for example, the shortest crack identified in this case is 117 μm in length with an aspect ratio *a/c* of 1.14, whereas it is only 0.94 for the longest crack (711 μm in length, as illustrated in Figure 4- 22(b)). Thus it appears that in the early stages of crack growth the crack length in the depth direction is longer than the projected half surface crack length, indicating that the crack propagated faster in the depth direction than along the surface. It is thought that the effect of the initiation process via cracking of brittle stringers aligned normal to the notch surface produces an initially higher aspect ratio at smaller crack sizes.

However the shot peening T0 condition, gave rise to a crack aspect ratio that was initially very small, indicating a shallow crack shape. The aspect ratio tended to increase gradually as the surface crack length increased. After the aspect ratio reached its maximum value (*a/c* = 0.8), it decreased somewhat with increase of the surface crack length; this is thought to be due to frequent crack coalescence. The effect of shot peening on aspect ratio can be seen more clearly if *a/c* is plotted against crack depth, as shown in Figure 4- 46 (b). The depth where the aspect ratio reaches the maximum value of *a/c* was ~ 120 – 150 μm, similar to the position of the maximum compressive residual stress (~150 μm, as shown in Figure 3-15) and/or the depth of the shot peened plastic deformation layer (~160 μm, as can be seen in Figure 3-19 for the T0 shot peened condition. This shallow crack shape indicated that the crack growth rate in the depth direction (i.e. growing into an increasing compressive residual stress field) was actually slower than the growth rate at the surface.

In the less intense shot peening case (T1), both microstructure and the shot peening effect played an important role in fatigue crack shape evolution. The crack morphology aspect ratio evolution shows features of both the polished

(baseline) and T0 shot peened cases: some of these aspect ratios fall into the data cluster for the polished condition while the others fit well with aspect ratios of the T0 condition.

### 4.3.2 Heat tinting test after interrupted fatigue process on plain bend bar samples

To further study early fatigue crack morphologies, the present study also conducted heat-tinted tests on plain bend bar sample after an interrupted fatigue test. Both the PBB polished and shot peened conditions underwent fatigue testing under the same strain range condition (0.68 %). In three-point bending of a U notched sample, the maximum stress level region is a line across the bottom centre of the U-notch; however, during four-point bending, the maximum stress level region in the plain bend bar samples tested is 10 mm wide, which indicates that fatigue cracks can occur anywhere within this maximum stress region during fatigue testing.

#### 4.3.2.1 Interrupted fatigue test on PBB polished samples

For the PBB polished condition, the sample was removed from the fatigue test rig after 5700 cycles. Figure 4- 47(a) is an optical micrograph of the top surface PBB polished sample after an interrupted heat-tinting fatigue test while Figure 4- 47(b) shows the optical micrograph of the fracture surface. Although a few fatigue cracks can be seen on the surface in the maximum stress region, only one single fatigue cracked region is clearly identified from the fracture surface. An inclusion stringer, which is in the central part of the fatigue region, is quite long (more than 2 mm based on the fracture surface) and clear even under optical microscopy. As shown in Figure 4- 48(a), the fatigue region is in the shape of a “funnel, which is parallel to the inclusion stringer. Although the crack length on the surface is only 587 μm, the fatigue area is still obvious in the region near the stringer even at 1125 μm beneath the surface. Figure 4-48(b) is the fatigue region labelled in Figure 4- 48(a) and the EDS results given in Figure 4- 48(c) indicate that the inclusion contains Al and Si, which acts as the fatigue crack initiation site. The morphology of this crack after various fatigue cycles is given in Figure 4- 49. It can be clearly recognized at around 3300 fatigue cycles. The inclusion can also be seen in the central region of the crack. As the fatigue process continues, the crack length increases gradually.

#### 4.3.2.2 Interrupted fatigue test on PBB shot peened samples

The fatigue test for the PBB T0 shot peened sample was stopped at 4000 fatigue cycles due to the sudden appearance of a long crack. The optical micrograph of the top surface and the fracture surface are illustrated in Figure 4- 50(a) and (b), respectively. An inclusion stringer which is parallel to the top surface of the sample is visible. Even though the fatigue test was stopped at only 4000 cycles, the fatigue region is larger than that observed in the PBB polished sample (where the fatigue test under the same strain range condition was interrupted at 5700 cycles). As shown in Figure 4- 51(a), the length of the stringer is ~ 3100 μm and it appears at ~ 300 μm beneath the shot peened surface. The total depth of the fatigue region is about 1000 μm. Figure 4- 51(b) shows the inclusion highlighted in Figure 4- 51(a) and the EDS results in Figure 4- 51(c) indicate again the presence of an alumina stringer. Figure 4- 52 shows the crack morphology after various fatigue cycles. At 2750 cycles, no obvious crack was observed clearly on the rough shot peened surface. However, after only 250 more fatigue cycles, an indication of a fatigue crack appeared on the surface, as indicated by the arrows. However, this crack opened quickly after another 1000 fatigue cycles. This indicates that this is a subsurface initiated fatigue crack.

### 4.3.3 Crack morphology studied by serial sectioning

In Section 4.3.1 and 4.3.2, the fatigue crack shapes have been revealed by heat-tinting in both U-notched and PBB samples followed by cryogenic fracture and crack aspect ratios have been obtained based on the crack shapes observed (in notched samples). As mentioned in Section 4.3.2, only the cracks that have formed the final fracture plane can be studied by this methodology. The fatigue crack behaviour of shot peened samples have been studied widely [9, 12, 20], but little research has focused on the evolution of the 3D fatigue crack morphology within the shot peening affected zone. Therefore, 3D crack morphologies were studied by serial sectioning of polished and T0 shot peened samples (in Section 4.3.3) and the 3D crack shapes in T0 and T1 shot peened samples will be presented in Section 4.3.4.

To simplify description in the present study, cracks which appeared on polished samples on the mechanically prepared serial sections will be

identified as $P_s$-1, $P_s$-2, ...; similarly, cracks on the T0 shot peened sample are designated $SP0_s$-1, $SP0_s$-2, where "P" and "SP" indicate the "polished" and "shot peened" condition, respectively, "0" means the "T0" process, and the subscript "s" represents serial sectioning.

#### 4.3.3.1 Crack morphology in polished samples

Figure 4- 53, of a fatigue tested polished sample, shows crack $P_s$-1(a) and $P_s$-1(b) revealed at different depths and thus illustrates the evolution of crack morphology in the polishing direction (the z direction). For both crack $P_s$-1(a) and $P_s$-1(b), the crack paths seem to be related to the positions of MnS inclusions. The distribution of MnS inclusions on the crack path indicated that they were the crack initiators. Figure 4- 54 shows the 3D fatigue crack reconstruction based on the 2D images of cracks $P_s$-1(a) and $P_s$-1(b). The crack discontinuities in the z direction are due to the intermittent nature of the polishing process itself, but the general 3D crack morphology is revealed. The crack region and inclusions are indicated as blue and red in crack $P_s$-1(a), and green and orange in crack $P_s$-1(b), respectively. The MnS stringers are discontinuous in the *z* direction (the rolling direction), which also agrees with observations on a fracture surface after an interrupted fatigue test, followed by heat tinting and breaking open of another specimen [21]. Due to the effect of the inclusions, the crack paths of cracks $P_s$-1(a) and $P_s$-1(b) are very tortuous in terms of both their 2D and 3D morphology.

The crack grouping $P_s$-2 is from the same sample but a different crack and again shows the effect of MnS on the fatigue crack morphology, Figure 4- 55 and Figure 4- 56. The green and red regions represent crack regions, while the purple and red regions are MnS stringers. This crack seems to be a single crack, judging from the serial 2D sections when the material removal was less than 120 μm, however, this single crack became two different cracks at a depth of ~ 126 μm. These separated cracks were more apparent at a depth of 136.5 μm. Three cracks which clearly initiated from inclusions were found at ~ 235 μm below the notch root. It seems that the inclusions (MnS) dominate the crack path, in both surface and depth crack growth directions. However, for crack $P_s$-3, only one single stringer (alumina) dominates the crack morphology; the 2D crack images at various depths and the 3D crack reconstruction are shown in Figure 4- 57 and Figure 4- 58, respectively. The stringer is in the central part

of the crack region, and seems to be the crack initiator. This is also consistent with those cracks observed in heat tinted and subsequently broken open interrupted fatigue tests reported in [21]. Crack $P_s$-3 is less tortuous than crack $P_s$-1(a), $P_s$-1(a), $P_s$-2, as the alumina stringer is the dominant crack initiator.

#### 4.3.3.2 Crack morphology in T0 shot peened sample

Figure 4- 59 shows the 2D images of crack $SP0_s$-1 at selected depths in the T0 shot peening condition and the 3D crack reconstruction is presented in Figure 4- 60. Crack $SP0_s$-1 is actually formed from 5 different cracks, denoted as cracks $SP0_s$-1(a), $SP0_s$-1(b), $SP0_s$-1(c), $SP0_s$-1(d), $SP0_s$-1(e).These five cracks appear to be individual cracks when observed via the conventional replication technique applied to the shot peened surface. The surface crack lengths of these cracks are 347, 415, 385, 181 and 341 μm respectively. However, as the shot peened layer was polished off, at 0.76 μm beneath the surface, crack tips were more clearly identified and when the polishing depth was 36 μm, the crack tips of SP0s-1(a) and SP0s-1(b) actually interacted with each other—the tendency to coalescence was apparent. From a depth of around 192 μm, cracks SP0s-1(a) and SP0s-1(b) had coalesced completely and at ~ 220 μm beneath the surface, crack $SP0_s$-1(a) $SP0_s$-1(b), $SP0_s$-1(c), became a single crack, denoted as crack $SP0_s$-1(abc). It is noteworthy that the crack tips of cracks $SP0_s$-1(c) and $SP0_s$-1(d), cracks $SP0_s$-1(d) and $SP0_s$-1(e) are starting to interact with each other, as indicated in Figure 4- 59, but these interactions have just started at the point when the fatigue process was interrupted.

In the present study, observation of sub-surface coalescence for the crack system $SP0_s$-1(abc) is not the only example found in the T0 shot peened condition. Figure 4- 61 shows the 2D section images of crack $SP0_s$-2, where sub-surface crack coalescence was also identified. Initially, crack $SP0_s$-2 was actually two individual cracks on the shot peened surface, labelled as cracks $SP0_s$-2(a) and $SP0_s$-2(b), respectively; after 0.76 μm of material was polished off, the crack morphology as well as the shot peened surface roughness was more clearly revealed. Complete crack coalescence occurred at a depth between 150 ~ 160 μm. As the polishing process continued, the crack shape became more tortuous, which might indicate the point at which the microstructure is affecting crack growth. For example, at ~ 600 μm beneath the shot peened surface, the crack morphology was quite tortuous, as can be

seen in both the 2D image slices (Figure 4- 61) and the 3D reconstruction crack morphology (Figure 4- 62). Compared to the cracks observed in the baseline test condition, the crack shapes in the shot peened condition are less tortuous and less inclusion or stringer-dominated.

### 4.3.4 Crack morphology in X-ray tomography

Due to the intrinsic limitation of the tomography technique, high spatial resolution depends on various factors especially the thickness of the sample, which has to be as thin as possible to avoid lateral spreading of the signal when a photon impinging on the screen is turned into visible light [22]. Therefore, the volume under investigation in the present study had to be limited for both the T1 and T0 shot peened conditions. In a similar manner to before, cracks in the T0 and T1 shot peened condition will be designated $SP0_x$-1, $SP0_x$-2,..., and $SP1_x$-1, $SP1_x$-2, where "SP" represents shot peened condition, "0" and "1" indicated T0 and T1 process, respectively, and the subscript "x" represents X-ray computed tomography imaging.

#### 4.3.4.1 T1 shot peened sample

Crack morphologies obtained by X-ray tomography in the T1 shot peened condition are presented in Figure 4- 65. The crack loading directions (the tensile axis) are indicated by the arrows. T1 shot peening was a less intense process, and the dimples induced on the sample surface were not as obvious in the cross sectional view of the notch geometry; the shot peened dimples are very shallow, as indicated in Figure 4- 63(a). The stringers overlap with the fatigue crack, labelled as crack $SP1_x$-1, so for the lighter shot peening condition (T1), inclusions actually acted as the crack initiation sites (as observed in the polished baseline case). This agrees with previous results which showed that the fatigue crack initiation and propagation behaviour under the less intense shot peened condition exhibits features of both the unpeened and more intensely shot peened cases. Figure 4- 63(b)-(f) illustrate how the crack morphology changes at different depths ($d$ = 20, 43, 112, 203, 417 μm). The inclusions are clear at this series of different depths. To visualize the fatigue crack morphology, the 3D crack reconstruction is presented in Figure 4- 64. The fatigue crack has been highlighted in blue while the inclusion is red. Generally, the crack shape was somewhat discontinuous, and

the crack tips were also irregular. The discontinuous nature of the fatigue crack can be partly explained by resolution issues and possible partial closure of the crack as well as the expected fatigue crack behaviour; the nature of the crack was similar to the crack morphology revealed on the fracture surfaces in previous heat-tinting and fractured interrupted fatigue tests. However, it is still apparent that this is a semi-elliptical crack and one of the inclusions is clearly located in the crack centre region. In addition, another two inclusions were also found in the volume studied but they did not seem to affect the fatigue crack shape, as the effects of shot peening dominate crack behaviour.

#### 4.3.4.2 T0 shot peened sample

The fatigue cracks studied by X-ray tomography in the T0 shot peened condition had undergone 34550 fatigue cycles (65 – 75 % of the established fatigue life). Figure 4- 65(a) presents a single XY slice of the cross section of fatigue crack $SP0_x$-1(a) and $SP0_x$-1(b) in the T0 shot peened condition, where the relation between crack path and tensile axis (TA) is clearly illustrated. The rough geometry of the shot peened surface is quite clear: Figure 4- 65(a) shows, the shot peened dimples are larger than those observed in the less intense shot peened condition T1 (in Figure 4- 63(a)). Interestingly, crack $SP0_x$-1(a) and crack $SP0_x$-1(b) were two separate cracks in the cross section view; when the depth from the shot peened surface reached ~ 200 μm, a clear tendency for these cracks to join was noted. Figure 4- 65(b)-(f) illustrate how the fatigue crack morphologies in the T0 shot peened condition change along the depth direction (z direction). To simplify the discussion, the fatigue cracks recognized on the top surface were identified as fatigue crack $SP0_x$-1(a), $SP0_x$-1(b), $SP0_x$-1(c), respectively. At 9 μm beneath the shot peened surface, these three fatigue cracks were clearly separated; as the depth increased, there was a sign that the crack tips of $SP0_x$-1(a) and $SP0_x$-1(b) moved toward each other gradually. At a depth of 173 μm, crack $SP0_x$-1(a) and $SP0_x$-1(b) coalesced and the crack morphology at a depth of 277 μm made this phenomenon more apparent. Although there was an indication that the crack tips of $SP0_x$-1(b) and $SP0_x$-1(c) also tried to coalesce sub-surface (at around 180 μm beneath the surface), there is insufficient evidence due to the resolution issue as well as the noise ahead of the crack tips. Therefore, definite conclusions about the sub-surface crack coalescence of cracks $SP0_x$-1(b) and $SP0_x$-1(c) cannot be drawn. However, the sub-surface crack coalescence captured for crack $SP0_x$-1(a) and

crack $SP0_x$-1(b) agrees well with the results from the serial sectioning examination. In Figure 4- 65(f), an inclusion was found about 160 μm away from the fatigue crack path on the top surface view. The corresponding cross section view is shown in Figure 4- 65(g). Although the inclusion stringer seemed close to the fatigue crack path, it did not actually interact with the cracks, indicating that the inclusion has little effect on the fatigue crack behaviour/shape in the T0 shot peened condition. 3D reconstruction of the fatigue cracks and inclusions in the T0 shot peened condition are presented in Figure 4- 66 at different angles of view. The reason why the 3D crack shapes here are not typically semi-elliptical is because only the crack tip regions have been scanned due to the requirement for a small match stick extraction. However, sub-surface crack coalescence has again been captured in the T0 shot peened case.

## 4.4 Discussion

### 4.4.1 Early fatigue crack evolution in U-notched samples

For many engineering components and structures, short fatigue crack behaviour controls the majority of total fatigue life. A number of researchers have reported that these short cracks propagate much faster than long cracks under equivalent stress intensity factor ranges ($\Delta K$). Conventionally, small crack data analysis approaches employ secant or polynomial data reduction, assuming small crack shapes are semi-circular ($a/c$ = 1, where $a$ is the crack depth and $c$ is half the surface crack length). However, the results of Ravichandran's study [23, 24] strongly indicate that some of these apparent characteristics of small cracks, often referred to as anomalous, are in fact partly due to the assumption that $a/c$ = 1. He found that allowing for the lower levels of crack closure found naturally in small cracks, and for the $a/c$ variations in $\Delta K$ calculations, the scatter in the growth data of small cracks was significantly reduced and was found to be of the same order as in large cracks. In the present study, it is also noteworthy that the crack aspect ratio varies with crack length $c$ (and, ergo, also crack depth $a$). The change of aspect ratio in the shot peened condition is especially obvious, varying between 0.38 and 0.83 for T0 and T1, while it is more consistent between 0.9 and 1.2 in the polished notch condition. Therefore, it is necessary to consider the aspect ratio

evolution when analysing fatigue crack initiation and propagation behaviour in terms of the crack tip stress intensity factor.

Generally, the crack aspect ratio in the polished notch condition was found to be larger than in the shot peened condition. In the former case, cracks were quite deep even when surface crack lengths ($2c$) were only around 100 μm. As the crack length increased, the crack aspect ratio moved closer to $a/c = 1$, which indicates the "expected" semi-circular or near semi-circular crack. Since the notch surface was well polished, the crack initiation and propagation behaviour was mainly dependent on the specimen geometry (i.e. occurring in the notch root), material microstructure, as well as the loading conditions. Material microstructure played an important role in fatigue crack initiation and propagation. Alumina and MnS are two of the most common non-metallic inclusions present in steel, and these stringers can be clearly identified in the present study. Since in this study, the fracture surface (crack plane) is actually parallel to the longitudinal direction where these stringers are distributed, in the baseline conditions, these stringers tended to be favoured crack initiation sites. The cracks initiated along the brittle aluminium oxide stringers or inclusions, which were either on the surface or slightly beneath the surface. Since the stringers are in the longitudinally aligned direction, which is parallel to the crack depth direction, at the very early fatigue stage, those fatigue cracks initiated at stringers (or inclusions) were encouraged to propagate in the depth direction, due to the higher stress intensity around these elongated, brittle and mechanically mismatched inclusions. So the initiating inclusion position and shape will strongly affect the initial fatigue crack morphology leading to an initially larger crack aspect ratio (around 1.2). As the crack propagated, the range of stress intensity factor around the initiation sites became less dominant and the crack grew to the more expected equilibrium shape, where the stress intensity factor at both the crack surface and depth are the same.

Whilst in the less intense shot peening process (T1), the effect of these inclusions was still significant, more intense shot peening (T0) overcame the microstructure dominated initiation process as evidenced by inclusions being seldom found in the fatigue region. The crack aspect ratio in the shot peening case initially increased with increasing crack depth $a$ in the range where $a$ was smaller than 120 ~ 150 μm. After that point, the crack aspect ratio actually

decreases from 0.8 gradually. Similar results were also found in Mutoh's research [20]. A reduction in crack aspect ratio was observed whereby the ratio of crack surface length to depth was higher in peened samples compared to unpeened samples of a high strength aluminium alloy. In discussing the different trends of crack aspect ratio in unpeened and peened samples, three important mechanical effects, namely surface roughness, local plastic deformation, as well as the compressive residual stress must be considered, as discussed extensively in a recent review by Soady [13].

Generally, the surface roughness is detrimental to fatigue life while the strain hardened layer and residual stress effects are beneficial. Fatigue cracks tend to initiate at the dimple regions due to the crack-like regions and the shot peened lips induced due to the severe plastic deformation during the peening process. In addition, these dimples are likely to act as a stress concentrator. In this case, almost all the cracks initiated from the surface with no clear evidence of subsurface crack initiation. Hence the initial crack may have a longer crack length on the shot peened surface compared to that produced in the polished notch condition. These cracks tended to propagate along the surface direction rather than the depth direction when the crack tip process zone is within the shot peened affected zone; the depth of crack at which it achieves "normal" *a/c* ratio is around 120 ~ 160 μm, which is comparable to the depth of maximum residual stress layer (150 μm in T0 shot peened condition) and plastic strain hardening layer (~ 150 μm in T0) [13]. The strain hardened layer and the compressive residual stress distribution beneath the surface may significantly reduce crack propagation in the depth direction in the early fatigue stage. As the crack front grows within this region, the residual stresses are expected to redistribute. Once it breaks through these shot peened affected regions, crack growth in the depth direction becomes faster. This explains why the smaller cracks are shallow (low *a/c*) in shot peened samples.

A Linear Elastic Fracture Mechanics (LEFM) calculation of *K*-equilibrium around the crack front was conducted based on Scott and Thorpe's review paper [20]. A local stress level ($\Delta\sigma_{11}$) of 1500 MPa in the loading direction was used in calculating the short crack $\Delta K$ levels in the notch root. This stress range was estimated using finite element modelling, implementing an isotropic hardening model based on the monotonic tensile data obtained in the direction perpendicular to rolling. Assuming a notional crack in the polished condition

(not considering the shot peening effect), its crack shape area A is fixed, the crack depth a at varying crack aspect ratio *a/c* (*a/c* = 0.1, 0.2, 0.3, …, 1.8, 1.9, 2.0) can be obtained. The variation of $\Delta K_{surface}$ and $\Delta K_{depth}$ for cracks with the same fatigue area but different *a/c* ratios is illustrated in Figure 4- 67(a). At low aspect ratios, the expected *K* in the depth direction is greater than that at the surface; whilst at a high aspect ratio the expected *K* in the surface direction is greater than that in the depth direction when *a/c* is 0.8, $\Delta K_{surface}$ and $\Delta K_{depth}$ are in equilibrium. This is consistent with the experimental crack aspect ratio evolution, where the aspect ratio (~0.8) was achieved in both the baseline and shot peening tests once the crack had grown away from the effect of microstructural initiation and the shot peened affected layer respectively.

In fact, the equilibrium *a/c* also varies with absolute crack size. But it is a challenge to unambiguously characterize this feature through these interrupted fatigue tests, since when the crack length 2*c* is longer than 1000 μm, the fatigue test is in the last stages of fatigue life and crack coalescence events are happening frequently and affecting the aspect ratio measurement for differing reasons. In Figure 4- 67(b), the characterization of the change of equilibrium *a/c* at different surface crack lengths was based on the assumption of isolated individual cracks with different surface crack length 2*c* (50, 100, 200, 500, 1000, 2000 μm). When the surface crack length 2*c* is no more than 500 μm, the equilibrium *a*/*c* is 0.8, as is the case in observations from the interrupted fatigue test cases. However, as the surface crack length increases, this equilibrium value decreases gradually, for example, $a/c_{equilibrium}$ is 0.75 at 1000 μm while it drops to 0.52 if the surface crack length 2*c* is 5000 μm. This trend is expressed as equation *g(x)* in Figure 4- 68(a) and (b), which shows the evolution of crack aspect ratio in both non-peened and shot peened conditions. In the polished and ground case, the evolution of *a/c* will be given by equation *k(x)* when crack length $2c \leqslant 2065$ μm, while equation *g(x)* will be applied to describe *a/c* if the surface crack length $2c > 2065$ μm. While for shot peened cases, equation *f(x)* describes the trend of crack aspect ratio when $2c \leqslant 289$ μm and equation *g(x)* is the appropriate one for cracks longer than 289 μm.

Frequent crack coalescence is also closely related to the development of the aspect ratio of short cracks. As the fatigue process continues, two or three (or

even more in the shot peened case) cracks are likely to coalesce due to the mulitiplicity of crack initiation sites and these combined cracks become one single crack. This larger crack is therefore shallow, so the aspect ratio is decreased after crack coalescence, resulting in lower *a/c* values at longer crack lengths (as observed).

### 4.4.2 The effect of stringers on fatigue behaviour in PBB samples

Microstructure plays an important role in early fatigue crack behaviour in U-notched samples. As mentioned in Section 4.3.2, the region of the maximum stress in the PBB is much larger than that in U-notched samples. In the polished PBB samples, a few cracks were observed to initiate from the inclusions, but only one fatigue region with a deep alumina stringer was revealed on the fracture surface. Similarly, in the shot peened conditions, only one fatigue region appeared on the fracture surface; however, the stringer orientation was parallel to the shot peened surface, which was different from that on the polished condition. From the morphology of the fatigue region on the PBB T0 shot peened fracture surface, the stringer was the subsurface crack initiator. The position of the inclusion was ~ 300 μm beneath the shot peened surface, where the benefit from shot peening was slight since strain hardening and compressive residual stress vanish gradually at this depth. The orientation, as well as the position and size of the stringers will strongly affect fatigue crack growth in both the baseline and T0 shot peened condition.

### 4.4.3 3D crack morphologies

#### 4.4.3.1 Crack morphology

To the best of the authors' knowledge, there has been to date little information available in the literature on how the 3D fatigue crack morphology is affected by the shot peened layer. In the present study, 3D crack shape reconstruction was conducted by serial sectioning and X-ray tomography. The cracks tips are not continuous. This is in agreement with previous research on 3D shape and propagation of fatigue cracks in a titanium alloy by CT imaging with ultra-bright synchrotron radiation [25]. Crack shape discontinuity occurs due to the interaction between grains, load condition, and stress condition.

The overall benefit of shot peening on fatigue behaviour is due to a complex interrelation of the effect of increased surface roughness, the compressive residual stress distribution in the surface as well as the work hardened layer. Due to the more intense shot peening process, the T0 condition has a rougher surface than the T1 condition. Mutoh et al. claimed that surface roughness produced by the shot peening process in an Al alloy contributed to the shorter crack initiation lives found when compared with the unpeened samples; the initial fatigue cracks were always sited at stress concentrations on the rough peened surface, especially the fold-like defects at a region of intense surface folding [4].

Compressive residual stress can significantly reduce the fatigue crack propagation rate [26]. Interestingly, Mutoh et al. found that the point at which the smallest crack growth rate is found roughly corresponded to the point of maximum compressive residual stress; the lower value of the crack aspect ratio in shot peened samples is the result of the sub-surface compressive residual stress caused by shot peening [4]. The decrease in the crack aspect ratio in the peened specimen in the surface layer is caused by the fact that the source of the crack in the peened specimen is always sited at a region of intense surface folding and the initial crack has a larger crack length on the surface [4].

It is well known that non-metallic inclusions are stress raisers and can initiate fatigue cracks. The MnO-SiO-$Al_2O_3$ family of inclusions in high strength steel is well known to be detrimental to fatigue properties while MnS stringers play a less dominant role (after [27]). The initiation of cracking at inclusions can be considered as occurring via three different possible processes: namely a slip band crack emanating from a debonded inclusion, the inclusion cracking due to impingement of slip bands and a slip-band crack emanating from an uncracked inclusion; the first normally occurs in high strength steels while the second and third mechanisms are typically observed in Al alloys [28]. In the present study, inclusions (Alumina/MnS) are the preferred fatigue crack initiation sites in the baseline (non-peened) condition. Debonding between inclusions and the matrix was seen for both Alumina and MnS inclusions at 170 μm depth in the serial sectioning study, as indicated in Figure 4- 69 (a) and (b), respectively. The occurrence of debonding between inclusion and matrix during the fatigue process is considered to be the initial stage of crack initiation at an inclusion [27].

However, a difference between alumina dominated cracks and MnS dominated ones can be identified. In the former case, the alumina stringer is normally located in the central region of the crack (indicating it is the primary initiation site); while in the MnS initiation-dominated cracks, MnS particles are distributed along the fatigue crack path, in other words, fatigue crack growth directions in the current FV448 material were dominated by inclusions in both the surface and depth propagation directions.

In the shot peened condition, however, the fatigue crack initiation behaviour is controlled by the shot peening intensity: in the less intense shot peened condition, crack behaviour exhibits features of both the baseline and more intensely shot peened materials. The more intense shot peened condition shows no evidence of fatigue cracks initiating from inclusions in either the serial sectioning and X-ray analysis results; instead surface roughness and pre-existing small cracks from the shot peening process cause fatigue crack initiation. Due to the plastic deformation induced by the shot peening process, a thin work hardened layer is formed in the near surface layer. According to the micro-hardness depth profiles of the ground, T0 and T1 shot peened samples, the micro-hardness of the sample in the T1 condition appears to be slightly harder at a distance 50 to 65 μm beneath the surface than the polished sample. However, measurement of the Vickers hardness closer to the surface than approximately 80 - 100 μm would not give a reliable value according to British standard BS EN ISO 6507-1:2005 [29] and thus based on these measurements it is not possible to assess the extent and hardness of the work hardened layer beneath the surface in the T1 condition. However, for the T0 shot peened case, it is clear that the microhardness has increased significantly and this layer extends to around 350 μm beneath the surface. It should be noted that the extent of the strain hardened layer and the compressive residual stress distributions have also been determined for these two conditions via X-ray diffraction in previous studies [12, 13] and the extent of both the strain hardened layer and the sub-surface zone of the residual compressive stress are greater in the T0 condition, and the maximum depth of the compressive residual stress zone also extends to ~ 350 μm beneath the surface. It seems likely therefore that microhardness evaluations are affected by both the strain hardened layer and the compressive residual stress zone.

The prediction of the fatigue strength is complicated, but studies have shown that the fatigue strength of steels is usually proportional to hardness and tensile strength [30], which leads us to expect a higher fatigue strength for a slightly harder steel. Therefore, if we assume there are equivalent areas of inclusion stringers in the unpeened, less intense (T1) as well as the intense shot peened (T0) samples, and these stringers are found at the surface, sub-surface and even in the interior, the variation in fatigue strength in these three different surface layers can be described qualitatively, as indicated in Figure 4-70.

In the baseline conditions (non-shot peened), the fatigue strength is constant in the depth direction; but in the regions near the surface stringers are apt to be vulnerable to fatigue crack initiation due to the stress concentration they provide. In the less intensely shot peened condition (T1), the benefit of the slight increase in the fatigue strength in the near surface layer is limited in line with the limited improvement of hardness after T1 shot peening as well as the very thin shot peening affected layer. Therefore, the possibility of a fatigue-crack initiating from a stringer or surface defects (shot peened dimples) is similar. For the intensely shot peened condition, however, the fatigue strength improvement is strongest in the near surface layer, leading to a shallow fatigue crack shape. The inclusions in this condition therefore play a less important role in fatigue crack initiation; it is the surface roughness induced defects produced during the severe plastic deformation in the shot peening process that preferentially initiate fatigue.

However, the fatigue crack behaviour in the shot peened condition is complicated by the increased surface roughness which is detrimental to fatigue properties, and the compressive residual stress distribution that is considered to be beneficial in retarding crack propagation. Inclusions will be a more significant stress raiser in the unpeened condition, acting as fatigue crack initiators. The near-surface layer of the shot peened sample is in fact expected to undergo a complex superposition of the stress state due to the applied load with the residual stress distribution and its relaxation during subsequent fatigue; the local effects of work hardening from the shot peening may also be expected to affect this stress distribution (or the evolution of local strain). Therefore, in the less intensely shot peened condition (the T1 shot peened condition in the present study), the detrimental effect from the roughened

surface is balanced out by the benefit of the work hardened layer and sub-surface compressive residual stress distribution. Thus the probability of a fatigue crack initiating from inclusions or surface roughness is almost the same. But for the more intense shot peening condition (T0), the actual stress experienced in the near surface layer is expected to be significantly smaller than the applied stress due to stress superposition with the larger compressive residual stress distribution over a larger area. In this case, it is relatively easier for cracks to initiate on the shot peened surface (due to the pre-existing defects), but it is not easy for these cracks to propagate due to the complex interaction of the crack with the sub-surface strain hardened layer and the compressive residual stress layer. Beneath the shot peened affected zone, the fatigue strength is lower than that on the surface. Hence, fatigue cracks may be expected to propagate faster once they breakthrough the shot peened affected zone. 3-D tomography (by both serial sectioning and X-ray tomography) provides direct evidence that is unobtainable with conventional surface observations, revealing, for instance, the sub-surface crack coalescence in T0 shot peened conditions.

## 4.5 Conclusions

Three different surface conditions in notched samples have been the focus of the present study: polished and ground (as baseline conditions), T0 (industry applied shot peening process) and T1 (less intense shot peening process). The conclusions drawn are as follows:

(1) The fatigue crack aspect ratio (*a/c*) evolution in the early stages of crack growth in polished and shot peened cases was investigated. In the polished samples, microstructure (alumina stringers as well as MnS) played an important role in early crack initiation and propagation. Initially, the aspect ratio for these short cracks was around 1.0 ~ 1.2; as the surface crack length 2*c* increased, the *a/c* ratio decreased to the equilibrium aspect ratio 0.8. In the T0 shot peened case, the aspect ratio was low and increases with increasing crack depth a when $a < 120 \sim 150\ \mu m$, after which the crack aspect ratio decreased gradually (due to frequent crack coalescence). However, *a/c* evolution in the T1 sample combines the trends observed in the T0 and polished conditions. The shallower aspect ratio in the shot peened case was

linked to the greater difficulties encountered by the crack in growing sub-surface into the compressive residual stress and strain hardened layer compared to the polished case.

(2) From the 3D crack morphology it was seen that, in the unpeened sample, inclusions (alumina and MnS) play an important role in early fatigue crack behaviour. They act as stress raisers, and thus crack initiators. For fatigue cracks initiated from alumina stringers, the crack morphology normally was dominated by only one (large) stringer, which was always in the central region of the crack; while the MnS inclusions seemed to dominate/affect the crack path in both the surface and depth crack growth directions as they formed in clusters. In the less intense shot peening condition (T1), the fatigue crack morphology is similar to the baseline (unpeened) case. Cracking initiated from an alumina stringer was observed, but there was no clear evidence for subsurface crack coalescence. For the intense shot peening condition, however, inclusions do not seem to affect crack behaviour. Subsurface crack coalescence was also captured by serial sectioning and X-ray tomography at around 150 ~ 180 μm beneath the shot peened surface. This may be linked to both the extent of the compressive residual stress and the depth of the plastic deformation from the shot peening process. The shot peening process has "de-activated" the underlying metallurgical defect distribution, and substituted a surface roughness initiated defect population. Comparison with previous studies in this material under the same conditions confirms that the beneficial role of shot peening is to slow crack propagation into the depth and that the evolution of both crack aspect ratio and the occurrence of crack coalescence events in the shot peened case can be linked to the extent of the work hardened layer and the compressive residual stress field. If insufficient shot peening intensity is applied, then the underlying metallurgical defect distribution still operates, and can outweigh any (limited) effect from a very thin work hardened layer and compressive residual stress zone.

(3) In the PBB samples, not only the orientation, but also the position and size of the stringers will strongly affect fatigue crack growth in both the baseline and T0 shot peened condition.

## 4.6 Figures

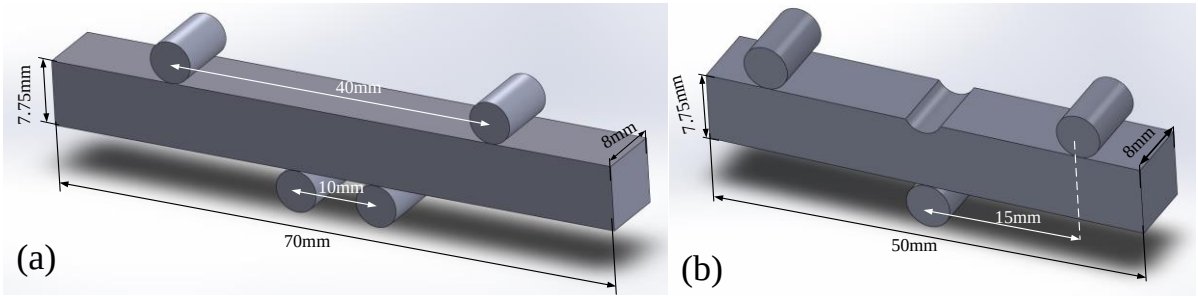


Figure 4- 1 (a)Four point bend fatigue test setup PBB sample; (b)Notched three point bend fatigue test setup.

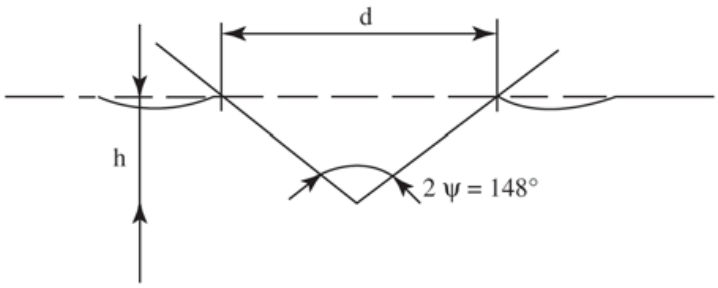


Figure 4- 2 A schematic of the relation between indentation depth *h* and diagonal *d*.

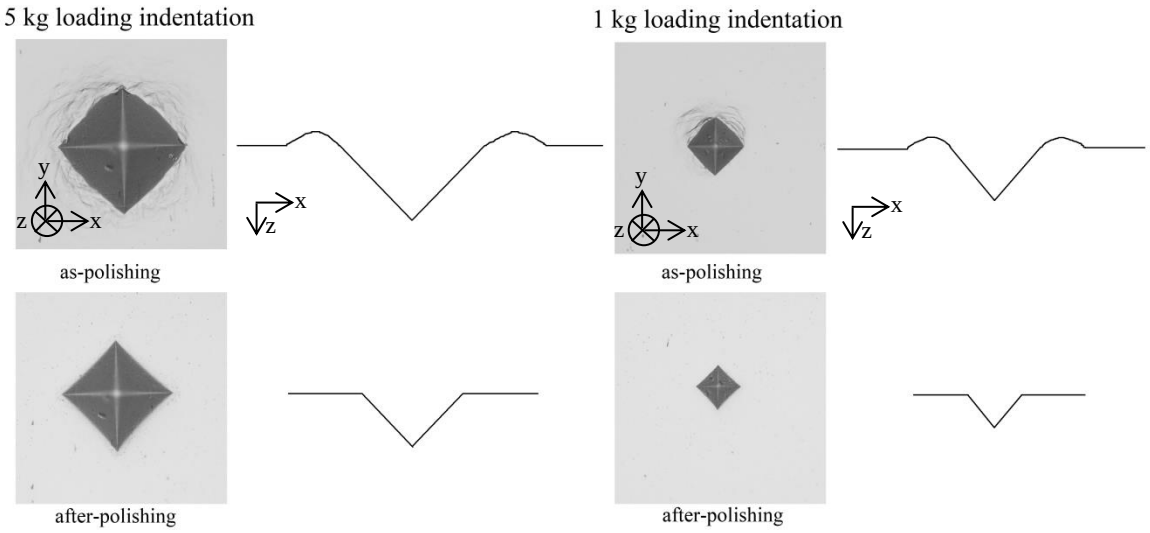


Figure 4- 3 Morphologies of indentations under different load conditions and a schematic of the pile up produced the indents.

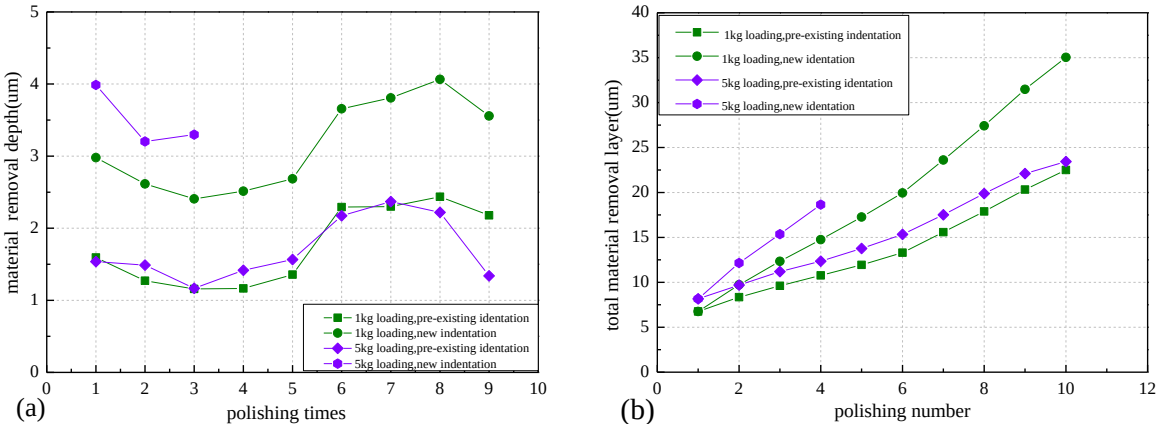


Figure 4- 4 (a) Specific material removal depth obtained by new and existing indentation markings under different loads at specific polishing times; (b) total material removal depth indicated by new and existing indentation markings under different loads as the polishing times increase.

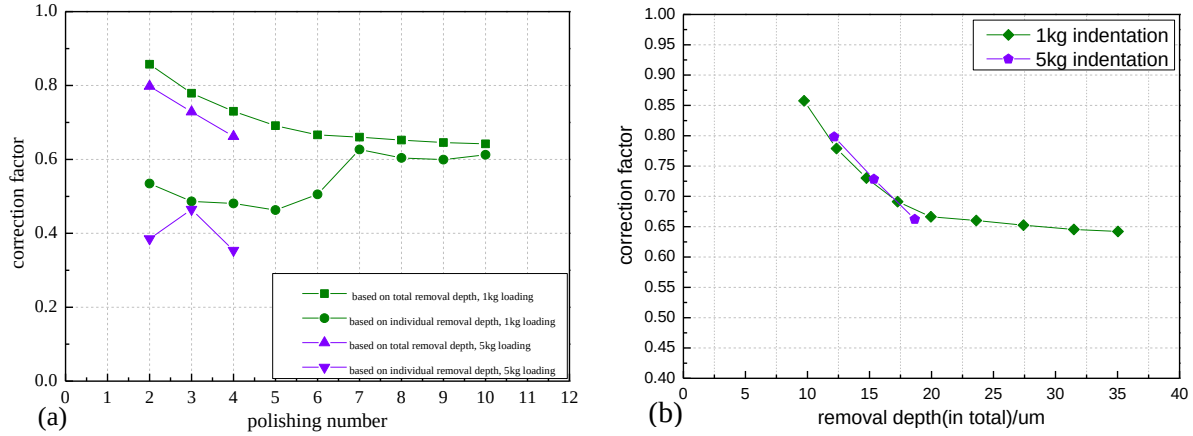


Figure 4- 5 (a) Depth correction factors based on the comparison of material removal depth obtained by new and pre-existing indentations under both 1 kg and 5 kg load; (b) depth correction factor changes with the total material removal depth.

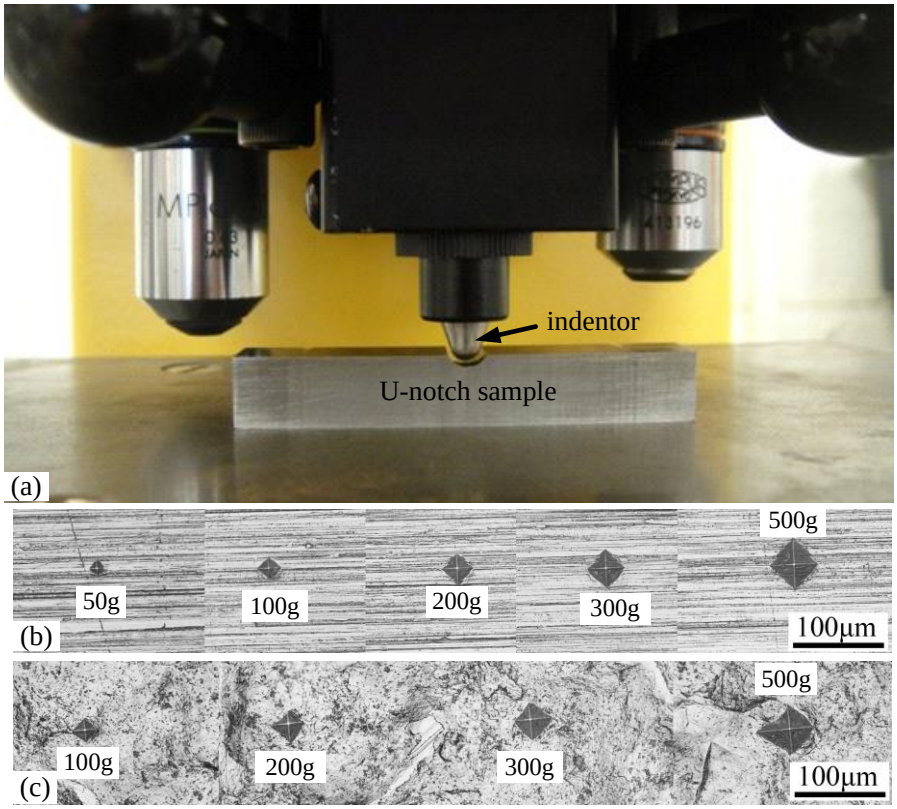


Figure 4- 6 (a) Indentation process in the notch (b) The indentation morphologies produced under varying loads for a 15 s dwell on the shot peened notch root.

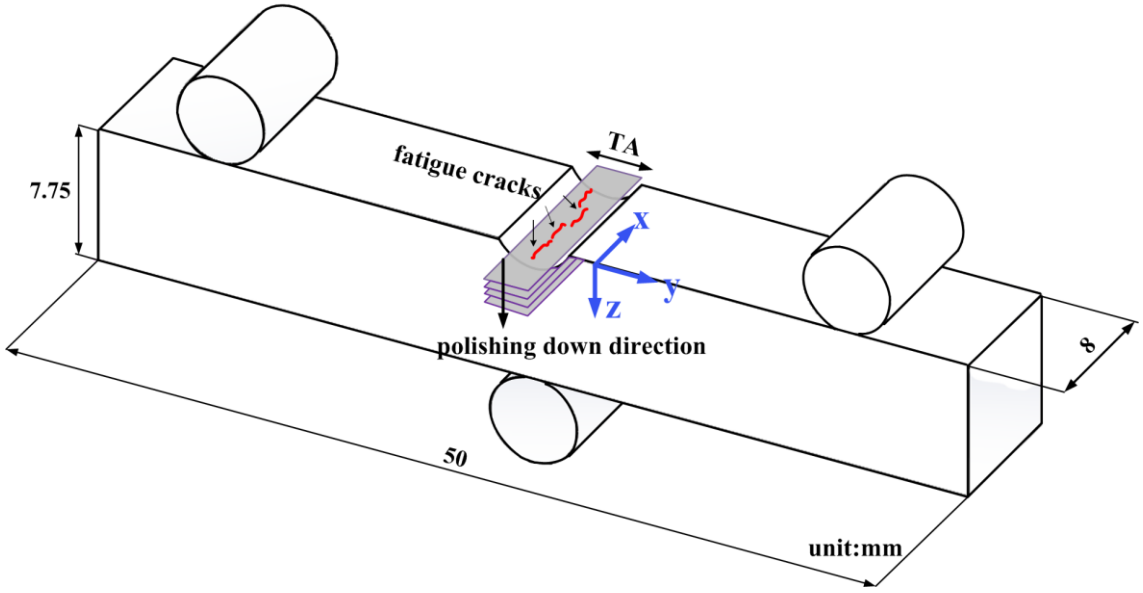


Figure 4- 7 Illustrates the polishing direction in the serial sectioning process.

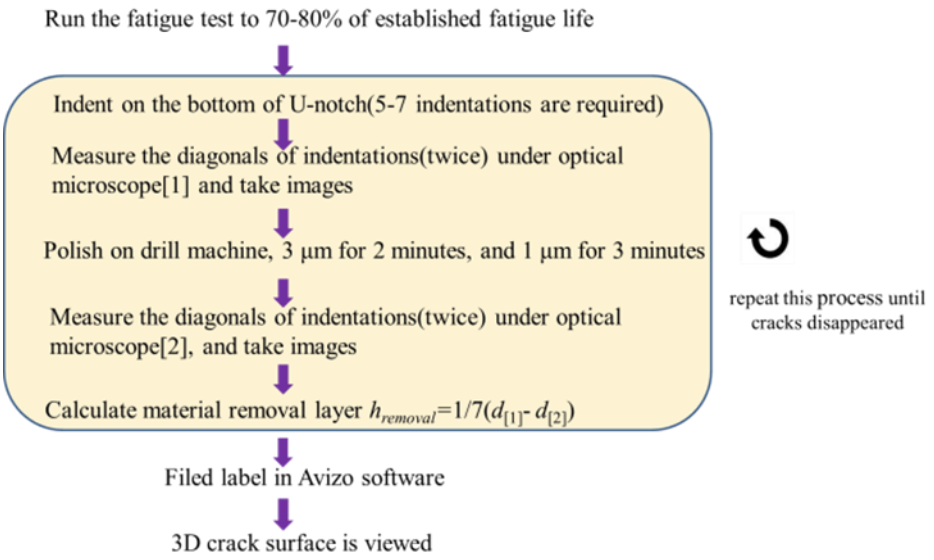


Figure 4- 8 Schematic of the 3D crack reconstruction experimental process.

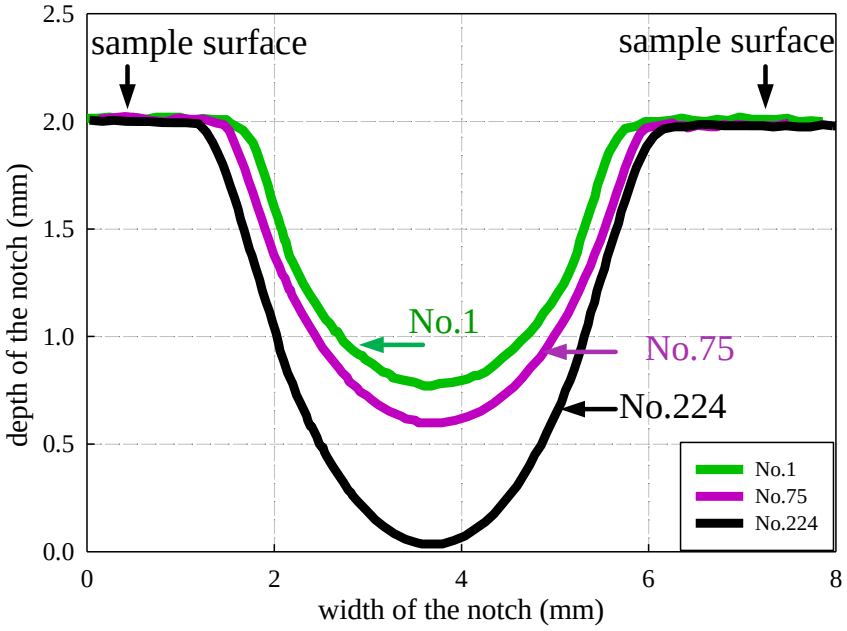


Figure 4- 9 The notch depth at different polishing stages, characterized by Talysurf.

Table 4- 1 Comparison between the depths of material removed measured by Talysurf and the calculated depth from indentation markings.

| | Notch profile by Tysurf/μm | Calculated material removal by indentation marking/μm | Corrected by factor 0.62 | Measured depth by Talysurf/μm |
|---|---|---|---|---|
| beginning | 1250 | | | |
| 1st | 1253.9 | 1.2 | 0.8 | 3.9 |
| 75th | 1392.8 | 297.7 | 184.4 | 142.8 |
| 224th | 1967.7 | 1109.1 | 687.6 | 717.9 |

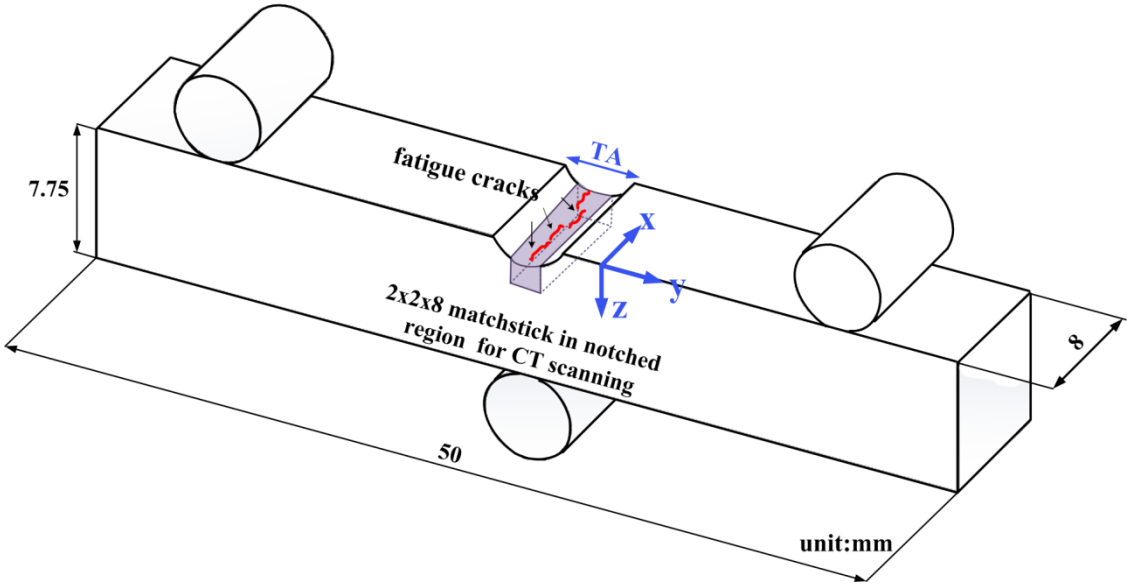


Figure 4- 10 Sample geometry schematic with a three-point bend set up shows the matchstick taken from the notch region for X-ray computed tomography imaging.

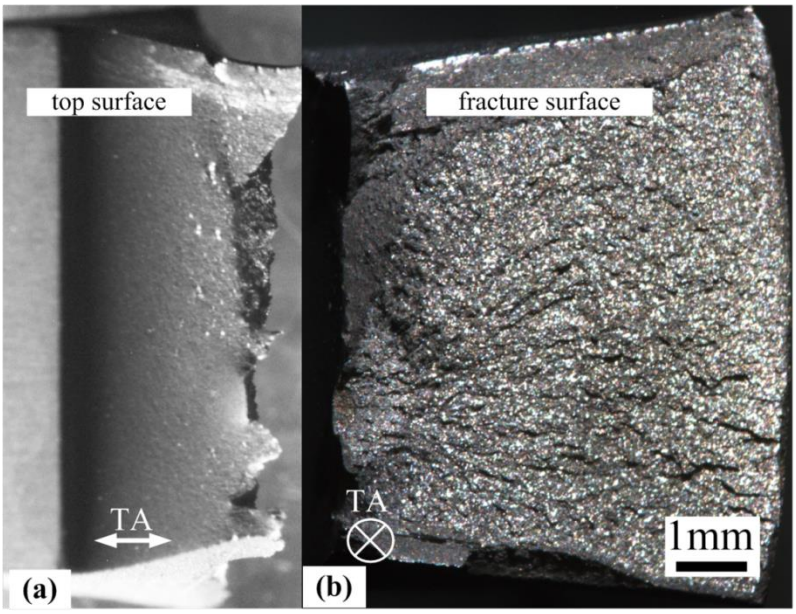


Figure 4- 11 Optical micrograph of polished notch interrupted heat-tinted fatigue sample after breaking open in nitrogen: (a) optical micrograph of notch top surface; (b) optical micrograph of the fracture surface.

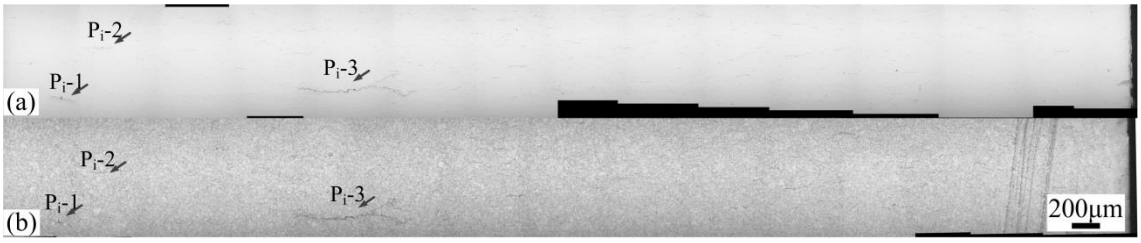


Figure 4- 12 (a) Optical micrograph of the polished notch surface when the fatigue process was interrupted at 2200 cycles; (b) optical micrograph of the notch surface after etching by Vilella's reagent.

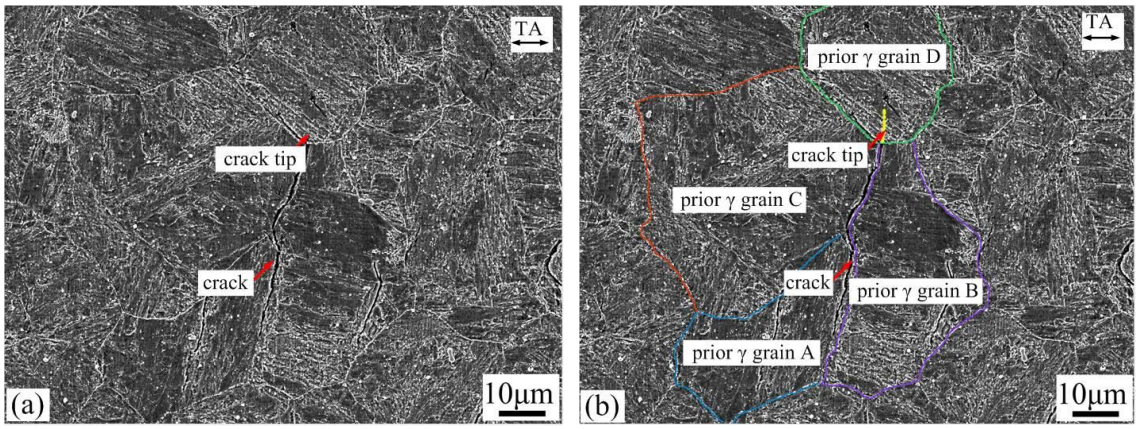


Figure 4- 13 The relation between crack propagation direction and microstructure: (a) a short crack among the prior γ grain boundaries; (b) γ grain boundaries are labelled artificially to reveal this relation more clearly.

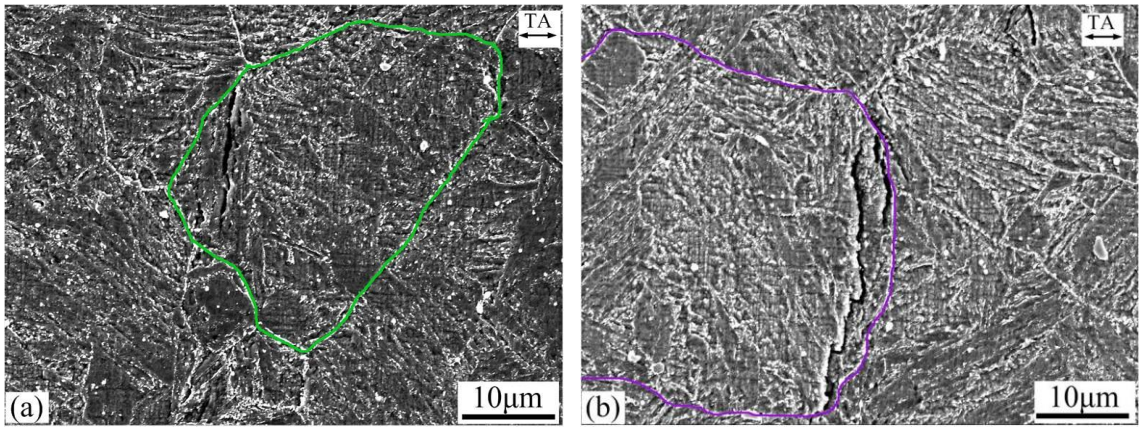


Figure 4- 14 (a) A tiny crack initiated within a grain boundary and propagated along martensitic lath, (b) or along a direction which is parallel to the grain boundary.

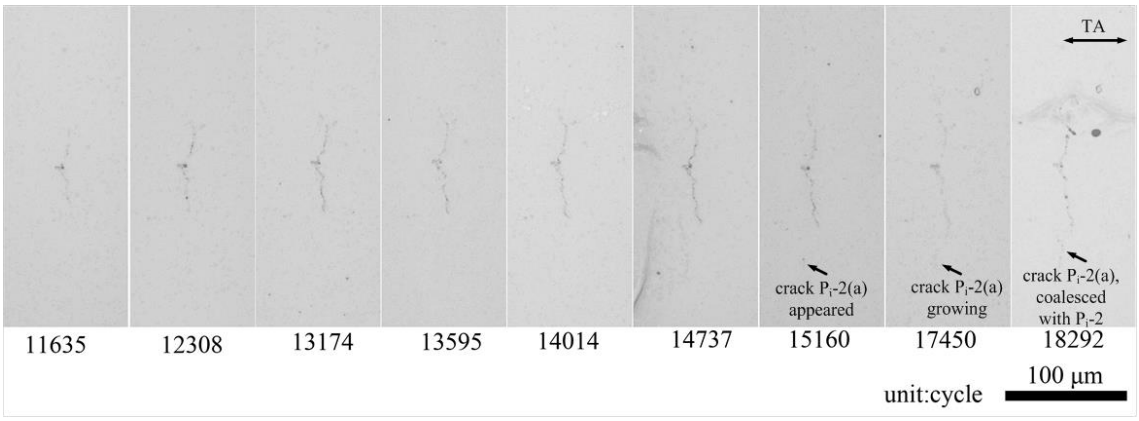


Figure 4- 15 Crack morphology at various fatigue stages for crack $P_i$-2.

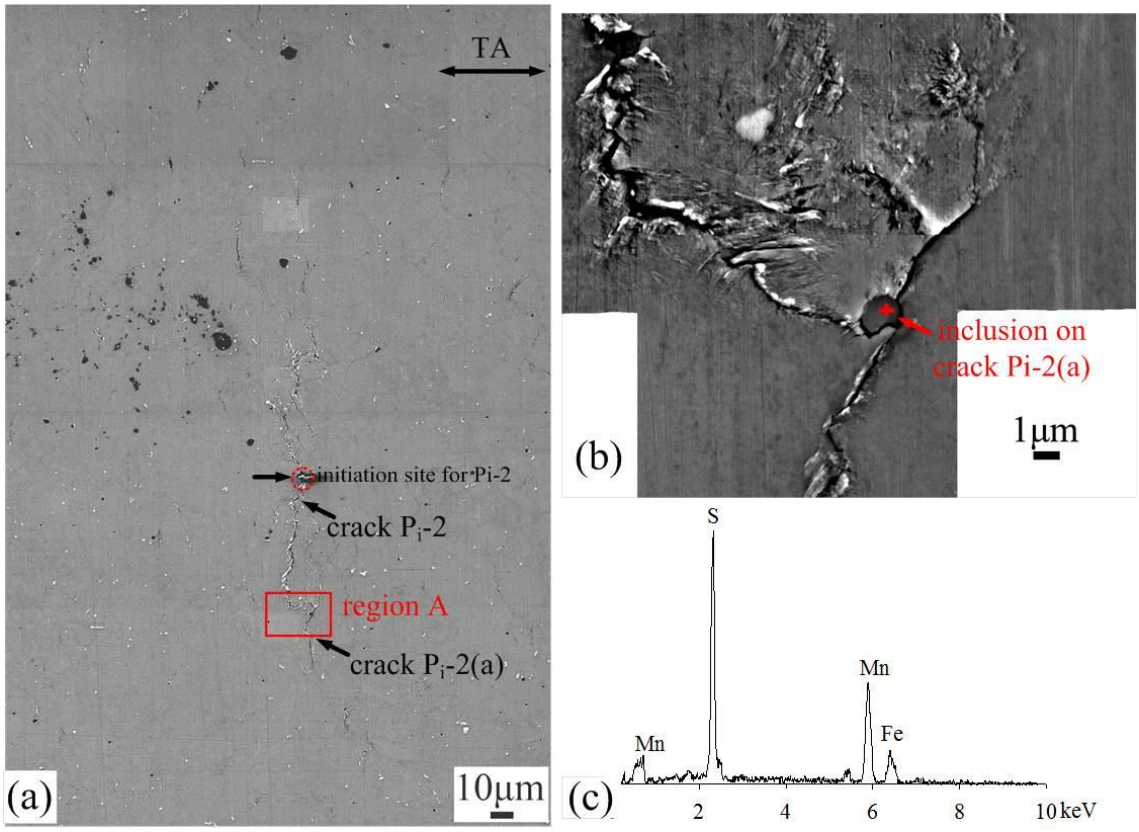


Figure 4- 16 (a) SEM micrograph of crack $P_i$-2, (b) a possible inclusion was found within the crack path of $P_i$-2 in region A; (c) EDS results indicate this is a MnS inclusion.

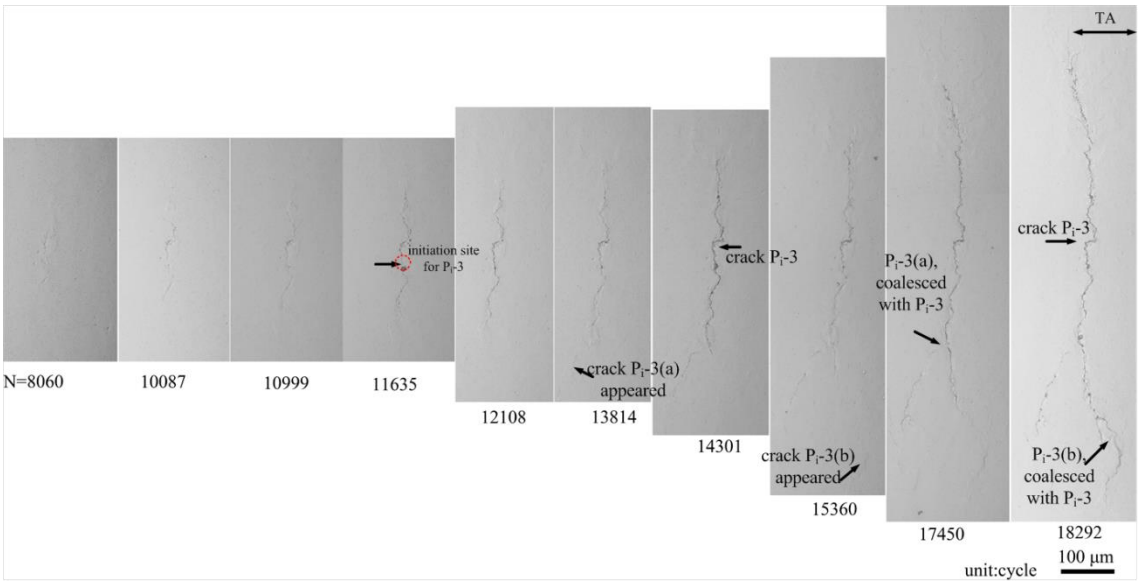


Figure 4- 17 Crack morphology at various fatigue stages for crack $P_i$-3.

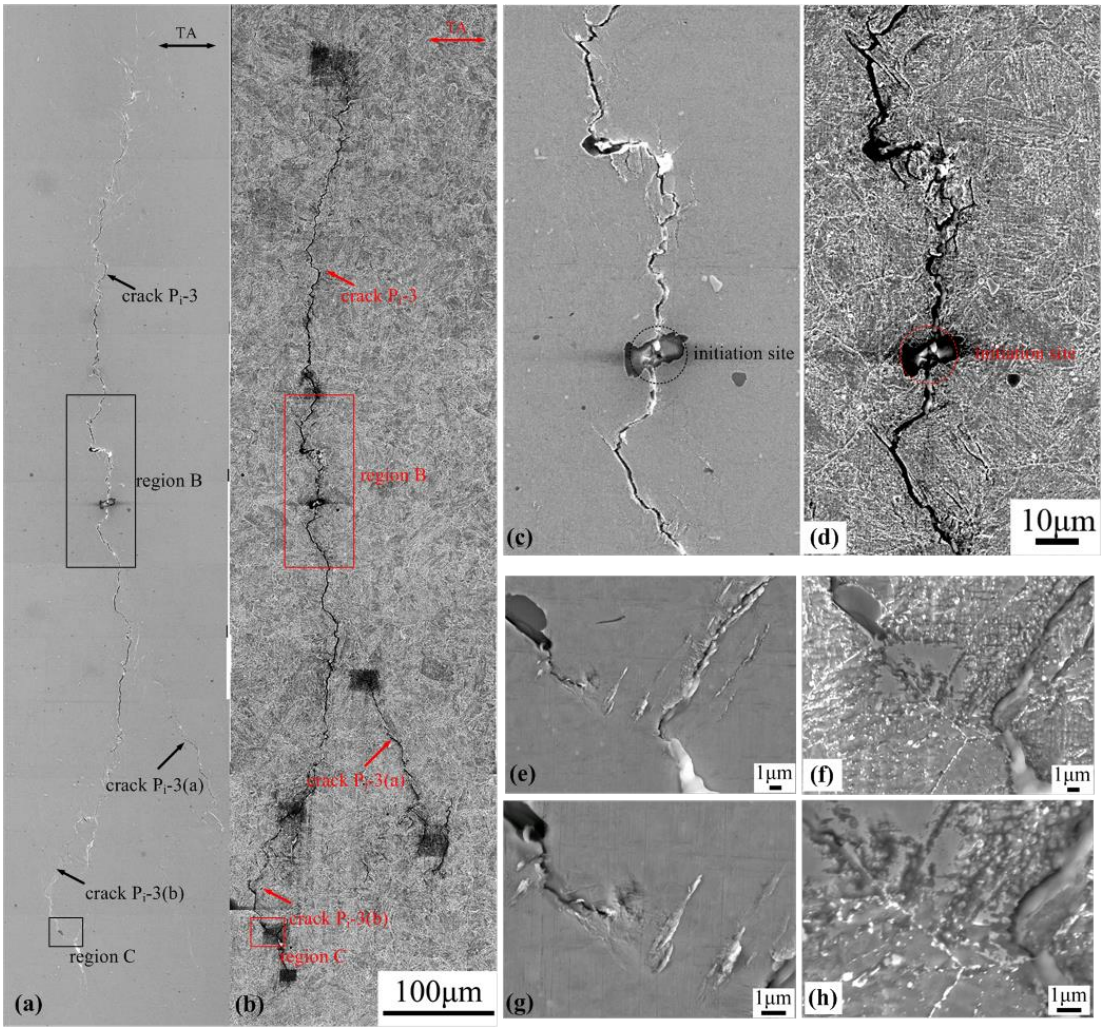


Figure 4- 18 SEM micrographs of crack $P_i$-3 morphology (a) before, (b) after microstructure revealed, (c) before, (d) after SEM micrographs of region C

in Figure 4-13(a) and (b), where is the initiation site of crack $P_i$-3; SEM micrographs of region C in (a) and (b).

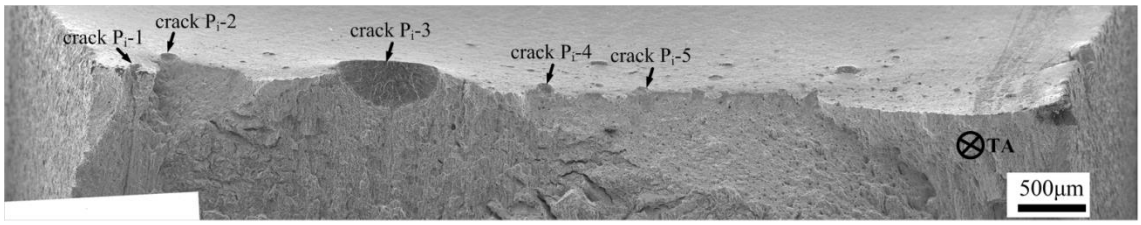


Figure 4- 19 SEM observation of the fracture surface after heat tinting on polished notch sample.

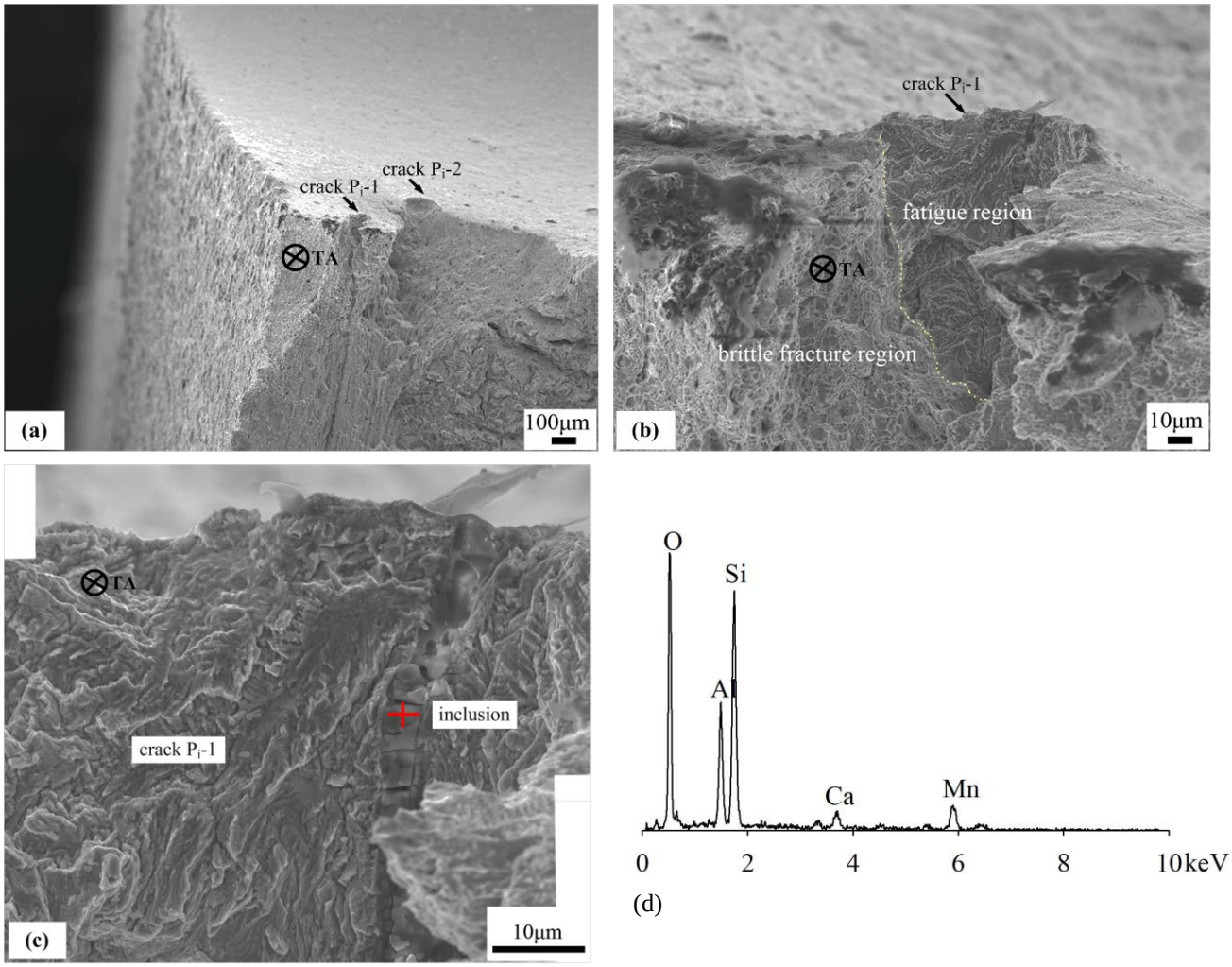


Figure 4- 20 (a), (b) and (c) are SEM micrographs of crack $P_i$-1 on fracture surface of notched polished sample at different magnifications. (d) EDS result of the possible aluminum oxide stringer.

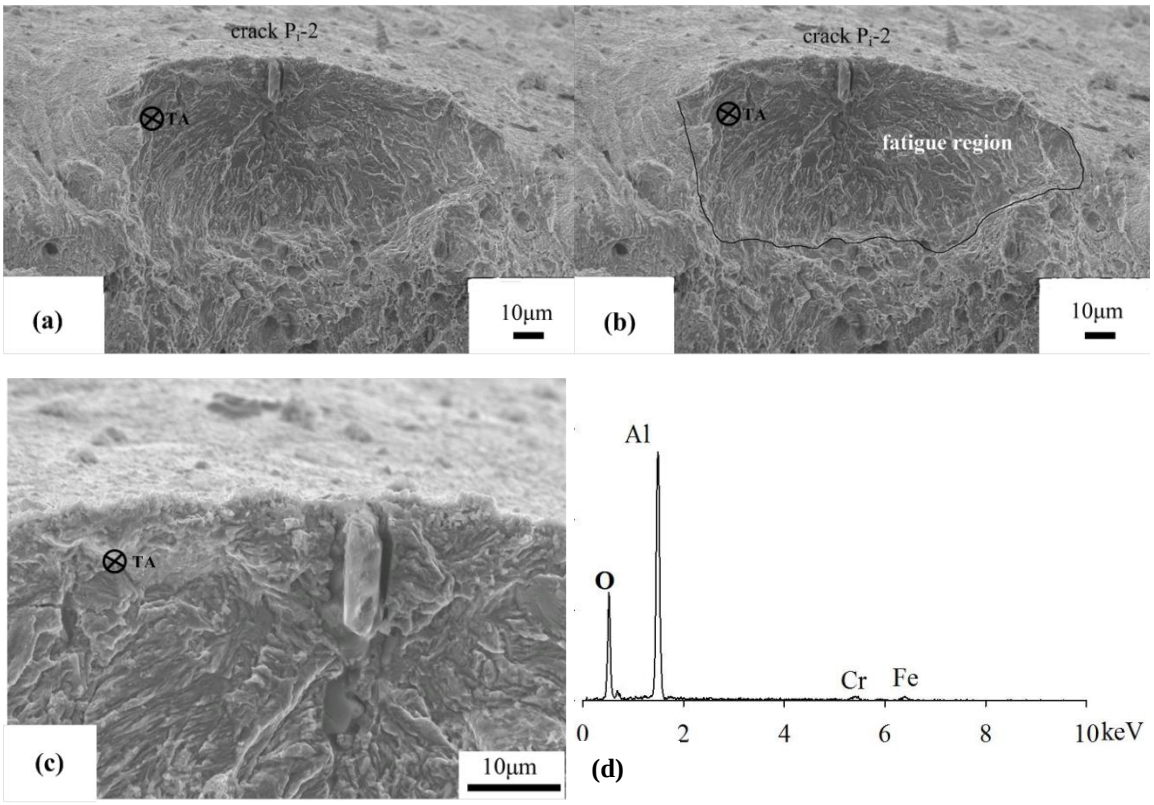


Figure 4- 21 SEM micrographs of crack $P_i$-2 on fracture surface of notched polished sample: (a) without artificial labelling, (b) with artificially labelling on the crack shape (c) A possible aluminum oxide stringer was found within the fatigue crack $P_i$-2 region on fracture surface of notched polished sample, (d) its EDS result.

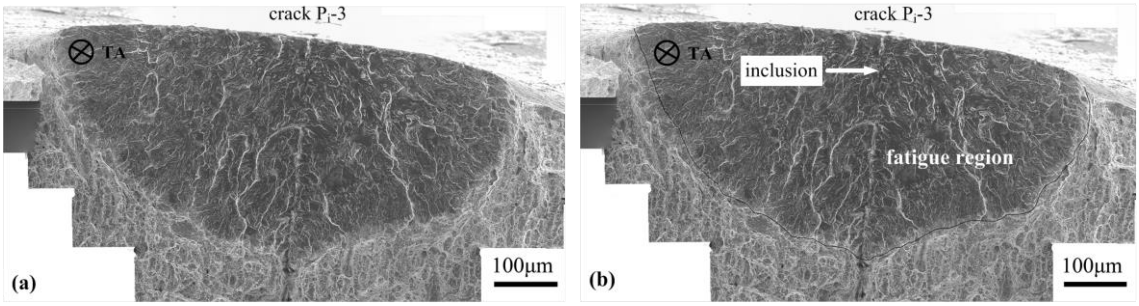


Figure 4- 22 SEM micrographs of crack $P_i$-3 on fracture surface of notched polished sample: (a) without artificial labelling, (b) with artificially labelling on the crack shape.

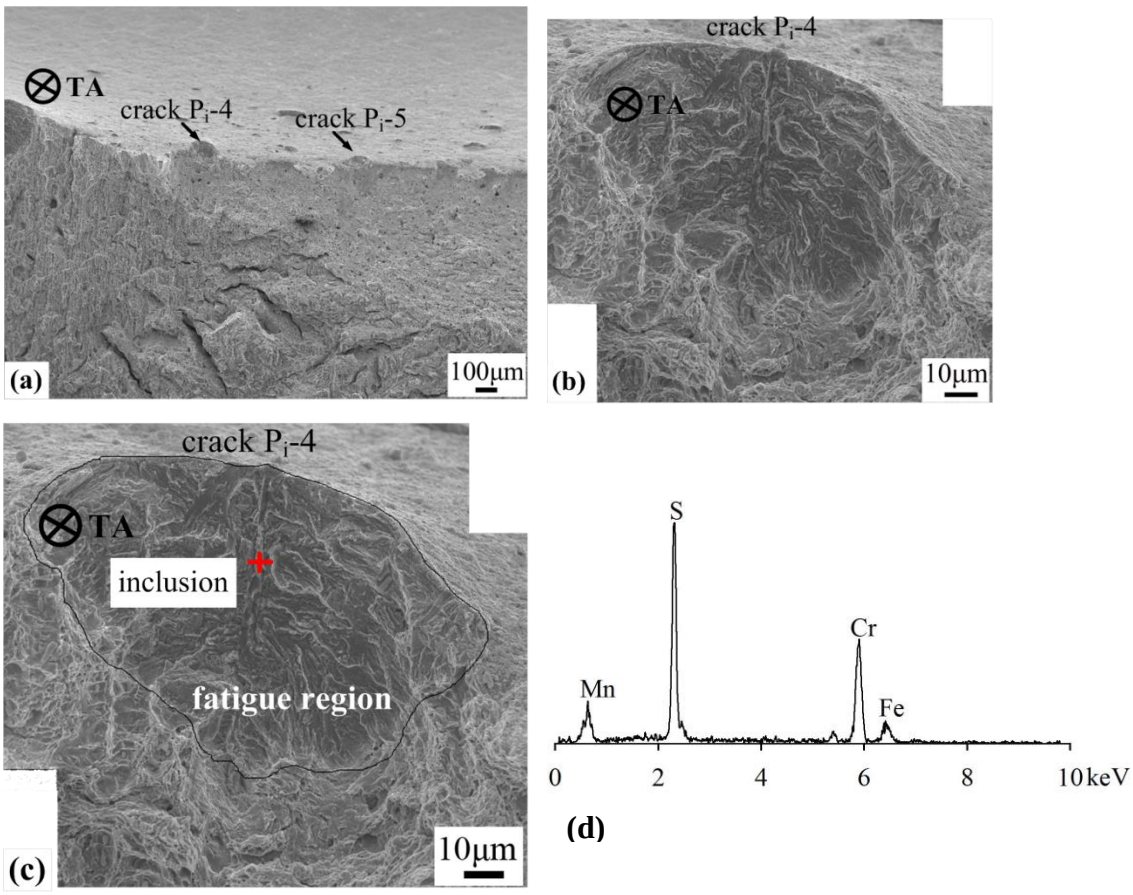


Figure 4- 23 (a) The position of crack $P_i$-4 and crack $P_i$-5 on the fracture surface of notched polished sample; (b) SEM micrographs of crack $P_i$-4 without artificial labelling, (c) with artificially labelling on the crack shape, and (d) EDS result on the possible inclusions or stringers.

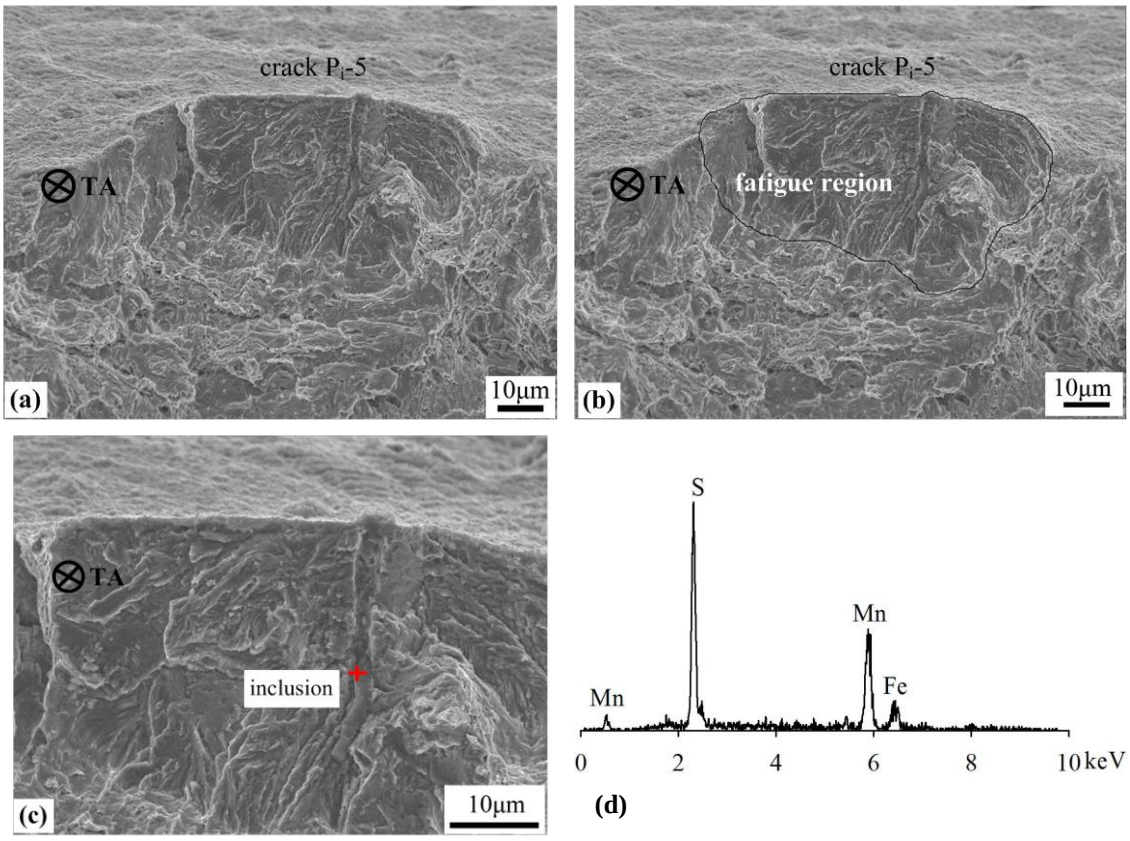


Figure 4- 24 (a) SEM micrographs of crack $P_i$-5 without artificially labelling; (b) with artificial labelling on the crack shape, and (c) a possible aluminium oxide stringer or inclusion which was found within the fatigue crack $P_i$-5 region; (d) EDS result on the possible inclusion or stringer.

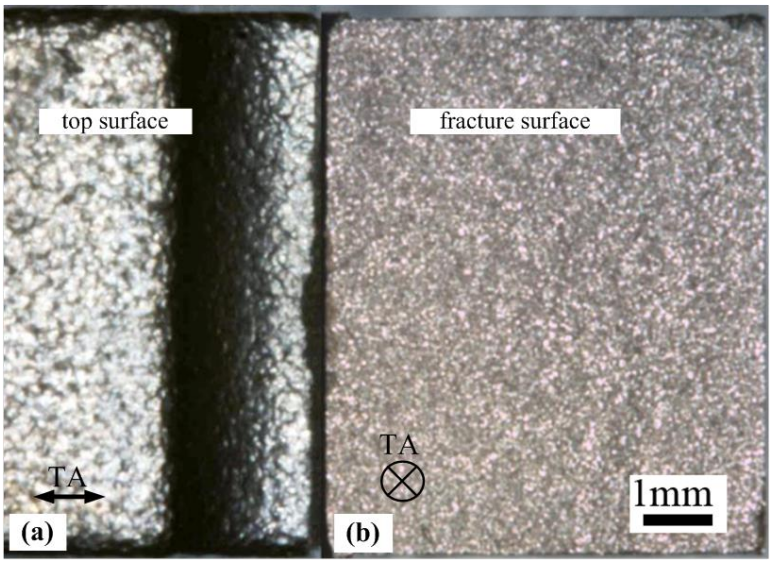


Figure 4- 25 Optical micrograph of shot peened interrupted heat-tinted fatigue sample after failure: (a) optical micrograph of notch top surface; (b) optical micrograph of the fracture surface fracture surface.

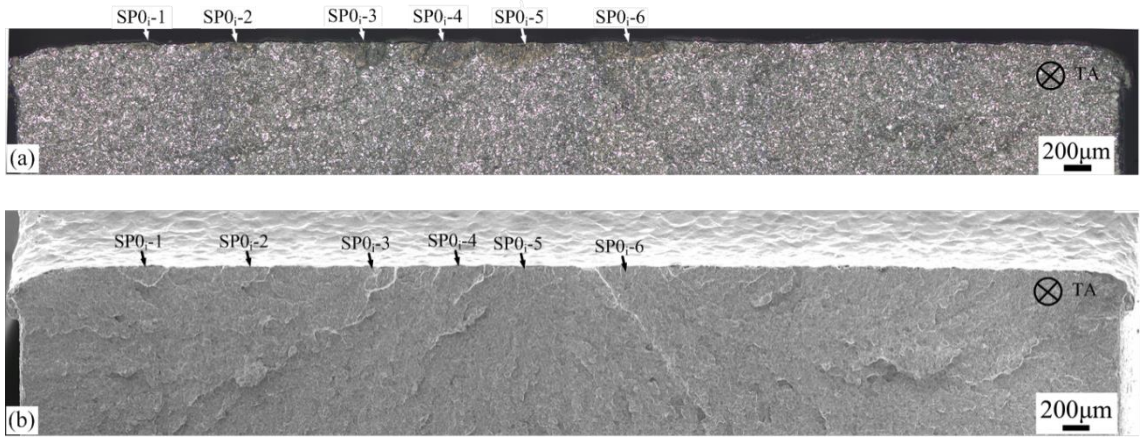


Figure 4- 26 (a) the fracture surface under SEM observation; (b) optical micrograph of the fracture surface.

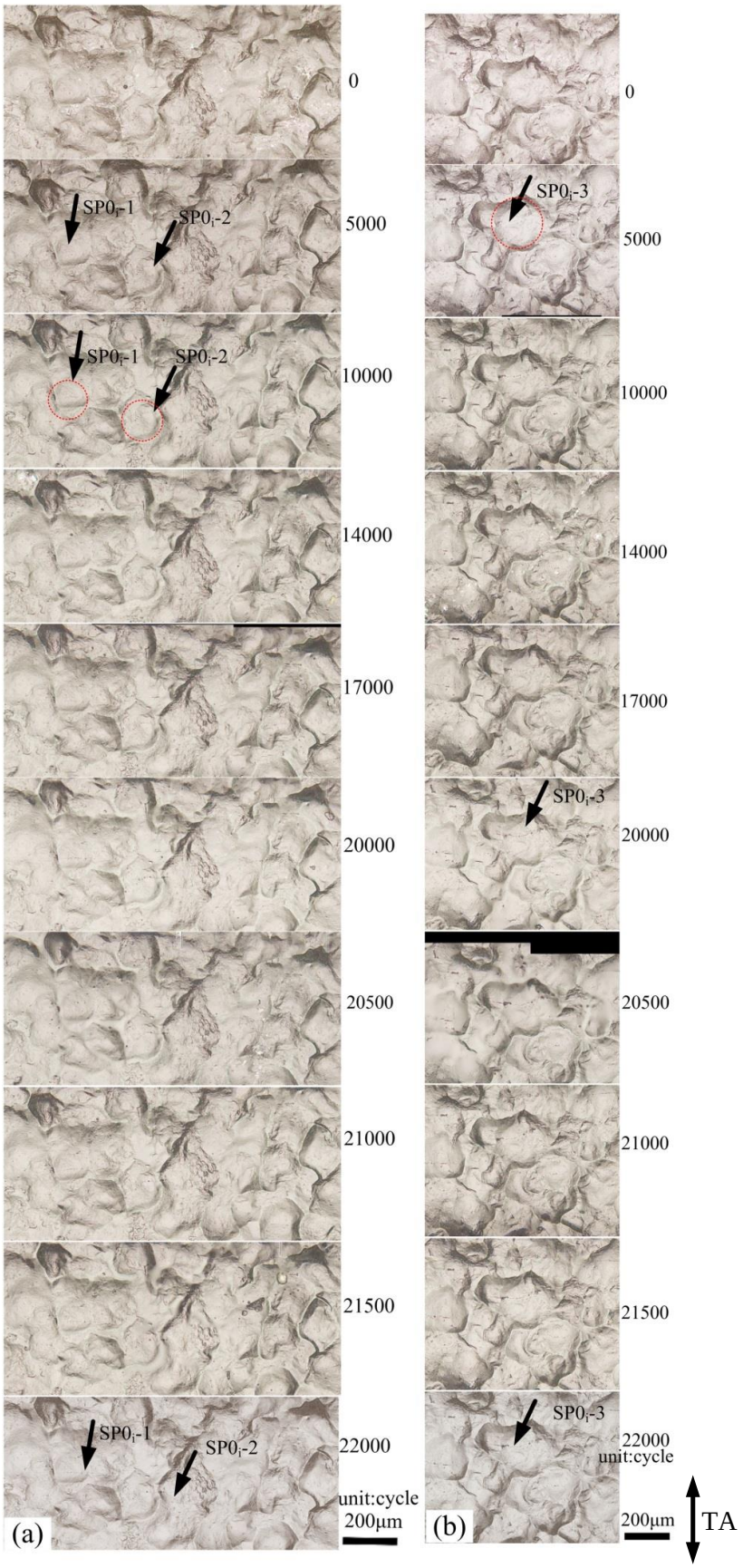


Figure 4- 27 Crack morphologies of (a) $SP0_i$-1 and $SP0_i$-2, (b) $SP0_i$-3 on the shot peened surface at different stages of fatigue life.

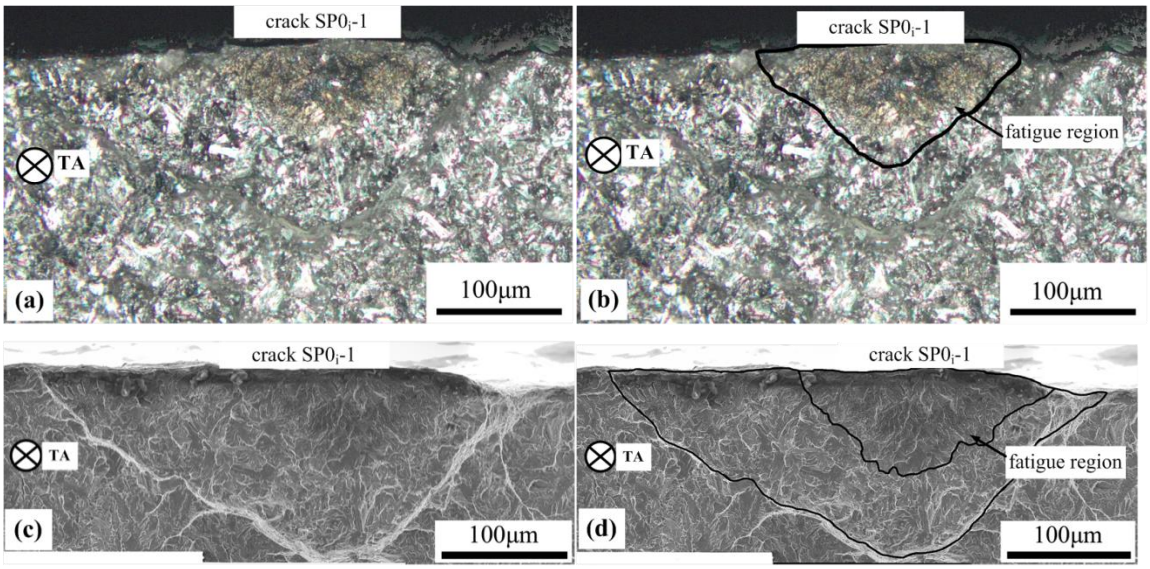


Figure 4- 28 Crack $SP0_i$-1 morphology under optical microscope: (a) the crack without artificial labelling; (b) artificially labelled crack; SEM micrographs of crack $SP0_i$-1 morphology, (c) crack $SP0_i$-1without artificial labelling; (d) artificially labelled along crack shape.

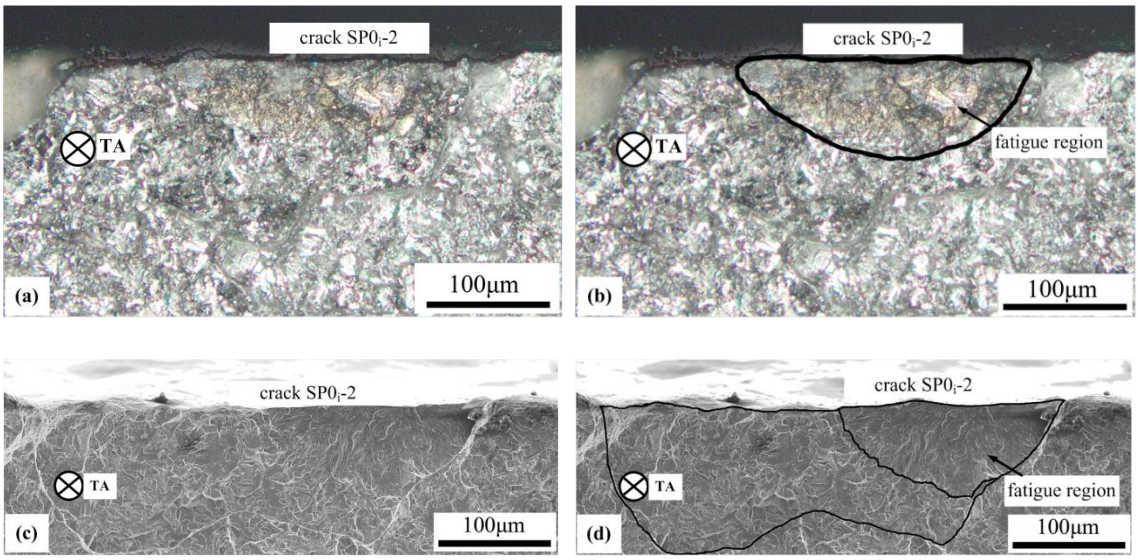


Figure 4- 29 Crack $SP0_i$-2 morphology under optical microscope: (a) the crack without artificial labelling; (b) artificially labelled crack; SEM micrographs of crack $SP0_i$-2 morphology, (c) crack $SP0_i$-2 without artificial labelling; (d) artificially labelled along crack shape

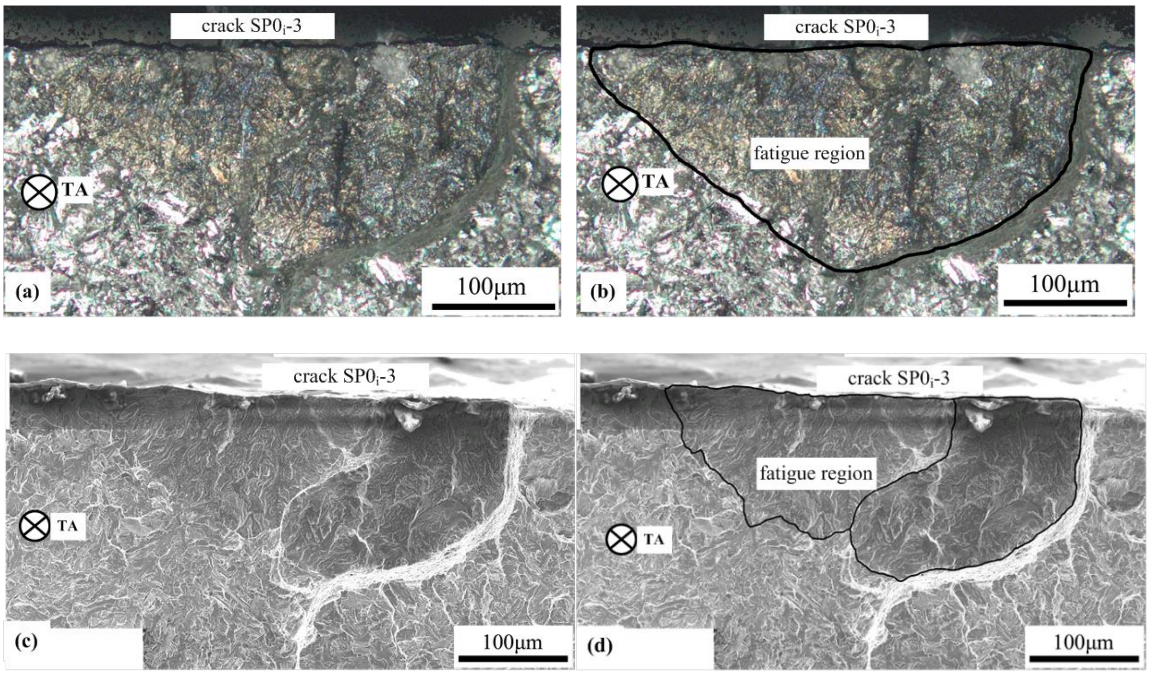


Figure 4- 30 Crack $SP0_i$-3 morphology under optical microscope: (a) the crack without artificial labelling; (b) artificially labelled crack; SEM micrographs of crack $SP0_i$-3 morphology, (c) crack $SP0_i$-3 without artificial labelling; (d) artificially labelled along crack shape

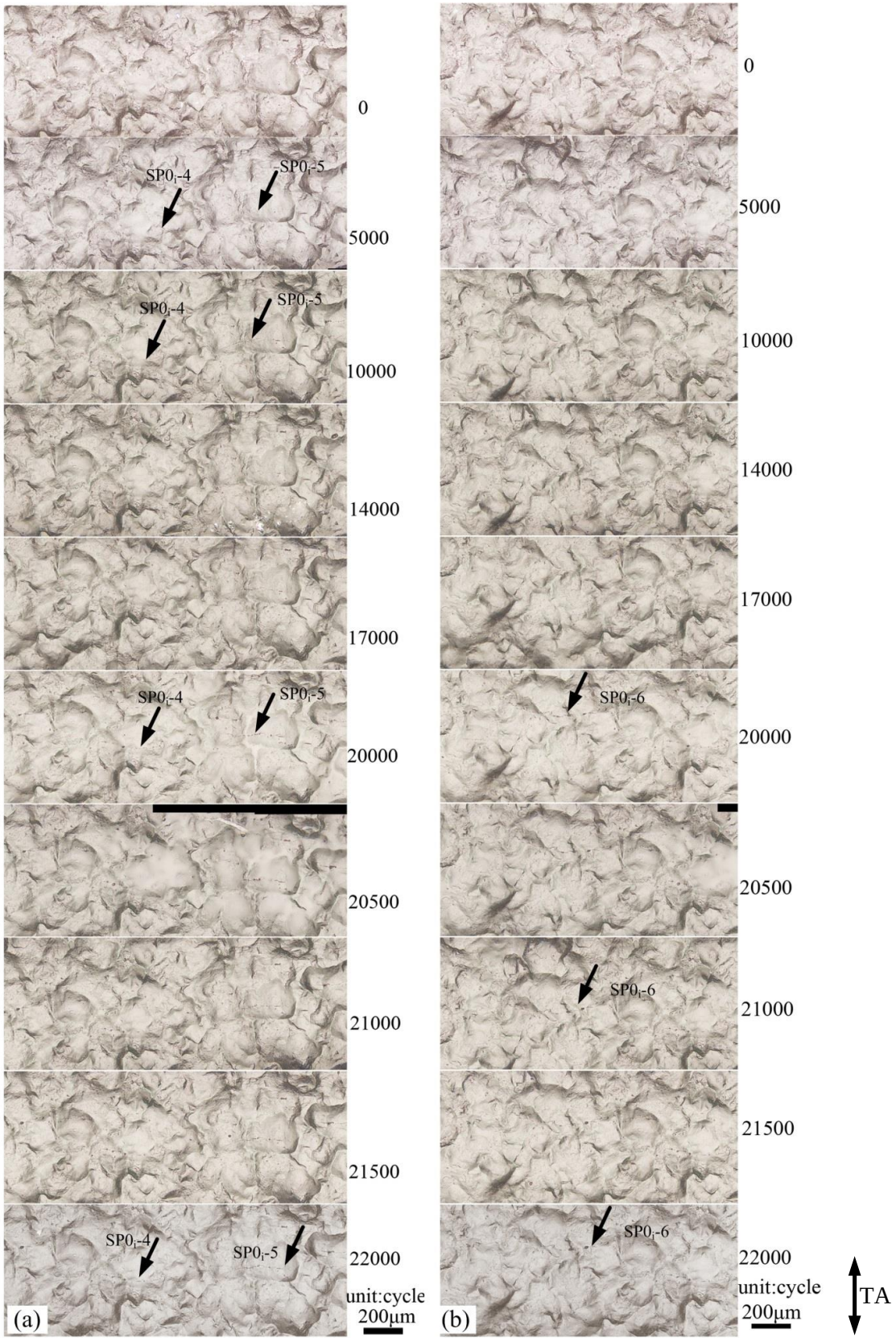


Figure 4- 31 Crack morphologies of (a) $SP0_i$-4 and $SP0_i$-5, (b) $SP0_i$-6 on the shot peened surface at different stages of fatigue life.

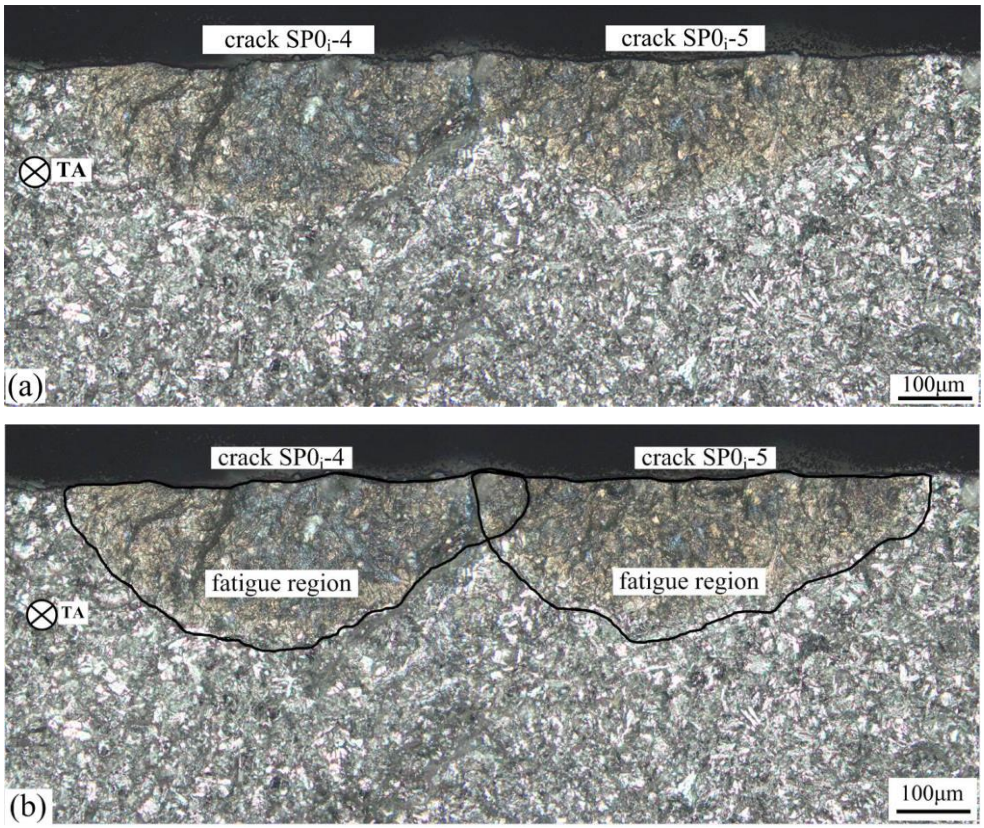


Figure 4- 32 Crack SP0$_i$-4 and SP0$_i$-5 morphology under optical microscope: (a) the crack without artificially labelling; (b) artificially labelled crack.

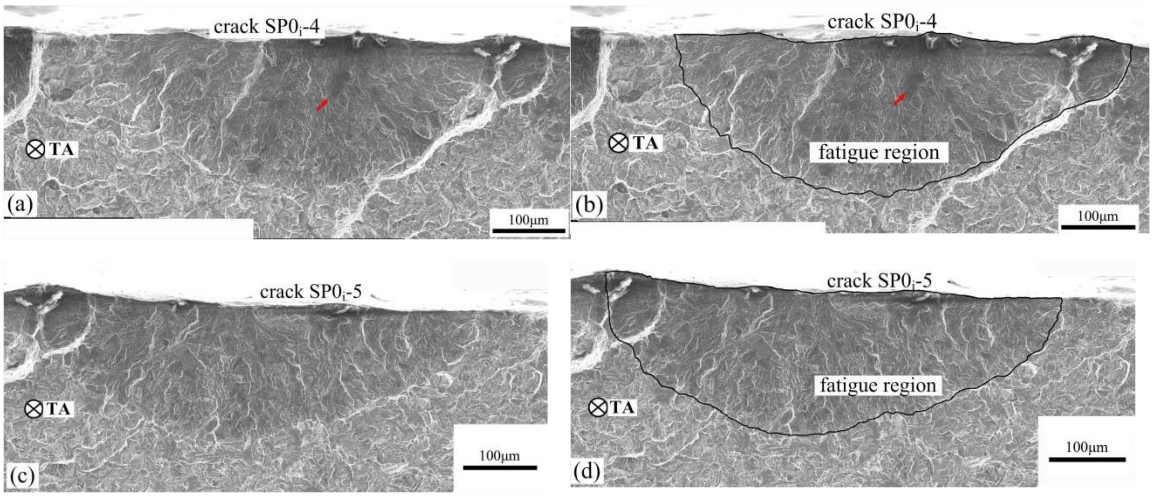


Figure 4- 33 SEM micrographs of crack SP0$_i$-4 morphology: (a) crack SP0$_i$-4 without artificial labelling; (b) artificially labelled along crack shape; (c) crack SP0$_i$-5 without artificial labelling; (d) artificially labelled along crack shape.

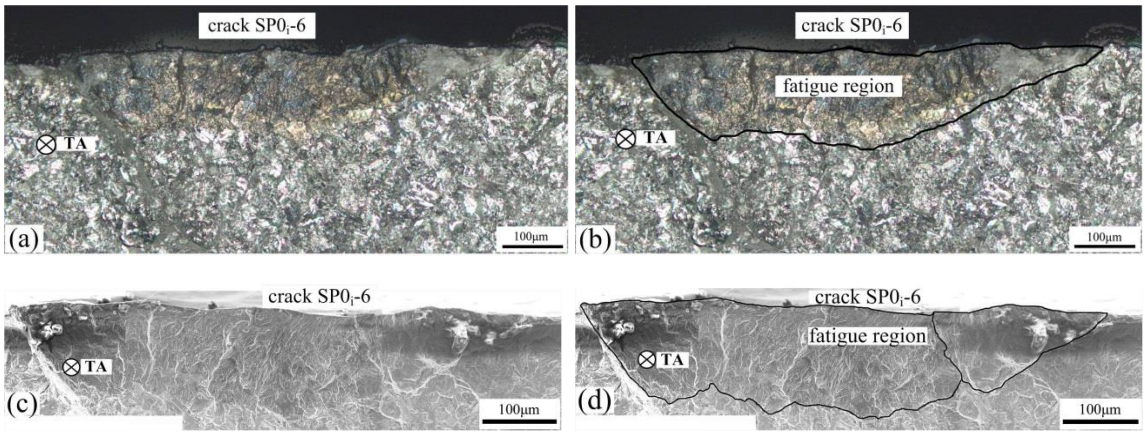


Figure 4- 34 Crack SP0$_i$-6 morphology under optical microscope: (a) the crack without artificial labelling; (b) artificially labelled crack; SEM micrographs of crack SP0$_i$-6 morphology, (c) crack SP0$_i$-6 without artificial labelling; (d) artificially labelled along crack shape.

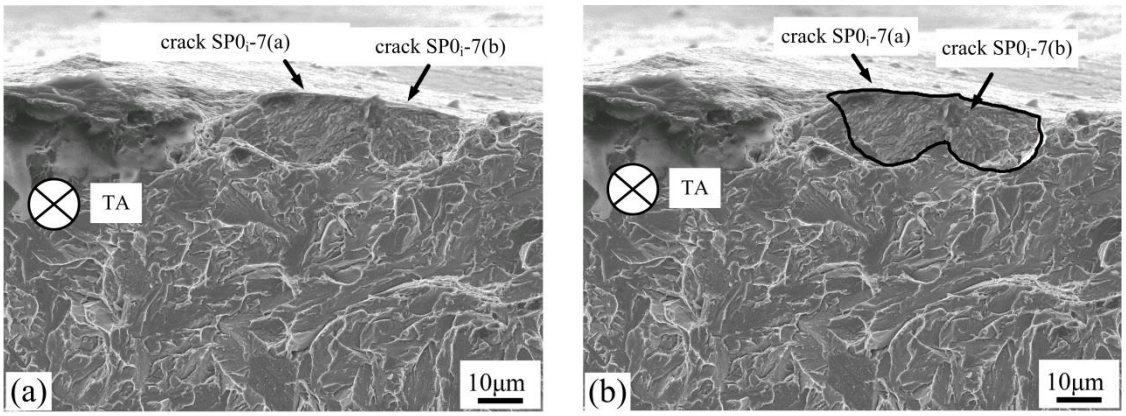


Figure 4- 35 SEM micrographs of crack SP0$_i$-7 morphology, (a) crack SP0$_i$-7 without artificial labelling; (b) artificially labelled crack shape.

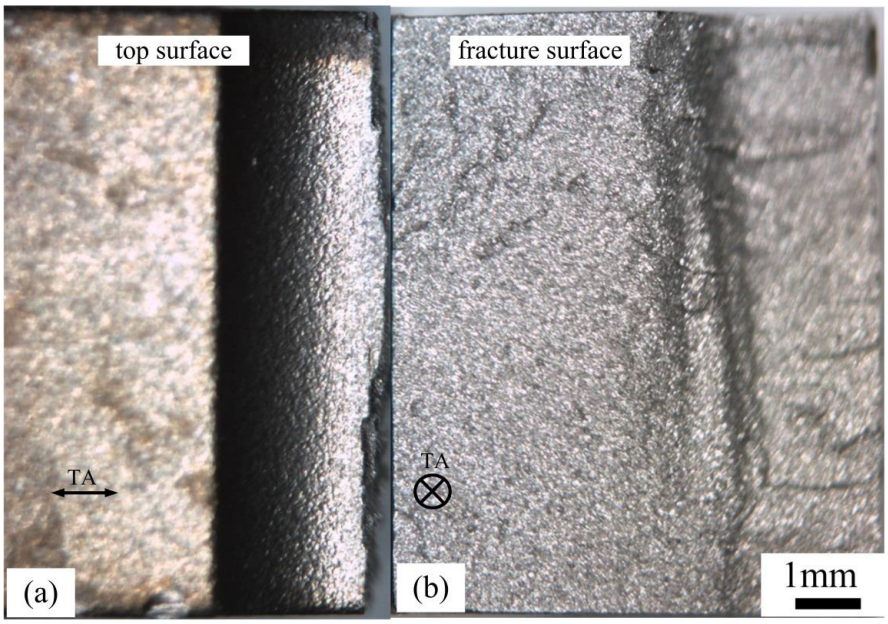


Figure 4- 36 Optical micrograph of T1 shot peening interrupt heat-tinting fatigue sample after failure: (a) optical micrograph of notch top surface; (b) optical micrograph of the fracture surface fracture surface.

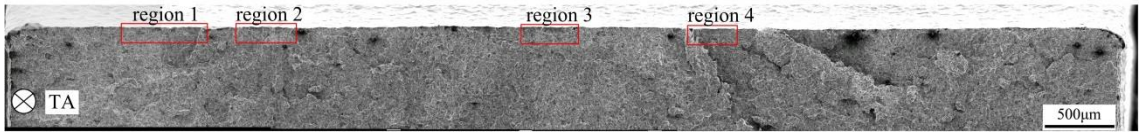


Figure 4- 37 SEM observation of the fracture surface after heat tinting on polished notch sample. Some of the fatigue regions, region1, region2, region 3 and region 4 are labelled.

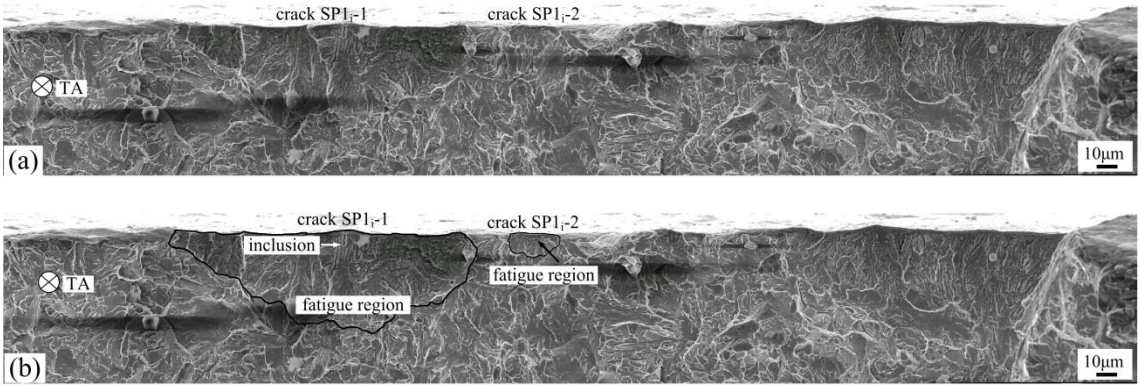


Figure 4- 38 Crack $SP1_i$-1 and crack $SP1_i$-2 initiated from inclusions: (a) the crack without artificial labelling; (b) artificially labelled crack.

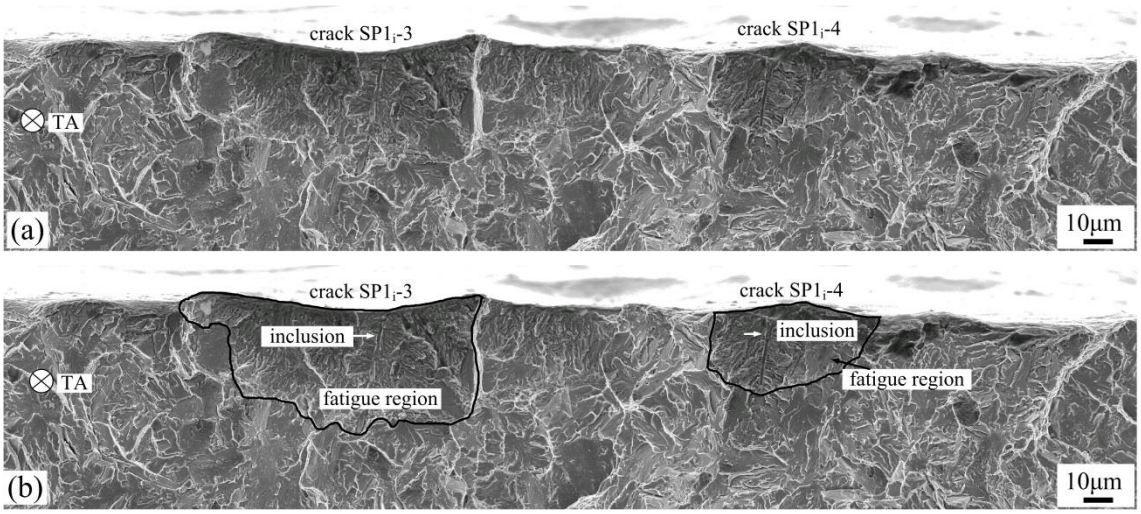


Figure 4- 39 Crack SP1$_i$-3 and crack SP1$_i$-4 initiated from inclusions: (a) the crack without artificial labelling; (b) artificially labelled crack.

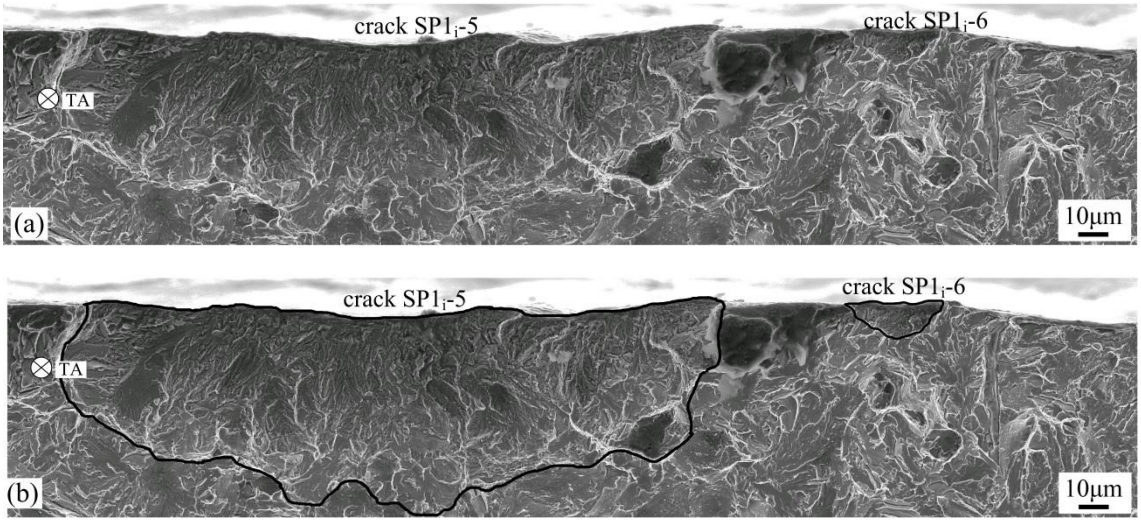


Figure 4- 40 Crack SP1$_i$-5 and crack SP1$_i$-6 initiated from inclusions: (a) the crack without artificial labelling; (b) artificially labelled crack.

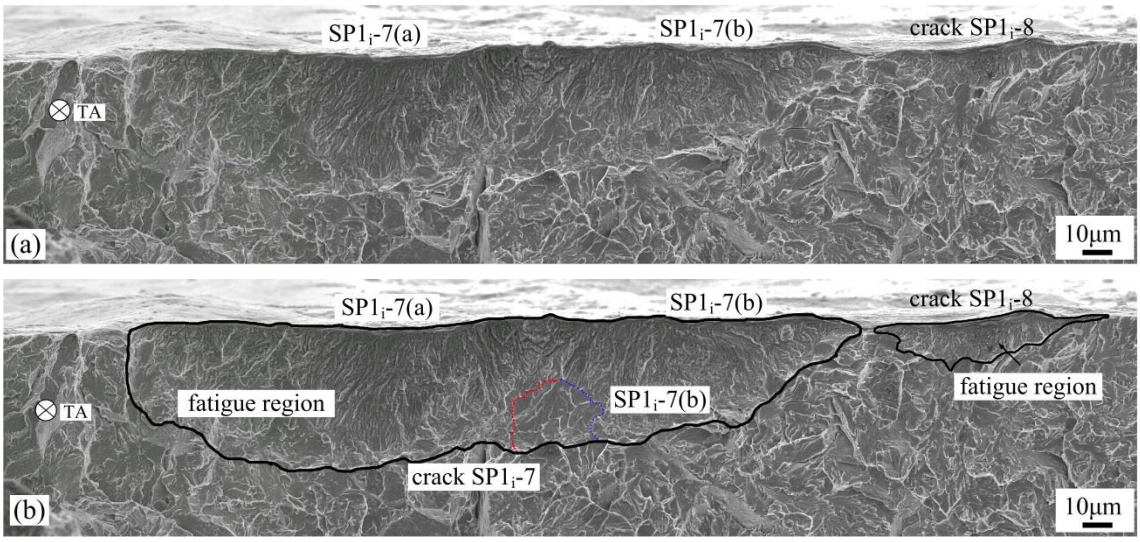


Figure 4- 41 Crack SP1$_i$-7 and crack SP1$_i$-8 initiated from inclusions: (a) the crack without artificial labelling; (b) artificially labelled crack.

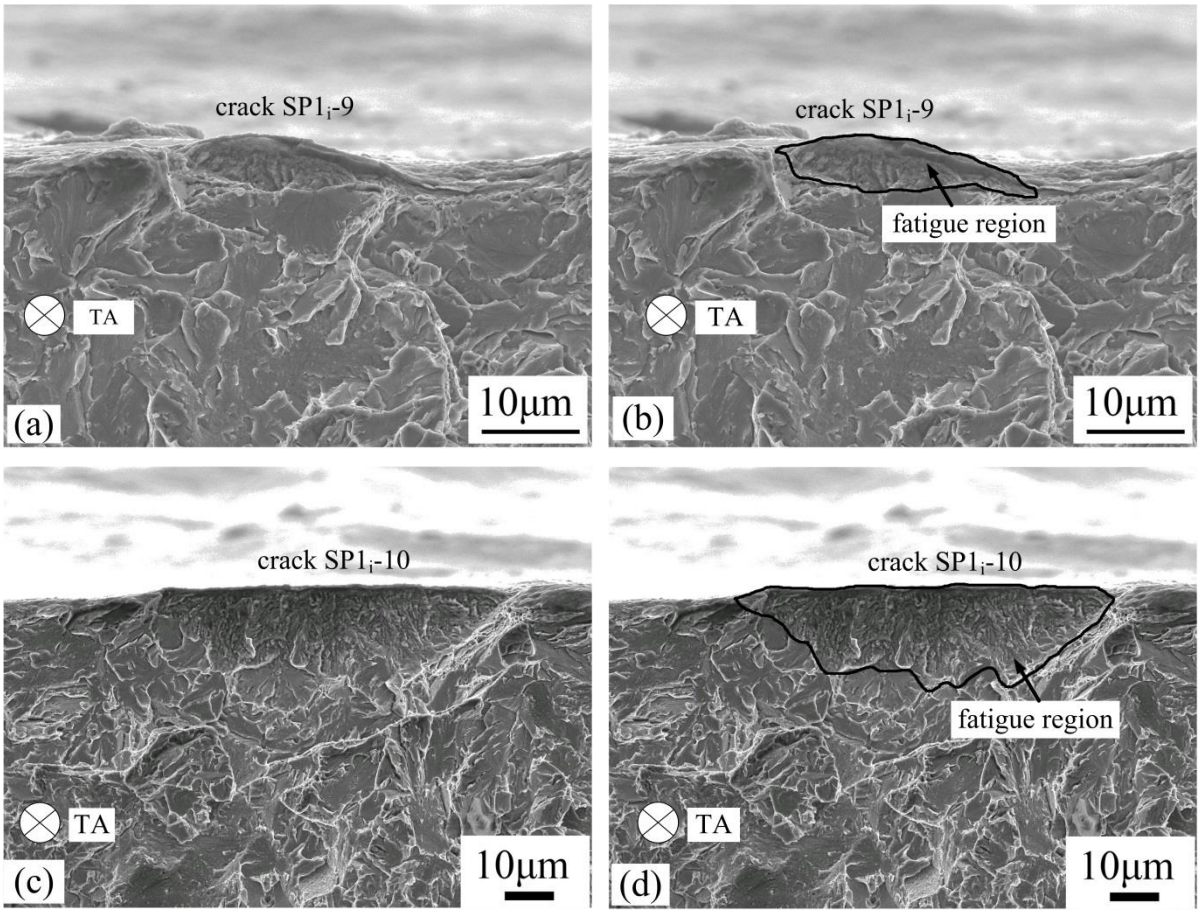


Figure 4- 42 (a ) and (b) a shallow crack SP1$_i$-9; (c) and (d) a shallow crack SP1$_i$-10.

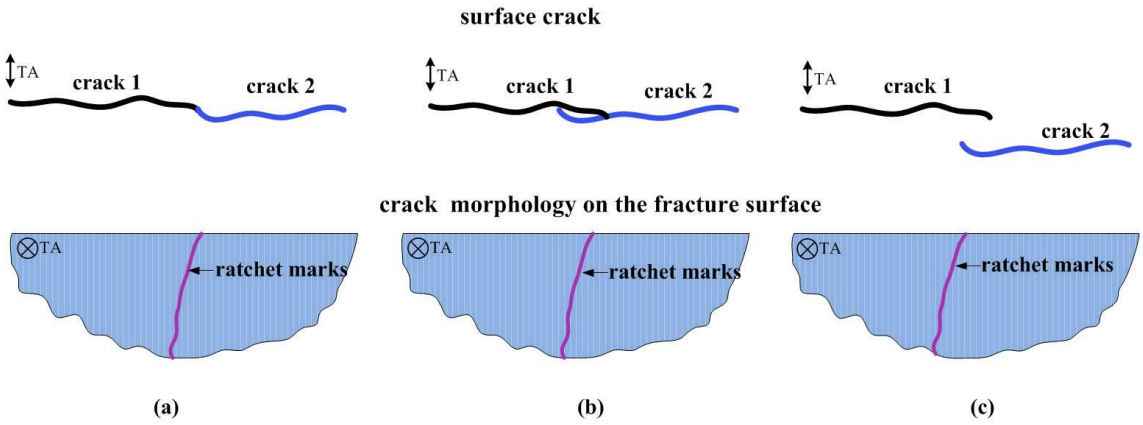


Figure 4- 43 Illustration of different positions of coalescence of cracks leading to the same crack morphology revealed by heat tinting on fracture surface.

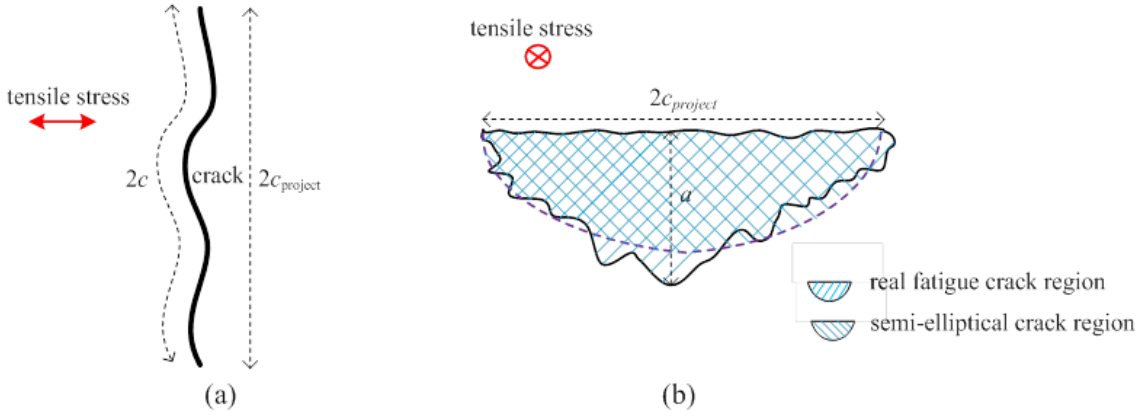


Figure 4- 44 Schematic diagram showing (a) the difference between the real crack length $2c$ and $2c_{project}$; (b) crack aspect ratio ($a/c$) calculation based on the crack morphology on the fracture surface.

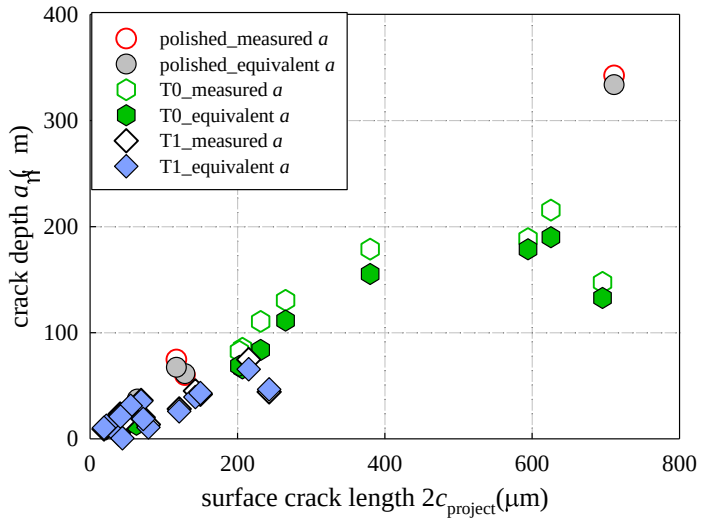


Figure 4- 45 The relationship between the equivalent crack depth $a$ and the actual maximum depth of the crack based on the SEM micrographs.

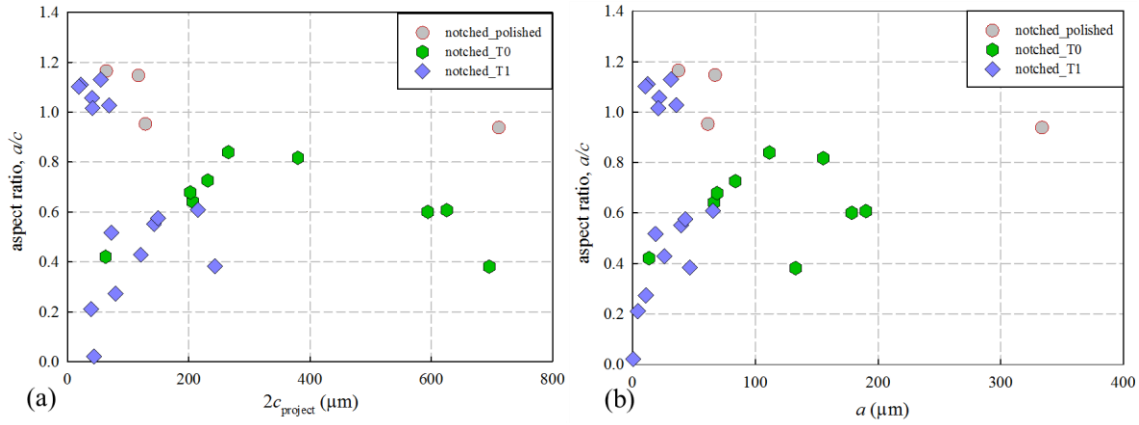


Figure 4- 46 Crack aspect ratio *a/c* based on the fatigue crack morphology on the fracture surface in T0 and T1: (a) *a/c* at various crack lengths $2c_{project}$; (b) *a/c* changes with crack depth a.

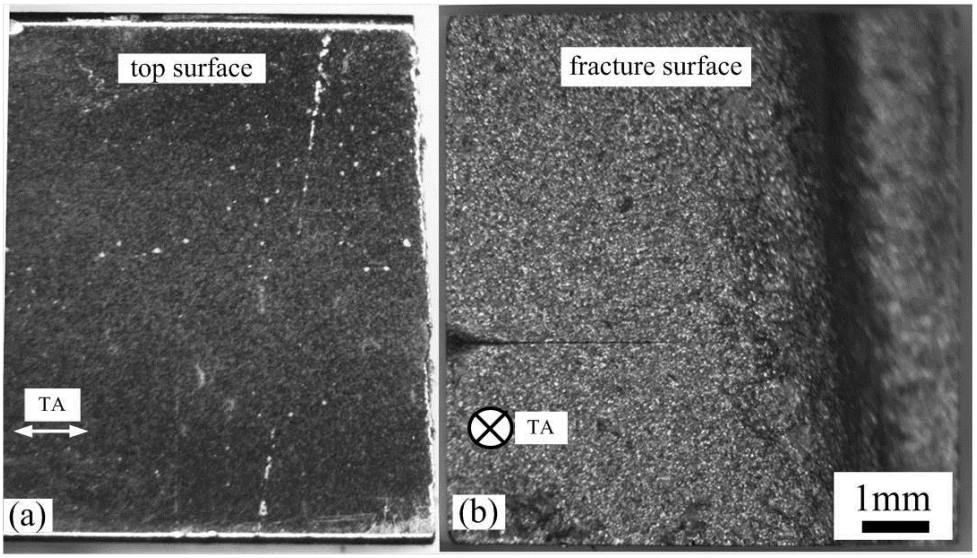


Figure 4- 47 Optical micrograph of PBB polished interrupted heat-tinted fatigue sample after failure: (a) optical micrograph of notch top surface; (b) optical micrograph of the fracture surface fracture surface.

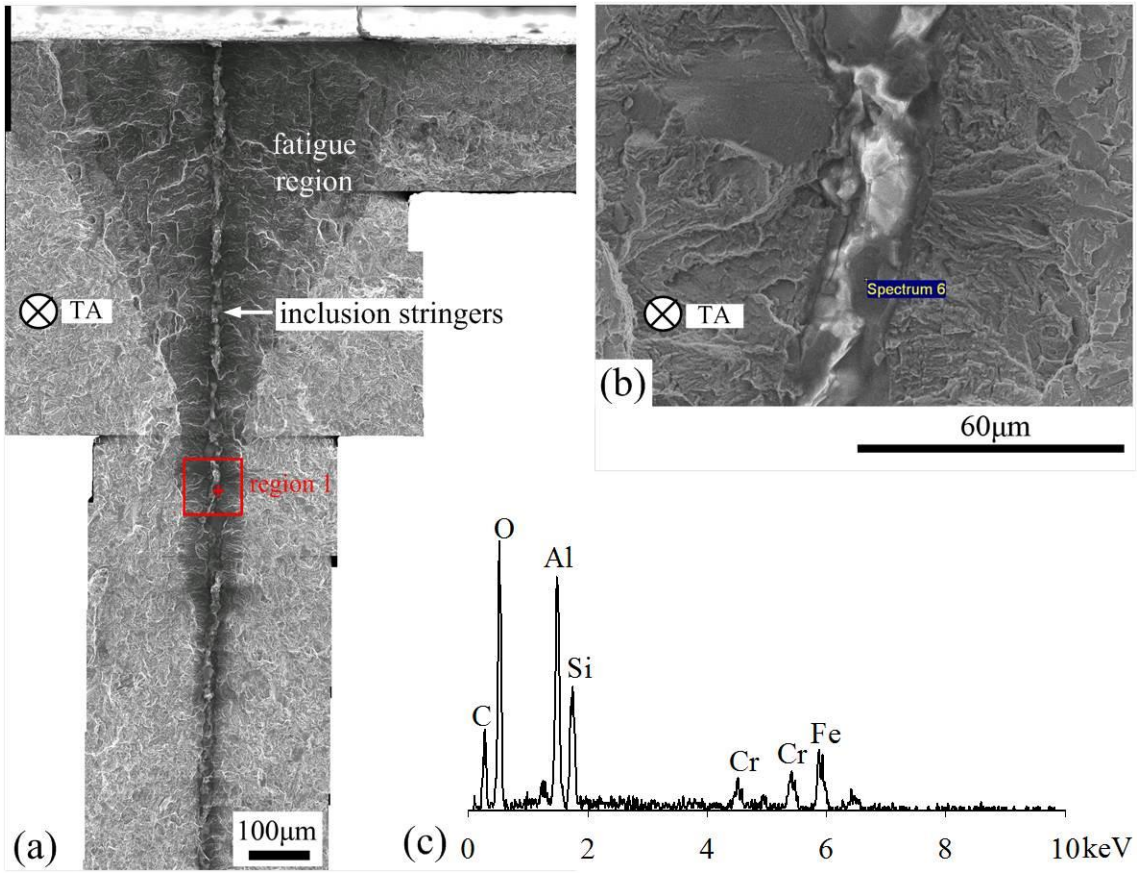


Figure 4- 48 (a) Fracture surface of PBB polished sample under SEM, where an inclusion stringer parallel to the specimen surface is observed; (b) inclusion in region 1; (c) EDS results indicating the inclusion is actually a combination of alumina, and silicon compound.

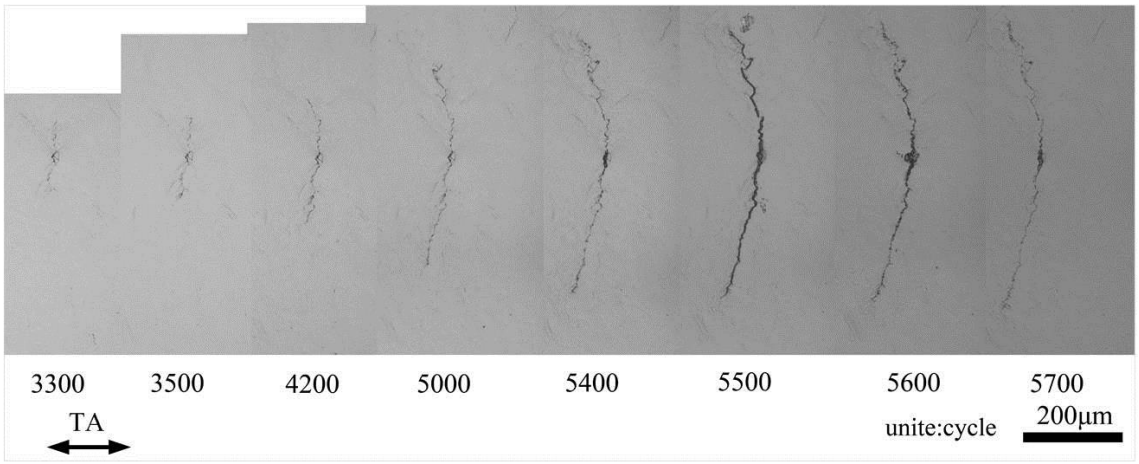


Figure 4- 49 Crack morphology at various fatigue stages for cracks in the PBB polished condition.

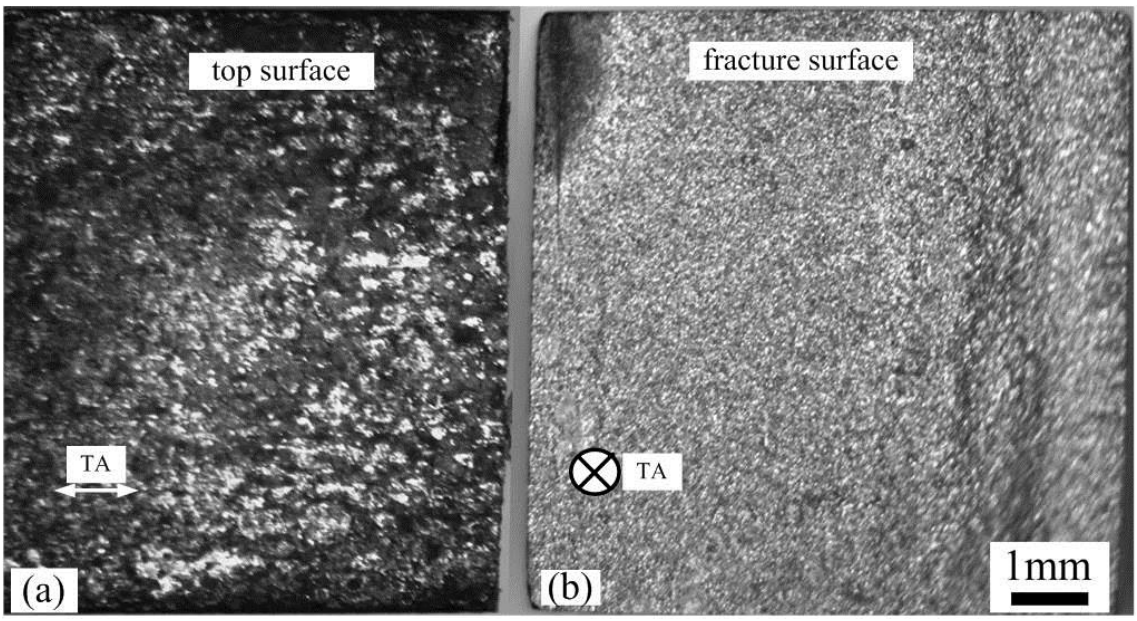


Figure 4- 50 Optical micrograph of PBB T0 shot peened interrupted heat-tinted fatigue sample after failure: (a) optical micrograph of notch top surface; (b) optical micrograph of the fracture surface.

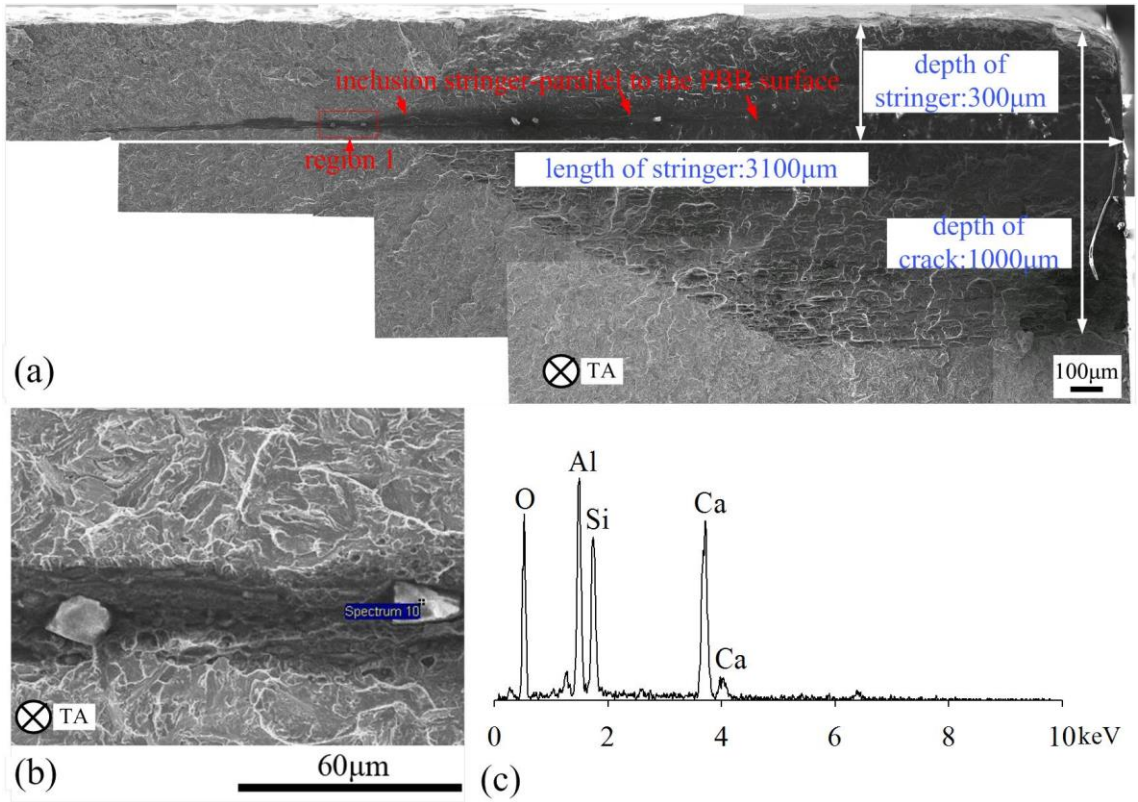


Figure 4- 51 (a) Fracture surface of PBB T0 shot peened sample under SEM, where an inclusion stringer parallel to the specimen surface is observed; (b) inclusion in region 1; (c) EDS results indicating the inclusion is MnS.

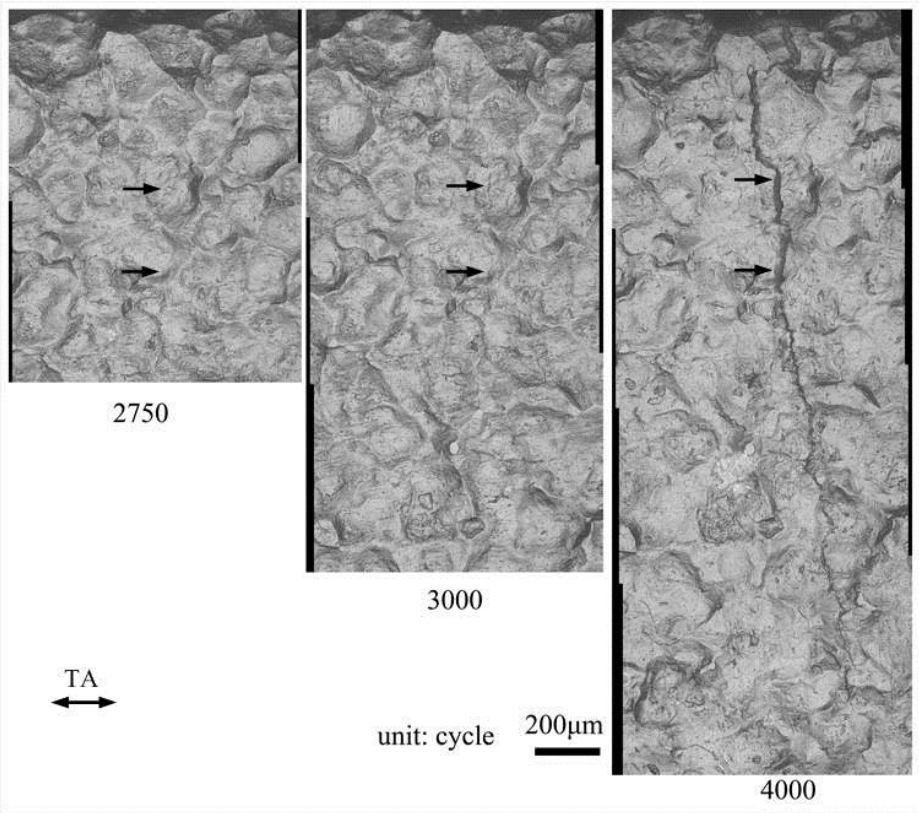


Figure 4- 52 Crack morphology at various fatigue stages for cracks in the PBB T0 shot peened condition.

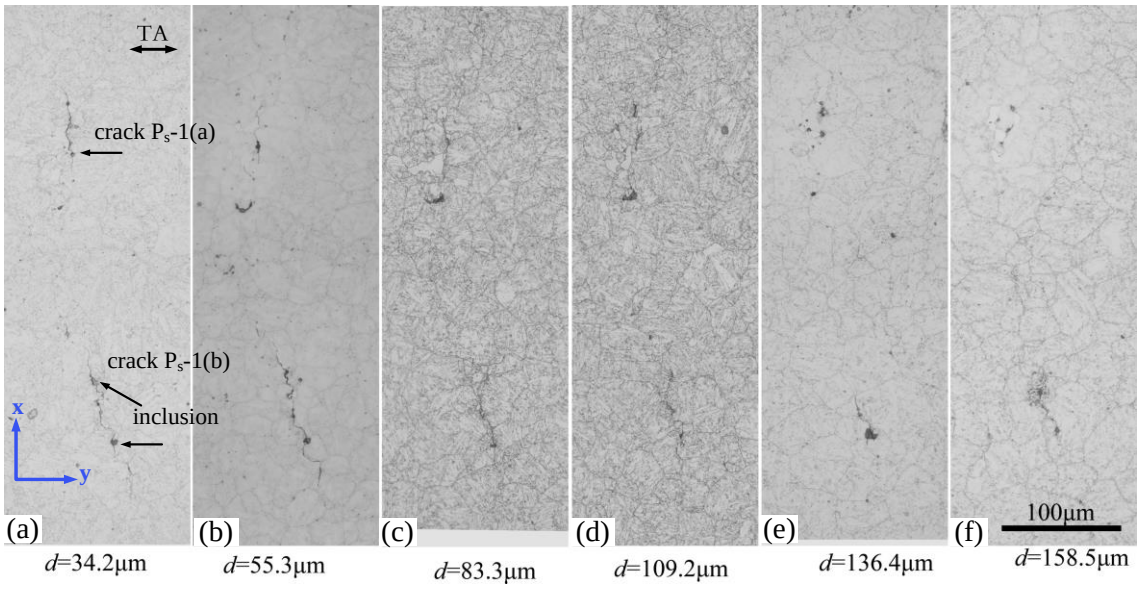


Figure 4- 53 2D slices of the serial sectioning illustrating the varied morphology of crack $P_s$-1 at different depths beneath the surface. MnS particles are observed on both the crack paths of crack $P_s$-1(a) and crack $P_s$-1(b).

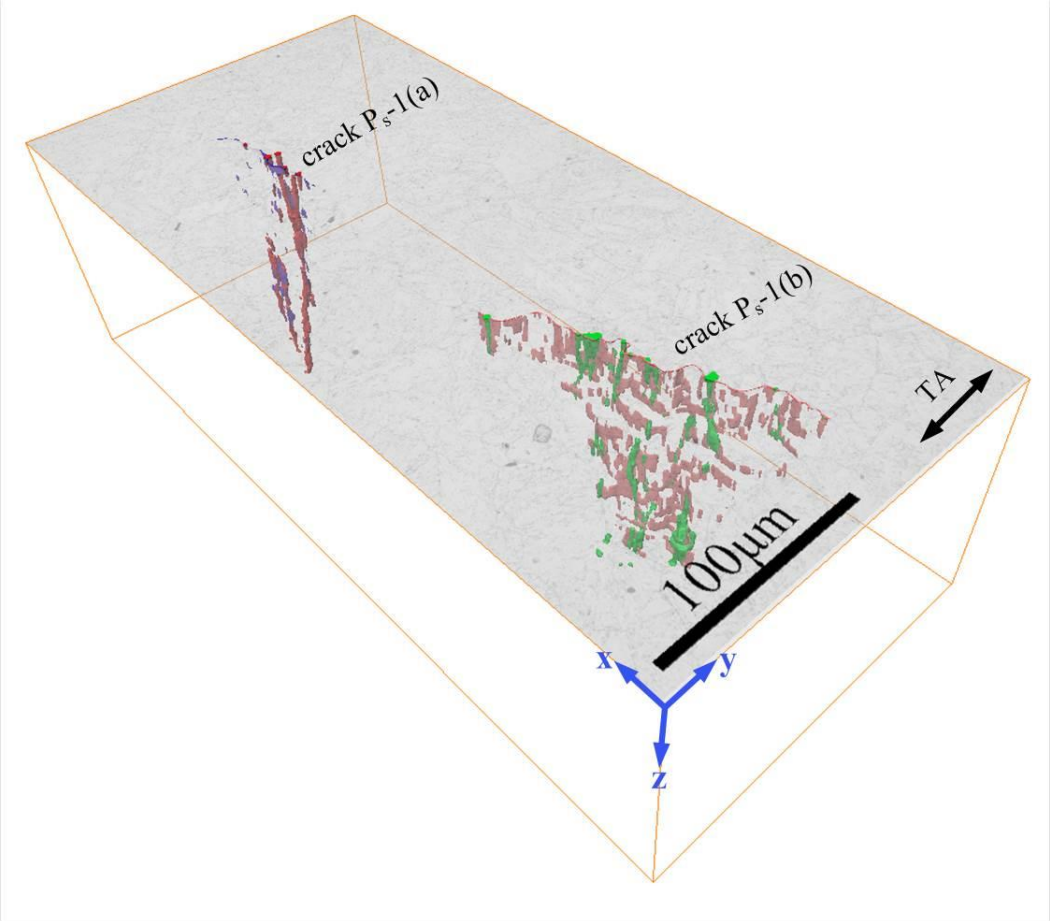


Figure 4- 54 3D reconstruction view of crack $P_s$-1 based on 2D slices of the serial sectioning. The red and green regions indicate the MnS, while the blue and orange coloured regions represent the fatigue crack.

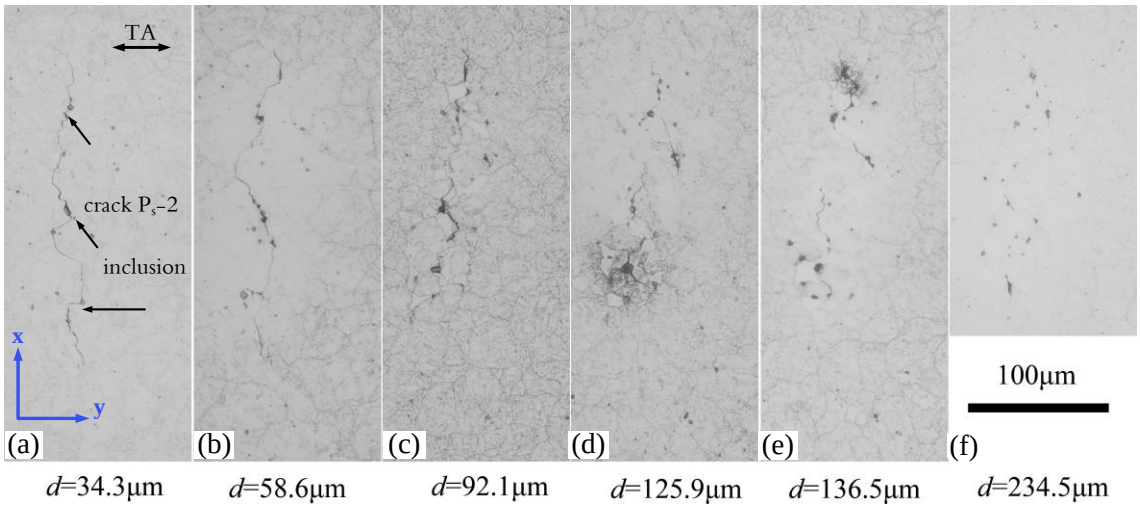


Figure 4- 55 2D slices of the serial sectioning illustrating the varied morphology of crack $P_s$-2 at different depths beneath the surface.

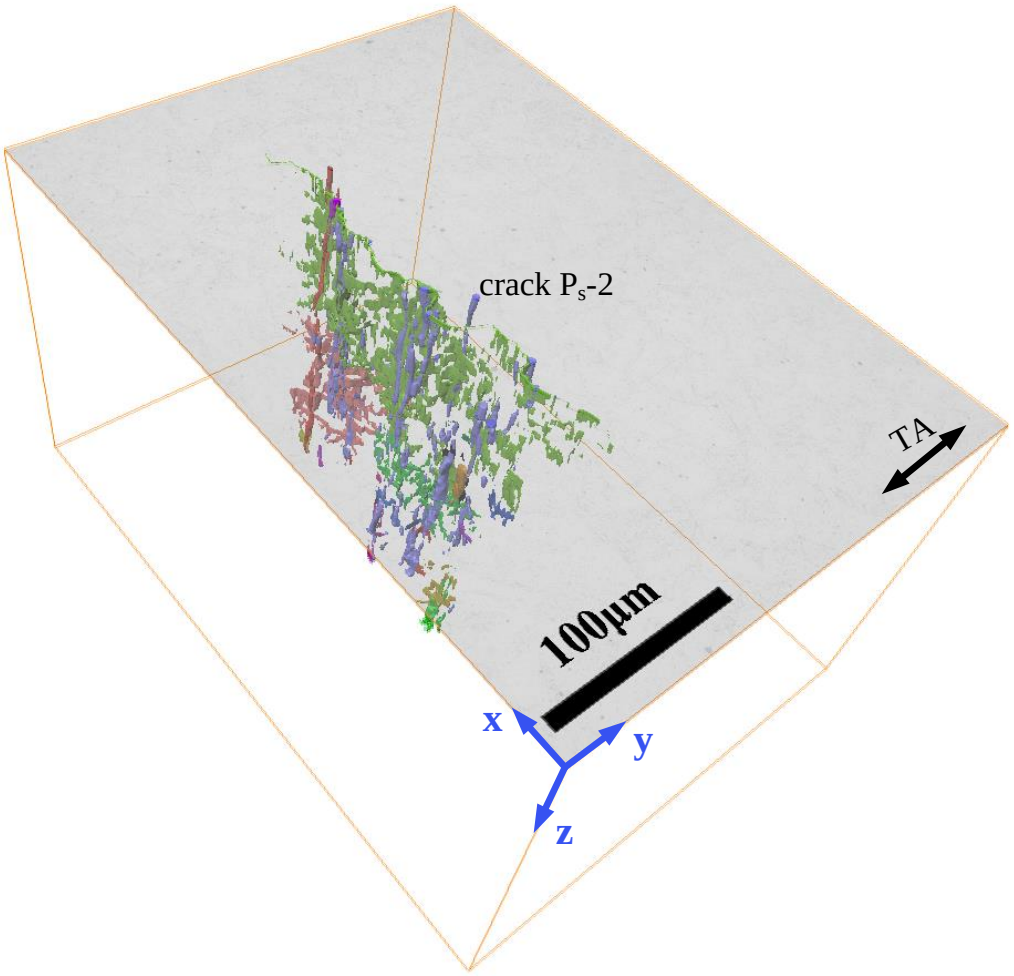


Figure 4- 56 3D reconstruction view of crack $P_s$-2 based on 2D slices of the serial sectioning. The green and red regions represent the fatigue crack while the MnS particles are coloured blue.

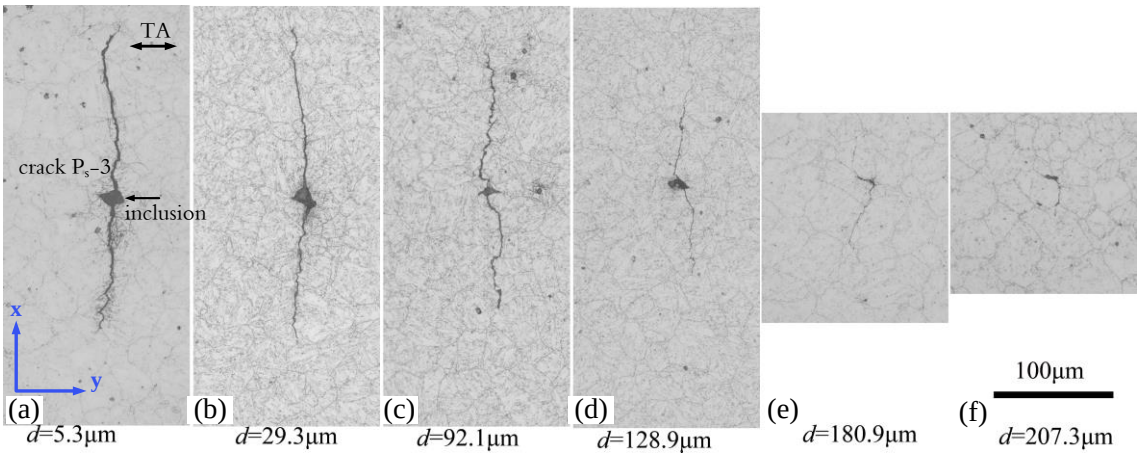


Figure 4- 57 2D slices of the serial sectioning illustrating the varied morphology of crack $P_s$-3 at different depths beneath the surface.

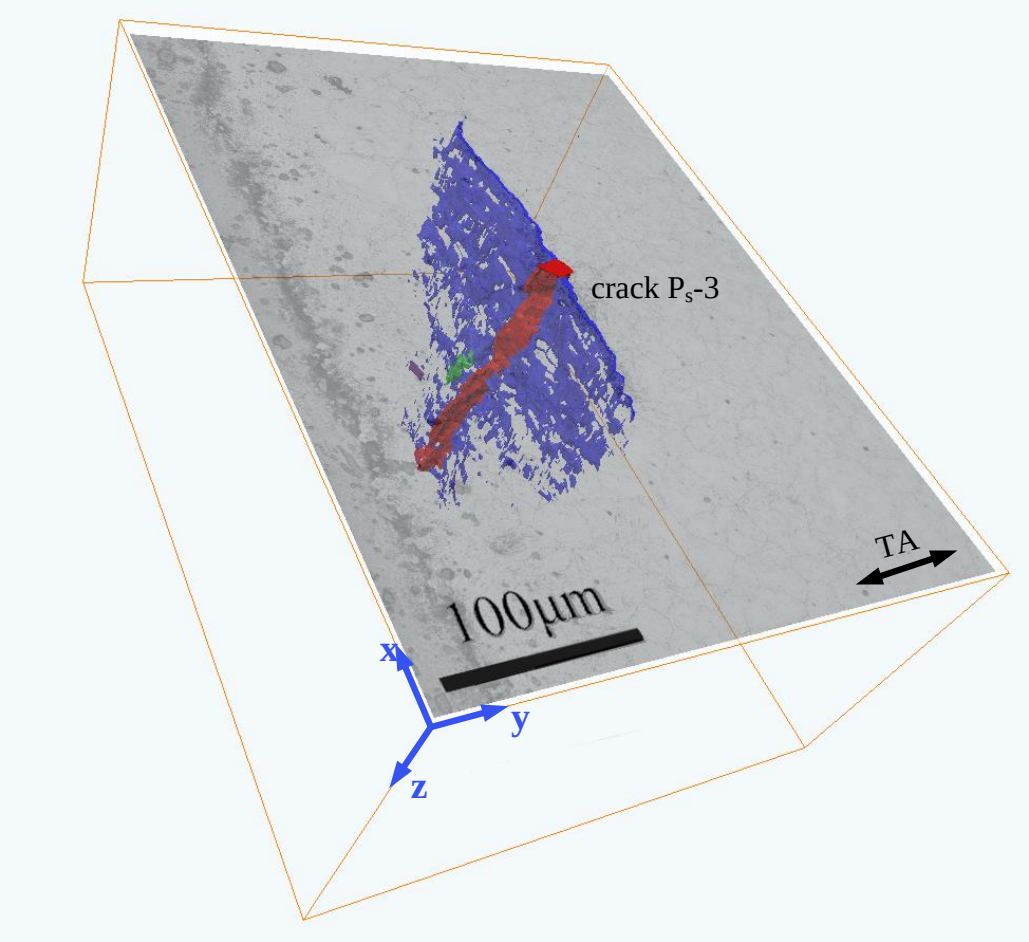


Figure 4- 58 3D reconstruction view of crack $P_s$-3 based on 2D slices of the serial sectioning. The blue regions represent the fatigue crack while the alumina stringers are coloured red and green.

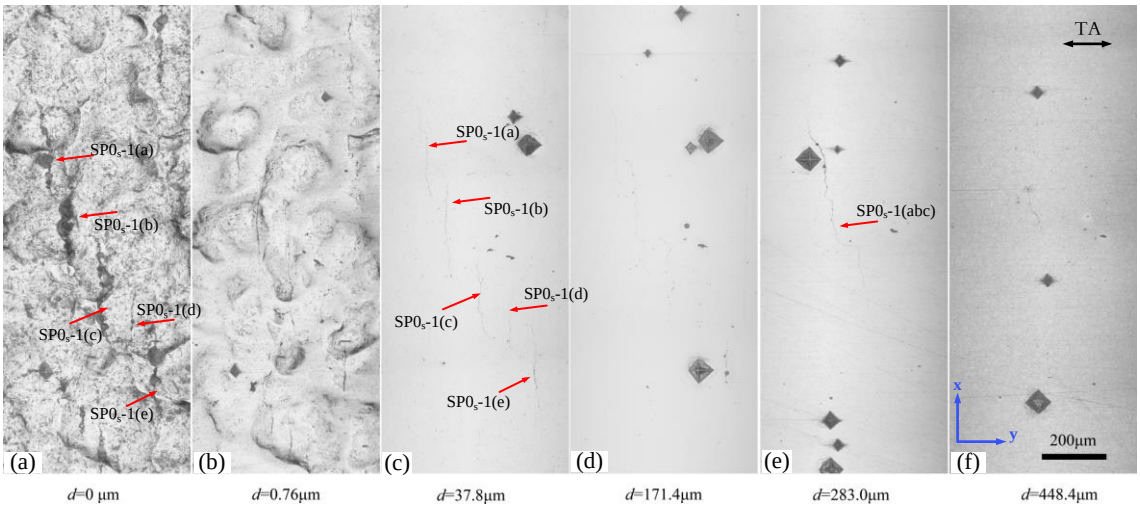


Figure 4- 59 2D slices of the serial sectioning illustrating the varied morphology of crack $SP0_s$-1 at different depths beneath the surface.

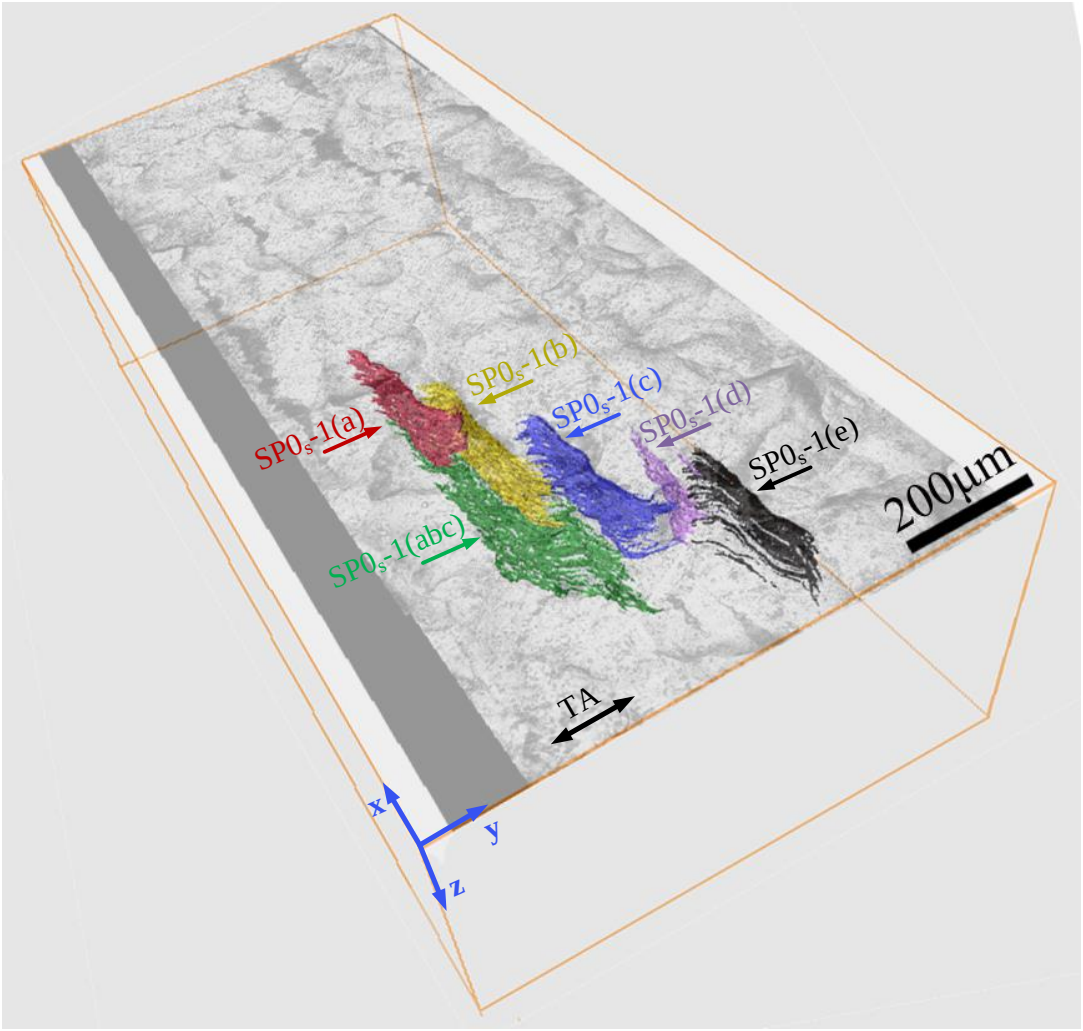


Figure 4- 60 3D reconstruction view of crack $SP0_s$-2 based on 2D slices of the serial sectioning. The cracks recognized on the shot peened surface are labelled as crack $SP0_s$-(a), $SP0_s$-(b), $SP0_s$-(c), $SP0_s$-1(d), $SP0_s$-1(e), and coloured red, yellow, blue, pink and black, respectively. The sub-surface coalesced crack is indicated by the green crack $SP0_s$-1(abc).

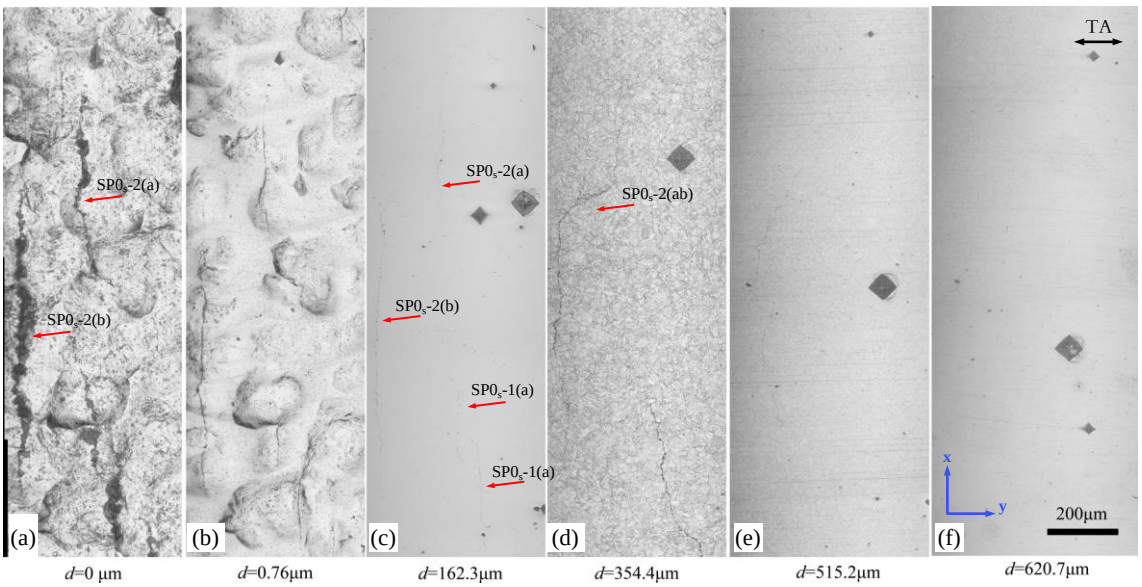


Figure 4- 61 2D slices of the serial sectioning illustrating the varied morphology of crack $SP0_s$-2 at different depths beneath the surface.

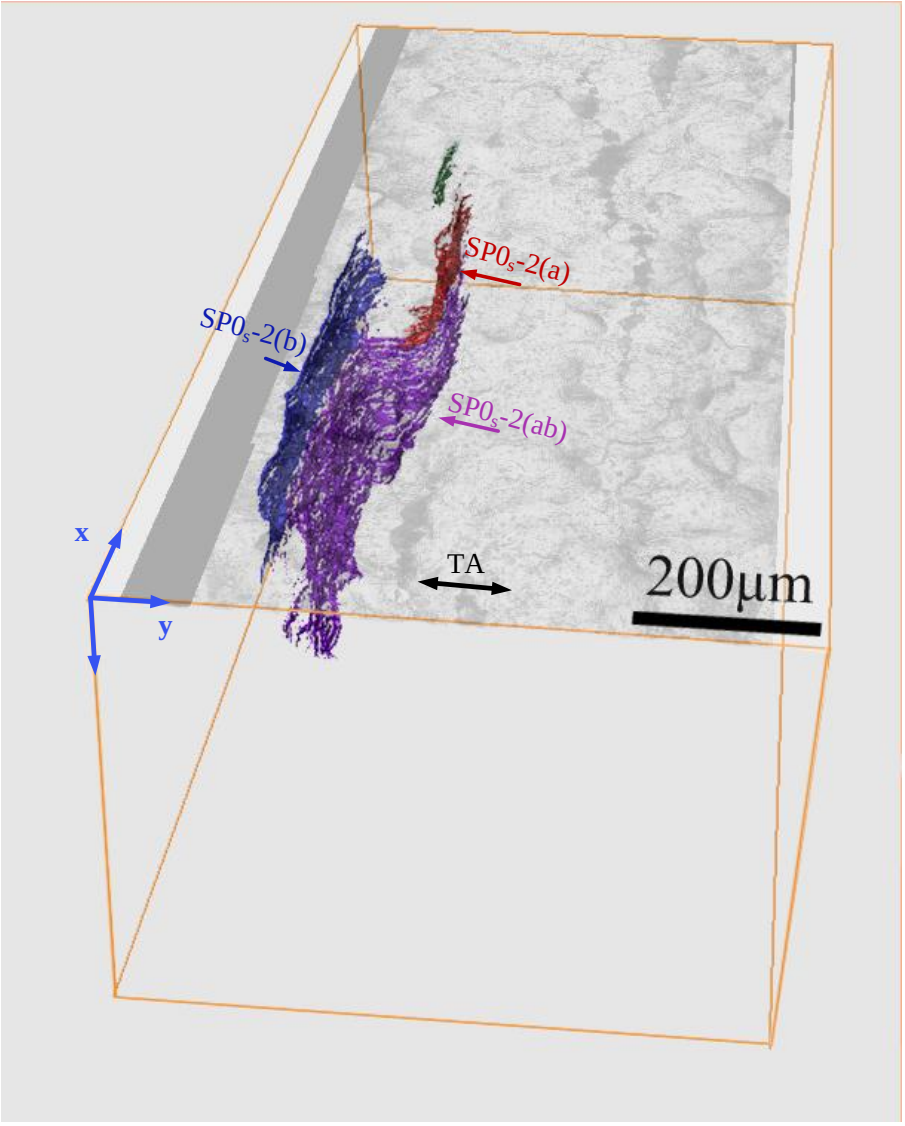


Figure 4- 62 3D reconstruction view of crack $SP0_s$-2 based on 2D slices of the serial sectioning. The cracks recognised on the shot peened surface are labelled as crack $SP0_s$-2(a), $SP0_s$-2(b), and coloured red and yellow, respectively. The sub-surface coalesced crack is indicated as a purple crack $SP0_s$-2(ab).

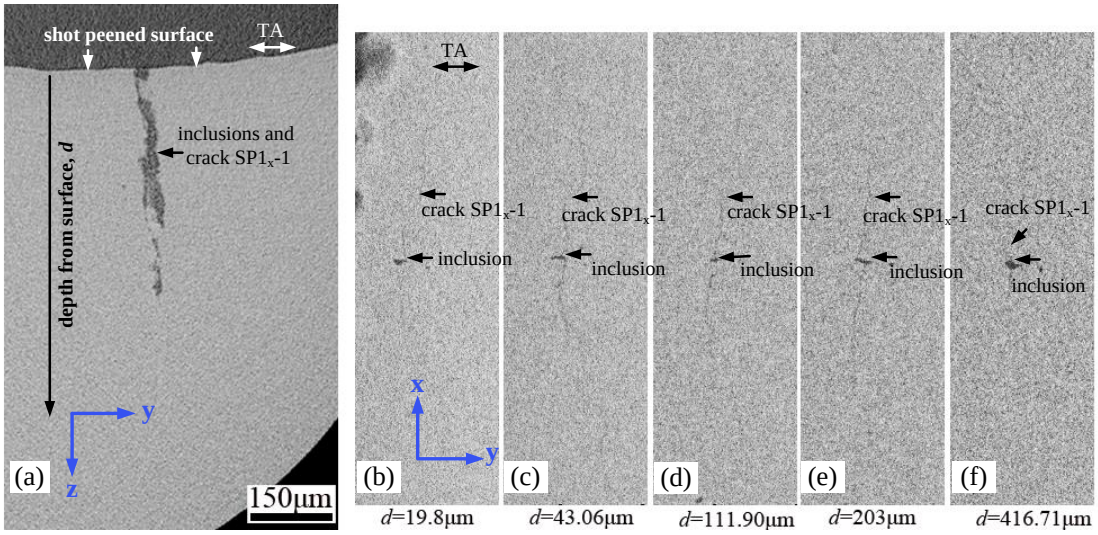


Figure 4- 63 (a) Reconstruction of a single 2D slice of the cross section of fatigue crack SP1$_x$-1 and inclusions in T1 shot peened case by CT images; (b)-(f) series of 2D reconstruction of X-Y plane showing the fatigue crack SP1$_x$-1 and its morphology change along the depth direction.

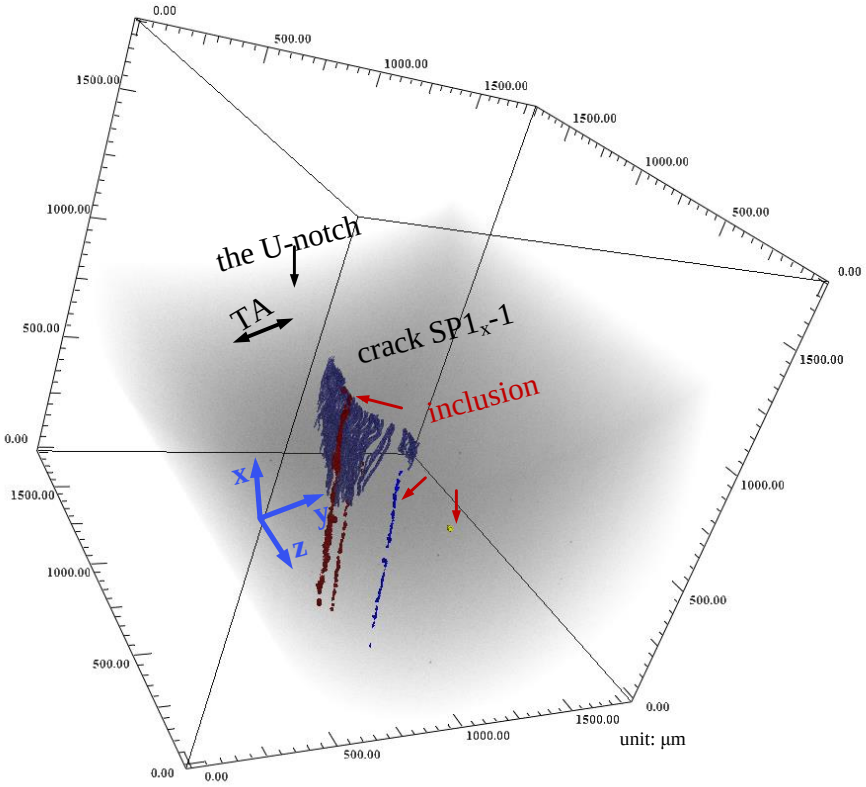


Figure 4- 64 3D reconstruction of the segmented fatigue crack SP1$_x$-1 and inclusion in T1 shot peened conditions by CT images. The fatigue crack was labelled blue while the inclusions are red, yellow as well as light blue; the opaque region indicates the matrix volume.

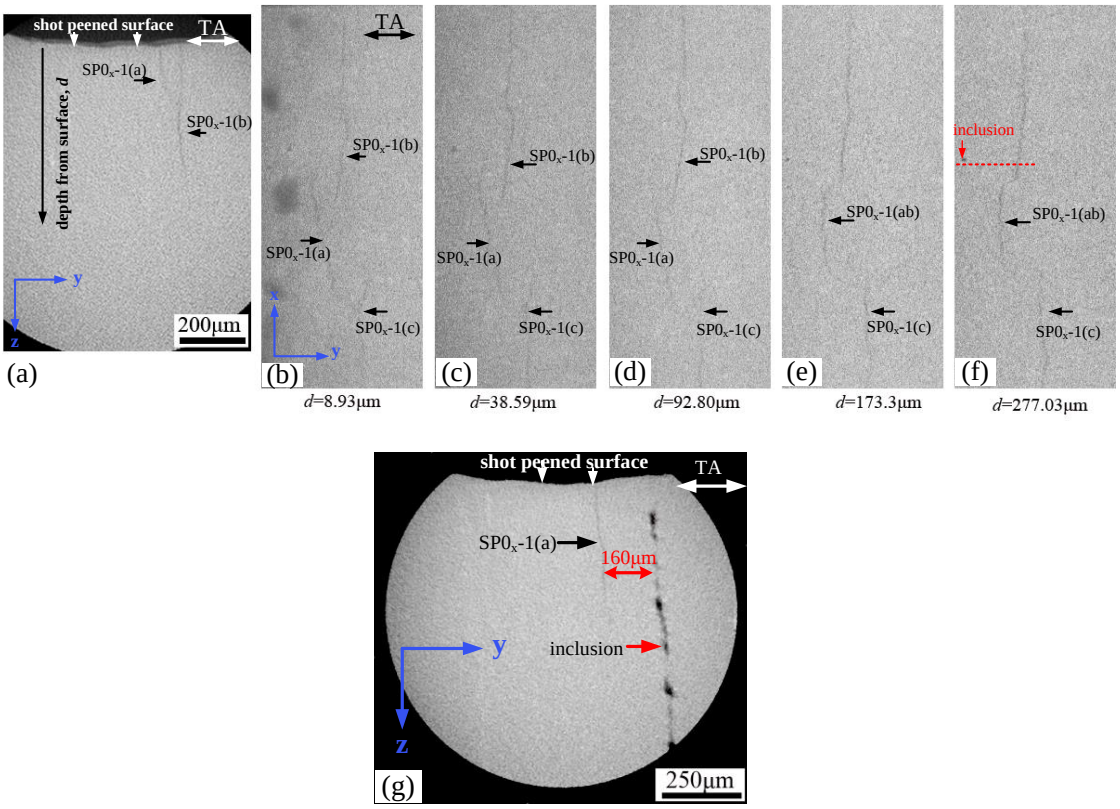


Figure 4- 65 (a) Reconstruction of a single 2D slice of the cross section of fatigue crack $SP0_x$-1(a) and $SP0_x$-1(b) in T0 shot peened condition by CT images: (b)-(f) series of 2D reconstruction of X-Y plane showing the $SP0_x$-1(a), $SP0_x$-1(b) $SP0_x$-1(c), indicating how the crack morphologies change along the depth direction; (g) shows the cross section of crack $SP0_x$-1(ab) and the inclusion stringer.

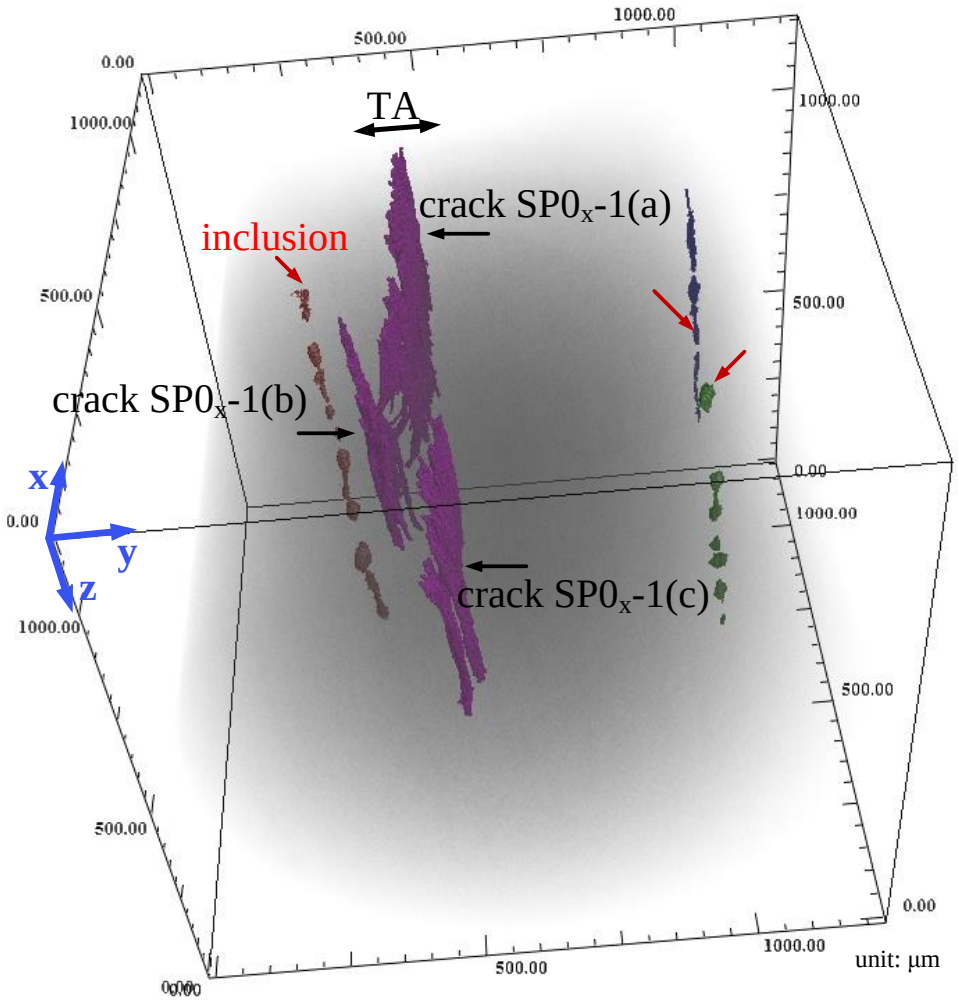


Figure 4- 66 3D reconstruction of fatigue crack and inclusion in T0 shot peened conditions by CT images. The fatigue crack was labelled blue while the inclusions were in red, yellow as well as a light blue colour; the opaque region indicates the matrix volume.

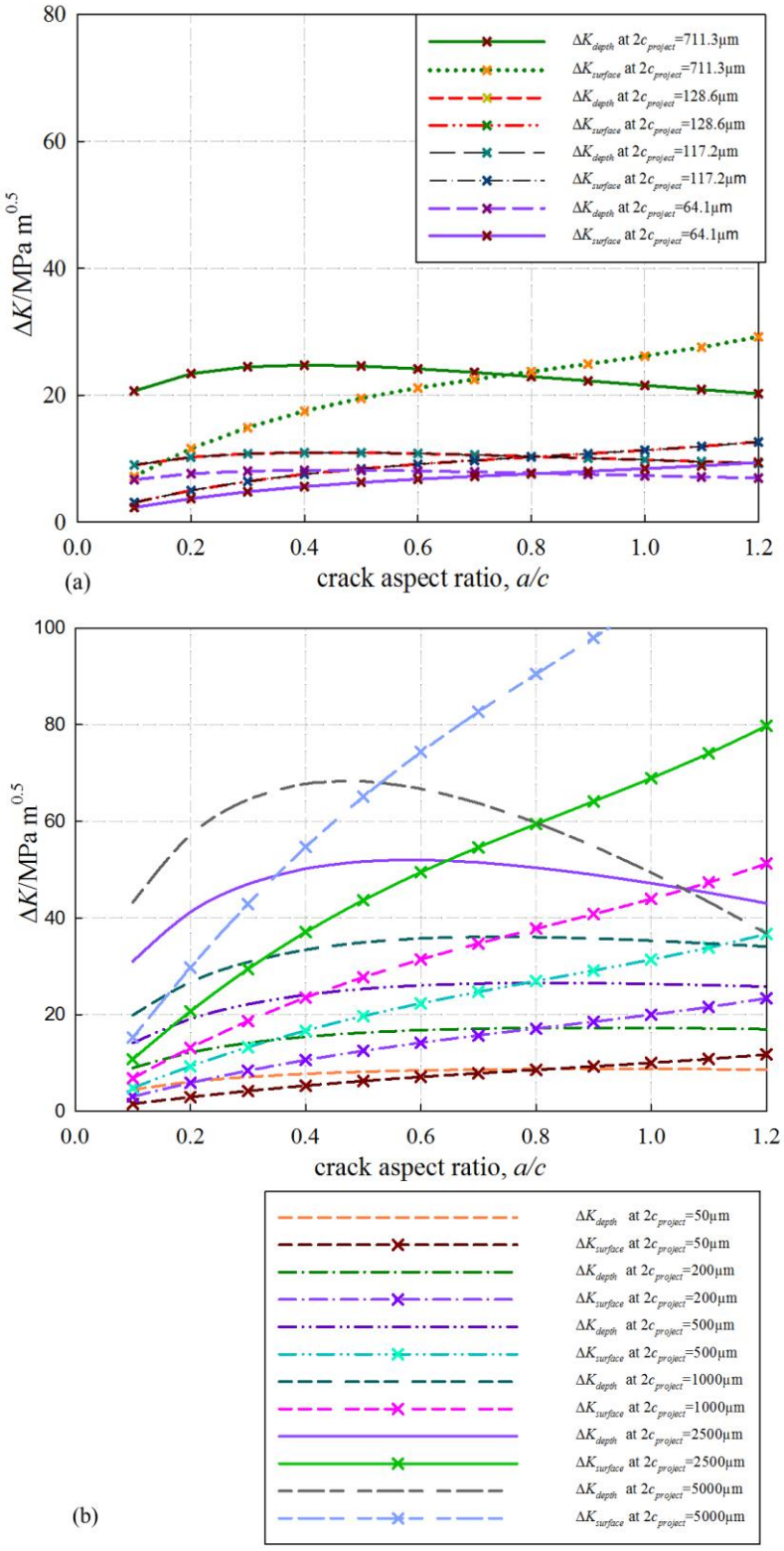


Figure 4- 67 (a) $\Delta K$ at various $a/c$ conditions assuming fatigue area was fixed (not considering the shot peening effects); (b) $\Delta K$ at various surface crack lengths $2c_{project}$.

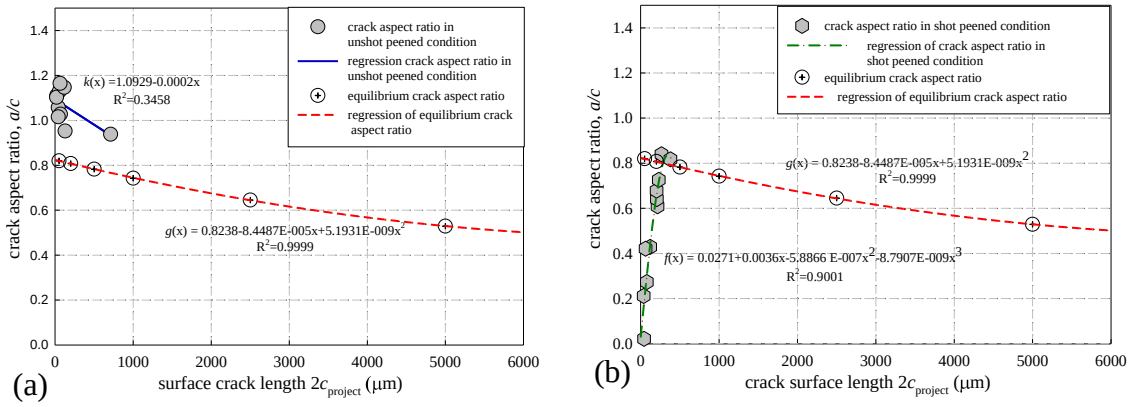


Figure 4- 68 *a/c* evolution in (a) non-shot peened and (b) shot peened conditions.

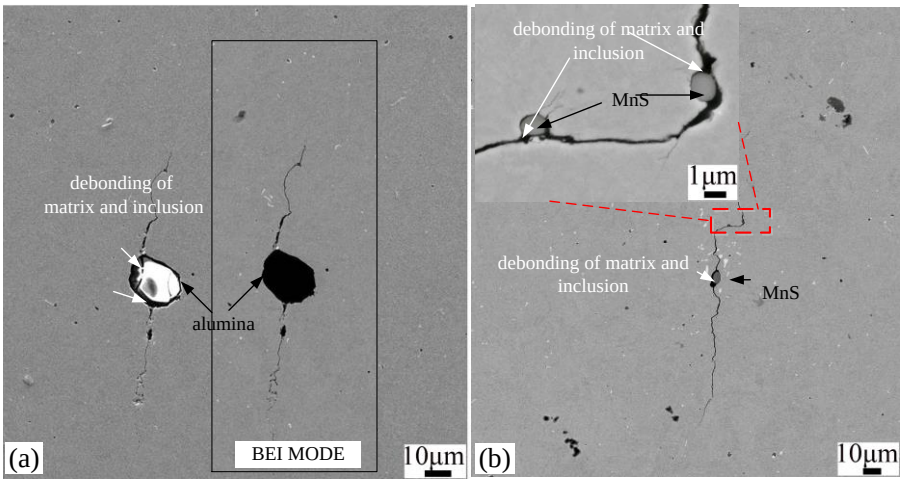


Figure 4- 69 The debonding of matrix and (a) alumina, and (b) MnS found on the fatigue crack paths at a depth of 200 μm.

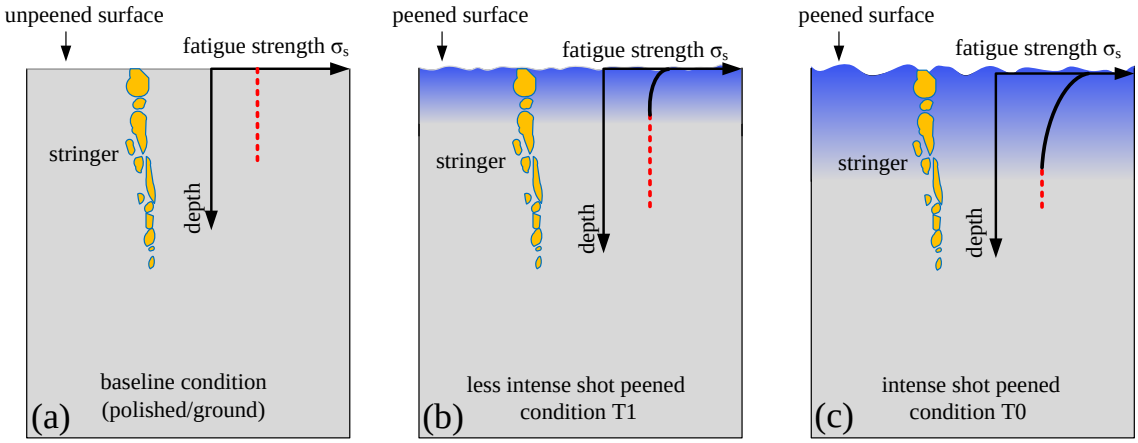


Figure 4- 70 A schematic of the fatigue limit in the near surface layers based on the microhardness values as a function of depth beneath the shot peened surface (assuming the areas of stringers are the same in these three conditions): (a) baseline condition: (b) less intense shot peened condition T1 and (c) intense shot peened condition T0.

## 4.7 References

[1] E.R. De los Rios, A. Walley, M.T. Milan, G. Hammersley, *Fatigue crack initiation and propagation on shot-peened surfaces in A316 stainless steel*, International Journal of Fatigue, 17 (1995) 493–499.
[2] Y.K. Gao, X.R. Wu, *Experimental investigation and fatigue life prediction for 7475-T7351 aluminum alloy with and without shot peening-induced residual stresses*, Acta Materialia, 59 (2011) 3737–3747.
[3] J. Lindemann, C. Buque, F. Appel, *Effect of shot peening on fatigue performance of a lamellar titanium aluminide alloy*, Acta Materialia, 54 (2006) 1155–1164.
[4] Y. Mutoh, G.H. Fair, B. Noble, R.B. Waterhouse, *The effect of residual stresses induced by shot-peening on fatigue crack propagation in two high strength aluminium alloys*, Fatigue & Fracture of Engineering Materials & Structures, 10 (1987) 261–272.
[5] I.E. Kopsov, *The influence of hammer peening on fatigue in high-strength steel*, International Journal of Fatigue, 13 (1991) 479–482.
[6] A.M. Eleiche, M.M. Megahed, N.M. Abd-Allah, *The shot-peening effect on the HCF behavior of high-strength martensitic steels*, Journal of Materials Processing Technology, 113 (2001) 502–508.
[7] L. Wagner, *Effect of mechanical surface treatments on fatigue performance of titanium alloys*, in: R.R. Boyer, D. Eylon, G. Lutjering (Eds.) fatigue Behaviour of Titanium Alloys, TMS, Warrendale, PA, 1999, pp. 253 – 265.
[8] P. Zhang, J. Lindemann, *Influence of shot peening on high cycle fatigue properties of the high-strength wrought magnesium alloy AZ80*, Scripta Materialia, 52 (2005) 485–490.
[9] K. Dalaei, B. Karlsson, L.E. Svensson, *Stability of shot peening induced residual stresses and their influence on fatigue lifetime*, Materials Science and Engineering: A, 528 (2011) 1008–1015.
[10] K.A. Soady, *Life assessment methodologies incoroporating shot peening process effects: mechanistic consideration of residual stresses and strain hardening part 1-effect of shot peening on fatigue resistance*, Materials Science and Technology, 29 (2013) 637–651.
[11] K.A. Soady, B.G. Mellor, P.A.S. Reed, *Life assessment methodologies incorporating shot peening process effects: mechanistic consideration of residual stresses and strain hardening: a review. Part 2: approaches to fatigue lifing after shot peening* Materials Science and Technology, 29 (2013) 652–664.
[12] K.A. Soady, B.G. Mellor, J. Shackleton, A. Morris, P.A.S. Reed, *The effect of shot peening on notched low cycle fatigue*, Materials Science and Engineering a-Structural Materials Properties Microstructure and Processing, 528 (2011) 8579–8588.
[13] K.A. Soady, B.G. Mellor, G.D. West, G. Harrison, A. Morris, P.A.S. Reed, *Evaluating surface deformation and near surface strain hardening resulting from shot peening a tempered martensitic steel and application to low cycle fatigue*, International Journal of Fatigue, 54 (2013) 106–117.
[14] B.Y. He, K.A. Soady, B.G. Mellor, A. Morris, P.A.S. Reed, *Effects of shot peening on short crack growth rate and resulting low cycle fatigue behaviour in low pressure turbine blade material*, Materials Science and Technology, 29 (2013) 788–796.
[15] K.A. Soady, *Reducing conservatism in life assessment approaches: Industrial steam turbine blade to disc interfaces and the shot peening process*,

in: Engineering Sciences Unit, Ph.D thesis, the University of Southampton, 2013.
[16] E.J. Pavlina, C.J. Tyne, *Correlation of yield strength and tensile strength with hardness for steels*, Journal of Materials Engineering and Performance, 17 (2008) 888-893.
[17] Y. Murakami, M. Isida, *Analysis of An Arbitrarily Shaped Surface Crack and Stress Field at Crack Front near Surface*, Transactions of the Japan Society of Mechanical Engineers Series A, 51 (1985) 1050-1056.
[18] Y. Murakami, *Analysis of stress intensity factors of modes I, II and III for inclined surface cracks of arbitrary shape*, Engineering Fracture Mechanics, 22 (1985) 101-114.
[19] Y. Murakami, M. Endo, *Effects of Hardness and Crack Geometries on Delta K sub th of Small Cracks Emanating From Small Defects*, Mechanical Engineering Publications, The Behaviour of Short Fatigue Cracks, (1986) 275-293.
[20] Y. Mutoh, G.H. Fair, B. Noble, R.B. Waterhouse, *The effect of residual stresses induced by shot peening on fatigue cracks propagation in two high strength aluminium alloys*, Fatigue & Fracture of Engineering Materials & Structures, 10 (1987) 261-272.
[21] B.Y.He, K.A. Soady, B.G. Mellor, P.A.S. Reed, *Fatigue crack growth behaviour in the LCF regime in a shot peened steam turbine blade material*, accepted by Internation Journal of Fatigue, (2015).
[22] J.Y. Buffiere, E. Ferrie, H. Proudhon, W. Ludwig, *Three-dimensional visualisation of fatigue cracks in metals using high resolution synchrotron X-ray micro-tomography*, Materials Science and Technology, 22 (2006) 1019-1024.
[23] K.S. Ravichandran, J.M. Larsen, *Effects of crack aspect ratio on the behavior of small surface cracks in fatigue: Part II. experiments on a titanium (Ti-8Al) alloy*, Metallurgical and Materials Transactions A, 28 (1997) 157-169.
[24] K.S. Ravichandran, *Effects of crack aspect ratio on the behavior of small surface cracks in fatigue: Part I. simulation*, Metallurgical and Materials Transactions A, 28 (1997) 149-156.
[25] D. Shiozawa, Y. Nakai, T. Murakami, H. Nosho, *Observation of 3D shape and propagation mode transition of fatigue cracks in Ti-6Al-4V under cyclic torsion using CT imaging with ultra-bright synchrotron radiation*, International Journal of Fatigue, 58 (2014) 158-165.
[26] Y. Mutoh, I. Sakamoto, *Fatigue crack propagation in the weld bond region of a type 304 stainless steel weldment*, in: S.R. Valluri, D.M.R. Taplin, P.R. Rao, J.F. Knott, R. Dubey (Eds.) Proceedings of the 6th International Conference on Fracture (ICF6), Pergamon, New Delhi, India, 1984.
[27] J. Lankford, F.N. Kusenberger, *Initiation of fatigue cracks in 4340 steel*, Metallurgical Transactions, 4 (1973) 553-559.
[28] K. Tanaka, T. Mura, *A theory of fatigue crack initiation at inclusions*, Metallurgical Transactions A, 13 (1982) 117-123.
[29] in: British Standard, BS EN ISO 6507-1:2005:Metallic materials - Vickers hardness test - Part 1: Test method, 2005.
[30] R. Steiner, *ASM Handbook Volume 1: Properties and selection: Irons, Steels, and High-Performance Alloys*, 1990.

# Chapter 5: Short fatigue crack behaviour

## 5.1 Introduction

As stated in Section 2.2.4, short fatigue cracks can be defined in several different ways. The most important to the present work is whether the crack length is comparable to the scale of local plasticity, e.g. a crack that is in the plastic zone of a notch, or indeed in the region of material affected by shot peening plasticity, or if the crack length is physically small (e.g 0.5 ~ 1 mm). In Chapter 3 and Chapter 4, qualitative insights have been gained about the combined effect of the surface roughness, strain hardened layer, and compressive residual stress induced by the shot peening process on the fatigue crack behaviour in the early stages of fatigue by interrupted fatigue tests. To be able to predict the fatigue life of a shot peened component from local stress and strain or fracture mechanics parameters, it is essential to understand the micromechanisms by which the crack first initiates in and then propagates through the shot peened affected layer. Therefore, the aim of this chapter is to quantify short fatigue crack behaviour systematically in samples containing stress concentration features that are subjected to LCF loading with varied surface conditions.

This work in this chapter has been published in two papers (listed below), and the chapter also contains some additional discussion on the effect of crack coalescence on fatigue growth behaviour, which is based on Scott and Thorpe's review papers (as stated in Chapter 4). The two published papers that form part of this thesis work are:

1) B.Y. He, K. A. Soady, B.G. Mellor, A. Morris and P. A. S. Reed. Effect of shot peening on short crack growth rate and resulting low cycle fatigue behavior in low pressure turbine blade material. Materials Science and Technology. 29(7), 2013, 788-796.
2) B.Y. He, K.A. Soady, B. G. Mellor and P. A. S. Reed. Fatigue crack growth behaviour in the LCF regime in a shot peened steam turbine blade material. In press. International Journal of Fatigue. March 2015.

## 5.2 Experimental methods

### 5.2.1 Short fatigue crack testing on U-notch samples

As detailed fully in Section 4.2.1, short fatigue crack behaviour was also evaluated by three point bend tests at ambient temperature with a sinusoidal waveform and at a frequency of 20 Hz in U-notched samples. Polished, ground, T0 and T1 shot peened conditions are the main focus in this short fatigue crack assessment. Again, short fatigue crack behaviour in these four different surface conditions are compared in terms of a similar applied (nominal) local strain range condition $\Delta\varepsilon_{11}$ = 0.68 % in the notch root.

### 5.2.2 Crack length measurement based on replicas taken during fatigue testing

To assess the effect of the shot peening process on crack growth behaviour, a replication technique was used to monitor crack initiation and short crack growth. A replica of the U notch top surface was taken every 1000 cycles until a crack was first clearly observed, and then every 500 cycles until failure. Possible crack initiation points were identified, and crack growth rates of surface cracks were calculated from the replica record. The replica material used in the current project was RepliSet-F5 (Struers Ltd). Replicas were analysed using an Olympus BX51 polarised light microscope, and crack images were stitched together by FIJI Image software so as to present an overview of these cracks. Measurements of the crack length from the digital images of the replica record were performed using Image-Pro Plus software after hand tracing along the crack's length, which makes the explicit measurement of these zigzag crack paths possible. During calculation, a calibration file automatically transforms pixel values to lengths in micrometres. Both the real surface crack length $2c$ and projected crack lengths $2c_{proj}$ were recorded. All the $2c$ and $2c_{proj}$ of cracks were measured at least 3 times, and the averaged value was taken. In the present research, half surface crack length $c$ was used to calculate crack growth rates by applying the secant method:

$$\frac{dc_i}{dN_i} = \frac{c_{i+1} - c_{i-1}}{N_{i+1} - N_{i-1}} \qquad \text{Equation 5- 1}$$

where $i$ is the datum taken at a particular replica interval during the fatigue process, $N_i$ is the number of fatigue cycles at that replica interval and $c_i$ is crack length at $N_i$ cycles. Since averaged crack length was taken to calculate the crack growth rate $dc/dN$, uncertainty will appear in this secant method especially when the crack propagated slowly or even show non-propagated. However, this uncertainty should still be controlled less than 5%. Detailed fractographic analysis of the fracture surfaces and notch roots was also carried out in a JEOL JSMT300 SEM, operating at an accelerating voltage of 15 KV, as stated in Section 4.2.2.

## 5.3 Experimental results

### 5.3.1 Fractography and qualitative analysis of the replica records

The number of cycles to failure, at the same nominal local strain range ($\Delta\varepsilon_{11}$ = 0.68 %) of the polished, ground, T1 and T0 conditions are 25353, 22816, 22745 and 54504 cycles, respectively, as can be seen in the S/N curve in Figure 5- 1. Under similar applied strain range conditions, the fatigue life of the polished, ground and T1 cases are quite similar, while the T0 case still shows significant benefit from the shot peening process, even in this low cycle fatigue regime. The fracture surfaces of these failed samples under the optical microscope are presented in Figure 5- 2. Comparing the top surfaces of the notch, and the number of ratchet marks on the fracture surfaces, it is clear that the cracks on the un-peened samples (polished and ground) are fewer than those in shot peened cases (T0 and T1) and more widely distributed across the notch root. In addition in the polished and T0 shot peened cases, one (or two) fatigue cracks appear much larger and to have dominated during the fatigue process. While in the ground and T1 shot peened cases, several cracks of similar depth appear to have initiated and grown roughly at the same time together at similar numbers of cycles. The fracture surfaces of the polished and ground samples appear very similar under the SEM, as shown in Figure 5- 3 and Figure 5- 4, respectively. Replica silicone was found on both fracture surfaces. Compared to the fracture surface of the unpeened samples, there are more ratchet marks in the T0 condition, as illustrated in Figure 5- 5(a) and these ratchet marks are finer, which can be related to the number of crack initiation sites. Figure 5- 5(b) and (c) is a region between two ratchet marks,

which is a possible sub-surface crack initiation site. On the T1 fracture surface in Figure 5- 6(a), stringers can be identified clearly in these regions between the ratchet marks, for example, region A and region B, as shown in Figure 5- 6 (b) and (c), respectively. This corresponds with the results and discussion section in Chapter 4 which indicates that the crack initiation behaviour in the T1 (lower intensity shot peened) sample combines the features of both the T0 and baseline ground/polished conditions. Figure 5- 6(d) is an example of a crack initiated from the shot peened surface.

Assuming that there is a fatigue crack initiated between each pair of ratchet marks, the number of ratchet marks can be used to estimate the number of initiation sites. As illustrated in Figure 5- 7 (based on previous work [1]), the larger the strain range in a given condition, the more initiation sites are produced during the fatigue process. Based on the number of ratchet marks on the fracture surface, 18 crack initiation sites were found in the T0 condition, while only 11 initiation sites were observed in each of the polished and ground baseline cases and only 7 initiation sites were observed in the less intense shot peening process (T1). Based on the replication studies, cracks in the early fatigue stages were very small and so ratchet marks left by very early stage crack coalescence may not be easy to distinguish from the final fracture surface. Compared to the shot peened cases, crack coalescence in the ground sample occurred infrequently even near the end of fatigue life, partly because there were significantly fewer initiation sites.

The fatigue test was interrupted by replication in order to obtain short fatigue crack initiation and propagation data. The fatigue cracks obtained from the replica at different stages of the fatigue life for all four surface conditions are presented in Figure 5- 8. The cracks discussed in this chapter will be labelled as crack $P_f$-1, $P_f$-2, …, crack $G_f$-1, $G_f$-2, …, crack $SP0_f$-1, $SP0_f$-2, … and crack $SP1_f$-1, $SP1_f$-2 to indicate those cracks in polished, ground, T0 and T1 shot peened conditions, respectively, where the subscript “f” indicates it is from a short fatigue crack test. Figure 5- 8(a) shows one of these replica records obtained from the polished notch sample. The longest crack (crack $P_f$-2) at this stage (83.3 % of fatigue life) is about 2000 μm, while the second longest (crack $P_f$-1) is about 800 μm in surface length. The cracks reported in the present research are those that coalesced in the late stages of fatigue life and hence led to final failure. In a quantitative analysis, it is necessary to also evaluate the

development of crack morphology at different fatigue stages, which should in turn provide a better understanding of the crack behaviour. Combined with the fracture surface and replica records, the cracks leading to the final fatigue failure were easily identified. In this polished notch case, crack $P_f$-1 and $P_f$-2 (shown in Figure 5- 8(a)) were such cracks. Crack $P_f$-2 was the first crack initiated on the polished surface at around 50 ~ 60 % of fatigue life.

Figure 5- 8(b) is a replica record from the ground sample taken at about 94.2 % of fatigue life. Even near the very end of fatigue life, only four cracks were visible on the notch surface, namely crack $G_f$-1, $G_f$-2, $G_f$-3, $G_f$-4. These cracks coalesced and led to the final failure, thus the fatigue crack analysis in the ground condition is based on these four cracks. However, in both T0 and T1 cases, an overview of all the fatigue cracks was harder to observe from the surface replica record (due to the roughness of the surface) even at the very end of fatigue life (95 % of T0 and 99 % for T1). In the T0 condition, crack $SP0_f$-1(a), $SP0_f$-1(b), $SP0_f$-2(a) and $SP0_f$-2(b), as labelled in Figure 5- 8(c) were studied in more detail. For the T1 sample, as can be seen from Figure 5- 8(d), the cracks are still not very evident.

By tracing back these replica records, crack morphologies at different fatigue stages can be characterized. Figure 5- 9 presents the crack $P_f$-2 morphologies at different fatigue stages (percentages of life) in the polished condition. At 98 % of fatigue life, replica material which has infiltrated the crack was observed, which indicates the crack was quite open near the end of life.

Figure 5- 10(a) shows the crack $G_f$-2 morphology development at different fractions of fatigue life. This crack was first captured at around 50 % of fatigue life. The fatigue cracks are parallel to the grinding direction which is also perpendicular to the maximum tensile stress direction. This crack was quite long already at 54.5 % of fatigue life, and the initiation area under higher magnification is also presented in the carefully labelled inset at the top left hand side in Figure 5- 10. The pre-existing grinding marks make it hard to distinguish the very early stages of crack growth. Once a crack forms it continues to propagate along the grinding marks. There are two initiation sites for crack $G_f$-2 and these two cracks coalesced at ~ 70 % of fatigue life, as indicated. After coalescence, the crack propagated symmetrically, at similar rates at both ends until 85.5 % of fatigue life, where the lower part of this crack

grew faster. An example of the fatigue crack preferentially propagating along the grinding marks is presented in Figure 5- 10(b).

The crack morphologies of crack $SP0_f$-2(b) at different fatigue stages are presented in Figure 5- 11(a). This crack on the rough shot peened surface was identified before the fatigue test. As the fatigue test continued, these 'pre-existing' cracks did not change length dramatically. At ~ 80 % of the fatigue life, the cracks started to propagate; after that, crack coalescence frequently occurred and secondary cracks also began to grow, leading to an overall faster growth rate. At the end of fatigue life, the crack identified as $SP0_f$-2(b) in Figure 5- 11(a) coalesced with other main cracks, for example $SP0_f$-2(a), then the sample failed. As previously mentioned, the surface roughness induced by the shot peening process in the present study is $R_a$ = 3.39 μm. Figure 5- 11(b) shows a crack that has initiated from a shot peened dimple on the notch surface; this would tend to support the viewpoint that the edges of the shot peening dimples act as stress concentrations with 'pre-existing cracks' (mentioned earlier) at the edges of shot peening dimples. Due to the small crack opening, and the rough surface condition, the observation of crack propagation in the T1 shot peened condition is quite difficult, as demonstrated by the crack morphologies of $SP1_f$-1 at different fatigue stages in Figure 5- 12. The difficulties in identifying such tiny cracks (or crack tips) in the T1 sample may in part contribute to the scattered crack growth data for T1, which will be discussed in the following section.

Based on the crack measurements from the replica record taken at different fatigue stages, the crack lengths as a function of fatigue cycles are presented in Figure 5- 13. To make a clear comparison between the different surface conditions, the variations in *c* at different numbers of cycles in the polished, ground, T0 and T1 condition are combined together and shown in Figure 5-13(a). It should be noted that all the fatigue cracks studied in the present research are the dominant (or primary) cracks which coalesced and led to the final failure. Half surface crack length *c* at different fatigue life ratios in all these four conditions are also illustrated in Figure 5- 13(b). Fatigue cracks in the baseline condition (polished and ground cases with little residual stress in the near surface layer) appeared at around 50 % of fatigue life and after that these cracks developed at a constant rate and accelerated near the end of fatigue life, when the main cracks coalesced, leading to failure. Although the

cracks in the T1 case were also clearly picked up at 50 % of fatigue life, they remained small without little apparent growth and coalesced toward the end of life. However, some of the cracks observed in the T0 case in the very early stages of fatigue life were pre-existing before cycling (for example, one of the initiating cracks was 51 μm, while the other one was 242 μm before any cyclic loading had been applied). This indicates that they were pre-existing on the shot peened surface (presumably from the shot peening process itself) and these pre-initiated cracks started to grow very slowly at ~ 0.1 – 0.2 of fatigue life but the crack lengths did not increase dramatically until 0.7~0.8 of fatigue life, where crack coalescence occurred frequently and secondary cracks also began to grow. Compared to the shot peened cases, crack coalescence in the unpeened (ground and polished) samples occurred infrequently even near the end of fatigue life, partly because there were significantly fewer initiation sites (and therefore cracks) during the fatigue process. Crack tortuosity $c/c_{project}$ at different crack lengths in the various surface conditions is described in Figure 5- 14. When the crack length $2c$ is less than 200 μm in polished or T0 surface, $c/c_{project}$ can get as high as 4 (for T0) and 2.2 (for the polished case) respectively; as the crack gets longer, the $c/c_{project}$ decreases gradually to ~ 1. For the ground and T1 case, however, $c/c_{project}$ was observed to be constant at around 1.

### 5.3.2 Short fatigue crack behaviour analysis

The corresponding fatigue crack growth rates *dc/dN* (calculated by the secant method) are plotted against crack length (in log-log form) in Figure 5- 15. Given the expected strain range in the notch root (ignoring any local effects of work hardening or compensating residual stresses), the *dc/dN* versus *c* data give a reasonable comparison of crack growth rates under similar externally imposed stress states. Highly scattered crack growth rates are observed in all cases, which is typical of short crack growth behaviour. It is noticeable that in the ground case, the crack growth rates are fairly constant (*dc/dN* levels of between $10^{-3}$ and $10^{-5}$ mm/cycle) during the fatigue process. The growth rates of the cracks on the T0 shot peened surface showed a wider range, generally increasing with crack length, and generally lower *dc/dN* values were observed (*dc/dN* levels of between $10^{-7}$ and $10^{-3}$ mm/cycle).

As described in Chapter 4, the crack aspect ratio *a/c* at early fatigue stages can be expressed as a function of surface crack length *c*. The crack depth *a* can be derived thereafter. For the sake of comparison, the calculation of crack depth *a* or stress intensity factor range $\Delta K$ crack aspect ratio *a/c* will be based on both a constant aspect ratio *a/c* = 0.8 (which is considered to the equilibrium crack shape) and the varying *a/c* ratio with *a*. Figure 5- 16(a) and (b) illustrate *da/dN* versus crack depth *a* (in log-log) based on a constant *a/c* (0.8) and varying *a/c* (as a function of *a*) respectively. Similarly to crack propagation rates on the surface, the predicted data points in *da/dN* are also quite scattered. When *a/c* is assumed constant, the scatter of the data points in all conditions are wider than in those when *a/c* is characterized as varying as a function of crack depth, so allowing for the *a/c* variation appears to help collapse the data somewhat.

As stated in Chapter 4, a Linear Elastic Fracture Mechanics (LEFM) calculation of the stress intensity factor range $\Delta K$ at both crack surface and maximum depth position is possible based on Scott and Thorpe's review paper [2]. A calculated local stress level ($\Delta\sigma_{11}$) of 1500 MPa [1] in the loading direction was used in calculating the short crack $\Delta K$ levels in the notch root. Figure 5- 17 illustrates the fatigue crack growth rates *dc/dN* (calculated by the secant method) for polished, ground, T0 and T1 notch samples plotted as a function of $\Delta K_{surface}$. In Figure 5- 17(a), $\Delta K_{surface}$ is calculated based on the assumption that *a/c* is constant at 0.8, while Figure 5- 17(b) considers the evolution of crack aspect ratio with crack depth. These data are highly scattered and exhibit typical short fatigue crack behaviour. For the baseline polished and ground conditions, the data points become somewhat less scattered when the crack aspect ratio evolution for these conditions is allowed for; but for the shot peened cases, allowing for the true crack aspect ratio evolution (which is very different in the shot peened case compared with the baseline case) the data seem even more scattered and become spread over a wider $\Delta K_{surface}$ range. When crack aspect ratio is considered as a function of crack depth for the baseline case, the data points move toward a higher $\Delta K_{surface}$ value at the same *dc/dN* within a relatively low $\Delta K_{surface}$ region; but in a higher $\Delta K_{surface}$ region, data points at the same *dc/dN* are now identified at a lower $\Delta K_{surface}$. For cracks in the shot peened cases, data points with the same crack propagation rate *dc/dN* are predicted to generally experience a smaller stress intensity factor range $\Delta K_{surface}$ when the variation in

*a/c* ratio is taken into account. The *dc/dN* versus $\Delta K_{surface}$ data gives a reasonable comparison of crack growth rates under similar externally imposed stress/strain states, ignoring any local effects of work hardening or compensating residual stresses. Short crack growth behaviour in both the polished and ground cases is similar. For the T0 case, almost all the data points are well below those in polished and ground cases, which indicates the intrinsic benefit of shot peening, even when the varying evolution of crack aspect ratio on $\Delta K$ is accounted for. However, the multi-mechanism controlled fatigue behaviour in the T1 case can be clearly identified as these data points overlap with both the baseline conditions as well as the T0 case. Figure 5- 18 shows the fatigue crack growth rates *da/dN* as a function of $\Delta K_{depth}$ in these four conditions. Similarly, two different calculations of stress intensity factor in terms of crack aspect ratio *a/c* have been applied, i.e. constant *a/c* (0.8) in Figure 5- 18(a) and evolving or varying *a/c* (as a function of crack length) in Figure 5- 18(b). For polished and ground conditions, only slight differences in $\Delta K_{depth}$ between the two different calculation methods can be identified. However, compared to the first calculation approach, smaller *da/dN* and $\Delta K_{depth}$ are obtained when considering crack aspect ratio evolution. Despite the data still being quite scattered in terms of *da/dN* versus $\Delta K_{depth}$, the shot peening benefit becomes more obvious as can be seen in Figure 5- 18(b), even in the T1 case. Thus indicating that crack growth into the depth (where compressive residual stresses exist) is slowed. At the same crack driving force ($\Delta K_{depth}$), *da/dN* in the shot peened cases are generally slower than in the baseline conditions. Figure 5- 19(a) and (b) allowing for a varying *a/c* (and comparing the effect on $\Delta K$ calculations when compared to a constant *a/c* assumption) the greatest effect is seen on $\Delta K_{surface}$ values for both the baseline and shot-peened conditions. The effect on $\Delta K_{depth}$ is less marked. In the baseline case, the $\Delta K_{surface}$ (calculated with appropriately varying *a/c*) is greater at smaller crack lengths, rising to a peak at $2c \sim 500$ μm and then decreasing to a value of $2c \sim 1400$ μm, after which the effect of allowing for varying *a/c* is in fact a lower $\Delta K_{surface}$ value when compared with a constant *a/c* assumption. In the shot-peened case a similar overall relative trend is seen, although in this case, allowing for an appropriately varying *a/c*, this results in a lower $\Delta K_{surface}$ being predicted for the shot-peened case at all *c*-values, expect when $2c \sim 500$ μm (the "peak" value), when the $\Delta K_{surface}$ calculations agree. In the depth cases a

relatively smaller effect of allowing for varying *a/c* ratio is seen, with lower $\Delta K_{depth}$ values being seen for the shot peened case down to a depth of $a \sim 200$ μm.

## 5.4 Discussion

### 5.4.1 Short fatigue crack initiation and propagation behaviour

Compared to the ground surface condition, the fatigue life benefits slightly from the polished notch surface, showing about 11 % improvement for this particular loading case in these single specimen comparisons. Shot peening does not always improve the fatigue life, for example, the T1 condition presents a similar fatigue life to the ground condition. However the industry standard shot peening process (T0), produces a fatigue life that is almost twice that for the polished or ground specimens under similar applied local strain conditions ($\Delta\varepsilon_{11}$ = 0.68%). The improvement of fatigue life is considered to be due to a complex interrelation of the surface roughness induced by the shot peening process, the compressive residual stress distribution and as well as the work hardened layer.

Conventionally, it has been reported that lower roughness results in a longer fatigue life in most cases; however, in the case of shot peening the fatigue behaviour is dominated by the residual stress condition and surface microstructure, as discussed in detail in the review paper [3]. In the absence of residual stress, machined surface roughness in excess of 0.1 μm $R_a$ has a strong influence on fatigue life, while this effect diminishes when $R_a$ is less than 0.1 μm, when cracks tend to initiate at persistent slip bands or grain boundaries [3]. In the current research, although the surface conditions are quite different, the polished and ground samples exhibit quite similar crack initiation and propagation behaviour. In the ground case the grinding marks induced by the grinding process can actually act as a micro-notch and stress concentrations are generated within these areas.

As stated in Chapter 3, there is a thin layer of tensile residual stress in the residual stress profile of the ground sample, which is different from the thin compressive residual stress layer produced in the polished condition. However, crack initiation is affected significantly by local environmental factors, such as

the presence of inclusions (alumina or MnS), which have been shown to play an important role in crack initiation and early propagation in the present material system, as discussed in Chapter 4. These inclusions dominated initiation and early propagation behaviour in both polished and ground conditions, regardless of the changes in surface condition and residual stress profile.

In the shot peened conditions however short fatigue crack initiation and propagation behaviour results from the complex interaction of rough surface, residual stress and plastic deformation. Fatigue crack initiation and propagation processes are therefore more complex. Prior studies in this area offer different analyses of the mechanisms in operation. Mutoh reported shorter initiation lives of both high strength aluminium alloys 7010 and 8090 after 12 – 16A intensity shot peening with a steel shot size of 0.84 mm, as well as reduced crack propagation rates in these shot peened samples up to a depth corresponding to the maximum compressive residual stress [4]; he also reported that the early initiation of cracks in these shot peened specimens was a result of intense surface folding by the heavy shot peening process, which was not removed by light polishing. But according to de los Rios's research on A316 stainless steel, both crack initiation and propagation were significantly delayed after shot peening, and shot peening significantly affected the crack growth within the short crack regime; and it was also found that polishing the shot peening surface to a 1 μm finish was detrimental to the subsequent fatigue properties, which suggested the immediate surface layer induced by shot peening was of significance based on a more complex set of factors rather than solely relying on the presence of compressive stresses [5]. In the current investigation, fewer initiation sites (only 7 based on the ratchet marks observed by optical microscopy) are identified on the T1 fracture surface, while as many as 18 are found in the T0 case. Although the compressive residual stress layer in T1 is ~ 180–200 μm, and the strain hardening layer is only evident ~ 40 μm below the shot peened surface, the dominant cracks are found to be initiated from Alumina stringers (as is the case in the baseline conditions). What's more, there were quite a lot of smaller ratchet marks seen on the fracture surface under SEM observation, which indicate coalescences may have occurred when fatigue cracks were very short. In the T0 case, the overall compressive residual stress produced in these samples extends to about 340 μm below the surface and the peak in the compressive residual stresses

was found to extend to ~ 150 μm. Indeed the work hardened material is also expected to extend to depths of 150 μm based on the relationship between local microstructural misorientation (used as an indicator of work-hardening) and residual stresses [6]. This may indicate that the preexisting cracks on the shot peened surface are likely to be contained within the expected work-hardened region (with its concomitant differences in yield strength and ductility), further complicating the analysis of short crack behaviour. Thus the "applied" local strain range in the notch root has been estimated based on the baseline materials constitutive laws (including yield strength, rates of cyclic softening/hardening etc.), and the work hardened layer in the notch root now effectively has a different set of materials constitutive laws, meaning that the actual $\Delta LE_{11}$ experienced in the work hardened notch root is likely to be lower than the nominal applied local $\Delta LE_{11}$. Further detailed FE analysis would be required to assess the effect of this surface layer on strain evolution in the notch root and to what extent this may explain the shot peening improvement in terms of simple Coffin-Manson law approaches [7]. Such a continuum solid mechanics approach is beyond the remit of the current project which instead aims to evaluate to what extent the shot peening benefit can be described and estimated more in terms of crack initiation processes; short crack growth behaviour and the use of a more micro-mechanistic analysis approach. The initial non-propagation may be a result of the reduced mean stress as a result of superposition of applied and residual stresses and of the work-hardening present in the material, which is typically considered to act mainly in increasing initiation life (i.e. Coffin Manson approach).

Though surface roughness is known to be detrimental in terms of fatigue life [8], the effect is often not considered as important as the effect of work hardening and compressive residual stresses [9], since LCF fatigue is typically propagation dominated. As evidenced in Figure 5- 13(a) and (b), a jump in crack length, resulting in a sharp increase in growth rate, was often seen in the later fatigue life stages, since frequent crack coalescence occurred in the shot peened samples. Compared to the ground sample behaviour, it is clear that the early stages of crack growth have been slowed in the shot peened samples. The total surface crack length in the shot peened case has to reach 300 ~ 400 μm before *dc/dN* levels start to match those observed in the ground samples. This correlates to an expected crack depth of around 250 – 300 μm,

i.e. the point where the crack may be expected to escape the region of very high compressive residual stresses. The slower crack growth observed in the shot peened samples is thought to be primarily a result of the crack growing through the region containing compressive residual stresses, which are generally considered to be the main cause of crack growth retardation [6].

Given the expected equivalent local applied strain range in the notch root (ignoring any local effects of work hardening or compensating residual stresses), the *dc/dN* versus *c* gives a reasonable comparison of crack growth rates under similar externally imposed stress/strain states. For the *K* calibration, considering the evolution of crack aspect ratio or not makes a significant difference. Despite the data still being quite scattered in terms of *da/dN* versus $\Delta K_{depth}$, the shot peening benefit is more obvious accounting for the *a/c* evolution, even in the T1 case. At the same crack driving force ($\Delta K_{depth}$), *da/dN* in the shot peening cases is generally slower than in the baseline conditions. After shot peening, there is an induced compressive residual stress in the near surface layer. When an external cyclic stress is imposed during a fatigue test, stress superposition will occur during loading, as well as possible relief of the compressive residual stress during the fatigue process. We should note here that Soady et al. saw little or no relaxation of residual stresses at 50 % of lifetime in their study [15]. As a result, the actual stress state in the surface layer arising from the applied stress and the pre-existing strain hardening and residual stress distributions, will affect fatigue crack growth behaviour in the affected surface layer. However, not only the compressive residual stress, the strain hardened layer but also the surface roughness will influence fatigue behaviour, so the slower fatigue crack propagation rate observed in the shot peened sample is actually due to the interaction of these three factors.

### 5.4.2 Apparent residual stress

The fatigue crack growth rates *da/dN* of T0 and T1 shot peened notch samples plotted as a function of $\Delta K_{depth}$, are compared with *da/dN* vs $\Delta K$ data for long crack SENB tests carried out in the same material at ambient temperature, as illustrated in Figure 5- 20(a) and (b). If we compare the SENB long crack propagation data with these two conditions, the long crack growth rate data fits well with the polished notch and ground conditions, although exhibiting

considerably less scatter. This gives some confidence in the $\Delta K$ levels calculated in the notch root and the more accurate calculation of crack aspect ratio evolution.

Based on equivalent crack driving force we can estimate the difference in $\Delta K$ (when the crack aspect ratio evolution is considered) for a given *da/dN*, hence an apparent residual stress. Due to the scattered data sets, a lower and upper bound can be drawn; therefore, the corresponding lower and upper bound of the apparent residual stress can be obtained. In Figure 5- 20(c) and (d), the overall trends of the apparent residual stress in T0 and T1 are both quite similar to the measured residual stress, respectively - decreasing gradually with increasing depth, and at some point, after reaching the minimum point, the apparent residual stress increases, which indicates the crack driving force decreases gradually. However the minimum point of these apparent residual stresses (i.e. the most significant retardation) coincides with the depth of the shot peening plastic deformation layer as well as the maximum compressive residual stress. The lower and upper bound of the apparent residual stress brackets the measured ones but extends far deeper in both T0 and T1 cases. This is probably due to the additional retardation effects of the strain hardened layer, effects of stress redistribution as the cracks grow and coalescence/shielding behaviours which are not captured by this simplifying "apparent residual stress" assumption.

### 5.4.3 Crack coalescence effect on fatigue crack behaviour

Crack coalescence events have been observed frequently during the fatigue process in the present study. This may have a significant influence on consequent propagation behaviour due to changes in the $\Delta K$ around the newly coalesced crack tip related to the sudden change in *a/c* ratio. Given that the shot peening process itself also seems to affect the equilibrium *a/c* ratio (which is then dependent on crack depth) the interaction of these two *a/c* effects on crack tip driving force (i.e. $\Delta K$ around the crack tip) should be assessed further. To analyse this further, a particular case has been considered in detail.

Here it is assumed that the two cracks have exactly the same morphology as shown in Figure 5- 21(a); when these surface crack tips touch coalescence

starts, as shown in Figure 5- 21(b). For simplification, the coalesced crack is then described as a single crack with the same crack depth but now twice the surface crack length, as illustrated in Figure 5- 21(c). In this study, the discussion on the effect of crack coalescence will therefore mainly focus on a range of surface crack lengths $2c_{project}$ before crack coalescence i.e. 25, 50, 100, 200, 500 and 1000, 2000, 3000 μm respectively. In this analysis the assumptions of equilibrium varying *a/c* ratio with crack length have been based on the baseline where the equilibrium *a/c* ratio is essentially derived from Scott and Thorpe's analysis as discussed in Chapter 4 and the experimental observations for single cracks in the T0 shot peened case. The coalescence effect analysis is based on predictions for these two varying equilibrium *a/c* conditions as well as the simplifying assumption that equilibrium *a/c* = 0.8 at all depths. Figure 5-22 shows how $\Delta K_{depth}$ and $\Delta K_{surface}$ change at the point when the crack tips coalesce to produce a sudden change in *a/c* ratio. Generally speaking, $\Delta K_{depth}$ increases while $\Delta K_{surface}$ decreases after coalescence for the varying *a/c* ratio assumption for both baseline and shot peened condition. Comparing *a/c* = 0.8 assumption and where the equilibrium *a/c* varies with crack length in both baseline and shot peened case, it is clear that crack aspect ratio *a/c* seems have no significant effect on the change of $\Delta K_{depth}$ and $\Delta K_{surface}$ when coalescence occurs. The longer the crack when the coalescence happens, the greater the effect can be seen on the change of both $\Delta K_{surface}$ and $\Delta K_{depth}$. Crack growth in the depth direction becomes faster as $\Delta K_{depth}$ increases when the cracks coalesce; meanwhile, crack growth in the surface direction decelerates.

Based on Chapter 4, crack coalescence occurs frequently in early fatigue stages in the T0 shot peened case. Although the coalesced crack would normally accelerate into the crack depth direction, its propagation becomes difficult due to the existence of the shot peened affected zone (compressive residual stress, plastic strain layer). This additional factor can also explain the slow observed surface crack propagation as well as the shallow coalesced crack morphology.

## 5.5 Conclusions

In this chapter, short fatigue crack analysis (initiation and propagation behaviour) has been conducted in polished, ground, T0 and T1 notched samples. Conclusions can be drawn as follows:

(1) Under the same expected strain range condition ($\Delta\varepsilon_{11}$ = 0.68%), the ground and T1 shot peened case have similar fatigue lives, while the polished case benefitted somewhat from the polished surface and the fatigue life improved by ~ 11 %. The T0 shot peened process exhibited the best fatigue life, almost twice that of the baseline and T1 cases even in the LCF regime. The crack growth behaviour in the polished (baseline) condition is similar to that in the ground condition, whilst crack growth rates in the shot peened case are significantly delayed while the crack grows through the expected depth of the significant compressive residual stress field/work hardened region. Evidence has been presented for small pre-existing cracks on the shot peened surface, which only started to grow at around 10 – 25 % of the fatigue life. At this stage, the crack propagation rate was lower than in the ground sample, until the depth of the crack exceeded the expected depth of the significant compressive residual stress field/work hardened region.

(2) The *a/c* evolution effects were incorporated into *K*-evaluations and assumptions about growth in the depth direction; apparent residual stress (based on crack driving force $\Delta K$ difference assumptions) shows crack growth retardation beyond the measured region of compressive residual stress, which is probably due to the effects of the strain hardened layer, stress redistribution as the cracks grow and coalescence behaviour which are not captured by this assumption.

(3) A simplified model was applied to discuss fatigue crack coalescence effects. When coalescence occurs, the stress intensity factor $\Delta K_{surface}$ decreases and $\Delta K_{depth}$ increases instantly.

## 5.6 Figures

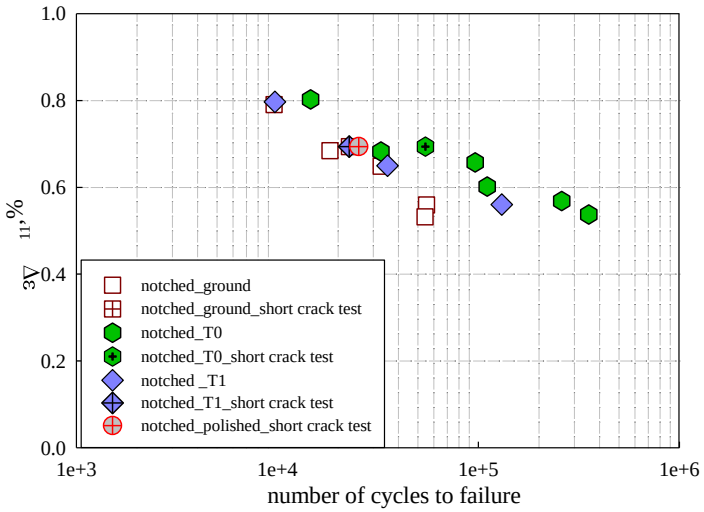


Figure 5- 1 Strain life comparison for notched samples in both ground and shot peened conditions (compared with data from Soady's work [1]).

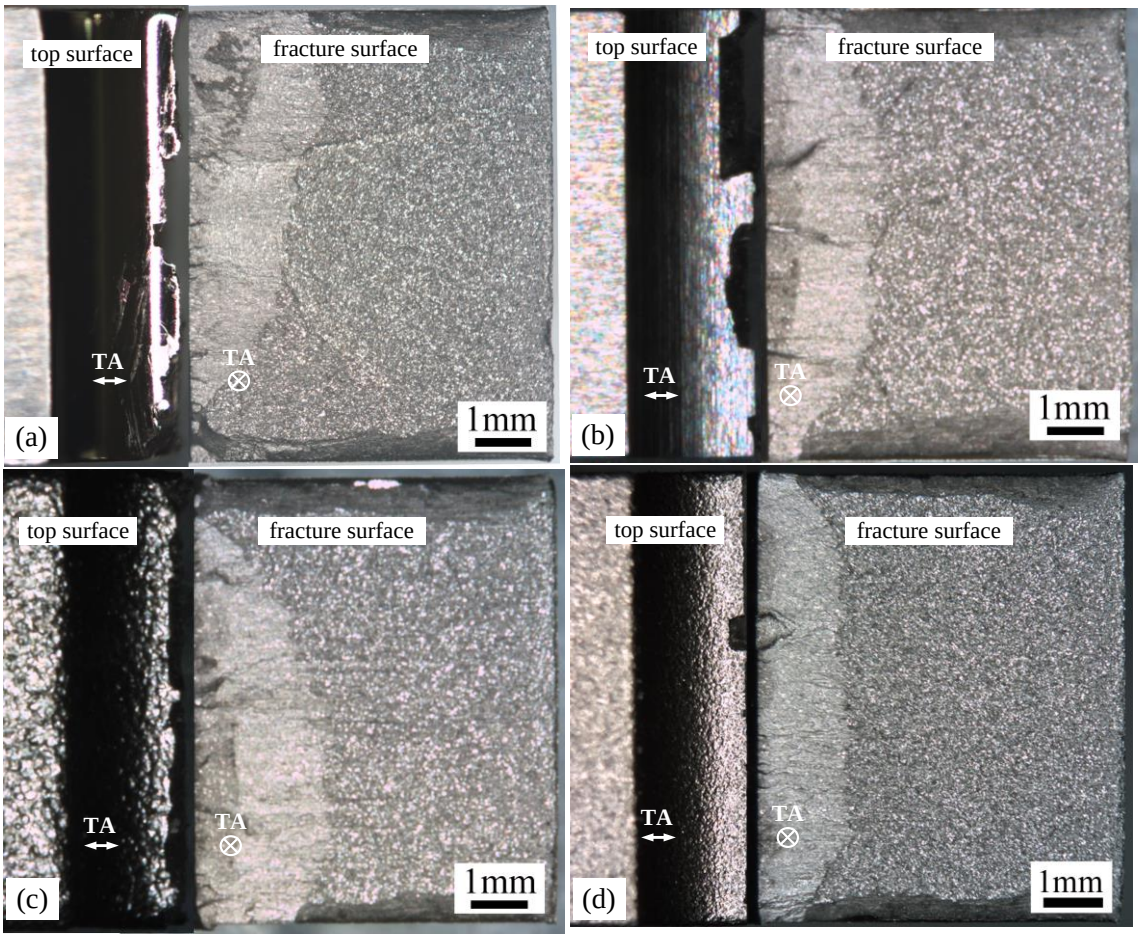


Figure 5- 2 Optical micrographs of the fracture surface: (a) polished; (b) ground; (c) T0 and (d) T1.

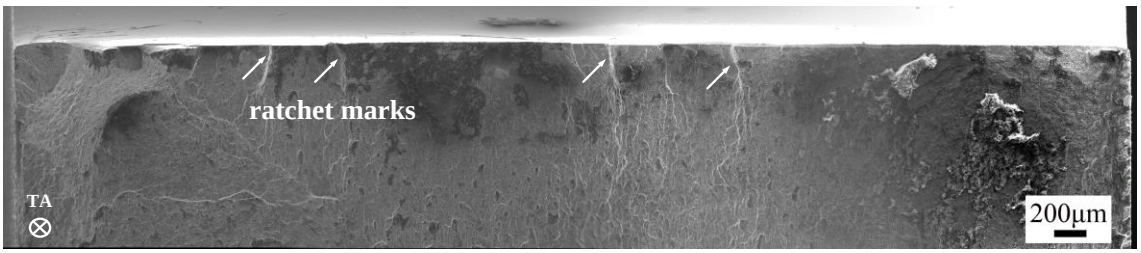


Figure 5- 3 SEM micrograph of the fracture surface in polished sample.

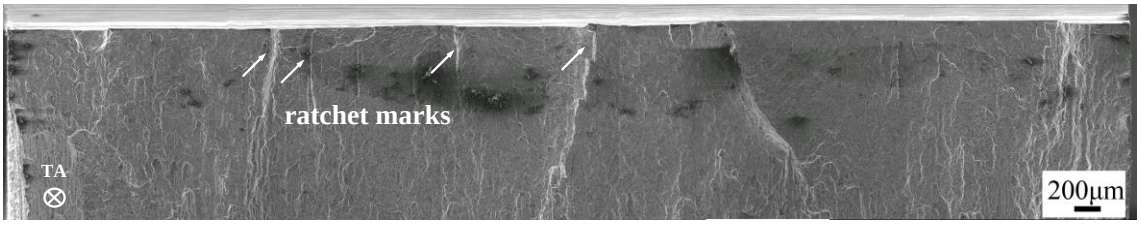


Figure 5- 4 SEM micrograph of the fracture surface in ground sample.

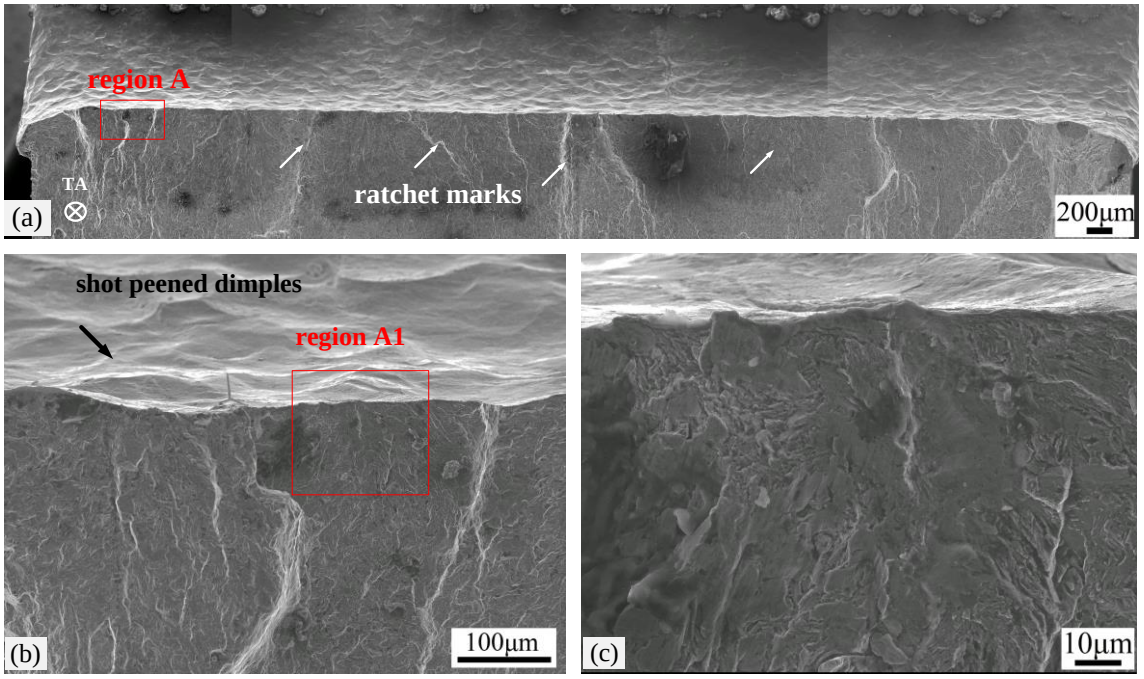


Figure 5- 5 (a) SEM micrograph of the fracture surface in T0 sample; (b) region A, and (c) region A1.

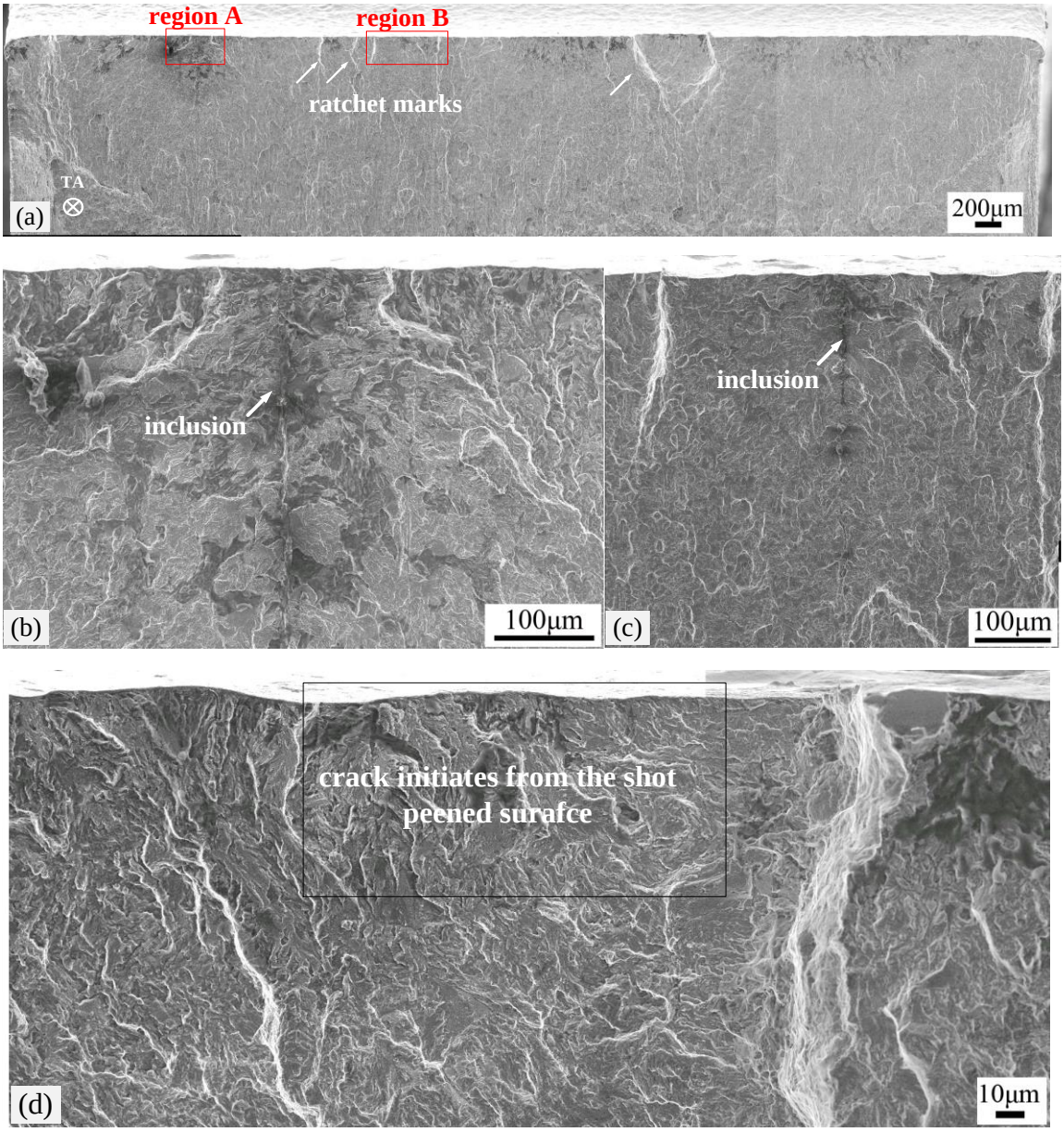


Figure 5- 6 (a) SEM micrograph of the fracture surface in T1 sample; (b) region A; (c) region B; (d) an example of a crack initiated from the shot peened surface.

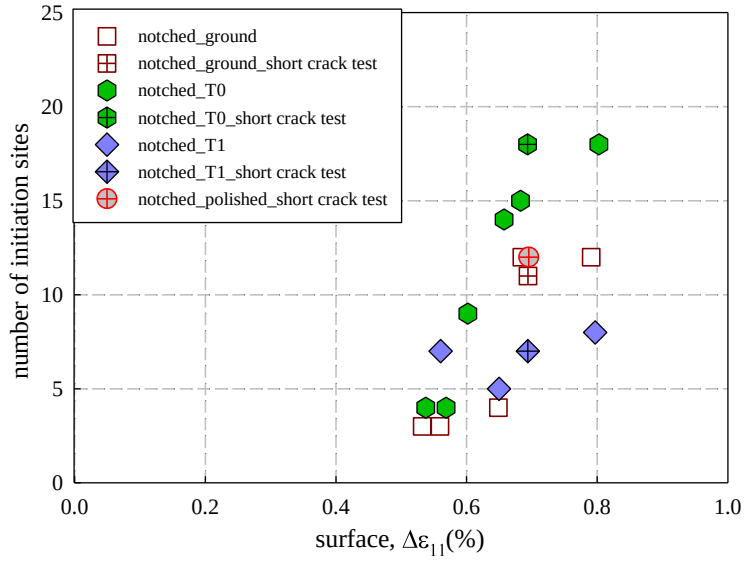


Figure 5- 7 Crack initiation sites based on the ratchet marks assessment in ground, polished, T0 and T1 samples (compared with results taken from [1]).

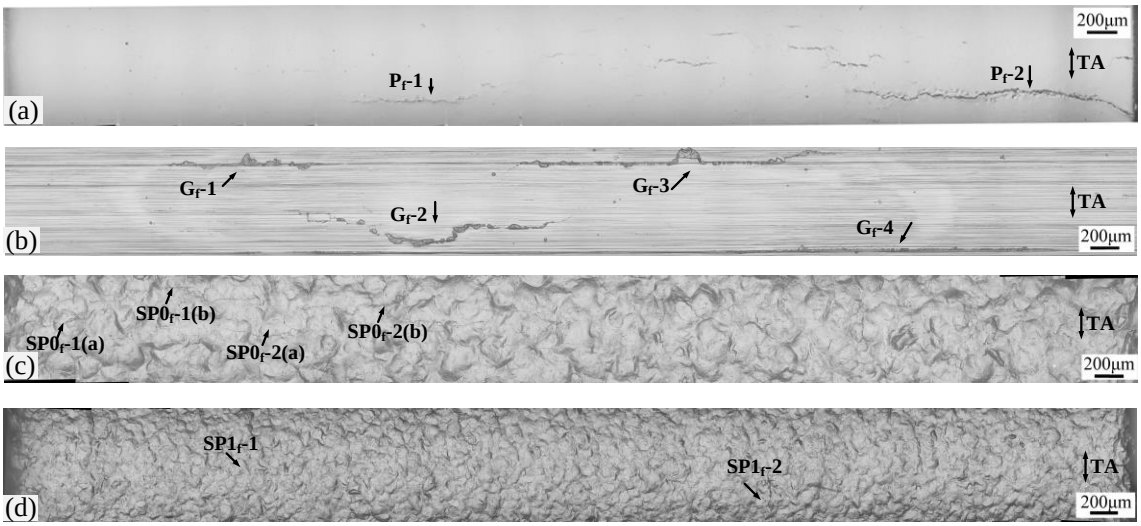


Figure 5- 8 Replica images of the four different surface conditions.

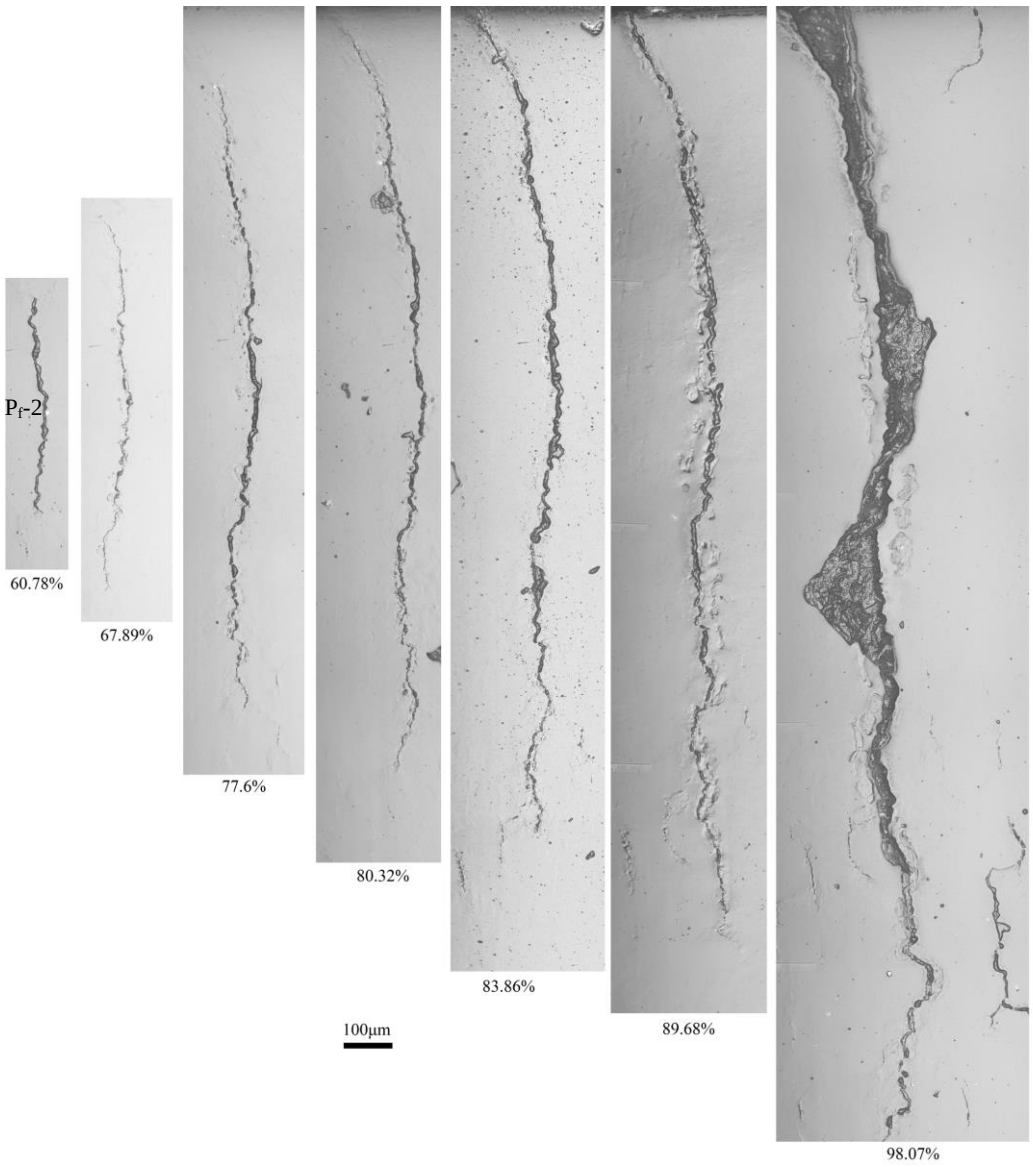


Figure 5- 9 Crack $P_f$-2 morphology on polished surface at different percentages of fatigue life.

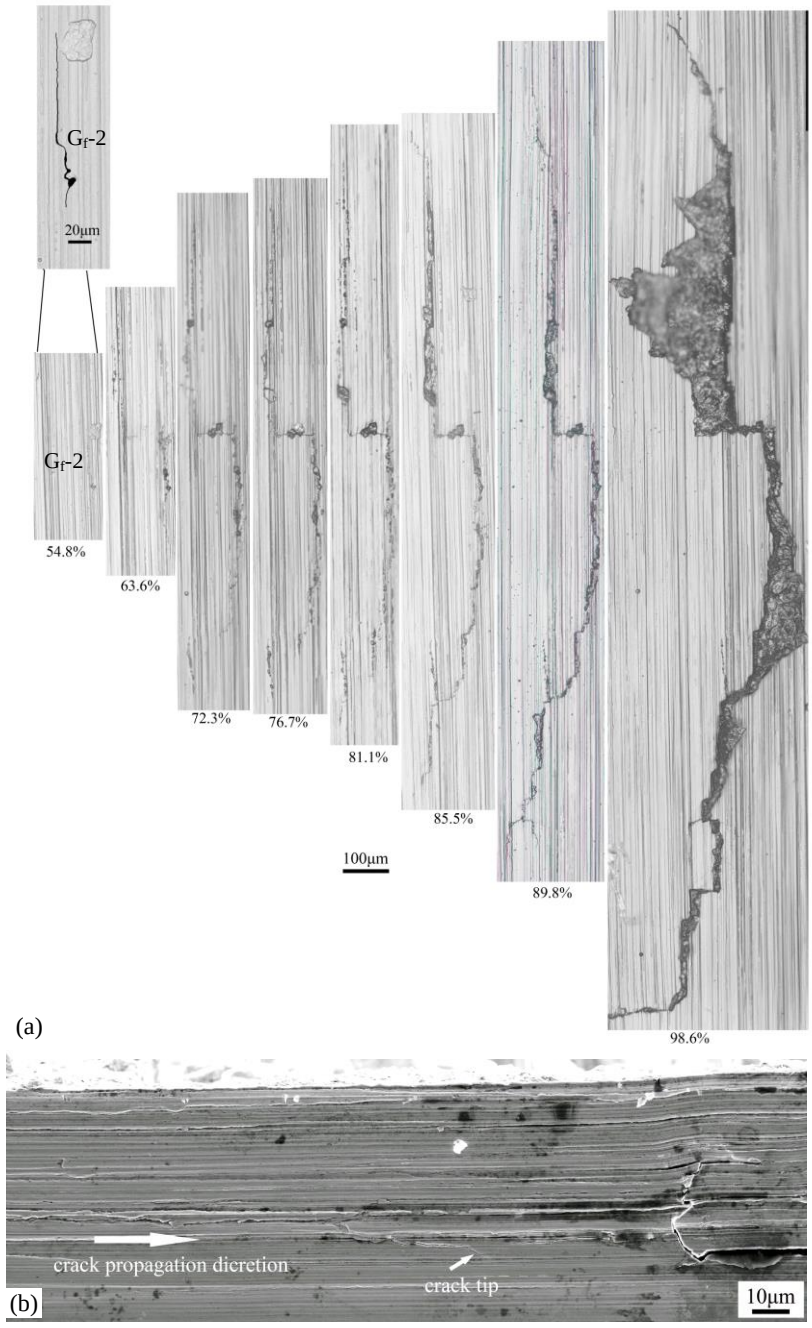


Figure 5- 10 (a) Crack $G_f$-2 morphology on ground surface at different percentages of fatigue life; (b) SEM image of crack propagating along grinding marks.

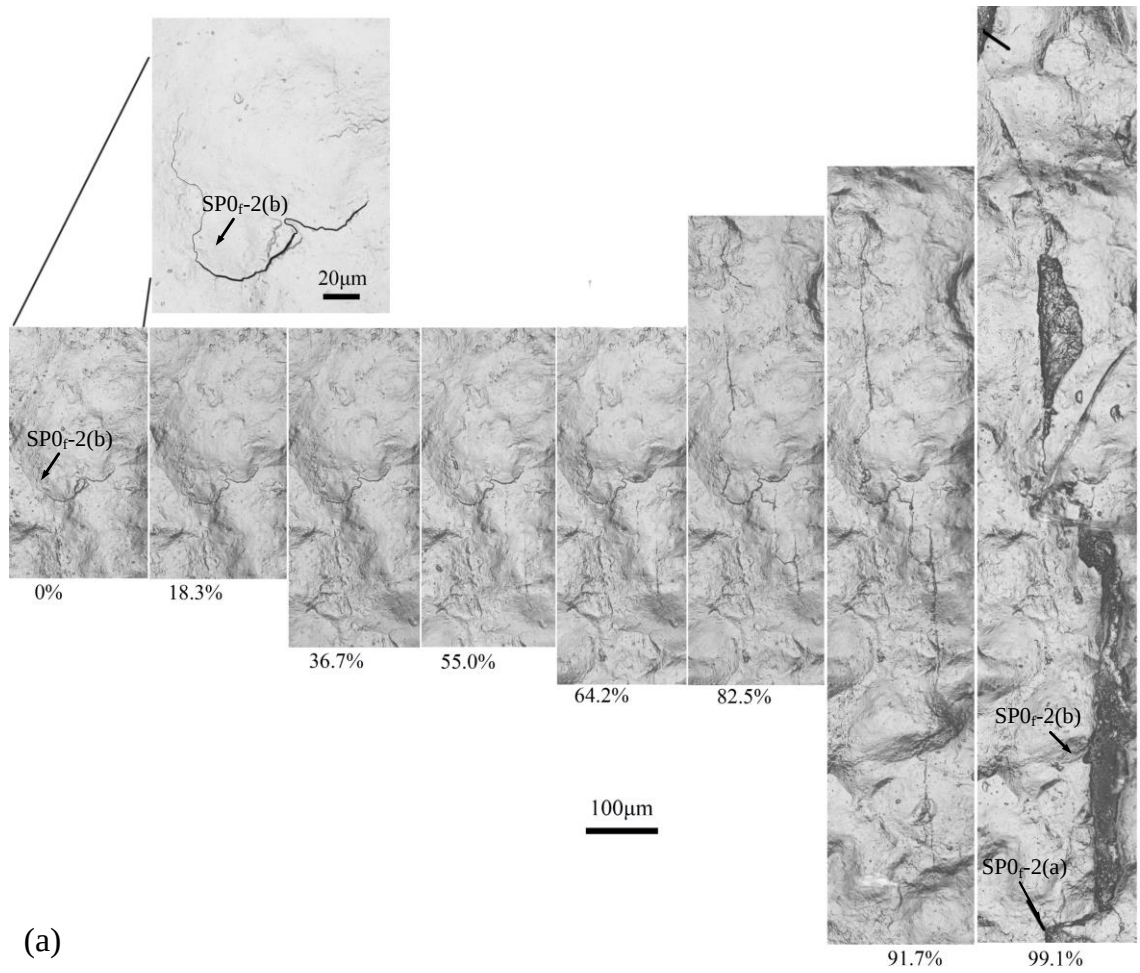


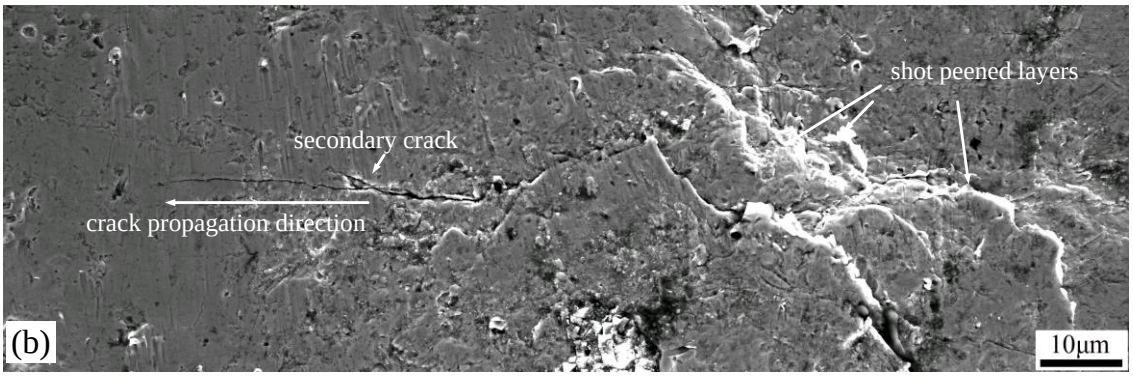


Figure 5- 11 (a) Crack morphology on shot peened surface at different percentages of fatigue life; (b) SEM image of surface short crack initiated from shot peened layers on shot peened notch surface.

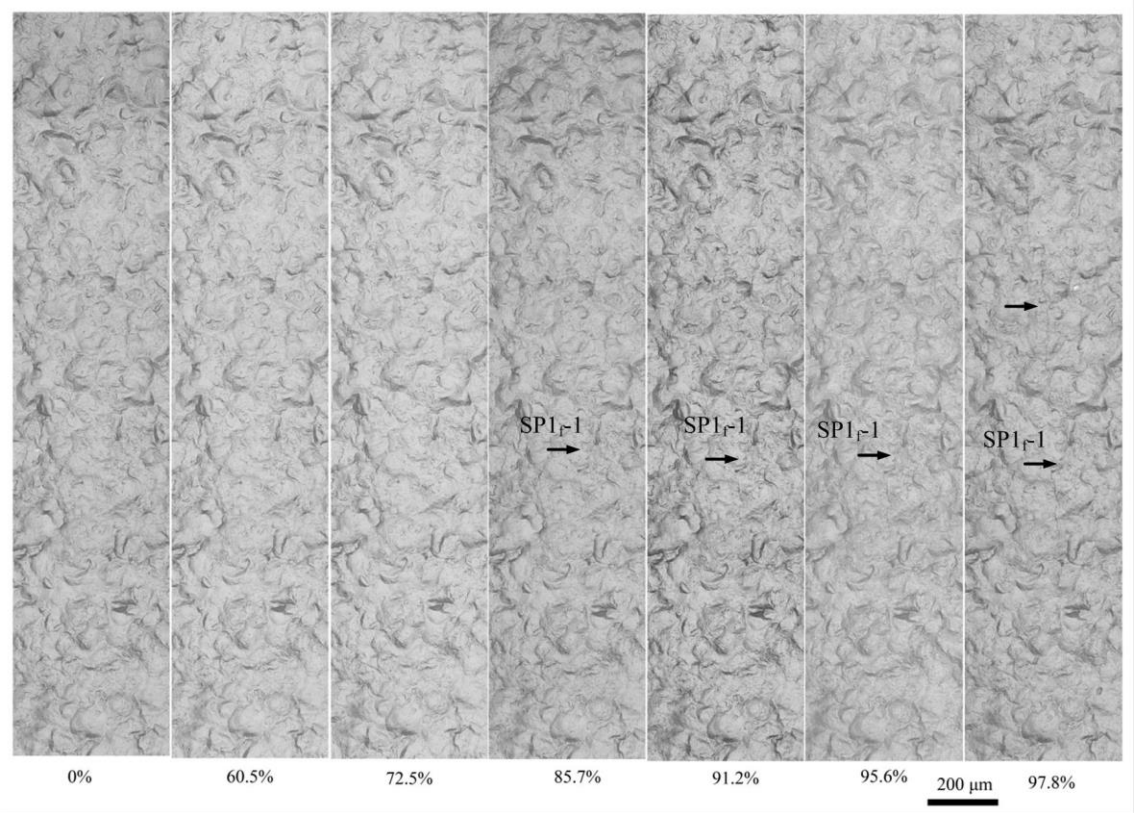


Figure 5- 12 Crack $SP1_f$-1 morphology of shot peened surface at different percentages of fatigue life.

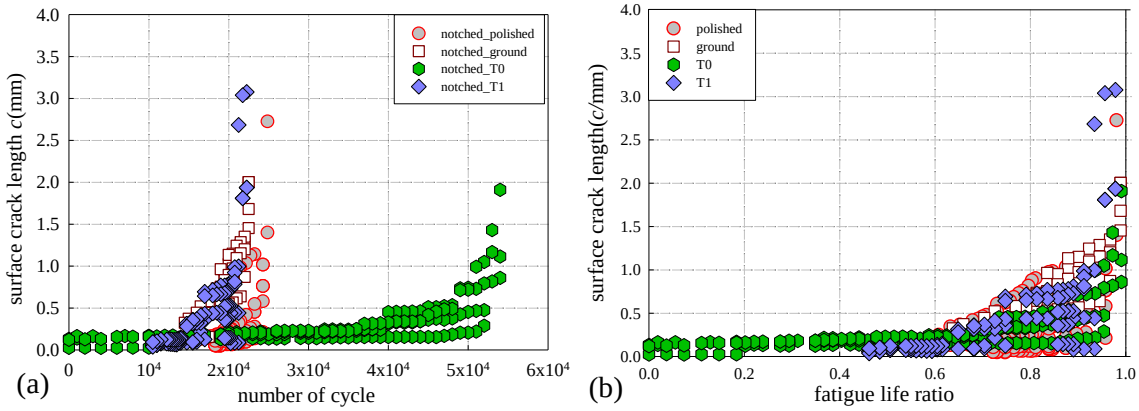


Figure 5- 13 (a) Half surface crack length *c* versus number of cycles in polished, ground, T0 and T1 condition; (b) half surface crack length *c* at different fatigue life ratios in all conditions.

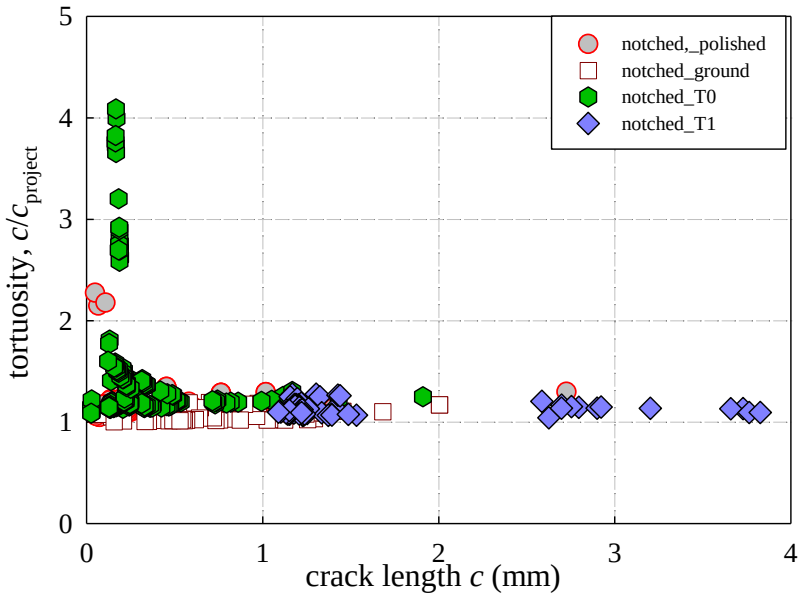


Figure 5- 14 Crack tortuosity $c/c_{project}$ at various crack lengths ofdifferent surface conditions.

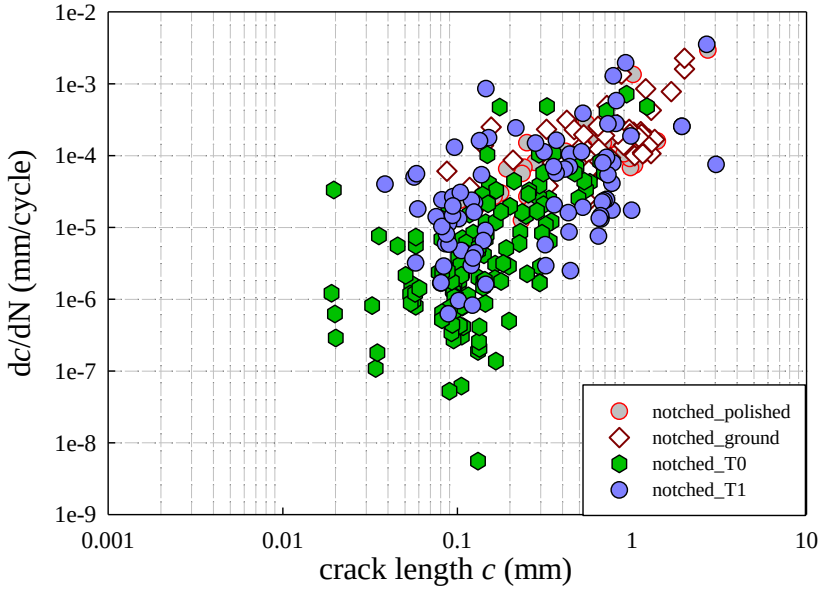


Figure 5- 15 Surface crack propagation rate *dc/dN* as a function of crack length *c*.

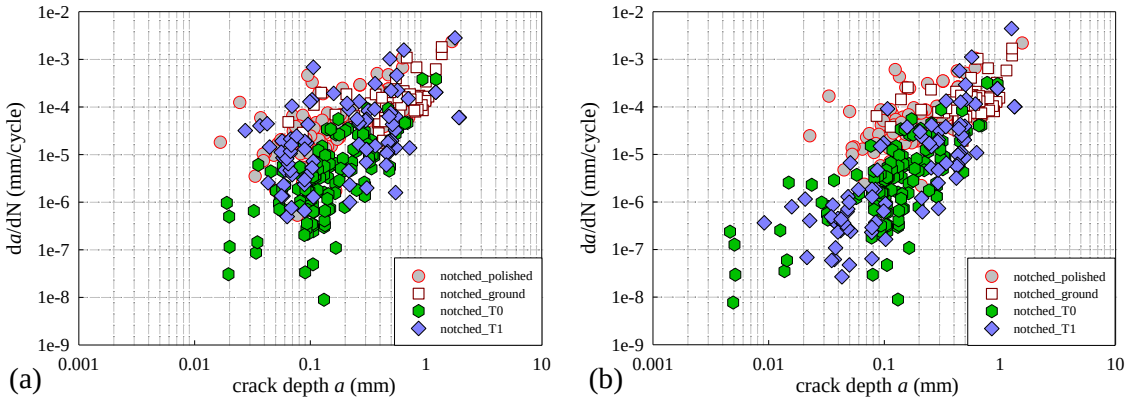


Figure 5- 16 Crack propagation rate *da/dN* vs crack depth *a*: (a) *a/c* = 0.8; (b) *a/c* varying with depth.

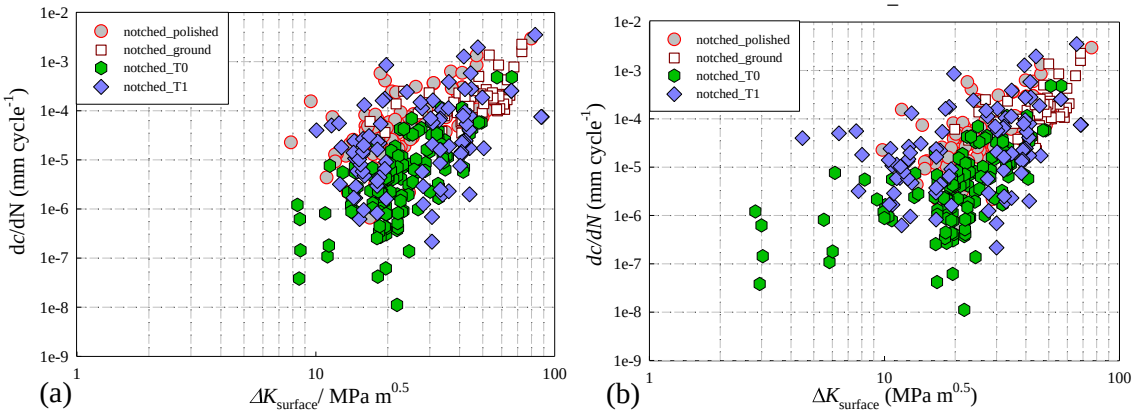


Figure 5- 17 a) *dc/dN* as a function of $\Delta K_{surface}$ on the basis of crack aspect ratio is constant (*a/c* = 0.8); (b) *da/dN* as a function of $\Delta K_{surface}$ on the basis of crack aspect ratio is a function of surface crack length.

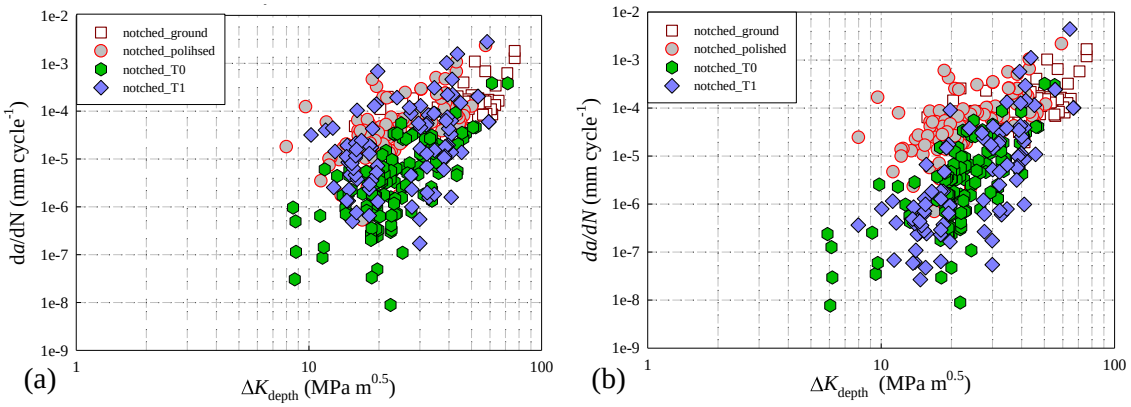


Figure 5- 18 (a) *da/dN* as a function of $\Delta K_{depth}$ on the basis of crack aspect ratio is constant (*a/c* = 0.8); (b) *da/dN* as a function of $\Delta K_{depth}$ on the basis of varying crack aspect ratio as a function of crack depth.

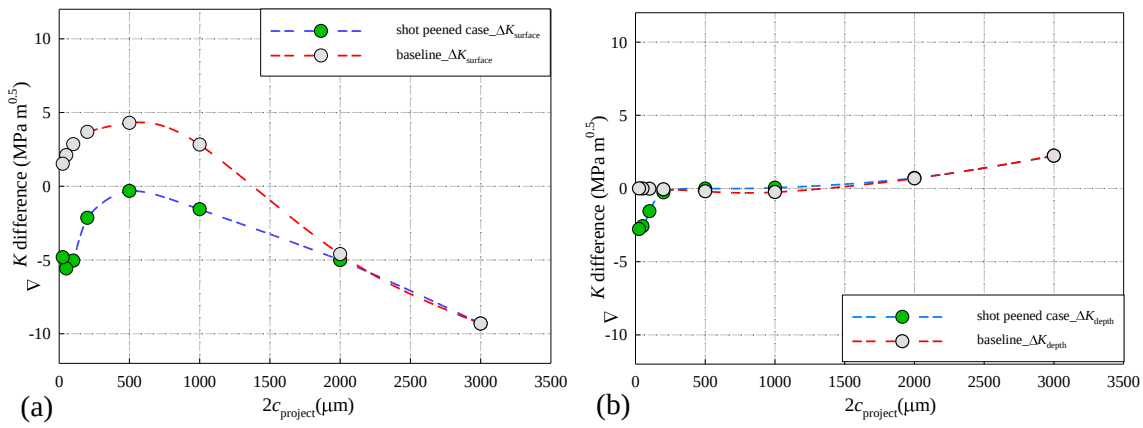


Figure 5- 19 (a) $\Delta K_{surface}$ and (b) $\Delta K_{depth}$ difference between two different estimation methods (i.e. $\Delta K_{depth}$ difference = $\Delta K_{depth}$(varying *a/c*)-$\Delta K_{depth}$(0.8) and $\Delta K_{surface}$ difference = $\Delta K_{surface}$(varying *a/c*)- $\Delta K_{surface}$(0.8))

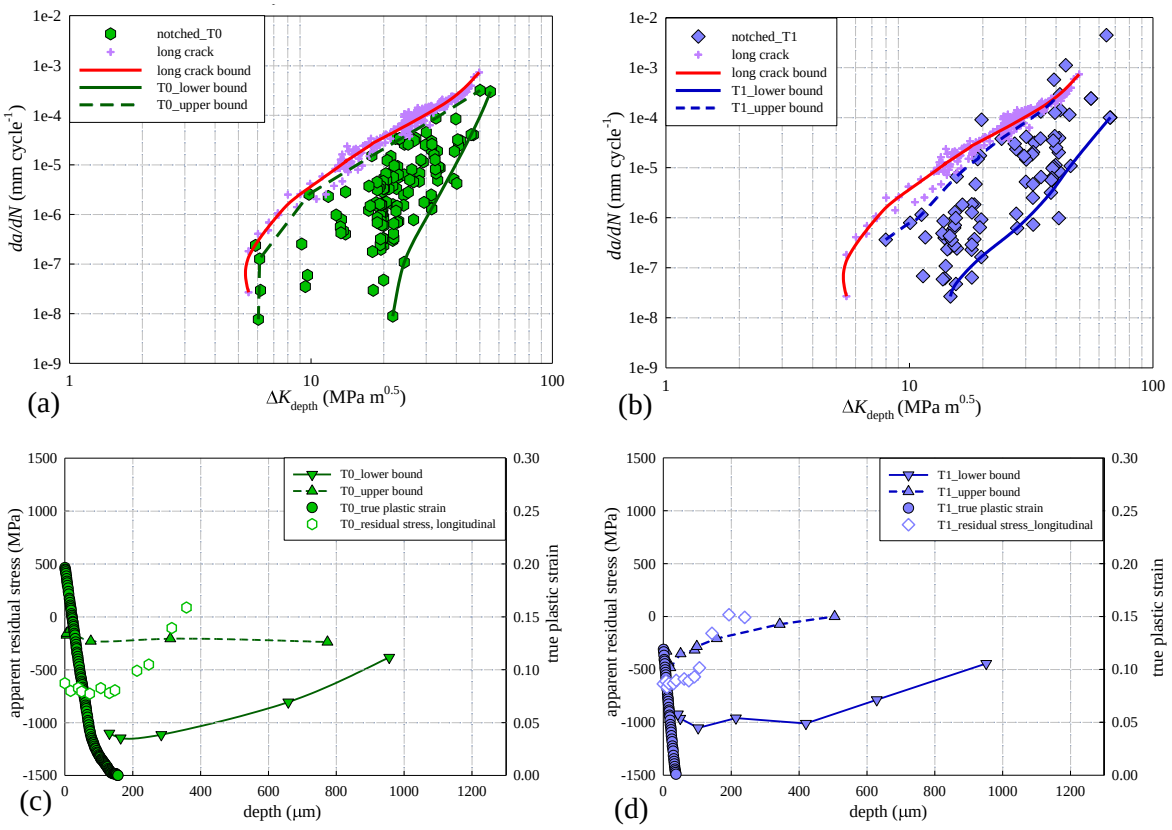


Figure 5- 20 Comparison of fatigue crack growth rates as a function of $\Delta K$ between long crack and short cracks in: (a) T0 and (b) T1; apparent residual stress based on the equivalent crack driving force as a function of depth in: (c) T0 and (d) T1. (long crack data taken from [1]).

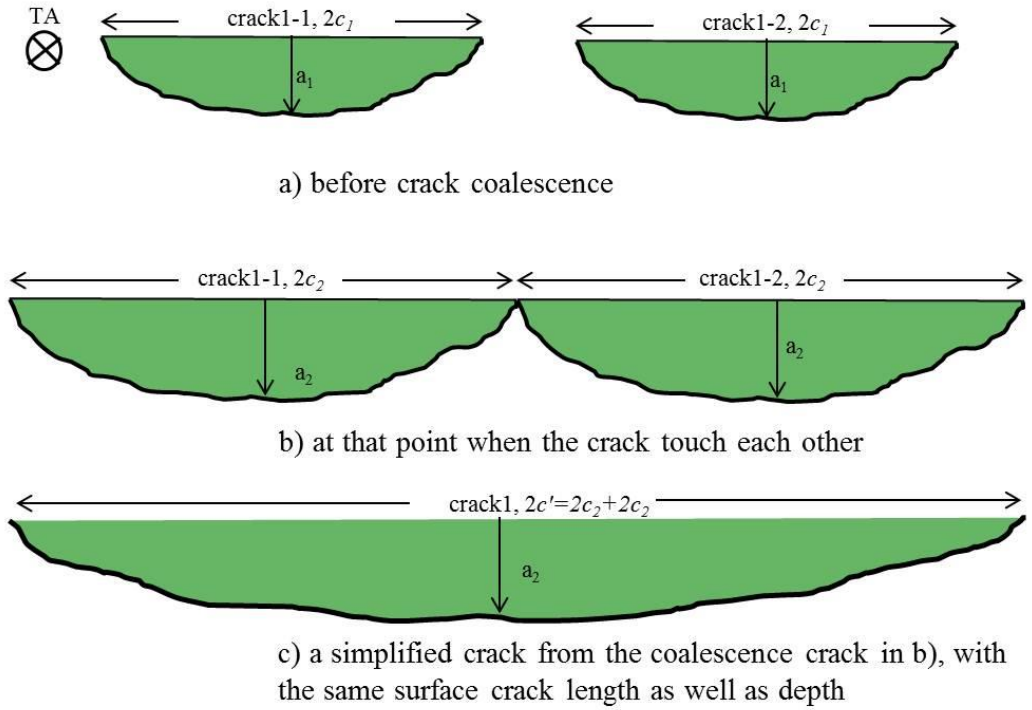


Figure 5- 21 Schematic of a simplified crack coalescence process: a) before crack coalescence, b) at a point when the crack tips touch each other, c) a simplified coalesced crack from the coalescence of cracks in b) with the combined surface crack length and the same depth.

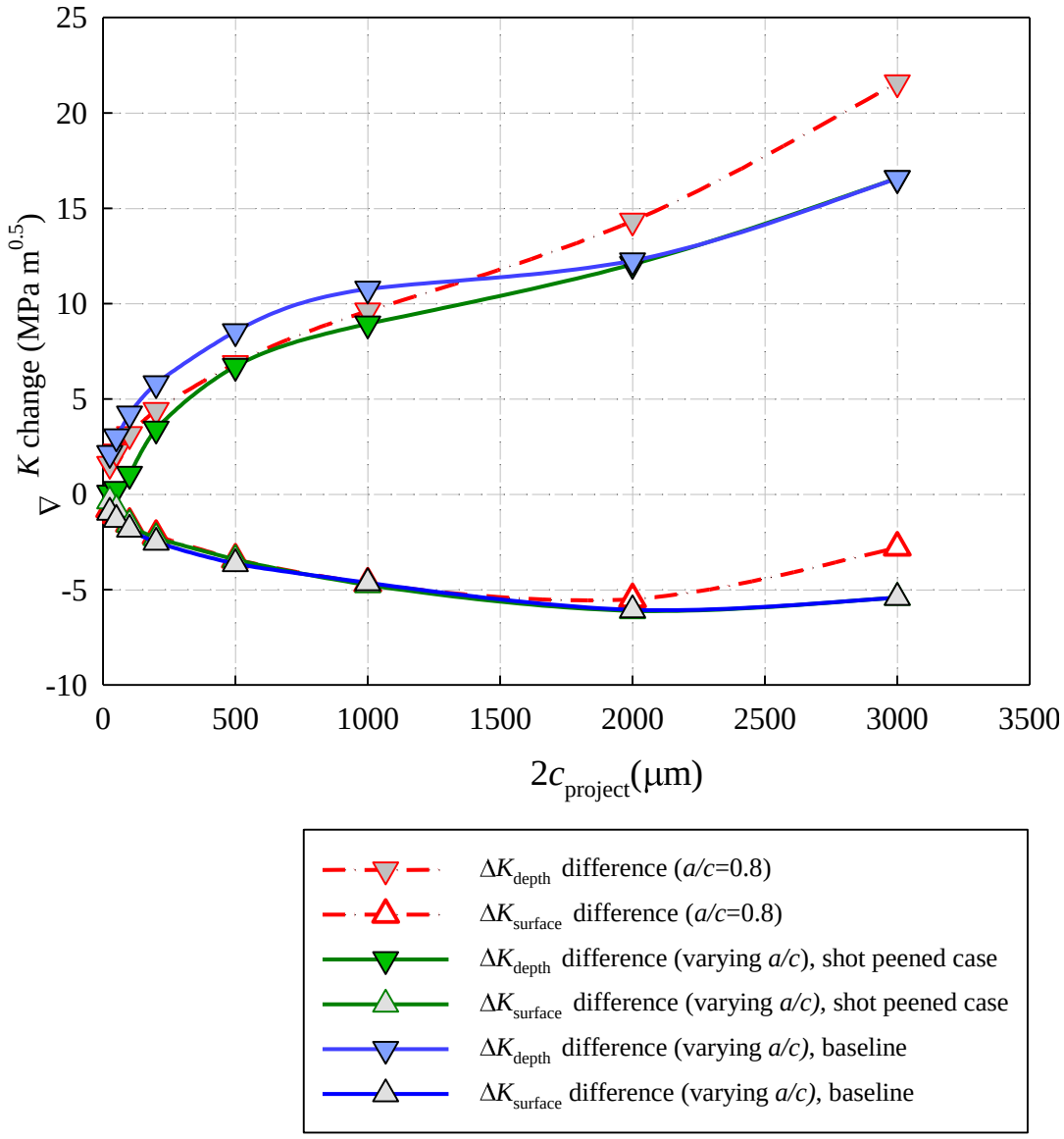


Figure 5- 22 The $\Delta K_{depth}$ and $\Delta K_{surface}$ change at the point when the crack tips coalesce to produce a sudden change in *a/c* ratio (N.B. $\Delta K_{depth}$ change = $\Delta K_{depth}$ (after coalescence) – $\Delta K_{depth}$ (before coalescence), $\Delta K_{surface}$ change = $\Delta K_{surface}$ (after coalescence) – $\Delta K_{surface}$ (before coalescence))

## 5.7 References

[1] K.A. Soady, *Reducing conservatism in life assessment approaches: Industrial steam turbine blade to disc interfaces and the shot peening process*, in: Engineering Sciences Unit, Ph.D thesis, the University of Southampton, 2013.
[2] P.M. Scott, T.W. Thorpe, *A critical review of crack tip stress intensity factors for semi-elliptic cracks*, Fatigue & Fracture of Engineering Materials & Structures, 4 (1981) 291-309.
[3] D. Novovic, R.C. Dewes, D.K. Aspinwall, W. Voice, P. Bowen, *The effect of machined topography and integrity on fatigue life*, International Journal of Machine Tools and Manufacture, 44 (2004) 125-134.
[4] Y. Mutoh, G.H. Fair, B. Noble, R.B. Waterhouse, *The effect of residual stresses induced by shot peening on fatigue cracks propagation in two high strength aluminium alloys*, Fatigue & Fracture of Engineering Materials & Structures, 10 (1987) 261-272.
[5] E.R. De los Rios, A. Walley, M.T. Milan, G. Hammersley, *Fatigue crack initiation and propagation on shot-peened surfaces in A316 stainless steel*, International Journal of Fatigue, 17 (1995) 493-499.
[6] K.A. Soady, B.G. Mellor, G.D. West, G. Harrison, A. Morris, P.A.S. Reed, *Evaluating surface deformation and near surface strain hardening resulting from shot peening a tempered martensitic steel and application to low cycle fatigue*, International Journal of Fatigue, 54 (2013) 106-117.
[7] C. You, *Mechanism-driven fatigue lifing developments in turbine systems*, in, Transfer report, the University of Southampton, 2015.
[8] ESDU, *The effect of surface roughness on the fatigue limit of steels at zero mean stress*, in: ESDU 74027, ESDU International PLC, London, UK, 1974.
[9] W. Koster, *Effect of residual stress on fatigue of structural Alloys*, in: 3rd Int. Conf. on 'Practical application of residual stress technology', ASM, IN, USA, 1991, pp. 1-9.

# Chapter 6: Blend-polish-peen repair in T0 shot peened U-notch sample

## 6.1 Introduction

Steam turbine blades are one of the most significant safety critical components in Power Plant, subjected to low cycle fatigue (LCF) stresses of thermal and mechanical origin during start-up and shutdown. In order to avoid any sudden and unexpected failure and also to constantly monitor reliability of the component systems, non-destructive testing (NDT) is carried out during routine maintenance inspections approximately every 12 years in order to locate and size any defects, especially at the fir tree blade disc interfaces, where several severe stress concentrations exist. A range of refurbishment activities are then undertaken to ensure the integrity of the turbine in the next operational cycle. Replacement of a new part of the component or even the entire component will considerably increase cost and extend the duration of outage (incurring further operational costs). A repair program may then be a cost-effective option if this can minimize maintenance costs, reduce outage time and extend the service life of components. Typical repair processes for turbine blades include blending, remachining, precision grinding [1] and welding [2, 3].

As discussed in previous chapters, the shot peening process is an effective way to enhance the fatigue performance in the steam turbine blade fir tree region (the stress concentration area). In the industrially applied shot peening process (T0), most of the fatigue cracks seem to initiate at the surface (although this situation is dependent on the distribution and size of inclusions or other defect populations) due to the combined effect of surface roughness, compressive residual stress and the strain hardened layer induced in the near surface layer after shot peening. Repair of shot peened fatigue damaged notched components could exploit this feature. Therefore, this chapter focuses on the blend-polish-peen repair technique. Shot peened notched samples were cycled to produce fatigue cracks, and then polished to a certain depth in order to eliminate the fatigue cracks, then re-shot peened (using the same parameters

as the original T0 process) and their subsequent fatigue performance evaluated.

## 6.2 Experimental methods

The blend-polish-peen repair process has only been considered for the T0 shot peened condition (the industrial standard applied parameters). The procedure of the blend-polish-peen repair process is detailed in Figure 6- 1. A three point bend fatigue test (1st) was conducted in two samples designated B1 and B2 so as to achieve a surface crack length $2c_{project}$ of ~ 1500 μm. Figure 6- 2 shows those cracks on the replica record at 22000 cycles (for B1) and 34000 cycles (for B2). Subsequent polishing of the notch was carried out. The notch geometry profiles after polishing were measured by Talysurf to provide geometry information for the re-calculation of $K_t$. Sample B1 was then fatigue tested again in the polished condition (to establish the effect of simply grinding out the crack, but removing the shot peened layer as well), while sample B2 was re-shot peened with the same parameters before a 2nd fatigue test was carried out. Notch geometry changes were accounted for by making sure the nominal local strain range condition $\Delta\varepsilon_{11}$ in the notch for the 2nd round of fatigue testing was the same as that in the 1st round of fatigue testing.

### 6.2.1 Fatigue test matrix

Fatigue testing was carried out in three point bend at a frequency of 20 Hz using a sinusoidal waveform and a load ratio of R = 0.1, using an Instron 8502 servo hydraulic machine, as detailed in Chapter 4 (Section 4.2.1). During the fatigue process, a replication technique was also used to monitor crack initiation and propagation behaviour, in order to assess the effect of the blend-polish-peen process on subsequent crack growth behaviour.

### 6.2.2 Polishing of the notch in the as-fatigued samples

The objective of the polishing step is to remove the fatigue cracks after a certain number of fatigue cycles. Based on the experimentally observed crack aspect ratio at different surface crack lengths, the depth of the crack can be calculated. The polishing process was controlled manually, as shown in Figure

6- 3. The points mounted in a drill are vitrified and resinoid bonded, can have a wide range of geometry, grit type sizes and hardness levels.

The profiles of the notch before and after polishing in both sample 1 and sample 2 were measured by a Taylor Hobson Form Talysurf 120L stylus profilometer. By comparing the profiles, the depth of the removed material layers can be calculated. $K_t$ of the notch geometry after polishing was calculated by FE analysis [4].

## 6.3 Experimental results

### 6.3.1 Notch geometry changes after the polishing process

In terms of the repair process, polishing out the fatigue affected region is an important step. The notch geometries of sample B1 from both side views before the polishing process are shown in Figure 6- 4(a) and (b). The corresponding geometries after fatigueing and then polishing are shown in Figure 6- 4(c) and (d), respectively. Figure 6- 4(e) is the top view of the notch of B1. As can be seen, the profiles of the notches after polishing are not reproducible due to the manual nature of the process. However, careful control was taken to attempt to ensure the depths of material removed were the same across the sample. The profiles of the notch geometries obtained by Talysurf for samples before and after polishing are illustrated in Figure 6- 4(f). Comparing the notch geometries of sample B2, which had been subjected to the fatigue-polish-re-shot peened process, before polishing (in Figure 6- 5(a) and (b)) to after polishing (in Figure 6- 5 (c) and (d)), it can be seen that the notch profile is not uniform across the sample width, which is most obvious from the notch top view in Figure 6- 5(e). The notch profiles of sample B1 and B2 are quite similar to each other after polishing, as can be seen in Figure 6- 4(f) and Figure 6- 5(f). In addition, the depth of the material removed in sample B1 and B2 is 743 μm and 762 μm, respectively. At the bottom of the notch regions, marks are clear in both the B1 and B2 conditions, as presented in Figure 6- 6(a) and (b), respectively. The surface roughness $R_a$ in the direction perpendicular to the polish marks in B1 and B2 samples is now 1.94 μm and 1.91 μm, respectively.

The U notch geometry was chosen to simulate the fir tree root geometry of the turbine blade and has an elastic stress concentration factor $K_t$ of 1.6 (calculated using an elastic finite element analysis). When the fatigue cracks in the notch region were polished off, the $K_t$ of the notch increased to 1.85, as shown in Table 6- 1. The FE model based on the geometry after polishing was then applied to calculate the nominal stress needed to achieve the same strain range $\Delta\varepsilon_{11}$ = 0.68 % at the notch region during the three point bend test; the nominal stress required before and after the polishing process is 1048.1 MPa and 849.9 MPa, respectively. Any application of this repair process will also have to allow for the detrimental effect of changing the local stress concentration factor in a notch. In this study this first order effect has been eliminated in order to study the effect of the proposed repair process on local crack initiation and growth behaviour.

### 6.3.2 Fatigue crack behaviour of repaired samples

For sample B1, the 1st round of fatigue testing was interrupted at 22000 cycles (several cracks with $2c_{project}$ length of ~ 1200 – 1500 μm were observed via replication), as shown in Figure 6- 2(a); the subsequent number of fatigue cycles to final failure in the 2nd test (after polishing out of the notch) was 35201 cycles. Sample B2 was removed from the fatigue rigs after 34000 cycles (when surface cracks of ~ 1200 – 1500 μm were observed via replication) as shown in Figure 6- 2(b); after the complete blend-polish-peen repair process, this sample failed after a further 22425 cycles in the 2nd fatigue process. The fracture surface of B1 and B2 under optical microscopy can be seen in Figure 6- 7 (a) and (b), respectively. The fatigue failure region of B1 appears uniform, which may indicate that crack initiation and propagation have occurred evenly across the sample. However, fatigue failure in the B2 case appears dominated by one main fatigue crack, based on the fracture surface observation.

From the fracture surface of B1 observed under SEM shown in Figure 6- 8, stringers in the regions between two ratchet marks are clearly visible, as indicated by blue arrows. In addition, regions between two ratchet marks can be recognized as a fatigue crack and they are labelled as crack B1-1, crack B1-2, crack B1-3, crack B1-4 and crack B1-5, for example. Crack B1-1 at higher magnification is detailed in Figure 6- 9. Inclusions are found beneath the

surface (Figure 6- 9(b)), which are considered to be the crack initiator. Similarly, inclusions are also identified in crack B1-2, crack B1-3, crack B1-4 and crack B1-5, as shown in Figure 6- 10(a), (b), (c) and (d), respectively. However, few ratchet marks are observed on the fracture surface of sample B2, as shown in Figure 6- 11. One possible crack initiation site for crack B2-1 is illustrated in Figure 6- 12(a) and (b). No clear inclusions are found in this region, and this may lead to the conclusion that this crack has possibly initiated from the re-peened rough surface, or from a crack tip that had not been successfully removed by the polishing stage. Although some small inclusions are identified in crack B2-2 region, as indicated in Figure 6- 12(c) and (d), they actually do not appear to be crack initiation sites and play little role in crack initiation. Figure 6- 12(e), (f) and (g) are three different positions within crack B2-2.

A replication technique was applied during both fatigue processes in sample B1 and B2. By tracing back through the replica records, crack morphologies of the fatigue crack B1-3 at different fatigue stages can be seen in Figure 6- 13. This crack was first identified at ~ 50 % of subsequent fatigue life, which appears very similar to the ground and polished baseline samples in Chapter 5. As the fatigue process went on, this crack propagated steadily, and it coalesced with crack B1-4 at a later fatigue stage. According to the replica records of sample B2, only one single fatigue crack was found during the fatigue process. What's more, this crack was detected at a very early fatigue stage (8 % of fatigue life). Region 1 and region 2 in the illustration of Figure 6-14 are two examples showing the possible pre-existing crack. No obvious crack propagation was observed until ~ 70 % of fatigue life, which again, is comparable to the crack growth behaviour in the T0 shot peened case in Chapter 5.

Figure 6- 15 (a) and (b) show the evolution of the half surface crack length $c$ at different numbers of fatigue cycles and fatigue life ratio, respectively. For comparison, crack length data for the polished, ground, and T0 shot peened cases are also plotted together with those observed in B1 and B2. Sample B1, where the initial fatigued region was removed following the 1$^{st}$ fatigue process, shows subsequent fatigue crack behaviour very similar to the baseline unpeened conditions (polished and ground) albeit slightly slower. The half surface crack length $c$ of the pre-existing fatigue crack in the B2 sample is up to 1200 μm even after the removal of the initial fatigue region, but it only

started to propagate at 60 - 70 % of the subsequent fatigue life ratio, as can be seen from Figure 6- 15(b). Crack tortuosity $c/c_{project}$ of the fatigue cracks in B1 and B2 are quite close to a constant value of 1.

The crack growth rates in both the B1 and B2 samples showed less scatter compared to those in polished, ground and T0 shot peened cases, as shown in Figure 6- 17(a) and (b). For sample B1, as the shot peened layer has been removed after the 1st fatigue process, and in light of the new rough surface induced by the material removal process, the cracks evaluated on this sample behave very similarly to those in un-peened conditions. Cracks propagated at a fairly constant rate and accelerated near the end of fatigue life. Cracks in sample B2, which has undergone a blend-polish-peen repair process, however, presented substantially lower $dc/dN$ values, typically between $10^{-8}$-$10^{-5}$ mm/cycle. In the later stage of fatigue life, the crack propagation rate increased but was still slower than observed in the B1 sample.

When the fatigue cracks were firstly picked up in sample B2, the surface crack length $2c$ was ~ 2400 μm. There is a strong possibility that this is a crack produced by the 1st fatigue process that was not completely removed by the polishing step. Given the complicated crack morphologies in the B2 sample, it is not appropriate to apply the crack aspect ratio evolution in the stress intensity range $\Delta K$ calculation. Hence, the crack aspect ratio is assumed to be a constant value 0.8 in all the $\Delta K$ level calculations. In terms of $dc/dN$ versus $\Delta K_{surface}$ or $da/dN$ versus $\Delta K_{depth}$, Figure 6- 18 also gives a reasonable comparison. The benefit of the repair process to sample B2 was clear, given it had a large pre-existing crack.

## 6.4 Discussion and recommendation for industry

### 6.4.1 Blend-polish-peen repair process

The 1st fatigue process of sample B1 and B2, was interrupted at 22000 cycles and 34000 cycles, respectively. This difference in the number of cycles until interruption was based on the similar surface crack lengths observed (~ 1200 - 1500 μm), which were captured by replication. In order to make sure the fatigue defects are sufficiently ground back, non-destructive testing with dye penetrant can be applied to size and locate. In order to pick up these defects

successfully, both the crack depth and the surface length scale should be detectable by nondestructive testing, which is typically around 500 μm. Theoretically, surface crack lengths from 1200 – 1500 μm will be sufficient for the NDT to detect (based on Chapter 4). However, NDT with dye penetrant was not able to identify the defects in both the B1 and B2 samples before grinding in the current study, which may be due to the closed nature of these cracks. The removal of material layers during the manual polishing in both conditions was controlled therefore to be ~ 750 μm. To compare the effects of the repair, sample B1 after the fatigue crack had been removed was then re-fatigue tested (the 2nd fatigue test); while sample B2 was shot peened again before the 2nd fatigue test was conducted. It's noticeable that the total fatigue life of B1 was 57201 cycles, while the blend-polish-peen repair sample had a life of 56425 cycles under similar externally applied local strain range conditions. Although there seems no obvious improvement in the total fatigue life for the B2 sample, fatigue crack growth behaviour still benefits from the repair process (from the viewpoint of *dc/dN*), especially when there was a large 'possible pre-existing crack'.

Based on the observations and discussion in Chapter 4 and Chapter 5, the shot peening process plays significant roles in affecting both fatigue crack initiation and propagation, especially in the T0 condition. The rough shot peened surface, such as the shot peened folds, or shot peened dimples, causes fatigue crack initiation. The strain hardened layer and compressive residual stress distribution beneath the surface may significantly reduce crack propagation in the depth direction in the early fatigue stages. Hence the fatigue crack tends to propagate along the surface. As the crack front grows within this region, the residual stresses are expected to redistribute. Once it breaks through these shot peened affected regions, crack growth in the depth direction becomes faster. This explains why fatigue cracks in the early fatigue stages are shallow (low *a/c*) in shot peened samples. When two or three cracks are close enough to each other, the faster crack propagation rate beneath the shot peened affected layers may contribute to sub-surface crack coalescence, which is more fully described in the serial sectioning (Section 4.3.3) and X-ray tomography section (Section 4.3.4).

Since the 1st fatigue process was based on the surface crack length 2*c*, the degree of subsurface crack coalescence was not clear. For sample B1, after about 750 μm of the material was removed from the notched region, the fatigue cracks seemed to have been completely removed. This may indicate that there was no subsurface crack coalescence or the coalescence had just started. However, for sample B2, the large possible pre-existing crack identified at the very beginning of the second fatigue test is considered to be a result of incompletely removed fatigue cracks. That is, due to sub-surface crack coalescence, the depth of the fatigue crack is much deeper than it was expected to be from the surface observations.

The surface roughness $R_a$ after the polishing process was ~ 1.9 μm in both B1 and B2. The crack initiation and propagation in the 2nd fatigue process show similarities to those in the basedline conditions, where the crack initiation was dominated by the inclusions, which can be clearly identified on the fracture surface. It is notable that the B1 underwent 35201 cycles in the 2nd fatigue process, which shows about a 38 % and 53 % improvement over the polished (25353 cycles) and ground samples (22745 cycles), respectively. The crack growth data were at the lower bound of those observed for the ground and polished cases. One possible reason could be the polishing marks left on the notched surface. The crack propagation direction was perpendicular to these marks, which may possibly impede the growth of cracks slightly.

In sample B2, the polishing marks seem less crucial since the second shot peening process followed. Although the pre-existing crack 2*c* is up to 2400 μm, the benefit of the second shot peening process on the crack growth is still obvious. In the present study, the effect of the shot peening process on fatigue behaviour is not simply dependent on the magnitude of the compressive residual stress induced by the shot peening process but also on the interrelationship between the surface conditions created by shot peening, including surface roughness and the work-hardened layer. The fatigue cycles for B2 in the 2nd fatigue process were 22425 cycles, equivalent to the ground condition, but only~ 50 % of the fatigue life in virgin T0 shot peened condition.

### 6.4.2 Recommendations to operators

During the maintenance or outage cycle, once the operators are considering a decision on a repair programme for the steam turbine components, it is recommended that replication or dye penetrant inspection should be taken at the fatigue regions where the blend polish-peen repair process is to be done. Special attention needs to be paid to cracks which are close to each other on a shot peened surface. Some of the damage inside the components will not be detectable through visual observation. Therefore, for these potential subsurface crack coalescence regions, non-destructive examinations (NDE) techniques may locate and provide more detailed defect information [5]. The depth of material removed should be based on the maximum expected depth of the fatigue cracks. In order to benefit from the re-peening process, it is suggested that all the fatigue cracks should be completely removed.

## 6.5 Conclusions

After the detailed analysis of the shot peening effect on fatigue crack initiation and propagation behaviour in previous chapters, this chapter has focused on the blend-polish-peen repair technique in the T0 shot peened condition. Two samples, B1 and B2, were interrupted at 22000 cycles and 34000 cycles respectively based on the apparently similar scale of surface crack length $2c_{project}$ (~ 1200 – 1500 μm) in the 1st fatigue process. Material was then removed from the notches to a depth of ~750 μm. Sample B1 was then re-fatigued by the 2nd fatigue process, without re-peening; while an interim T0 shot peened process was conducted on sample B2, then the 2nd fatigue test was applied. Some conclusions can be drawn as follows:

(1) The notch geometry profiles were measured by Talysurf profilometer. The stress concentration factor $K_t$ increased from 1.6 to 1.8 after ~750 μm of material was removed from the notch. An FE model based on the geometry after polishing was applied to make sure the samples were under the same strain range $\Delta\varepsilon_{11}$ in the notch region for the 2nd fatigue process. Any use of this repair procedure also needs to account for the increase in stress concentration factor through any deepening of the notch.

(2) Sample B1, without a re-peening process, exhibited slightly longer total cycles to failure. Fatigue crack initiation and propagation behaviour in the 2nd fatigue process exhibited great similarity to the unpeened baseline conditions (polished and ground), but the fatigue crack growth seems to benefit slightly, perhaps from the new set of polishing marks which are perpendicular to the crack tip growth direction.

(3) In the blend-polish-peen repair process (sample B2), although there seems no obvious improvement in the total fatigue life, fatigue crack growth behaviour still benefits from the repair process (in terms of *dc/dN*). It was noted there was a large 'possible pre-existing crack' that had not been completely removed by the polishing step.

## 6.6 Figures

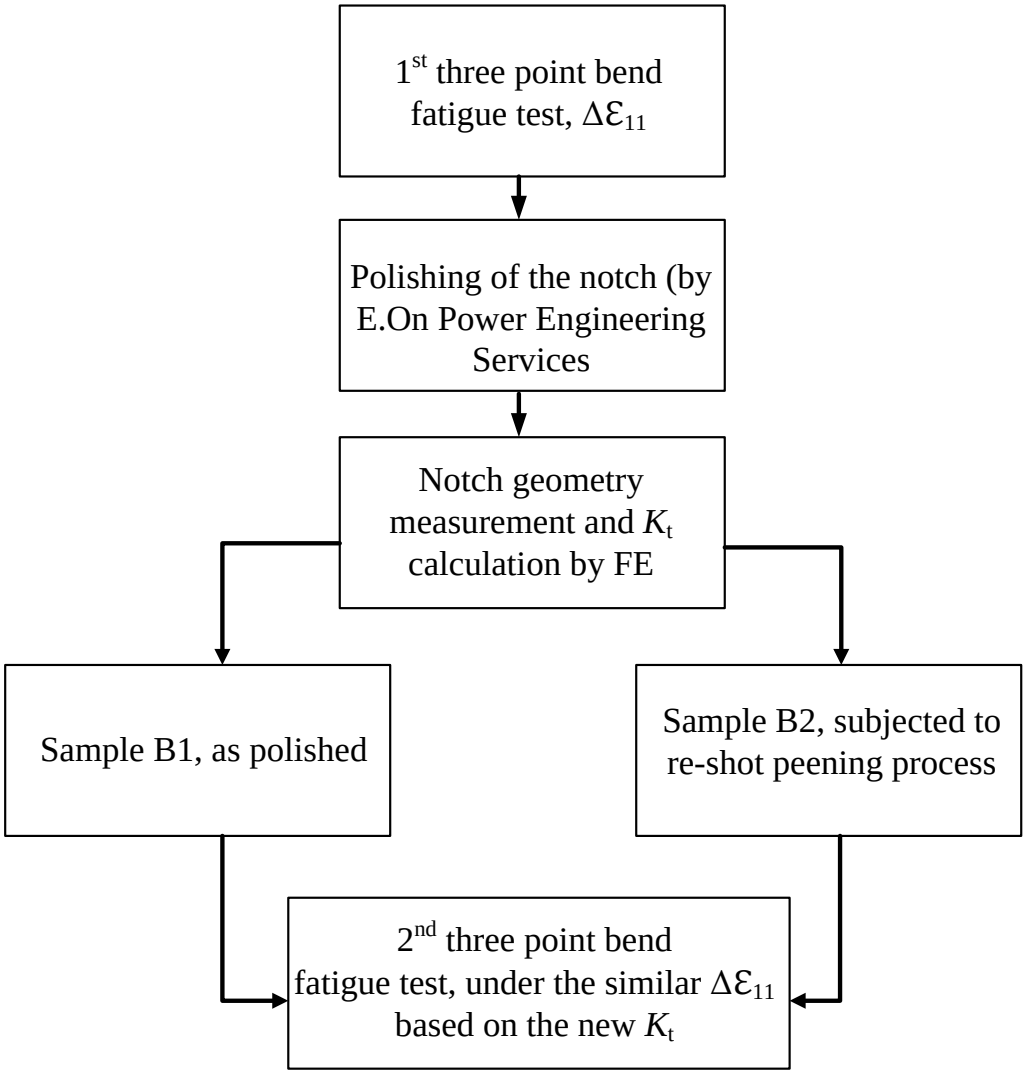


Figure 6- 1 Flow chart of the blend-polish-peen repair process.

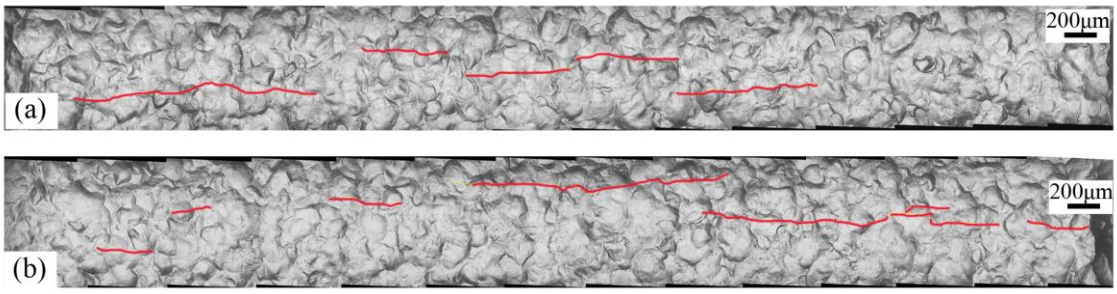


Figure 6- 2 Fatigue cracks detected on the replica record after fatigue cycles of (a) 22000 cycles (for B1) and (b) 34000 cycles (for B2).

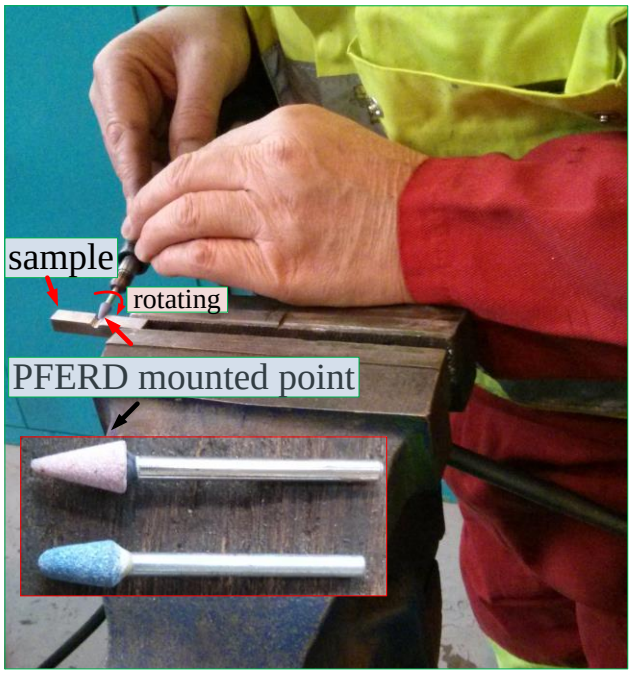


Figure 6- 3 Manual polishing process in the notch region.

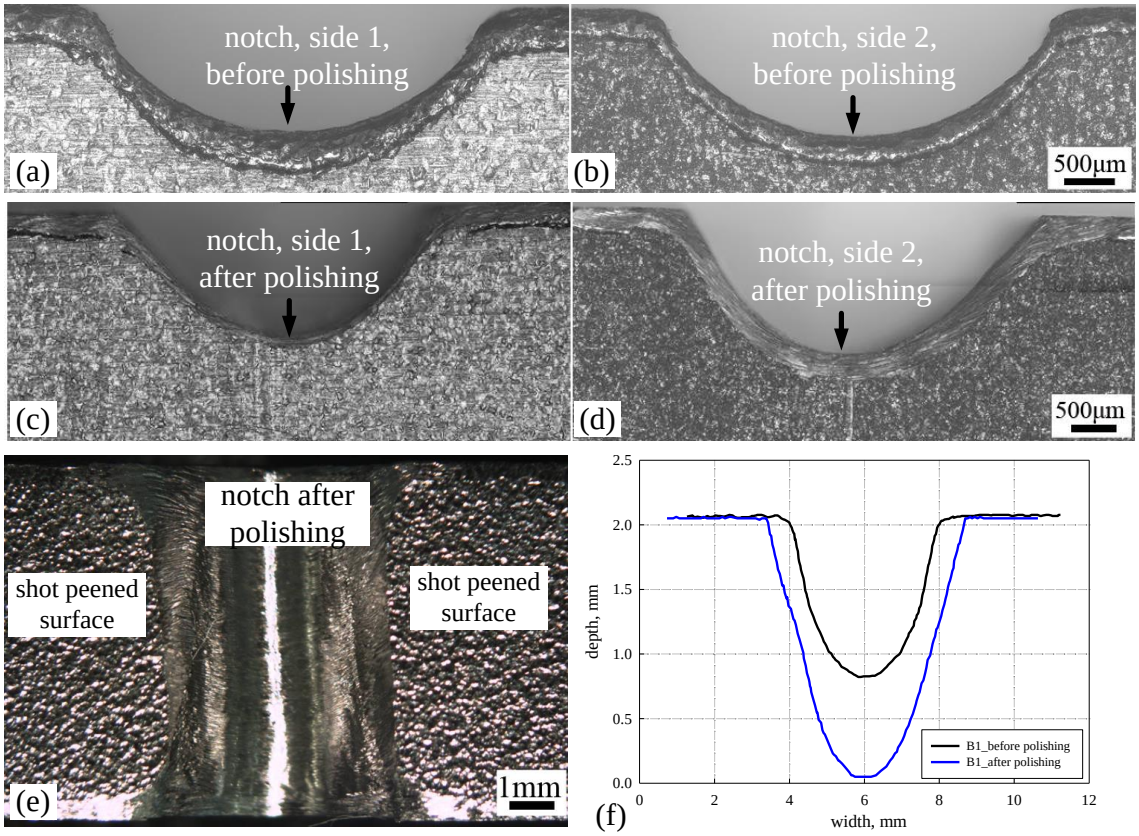


Figure 6- 4 The notch geometries of sample B1: (a) and (b) before the polishing process; (c) and (d) corresponding side views of the notch after polishing; (e) plane view of the notch; (f) comparison of the notch profiles by Talysurf.

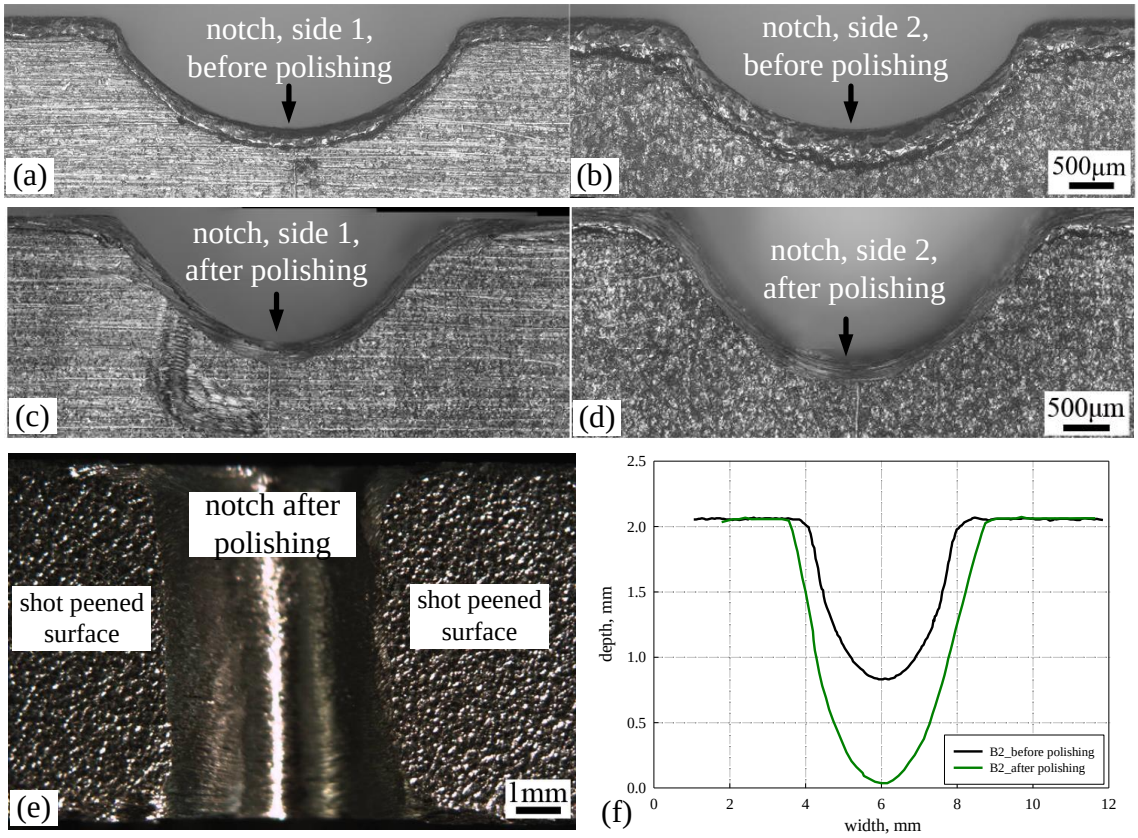


Figure 6- 5 The notch geometries of sample B2: (a) and (b) before the polishing process; (c) and (d) corresponding side views of the notch after polishing; (e) plane view of the notch; (f) comparison of the notch profiles by Talysurf.

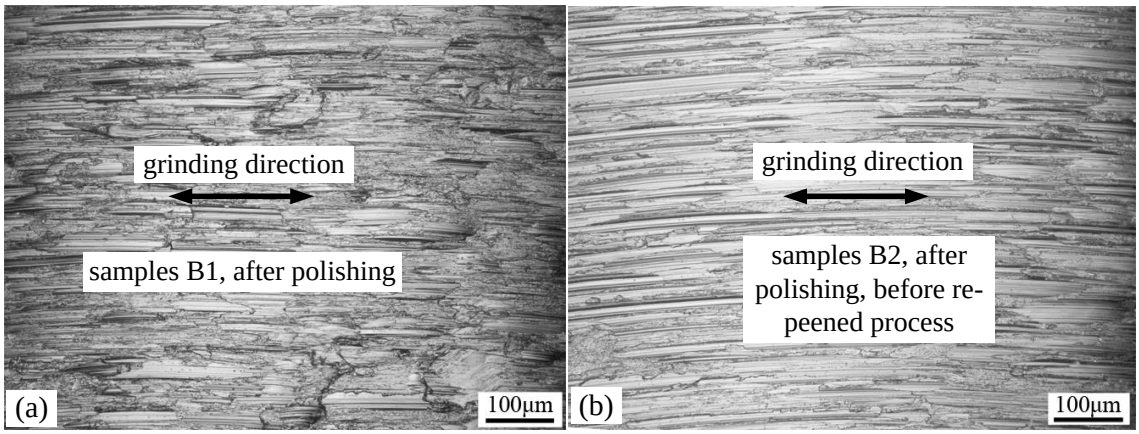


Figure 6- 6 The surface after polishing: (a) sample B1 and (b) sample B2.

Table 6- 1 The stress concentration factor $K_t$ and the nominal stress required before and after the removal of the fatigue cracks to reach the same value of $\Delta\varepsilon_{11}$ = 0.68 %.

| | Before polishing | After polishing |
|---|---|---|
| Stress concentration factor $K_t$ | 1.6 | 1.85 |
| Nominal stress required for $\Delta\varepsilon_{11}$ = 0.68% | 1048.1 MPa | 849.9 MPa |

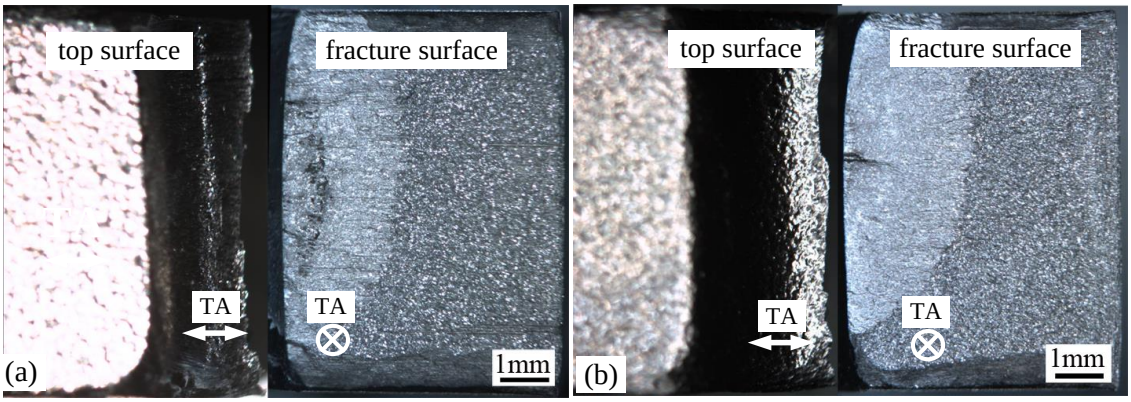


Figure 6- 7 Optical micrograph of fracture surface: (a) sample B1; (b) sample B2.

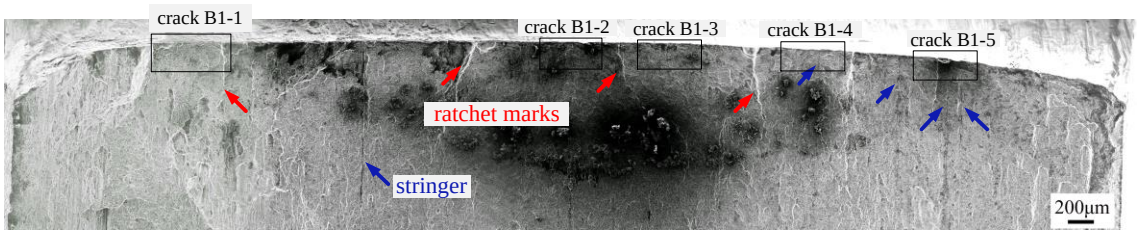


Figure 6- 8 SEM micrograph of B1 fracture surface.

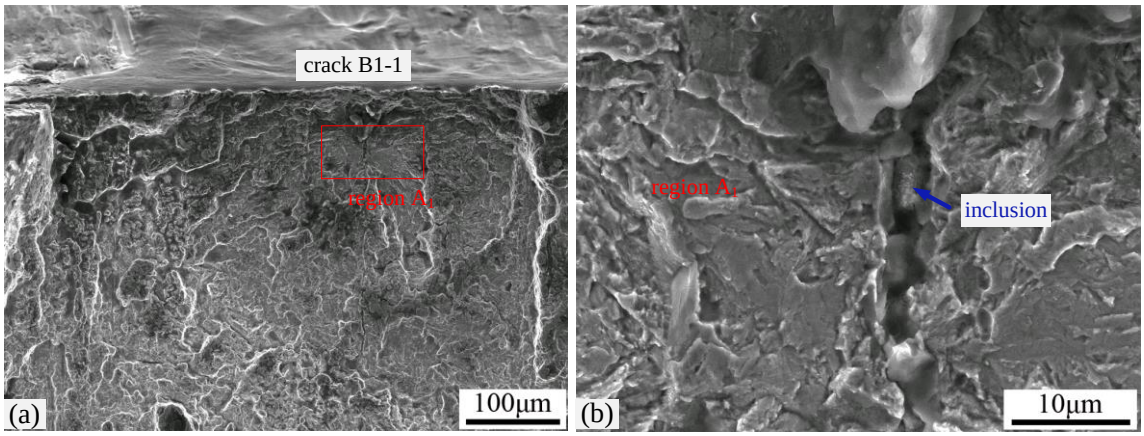


Figure 6- 9 SEM micrograph of crack B1-1.

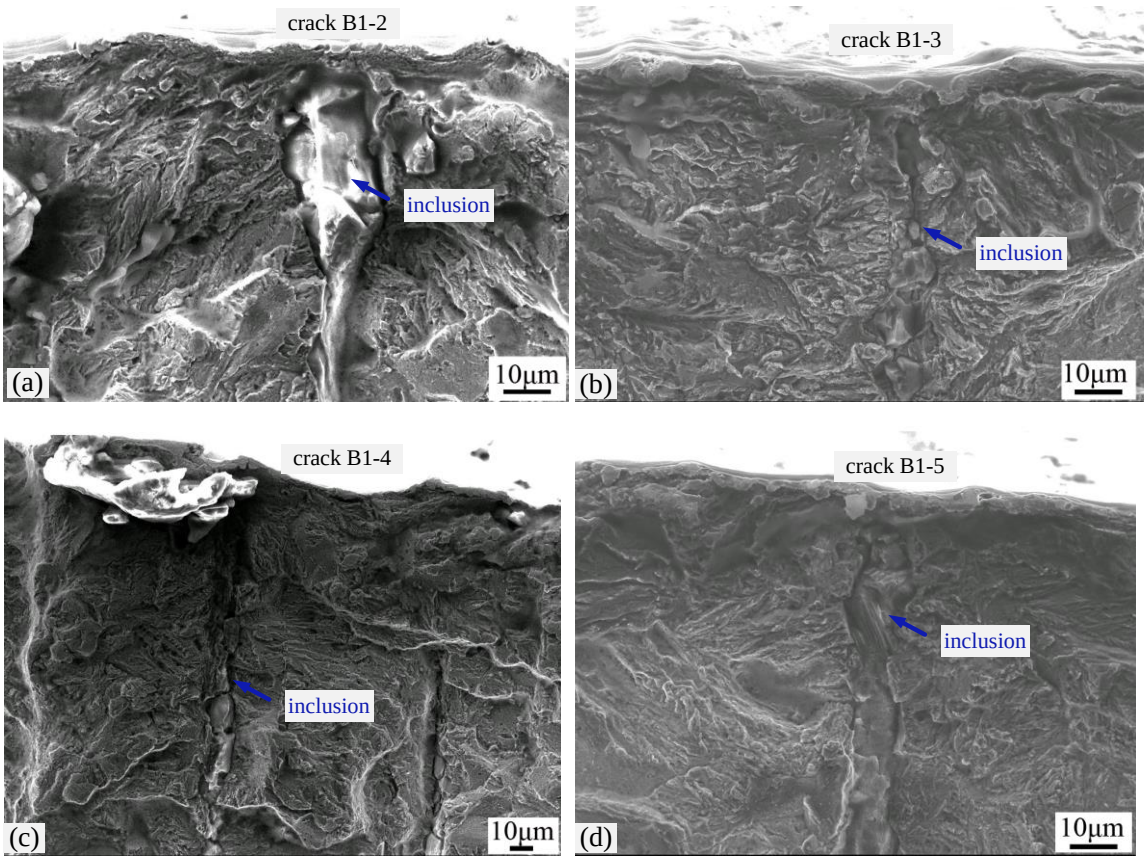


Figure 6- 10 SEM micrograph of (a) crack B1-2, (b) crack B1-3, (c) crack B1-4 and (d) crack B1-5 in sample B1.

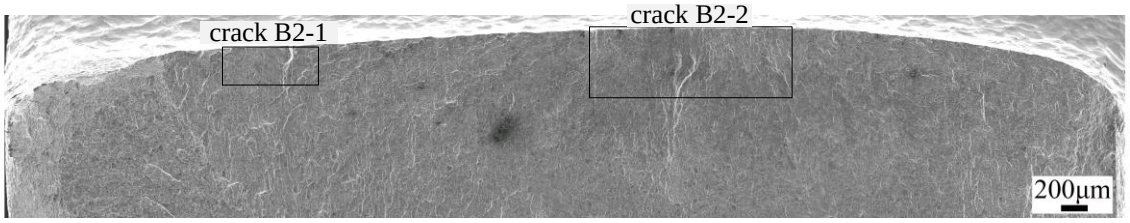


Figure 6- 11 SEM micrograph of B2 fracture surface.

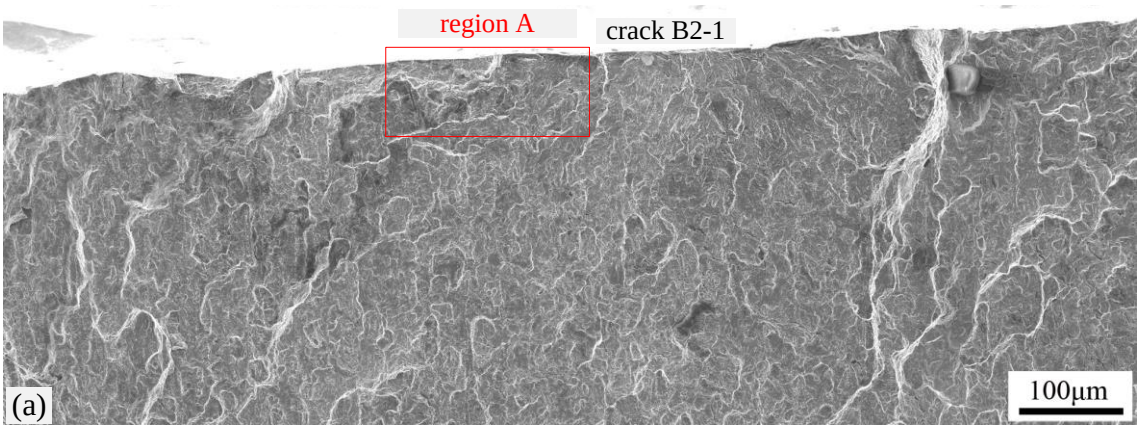

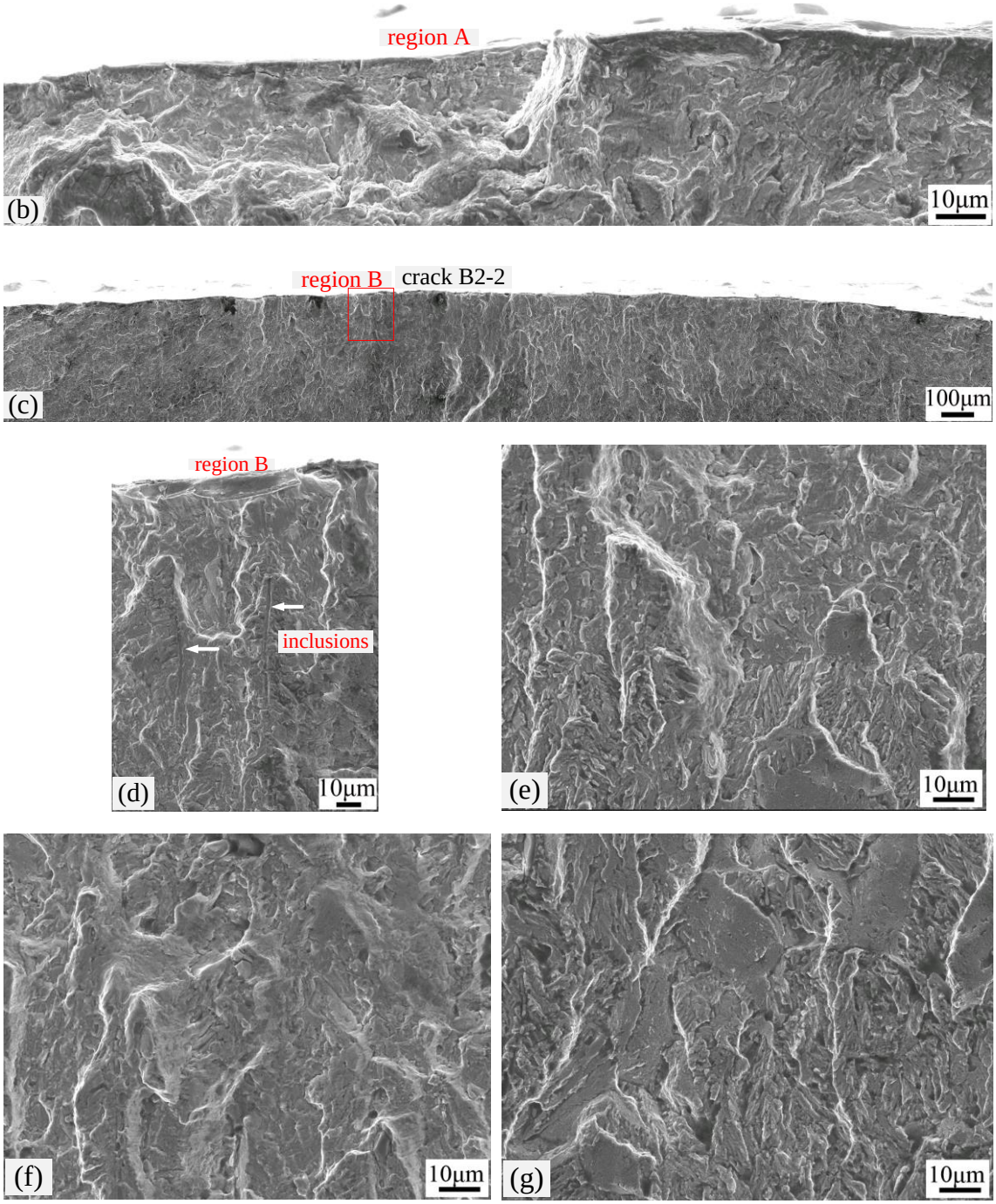


Figure 6- 12 (a) SEM micrograph of the crack B2-1; (b) region A labelled in crack B2-1; (c) crack B2-2; (d) region B in crack B2-2; (e) (f) and (g) are three different regions in crack B2-2.

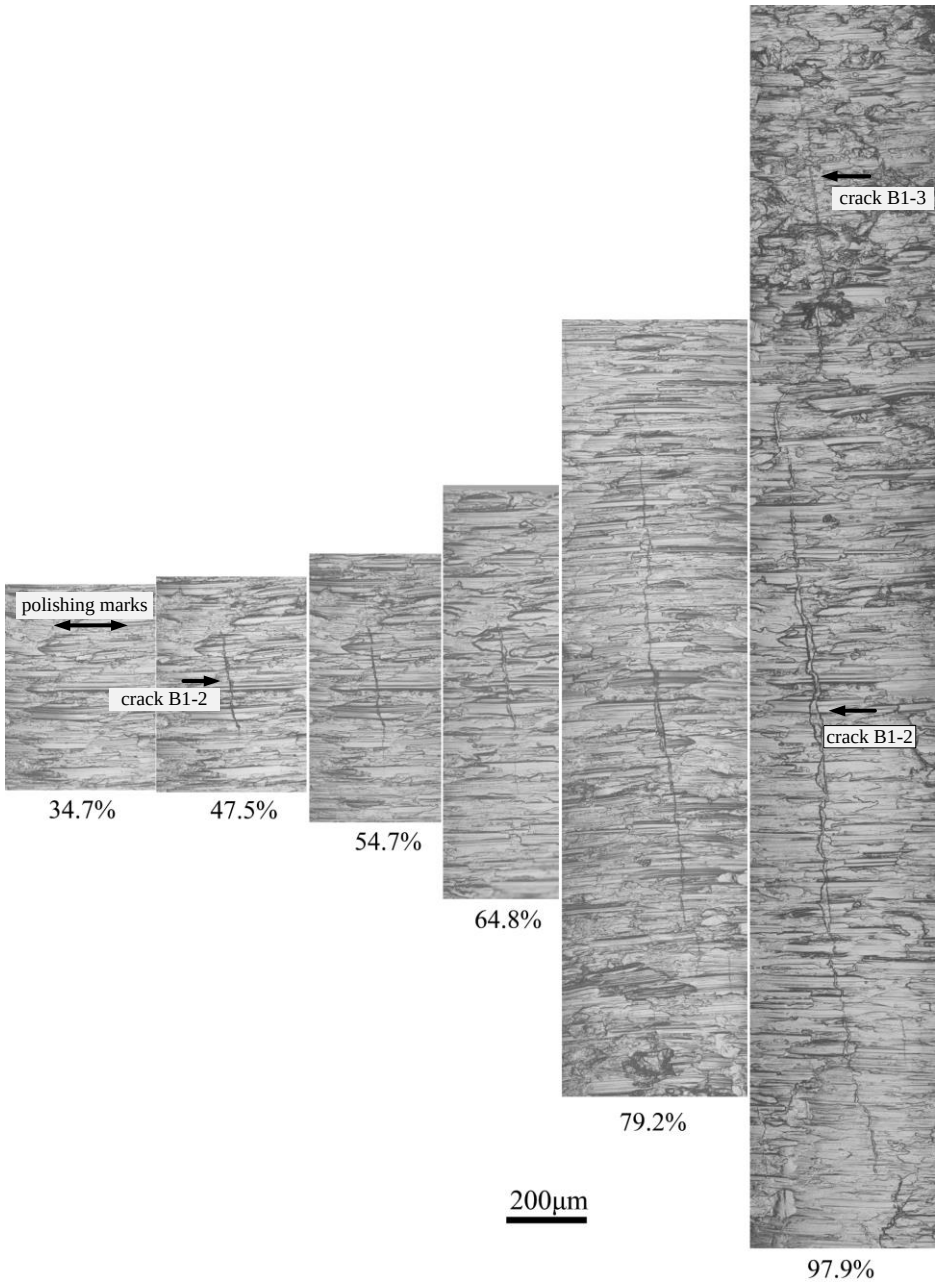


Figure 6- 13 The morphology at different percentages of life of crack B1-2 in sample B1 during the 2nd (post blend-polish) fatigue process.

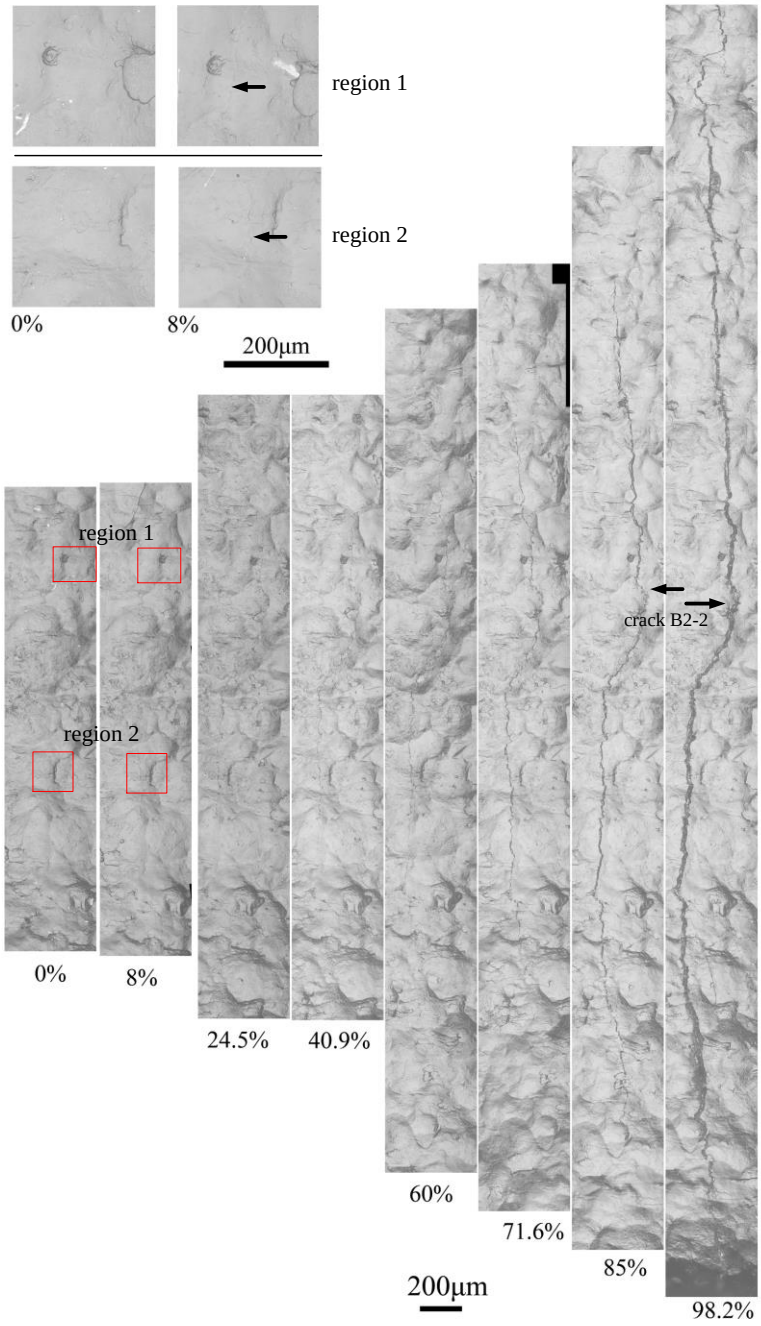


Figure 6- 14 The morphology at different percentages of fatigue life of crack B2-2 in sample B2 during the 2nd (post blend-polish-peen) fatigue process.

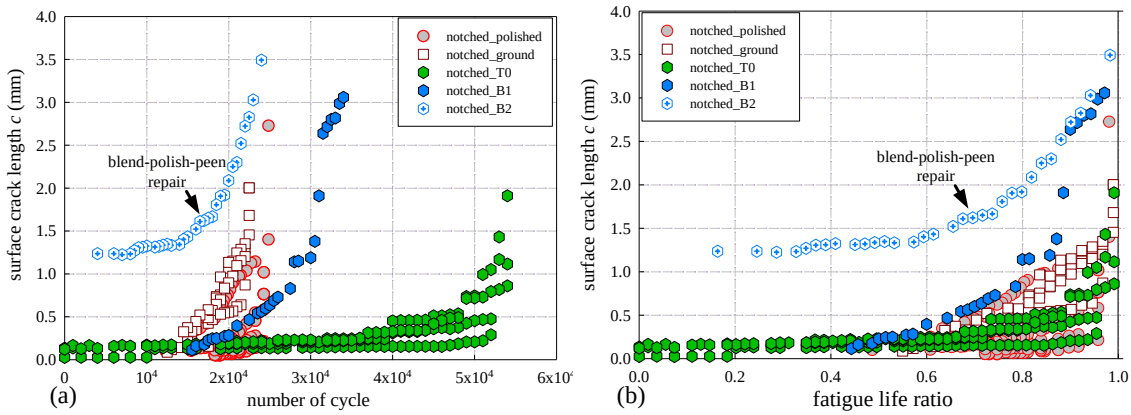


Figure 6- 15 (a) Half surface crack length *c* at different number of fatigue cycles; (b) half surface crack length *c* at different fatigue life ratios.

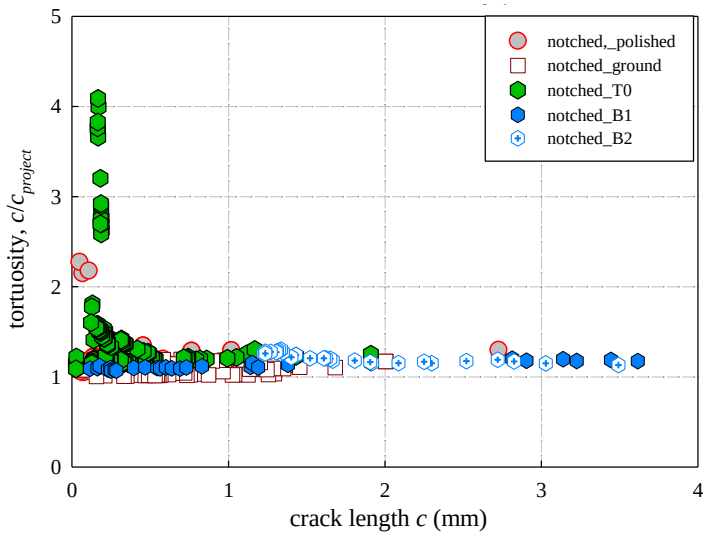


Figure 6- 16 Crack tortuosity $c/c_{project}$ at various crack lengths.

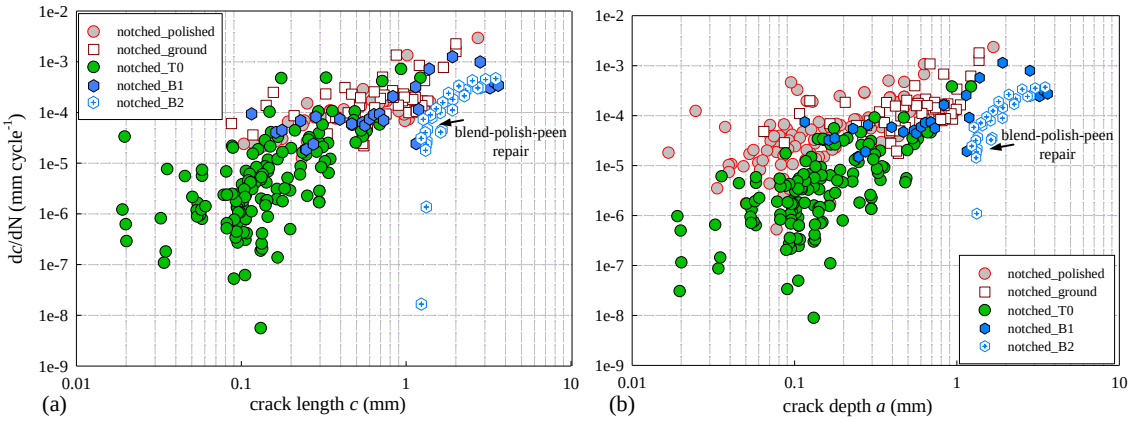


Figure 6- 17 (a) Crack propagation rate *dc/dN* vs half surface crack length *c*; (b) crack propagation rate *dc/dN* vs crack depth *a*, assuming crack aspect ratio is a constant 0.8.

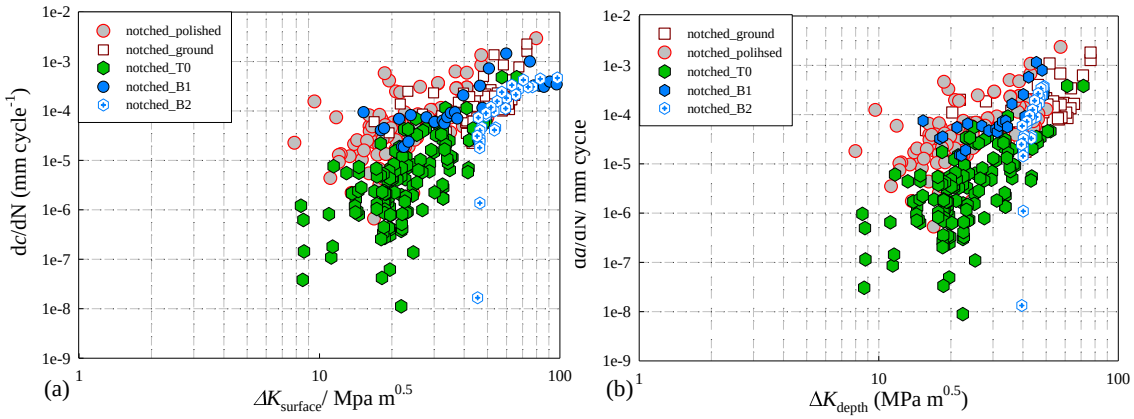


Figure 6- 18 (a) Crack propagation rate *dc/dN* as a function of stress intensity factor range $\Delta K_{surface}$ and (b) *da/dN* as a function of $\Delta K_{depth}$ (assuming a constant crack aspect ratio $a/c$ = 0.8).

## 6.7 References

[1] X. Chen, Z. Gong, H. Huang, L. Zhou, S. Ge, Q. Zhu, L. Woon, *An automated 3D polishing robotic system for repairing turbine airfoils*, Industrial Automation Journal, 8 (1999) 6-11.
[2] K. Hollingworth, R. Ortolano, *The application of weld repair techniques to reduce costs and outage time of steam turbines*, Proceedings of the Institution of Mechanical Engineers, Part A: Journal of Power and Energy, 204 (1990) 87-97.
[3] R.E. Clark, D.R. Amos, *Method for repairing a steam turbine or generator rotor*, in, Google Patents, 1987.
[4] K.A. Soady, *Reducing conservatism in life assessment approaches: Industrial steam turbine blade to disc interfaces and the shot peening process*, in: Engineering Sciences Unit, Ph.D thesis, the University of Southampton, 2013.
[5] K.J. Pallos, *Gas turbine repair technology*, 2001.

# Chapter 7: Conclusions

Shot peening is a well-established manufacturing process applied to various components, especially the regions of stress concentrations, to improve their fatigue resistance. Although the beneficial effect of shot peening on the high cycle fatigue regime is well documented, the relationship between the shot peening process and low cycle fatigue short crack behaviour is less well understood, and the retention of any shot peening effect appears more service condition dependent in the LCF regime.

A tempered martensitic microstructure was identified in FV448 (the material studied) in this work. The prior austenite grain boundaries were clearly identified in the longitudinal, transverse and short transverse directions of the barstock material. In addition, the grain size distributions of the prior austenite were not found to be significantly different in these three directions. However, inclusions of aluminium oxide/silicate and manganese sulphide were found aligned in the longitudinal direction.

Two different shot peening processes were focused upon in this study. To gain a better understanding about the effect of shot peening, the polished surface condition, and the ground surface condition (the state of samples before any peening process) were also studied. Compared to the less intense shot peened case T1, the T0 shot peening process (the industry applied standard) induced more severe surface plastic deformations (such as shot peening lips at the edge of samples) and larger shot peened dimple sizes on the surface. The surface roughness $R_a$ and $R_z$ linear measurements obtained by both contact and optical approaches were found to be much lower that the areal measurements $S_a$ and $S_z$ captured via the optical approach, which indicates that the most severe surface features (which are most likely to initiate fatigue) may not be detected/sampled by conventional linear contact measurements of surface roughness. The residual stress distributions were measured by X-ray diffraction using the $\sin^2\psi$ technique in both the longitudinal and the transverse directions in polished, ground, T0 and T1 shot peened conditions notched samples. In the ground sample, there was thin layer of compressive residual stress in both the longitudinal (perpendicular to grinding marks) and transverse (parallel to grinding marks) directions which decreased going into the bulk of the sample and turned into a balancing tensile residual stress;

these reached a maximum value at ~ 50 μm beneath the surface, and then decayed gradually to zero. The tensile residual stress observed in the ground condition was removed by polishing. Conversely, in the polished case there also existed a thin but slightly greater residual compressive stress layers in both longitudinal and transverse directions to ~ 20 μm.

The depth of the maximum compressive residual field in the T1 and T0 condition is almost the same, but the total compressive residual stress layer in T0 extends to a greater depth (~ 300 – 350 μm) than the T1 case (~ 180 – 200 μm). In addition, the surface compressive residual stress in the intense shot peening condition (T0) is slightly greater than in the less intense (T1) condition.

Fatigue crack aspect ratio (*a/c*) evolution in the early stages of crack growth in polished and shot peened cases was investigated. In the polished sample, microstructure (alumina stringers as well as MnS) played an important role in early crack initiation and propagation. Initially, the aspect ratio for these short cracks was around 1.0 ~ 1.2; as the surface crack length 2*c* increased, the value decreased to the equilibrium aspect ratio of 0.8. In the T0 shot peened case, the aspect ratio was low and increases with increasing crack depth *a* when $a < 120 \sim 150$ μm, after which the crack aspect ratio decreased gradually (due to frequent crack coalescence). However, *a/c* evolution in the T1 sample combines the trends observed in the T0 and polished conditions. The shallower aspect ratio in the shot peened case has been linked to the greater difficulties encountered by the crack to grow sub-surface into the compressive residual stress and strain hardened layer compared to the polished case.

From the 3D crack morphology, in the un-peened sample, inclusions (alumina and MnS) play an important role in early fatigue crack behaviour. They act as stress raisers, and thus crack initiators. For fatigue cracks initiated from an alumina stringer, the crack morphology normally was dominated by only one (large) stringer, which was always in the centre region of the crack; while the MnS inclusions, seemed to dominate/affect the crack path in both surface and depth crack growth directions as they formed in clusters. In the less intense shot peening condition (T1), the fatigue crack morphology is similar to the baseline (unpeened). Cracking initiated from an alumina stringer was observed, but there was no clear evidence that there is subsurface crack coalescence. For

the intense shot peening condition (T0), however, inclusions do not seem to affect crack initiation behaviour. Subsurface crack coalescence was also captured by serial sectioning and X-ray tomography at around 150 ~ 180 μm beneath the shot peened surface. This may be linked to both the extent of the compressive residual stress and the depth of the plastic deformation from the shot peening process. The shot peening process has "de-activated" the underlying metallurgical defect distribution, and substituted a surface roughness initiated defect population. If insufficient shot peening intensity is applied, then the underlying metallurgical defect distribution still operates, and can outweigh any (limited) effect from a very thin work hardened layer and compressive residual stress zone. However, in the PBB sample, not only the orientation, but also the position and size of the stringers will strongly affect fatigue crack growth in both baseline and T0 shot peened condition

Short fatigue crack analyses (initiation and propagation behaviour) were conducted in polished, ground, T0 and T1 samples containing a stress concentration feature. Under the same expected strain range condition ($\Delta\varepsilon_{11}$ = 0.68 %), the ground and T1 shot peening case have similar fatigue life, while the polished case benefitted somewhat from the low roughness surface and fatigue life improved by ~ 11 %. The T0 shot peened process exhibited the best fatigue life, almost twice that of the baseline and T1 cases even in the LCF regime. The crack growth behaviour in the polished (baseline) condition is similar to that in the ground condition, whilst crack growth rates in the shot peened case are significantly delayed while the crack grows through the expected depth of the significant compressive residual stress field/work hardened region. Evidence has been presented for small preexisting cracks on the shot peened surface, which only started to grow at around 10 – 25% of the fatigue life. At this stage, the crack propagation rate was lower than for the ground sample, until the depth of the crack exceeded the expected depth of the significant compressive residual stress field/work hardened region. The beneficial role then of shot peening is to slow crack propagation into the depth and the evolution of both crack aspect ratio and the occurrence of crack coalescence events in the shot peened case can be linked to the extent of the work hardened layer and the compressive residual stress field.

The *a/c* evolution effects were incorporated in *K*-evaluations and assumptions about growth in the depth direction; apparent residual stress (based on crack

driving force $\Delta K$ difference assumptions) shows crack growth retardation beyond the measured region of compressive residual stress, which is probably due to the effects of the strain hardened layer, stress redistribution as the cracks grow and coalescence behaviour which are not captured by this assumption.

After the detailed analysis of the shot peening effect on fatigue crack initiation and propagation behaviour, the final chapter focused on assessing the blend-polish-peen repair technique in the T0 shot peened condition. The notch geometry profiles changed significantly after the polishing process, the stress concentration factor $K_t$ increased from 1.6 to 1.85 after ~ 750 μm of material was removed from the notch. A FE model based on the geometry after polishing was applied to make sure the samples were subsequently tested under the same strain range $\Delta\varepsilon_{11}$ in the notch region in the 2nd fatigue evaluation.

Without re-peening a slightly longer total fatigue life was seen. The fatigue crack initiation and propagation behaviour were very similar to the unpeened baseline conditions (polished and ground) despite the increased surface roughness after the polishing repair.

In the blend-polish-peen repair process although there seemed no obvious improvement in the total fatigue life, the fatigue crack growth behaviour still benefitted from the repair process (from the viewpoint of *dc/dN*), especially when there was a large 'possible pre-existing crack' from insufficient material removal in the polishing stage.

# Appendix A *K* evaluation based on Scott and Thorpe's review paper[1]

Schematic of semi-elliptical crack is shown in Figure A- 1. At the bottom (θ=π/2) of the notch, crack tip intensity factor:

$$K_I = M_{f(\frac{\pi}{2})}\left[1 - 1.36\left(\frac{a}{t}\right)\left(\frac{a}{c}\right)^{0.1}\right]\frac{\sigma_b}{E(\mathrm{K})}\sqrt{\pi a}$$

Equation A- 1

While the front face magnification factor:

$$M_{\mathrm{f}(\frac{\pi}{2})} = 1.13 - 0.07\left(\frac{a}{c}\right)^{0.5}$$

Equation A- 2

While

$$\mathrm{E(K)} = \left[1 + 1.47\left(\frac{a}{c}\right)^{1.64}\right]^{0.5}$$

Equation A- 3

is the elliptic integral of the second kind;

And the finite area correction for bending case is:

$$B_w = 1 + \frac{F\left(\frac{a}{c}\right)G\left(\frac{c}{w}\right)H\left(\frac{a}{t}\right)}{(0.2745)^2}$$

Equation A- 4

$$\mathrm{F}\left(\frac{a}{c}\right) = 0.38 - 0.141\left(\frac{a}{c}\right) - 0.366\left(\frac{a}{c}\right)^2 + 0.569\left(\frac{a}{c}\right)^3 - 0.248\left(\frac{a}{c}\right)^4$$

Equation A- 5

$$\mathrm{G}\left(\frac{c}{w}\right) = -0.0239 + 1.434\left(\frac{c}{w}\right) - 2.984\left(\frac{c}{w}\right)^2 + 7.822\left(\frac{c}{w}\right)^3$$

Equation A- 6

$$\mathrm{H}\left(\frac{a}{t}\right) = -0.0113 + 0.323\left(\frac{a}{t}\right) + 0.749\left(\frac{a}{t}\right)^2 - 0.535\left(\frac{a}{t}\right)^3$$

Equation A- 7

F(a/c), G(a/c) and H(a/c) are polynomial functions based on typical laboratory specimens size.

At the surface (θ=0), the crack tip intensity factor

$$K_I = \left(\frac{1+\gamma}{3+\gamma}\right)\sigma_b\sqrt{\pi c}$$

Equation A- 8

Since in this steel, Poisson's ratio, ɣ=0.3, so

$$K_I = 0.394\sigma_b\sqrt{\pi c}$$

Equation A- 9

With interpolation at a/t:

$$K_I = \left[\left[M_{f(0)}\left(1-0.3\frac{a}{t}\right)\left(1-\left(\frac{a}{t}\right)^{12}\right)\right]+\left[0.394\cdot E(k)\cdot\left(\frac{a}{t}\right)^{12}\cdot\sqrt{\frac{c}{a}}\right]\right]\frac{\sigma_b}{E(k)}\sqrt{\pi a}$$

Equation A- 10

Where

$$M_{f(0)} = \left[1.21-0.1\left(\frac{a}{c}\right)+0.1\left(\frac{a}{c}\right)^4\right]\sqrt{\frac{a}{c}}$$

Equation A- 11

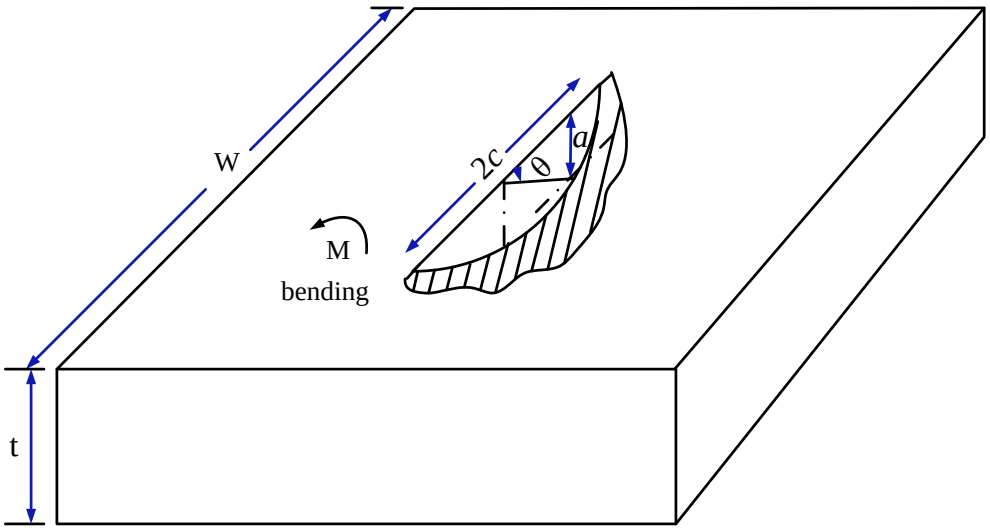


Figure A- 1 Schematic of semi-elliptical crack.

[1] P.M. Scott, T.W. Thorpe, *A critical review of crack tip stress intensity factors for semi-elliptic cracks*, Fatigue & Fracture of Engineering Materials & Structures, 4 (1981) 291-309.